INERTIAL CONFINEMENT FUSION

Lawrence Livermore National Laboratory

*ICF Quarterly Report* *October—December 1998, Volume 9, Number 1*

# *Special Issue: Laser Technology for the National Ignition Facility*

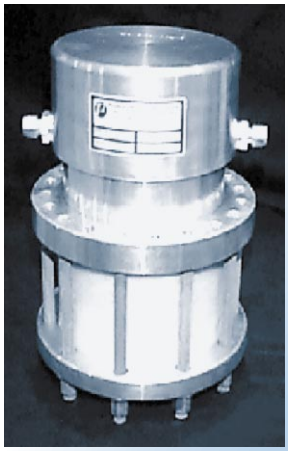

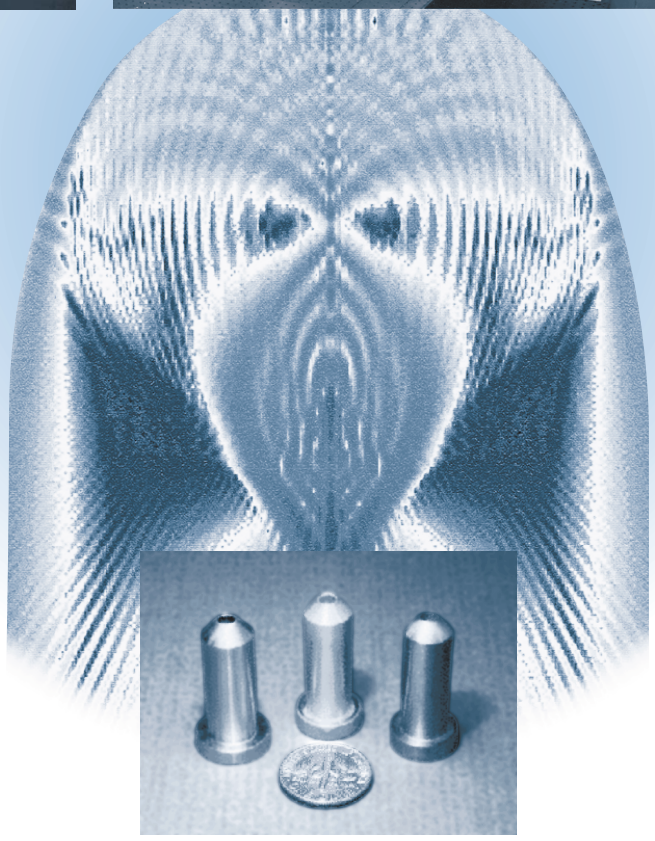



UCRL-LR-105821-99-1

**The Cover:** Several components and results stemming from the NIF laser technology and *engineering* developments are shown. In the *upper left* is a picture of the 500-kA spark gap switch developed by Maxwell/Physics International, which enables the cost-effective, high-energy, pulse-power modules designed for the NIF (see the article "Main Amplifier Power Conditioning for the NIF" on p. 15). On the *upper right* is a picture of a prototype 4 × 1 plasma electrode Pockels cell (PEPC) mounted on its side for convenient testing in the laboratory. The PEPC, when energized, rotates the polarization of the light across the apertures of four beams to allow four-pass pulse amplification in the main amplifier cavity (see the article "Multiaperture Optical Switch for the NIF" on p. 33). The contour plot resembling a bird's face, shown in the *center*, is actually the calculated intensity distribution of laser light after it passes through a small (4-$\mu$m-diam) zirconia inclusion imbedded in fused silica. The light, which propagates from top to bottom, shows local intensifications as large as 1000 times that can readily cause optical damage because of the focusing action of the inclusion and interference with the main beam (see the article "Modeling the Interaction of the NIF Laser Beam with Laser Components" on p. 63). The three tubular objects compared to a dime at *bottom* are actually conical pinholes of the type tested in the Beamlet laser. The use of high-Z conical pinholes allows temporally shaped NIF pulses to be spatially filtered down to 150 $\mu$rad. This filtering produces more uniform beams that allow increased NIF output energy without the threat of plasma generated in the pinhole cutting off the pulse in time (see the article "Beamlet Experiments" on p. 43).

**The *ICF Quarterly Report*** is published four times each fiscal year by the Inertial Confinement Fusion Program at the Lawrence Livermore National Laboratory. The journal reports selected current research within the ICF Program. Major areas of investigation presented here include fusion target theory and design, target fabrication, target experiments, and laser and optical science and technology. In addition, the Laser Science and Technology program element of LLNL's Laser Programs serves as a source of expertise in developing laser and electro-optics capabilities in support of the ICF mission and goals and also develops new lasers for government and commercial applications. To keep our readers informed of these new capabilities, the *ICF Quarterly Report* now covers additional non-ICF funded, but related, laser research and development and associated applications. As another improvement, we have added a short summary of the quarterly activities within Nova laser operations and NIF laser design. Questions and comments relating to the technical content of the journal should be addressed to the ICF Program Office, Lawrence Livermore National Laboratory, P.O. Box 5508, Livermore, CA 94551.

**On the Web:**
*http://lasers.llnl.gov/lasers/pubs/icfq.html*

UCRL-LR-105821-99-1
October–December 1998



Printed in the United States of America
Available from
National Technical Information Service
U.S. Department of Commerce
5285 Port Royal Road
Springfield, Virginia 22161
Price codes: printed copy A03, microfiche A01.

Work performed under the auspices of the U.S. Department of Energy by Lawrence Livermore National Laboratory under Contract W–7405–Eng–48.

INERTIAL CONFINEMENT FUSION

*ICF Quarterly Report* October–December 1998, Volume 9, Number 1

# In this issue:

UCRL-LR-105821-99-1

# FOREWORD

In 1994, a group of scientists and engineers at Lawrence Livermore National Laboratory (LLNL), with input from the other U.S. inertial confinement fusion (ICF) laboratories, formed a four-year laser development plan to enable the construction of the laser hardware for the National Ignition Facility (NIF).* The risk-reduction laser activities necessary to complete detailed Title II engineering for NIF were defined, the manpower requirements and overall costs in each area were estimated, the required development laboratories and teams were identified, and preliminary milestones were proposed. With both financial and technical help from the French Commissariat a l'Energie Atomique (CEA), we began laser development activities in earnest in 1995. Simultaneous with the laser-component development activities, a NIF Project engineering team was assembled and began the design of the real NIF hardware, interfaces, and assembly plans. The development and engineering activities were completely on schedule four years later at the end of 1998, as marked by the completion of detailed Title II engineering reviews.

The activities in the intervening four years were intense and involved a large number of people from LLNL, Sandia National Laboratories (SNL), Los Alamos National Laboratory (LANL), the French CEA, and many other groups. Laser-development activities covered most of this period while the team continuously redefined the milestones and conducted frequent laser-technology reviews. This issue of the *ICF Quarterly Report* describes the NIF laser component designs that resulted from these laser development and engineering activities.†

In this issue, the article "The NIF Injection Laser System" by Crane et al. describes the ultrastable and ultraflexible laser pulse generation system that provides input to each of the 192 beams of the NIF. The article "Main Amplifier Power Conditioning for the NIF" by Newton et al. summarizes the work of the joint LLNL and SNL team, who successfully tested a "first-article" 1.7-MJ power conditioning module at Sandia in Albuquerque, NM. The article "Integrated Computer Control System" by VanArsdall et al. describes the complex, distributed computer control system for the NIF, which may be a model for other large computer control systems. The article "Multiaperture Optical Switch for the NIF" by Rhodes et al. describes the design basis and performance of a prototype 4 × 1 plasma electrode Pockels cell that matches the NIF beam architecture. The article "Beamlet Experiments" by Wegner et al. gives the results of the experimental campaigns on the Beamlet laser to define the design and performance limits of the NIF. The article "Modeling the Interaction of the NIF Laser Beam with Laser Components" by Feit and Boley describes the use of target-interaction modeling to understand and improve the laser performance limits. The article "Beam Control and Laser Diagnostic Systems" by Bliss et al. describes the wavefront system and the alignment and diagnostic system resulting from development and engineering. Finally, the article "Design and Performance of Flashlamp-Pumped Nd:Glass Amplifiers for the NIF" by Erlandson et al. describes the work of an integrated U.S.–French team to design and prototype the large 4 × 2 power amplifiers. This article is reprinted from the last *Quarterly* issue (Vol. 8, No. 4) for this special issue in order to cover all the NIF laser design and development results.

Howard T. Powell
Scientific Editor

*See Chapter 1 of the document *Core Science and Technology Plan for Indirect Drive ICF Ignition*, H. Powell and J. Kilkenny, Lawrence Livermore National Laboratory, Livermore, CA, UCRL-ID-117076 Rev. 1 (December 1995).

†More scientifically detailed descriptions of both the U.S. and French work, as well as work of smaller ICF laser research groups around the world, can be found in *SPIE*, Volumes 2633, 3047, and 3492. These volumes were published following the First, Second, and Third International Conferences on Solid-State Lasers for Application to Inertial Confinement Fusion held respectively in Monterey, CA; Paris, France; and Monterey, CA, in 1995, 1996, and 1998.

# THE NIF INJECTION LASER SYSTEM

*J. K. Crane* *R. B. Wilcox* *M. Hermann* *M. Martinez* *B. Moran*
*M. Henesian* *G. Dreifuerst* *B. Jones* *J. E. Rothenberg* *K. M. Skulina*
*D. Browning* *L. A. Hackel* *L. Kot* *F. Penko* *F. Deadrick*

The injection laser system (ILS), or "front end," is the portion of the National Ignition Facility (NIF) where a single pulse is produced, modulated, and shaped, then amplified and multiplexed to feed the 192 main amplifier chains in the NIF.[1] The ILS's three major subsystems are summarized in the overview, then described in detail in their own sections. In many cases, the subsystems have been developed and are in an engineering prototype phase in which we work with outside vendors to produce hardware. We have also connected two of the subsystems, the master oscillator room (MOR) and preamplifier module (PAM) development labs, to perform integrated performance measurements on a combined system.

## Overview

The ILS is composed of three major subsystems: the master oscillator room (MOR), the preamplifier modules (PAMs), and the preamplifier beam transport system (PABTS).

The master oscillator room is responsible for generating the single pulse that seeds the entire NIF laser system. In the MOR, this single pulse is phase-modulated to add bandwidth, then multiplexed into 48 separate beamlines on single-mode, polarizing fiber. Before leaving the MOR, the pulses are temporally sculpted into high-contrast shaped pulses designed to produce ignition of the deuterium–tritium (D–T) targets. Forty-eight single-mode fibers from the MOR serve as inputs to the 48 PAMs that are the second major subsystem in the ILS.

The preamplifier modules provide the largest amount of amplification in the entire NIF laser system, >100 dB. In addition to providing amplification, the PAMs spatially shape the Gaussian beam that emerges from the single-mode fiber to form a square beam that is shaped to compensate for the spatial gain profiles of the main slab amplifiers. A third function performed in the PAMs is spectral dispersion of the phase-modulated light produced initially in the MOR. This dispersion is part of a scheme called smoothing by spectral dispersion, or SSD,[2] that reduces the spatial coherence of the laser light irradiating the target. The 48 17-J outputs from the PAMs enter the final subsystem of the ILS, the preamplifier beam transport system.

In the PABTS, the 48 beams from the 48 PAMs are split into 192 separate beams that feed the main amplifier chains. After this four-way split of the beams, each leg has an optical trombone section for precisely adjusting the timing so that all 192 beams converge on target simultaneously.

Figure 1 shows a schematic block diagram of the ILS and its constituent systems. The requirements for the ILS are derived from the overall laser system requirements at the target. Table 1 lists the overall system requirements at the target and the resulting parameters for the ILS determined from the flowdown.

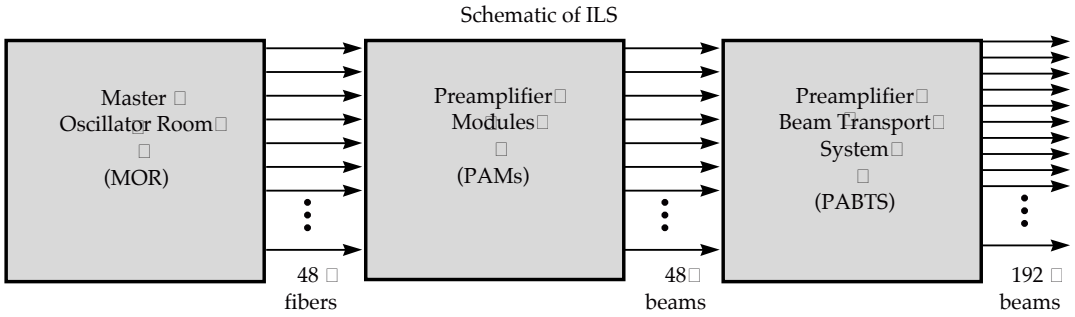


FIGURE 1. The NIF injection laser system (ILS). (70-00-0299-0358pb01)

TABLE 1. System requirements for the laser at the target and the requirements at the output of the ILS, determined from a flowdown of the system requirements back to the front end.

| NIF System Requirements[a] | | Injection Laser System Requirements | |
|---|---|---|---|
| Output energy | 1.8 MJ | Injected energy into main amps | 3 J |
| Peak power | 500 TW | Peak power at injection | 1.2 GW |
| Wavelength | 352 nm | Preamp output energy (flat-top beam) | 22 J |
| Pulse duration | 20 ns | Preamp power energy (shaped beam) | 16.9 J |
| Power balance | 8% in 2-ns window | Wavelength | 1053 nm |
| Pointing accuracy @ target | 6 μrad | Pulse duration | 20 ns |
| Power dynamic range | >50:1 | Output pulse rate | 1/20 minute |
| Prepulse in 20-ns window | $<10^8$ W/cm$^2$ | Prepulse contrast | $>2 \times 10^6$ |
| Number of beamlets | 192 | Square pulse distortion | <2.3 |
| | | Bandwidth | 81 GHz |
| | | Critically dispersed (SSD) | – |
| | | Spatially shaped for gain compensation | – |
| | | Number of preamplifier modules | 48 |

[a]Reference 1.

## Master Oscillator Room

This section describes the subsystems that make up the MOR. All these systems have been demonstrated at the scientific prototype stage and are being engineered for the final NIF version. A simplified version of the MOR architecture is shown in Figure 2.[3]

The 192 pulses that converge on the target with a combined energy of nearly 2,000,000 J originate as a low-power continuous-wave (CW) signal in the MOR's master oscillator. This oscillator is a fiber distributed feedback (DFB) laser, made by imprinting linear Bragg gratings in an Yb-doped fiber using UV light. This technology is similar to that used in Er-doped fiber lasers for communications.[4] The Bragg gratings define the cavity end reflectors, which are such narrow band reflectors that they allow only one cavity mode to lase.

When pumped with a 120-mW laser diode, the oscillator produces about 50 mW CW in a single longitudinal mode. The master oscillator wavelength is precisely tuned to within 0.01 nm of the desired value by temperature-controlling its mount, which changes the Bragg

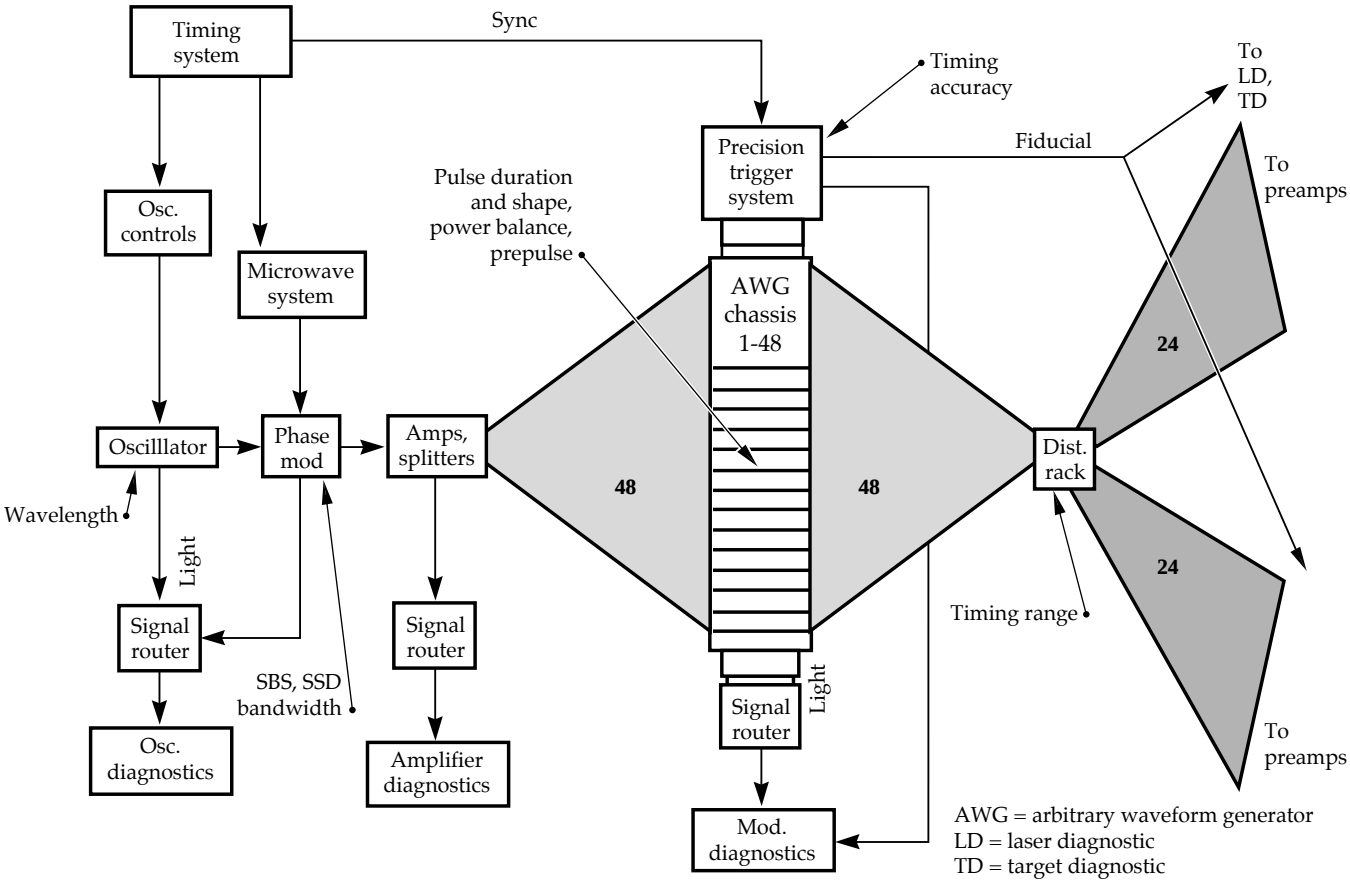


FIGURE 2. The master oscillator room (MOR) architecture. (70-00-0299-0359pb01)

wavelength by strain and the thermooptic effect. Figure 3 shows a picture of a pumped, unmounted oscillator, and a schematic of the fiber master oscillator.

## Amplification and Modulation

The CW signal from the oscillator is chopped by an acoustooptic modulator to a pulse width of 100 ns and passed through a double-pass fiber amplifier with a gain of 500. The amplifier is internally filtered to reduce the amount of noise it adds to the oscillator signal. When the signal has passed through the amplifier once, it reflects off a 2-Å-wide passive fiber Bragg grating filter. This reduces amplified spontaneous emission (ASE) noise from the first pass. After a second pass, the output signal is filtered through a 5-nm bandpass filter to further reduce ASE. A directional coupler is used to multipass the amplifier because it has low back reflection, high damage threshold, and nearly the same loss as a circulator at this wavelength. After passing through this amplifier and undergoing several component losses, the 100-ns pulse has a peak power of about 1 W.

At this point, phase modulation is applied to the single-frequency signal to control its eventual interaction with the final NIF optics and the target. Phase modulation at 1.5 GHz produces about 10 optical sidebands, which reduce the spectral intensity in the final optics and prevent stimulated Brillouin scattering (SBS), which could damage the optics.[5] Phase modulation at 17 GHz creates a bandwidth of 3 Å. When diffracted from a grating in the PAM, the 3-Å bandwidth quickly moves the focused laser beam on target to smear out speckle through a process called smoothing by spectral dispersion (SSD).

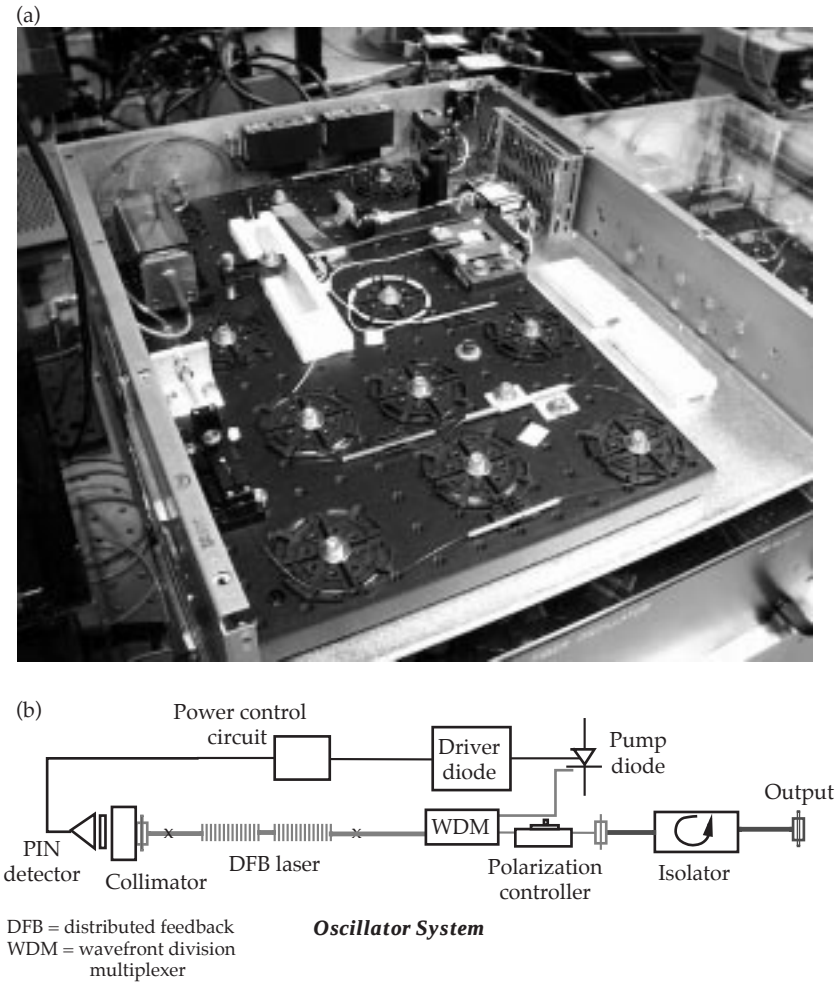


FIGURE 3. (a) Photo of a pumped, unmounted oscillator. (b) Schematic of the fiber master oscillator. (70-00-0599-1058pb01)

Both modulations are applied with lithium niobate, electrooptic waveguide modulators similar to those used in fiber-optic communications. Modulators that produce these modulations require only a few watts of microwave power, reducing the complexity of the drive circuit and enhancing reliability. Because it is important that SBS not damage the NIF optics, a doubly redundant, fail-safe circuit monitors the presence of 1.5-GHz phase modulation and blocks the laser pulse if the amount of modulation is too low. Several parameters are measured on each pulse to ensure that each one has the required bandwidth.

To reduce gain saturation in the fiber amplifiers, the 100-ns pulse is reduced in another waveguide modulator to 30 ns before being introduced into the fiber amplifier and splitter array.

The amplifiers in the array are Yb-doped, two-stage, CW-pumped fiber amplifiers, shown in Figure 4 and developed with JDS Feitel. The first stage is a small core, Yb-doped, gain fiber with gain of 12, followed by a band-stop filter to prevent saturation of the second stage by ASE. The second stage, a power amplifier, is made of larger core fiber and has a gain of 3, for a total gain of 36 for each fiber amplifier. The amplifiers for NIF will be produced to our design and specifications by a commercial manufacturer.

After each stage of amplification, the pulse is split four ways. In the first stage, three outputs are used, so that the total number of outputs in three stages of amplification is $3 \times 4 \times 4 = 48$. The 48 outputs each produce about 2 W in 30 ns.[6]

## Arbitrary Waveform Generator

The final temporal pulse shape is sculpted from the 30-ns square pulse after the laser

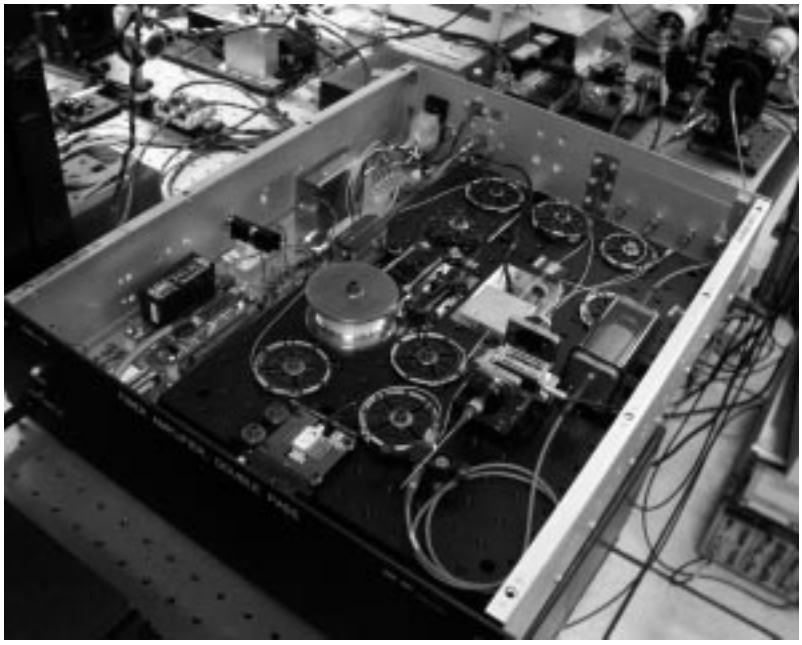

FIGURE 4. The Yb-doped, two-stage, CW-pumped fiber amplifiers in the splitter array. (70-00-0599-1059pb01)

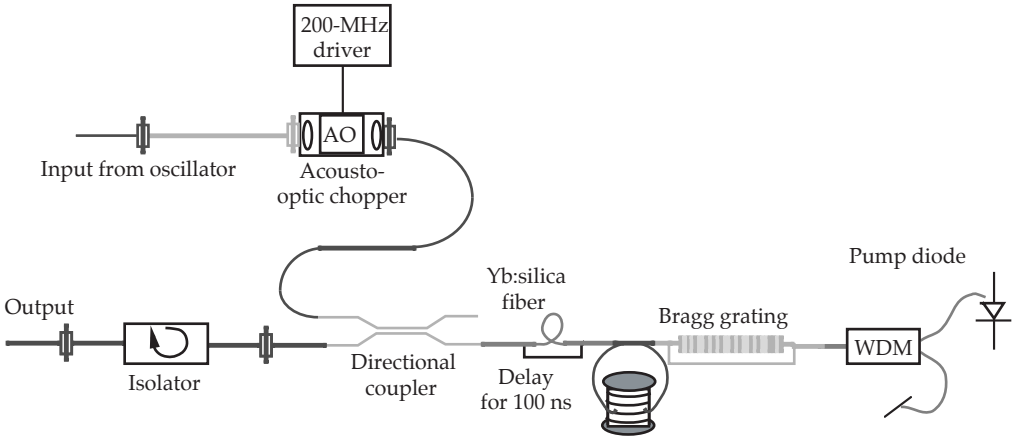


Diode-Pumped High-Gain Amplifier

has fanned out to 48 parallel fiber lines. Together with Highland Technology, we developed a high-bandwidth, programmable, arbitrary waveform generator (AWG) to produce the high-temporal-contrast pulses that are needed for fusion ignition.[7]

An electronic waveform generator supplies a shaped-voltage pulse to an integrated optic, lithium niobate amplitude modulator, which modulates the light pulse. The electronic waveform generator works by adding 300-ps voltage pulses separated in time by 250 ps. NIF will have 96 300-ps pulse generators, each of which can be precisely controlled in amplitude. By programming these pulse amplitudes, we can create an arbitrary pulse shape.

There are some applications where a shorter pulse is required. This is provided by a second pulse generator through a special circuit. For example, some targets employ a secondary target that is illuminated by a short laser pulse. When the pulse strikes the target, x rays are produced. These x rays act like a photo flash to capture an instant in the target implosion. Also, timing of the 192 beams to coincide in the center of the target chamber requires a short pulse for timing precision. In these cases, a pulse of about 150 ps is produced.

The electronic waveform generator and optical modulator are combined in a single chassis that is being produced by an outside manufacturer. There will be 48 of these units in the final NIF laser system. Figure 5a shows the generator.

Figure 5b shows a typical, high-temporal-contrast pulse generated by the AWG. It is essential that these pulses arrive at the target simultaneously to provide uniform target implosion. Only 12 ps of timing uncertainty is allowed for the pulses leaving the MOR.

Synchronization of the pulse generators is accomplished by triggering each one with a short optical pulse passively split from a single, high-energy optical pulse. In this trigger system, a 100-ps electrical pulse synchronized with the integrated timing system (ITS) drives an electrooptic modulator to produce a 100-ps optical pulse. This is amplified in fiber amplifiers and split to trigger the pulse waveform generators. A portion of this pulse is also sent out of the MOR to fiducial laser and target diagnostic systems to be used as a timing marker exactly synchronized with the main optical pulses.

After final temporal shaping, the 48 parallel fiber lines are routed through a central distribution rack. From there they are sent to the 48 PAMs. The central fiber distribution is carefully designed to ensure that the individual lines produce the correct timing delay to each PAM.

We can add or subtract fiber jumpers to discretely vary the delay of each beamline for needed adjustment, or to satisfy the requirements of special experiments. In addition to the laser itself, the MOR contains auxiliary systems for controls, diagnostics, and precision timing.

## Preamplifier Modules

As part of the development effort for the ILS, the various subsystems in the MOR and PAM were assembled and tested in the laboratory, and then combined into an Integrated ILS testbed.[8] Using this combined system, we were able to test those specifications of the ILS that required the functions of both the MOR and PAM.

Each of the 48 fibers from the MOR distribution rack feeds one of the 48 PAMs in the NIF laser system. The PAM is a high-gain (>100 dB) preamplifier that also spatially shapes the beam for the main amplifier chain. Figure 6 is a schematic of the PAM showing the three major subsystems: an ultrastable, high-gain, diode-laser-pumped, Nd:glass regenerative amplifier; a beam-shaping module; and a four-pass amplifier.

(a)

(b)

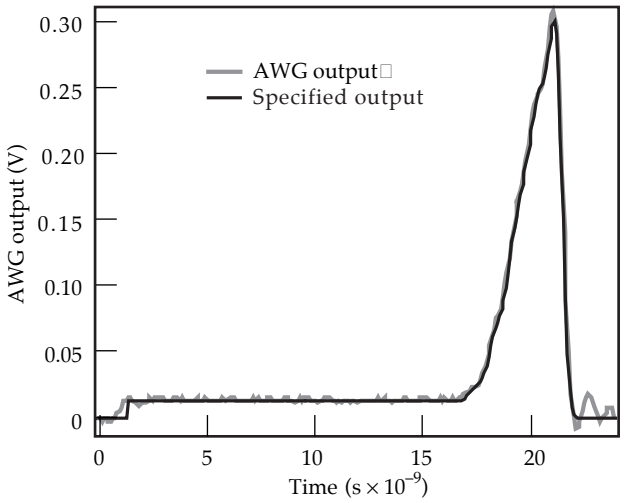


FIGURE 5. (a) The arbitrary waveform generator (AWG) chassis. (b) Plot showing specified (black) and measured (gray) electronic pulse shapes produced by the AWG. (70-00-0299-0360pb01)

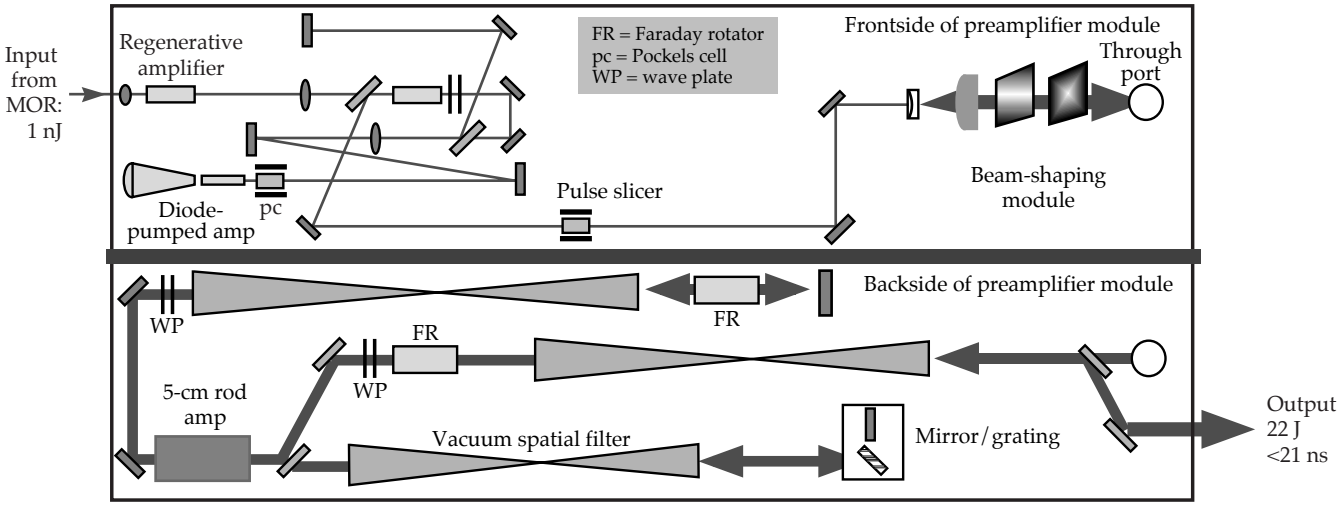


FIGURE 6. Optical layout of the preamplifier module (PAM). (70-00-0299-0361pb01)

## Regenerative Amplifier

The regenerative amplifier is the highest gain amplifier in the entire NIF laser chain.[9–11] The optical layout for the regenerative amplifier, or "regen" for short, is shown in Figure 6. The input section to the regen consists of a fiber launch, where the pulse from the MOR is launched from single-mode fiber into free-space via a precision fiber positioner and a short-focal-length lens. Next, two Faraday isolators in series protect the single-mode fiber from a high-intensity pulse reflecting, or propagating back, from the regen output. A second lens, in conjunction with the short-focal-length lens in the fiber launch, forms a telescope to match the beam size at the fiber output to the laser cavity mode for efficient coupling of energy into the regen.

A Faraday rotator, a half-wave plate (WP), and a thin-film-polarizer (TFP) form a unidirectional coupler to separate the counterpropagating input and output laser pulses. The input laser pulse from the MOR is injected into the regen cavity through a second TFP.

The regen cavity is a long, asymmetric cavity with a single, diode-laser-pumped, Nd:glass amplifier located at one end. The amplifier has a single-pass gain of $G = 1.4$ in a 5-mm diameter × 50-mm rod that is end-pumped by a 4-kW diode array. The cavity transmission is $T = 0.77$, so the net gain per round trip of the regen is $G_{net} = G^2 \cdot T = 1.5$. A cavity Pockels cell switches polarization of the input pulse after it has made a single pass, trapping the pulse in the regen until the Pockels cell is switched back to its original polarization.

Each time the circulating pulse makes a round trip in the cavity, the pulse is amplified by $G_{net}$. The total gain of the regenerative amplifier is the net gain raised to the power of the number of round trips that the pulse makes in the cavity before being switched out. For example, if the number of round trips in the regen cavity is $k = 40$, then the total regen gain is

$$G_{total} = (G_{net})^k = (1.50)^{40} = 1.4 \times 10^7 \quad . \qquad (1)$$

Eventually the amount of extracted energy depletes the available stored energy in the amplifier (amplifier saturation) and the net gain drops below unity. In typical operation we extract 12 mJ from the regen for 0.8-nJ input, for a total gain of 72 dB. Upon leaving the regen cavity, the amplified pulse passes through a second Pockels cell called the slicer, which acts as an optical gate. The slicer passes the main regen pulse while rejecting pre- and postpulses that leak out of the cavity due to imperfect polarization switching.

The output mode from the regen is a 3.5-mm-diam circular Gaussian-shaped beam.

## Beam-Shaping Module

The next subsystem in the PAM is the beam-shaping module, where the round Gaussian beam is converted to a square-shaped beam that is sculpted in a well defined manner to precompensate for the spatial gain profile of the main amplifiers.[12] The goal is to produce a spatially flat-top beam at the NIF target chamber to yield the maximum irradiance at the target.

First the round beam is magnified by a 20× telescope. The expanded Gaussian beam is shaped by an anti-Gaussian filter that flattens the center of the beam. This truncated Gaussian beam is further shaped by a gain-compensating mask that carves out the center of the beam to produce the final shape. We determine this final shape based on a complex diffraction code that models an entire beamline, including the spatial gain profiles of the main amplifiers.[12] The final mask in the beam-shaping module, a serrated aperture, apodizes the beam so that it will propagate over a long distance with minimal ringing at the edges of the beam from diffraction.[13]

All of the beam-shaping masks in the module are made by depositing chrome on glass in a standard photolithographic process. The shaping masks reduce the energy from the regen by a factor of 10 to 15, from 12 mJ down to <1 mJ. This spatially shaped beam is injected into the final PAM system, the four-pass amplifier.

## Four-Pass Amplifier

The final amplifier in the PAM is laid out in a four-pass configuration as shown in Figure 6. The input beam is spatially filtered by a vacuum relay telescope with a pinhole that blocks the higher spatial frequencies produced by the high-frequency teeth in the final apodizing mask. The filtered input beam passes through a combination of Faraday rotator, half-wave plate, and thin-film polarizer that acts as a directional coupler to separate the input beam from the counterpropagating output beam exiting from the four-pass cavity.

The four-pass cavity contains a Nova, 5-cm, flashlamp-pumped, rod amplifier at the cavity center. This amplifier can operate with a single-pass gain of 20.

Due to the high, single-pass gain of the 5-cm amplifier, the cavity is especially susceptible to unwanted, parasitic oscillation. Parasitic oscillation can occur in a high-gain amplifier if there is sufficient gain and feedback to cause oscillation. This oscillation is uncontrolled and chaotic and produces a background of intense light that can propagate into the main amplifier chain along with the amplified and formatted pulse from the MOR.

We take several steps to successfully eliminate unwanted oscillation in the four-pass cavity. These include carefully controlling the polarization of the light using the Faraday rotator and the quarter-wave plate, and offsetting the beam slightly from the optical axis as it propagates through the cavity so light is never reflected directly back on itself.[14]

Figure 7 shows the measured output energy of the four-pass amplifier as a function of energy at the input. The solid curve in the plot is the predicted performance based upon a Frantz–Nodvik model for saturated gain.[15] The dashed line shows the required performance of the four-pass amplifier for an unshaped input pulse (see Table 1).

A second function of the four-pass amplifier optical layout is to provide angular dispersion of the light that has been frequency modulated in the MOR for SSD. To achieve this, we replace one of the end mirrors in the four-pass cavity with a diffraction grating positioned at the Littrow angle so the first diffraction order is reflected back in the same direction as the incoming beam. If the four-pass output is viewed in the far field (i.e., at the focus of a lens), the focal spot is dithered in one dimension at the sinusoidal frequency of the rf driver to the modulator (e.g., 17 GHz). The angularly deflected light from the amplifier propagates through the rest of the amplifier chain to the target chamber and final optics assembly, where it passes through a special phase plate.

The combination of the rapid dithering of the FM light due to dispersion from the grating, and the smearing of the focal spot

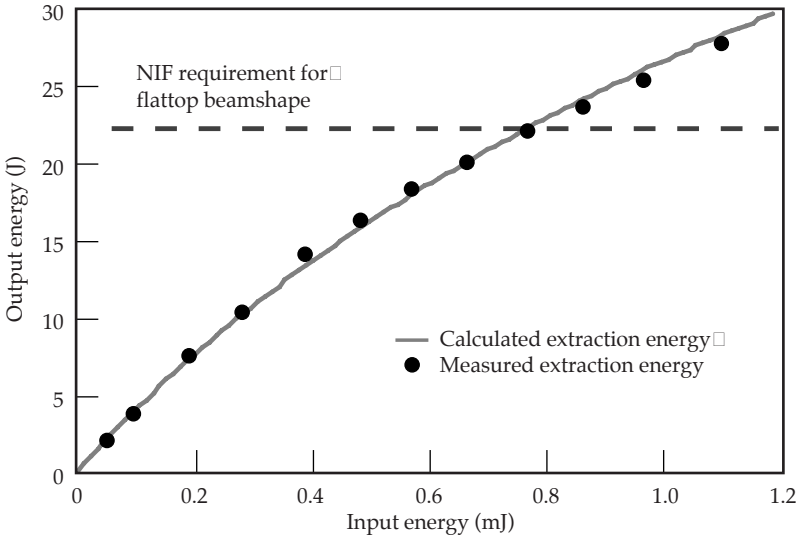


FIGURE 7. PAM output energy as a function of four-pass input energy. Solid curve is a Frantz–Nodvik model for saturated gain. (70-00-0299-0362pb01)

produced by the random phase plate, reduces the spatial coherence (or speckle pattern) normally associated with coherent light and increases the uniformity of the target illumination.

The current beam-smoothing requirement for the NIF is a 3-Å bandwidth, critically dispersed in one dimension (see Table 1). "Critically dispersed" means that the temporal skew produced across the 3-cm beam by the grating at Littrow angle must be equal to the period of the sinusoidal rf waveform that drives the phase modulator. The temporal skew $\Delta T$ is given by

$$\Delta T = 2D\tan\theta_L / c = 1/f_{mod}\,, \qquad (2)$$

where $D = 30$ mm is the beam dimension at the grating in the dispersion direction, and $f_{mod}$ is the rf driver frequency. The Littrow angle is given by $\theta_L = \sin^{-1}(\lambda/2d)$, where $\lambda$ is the wavelength of the laser and $d$ is the grating groove spacing.

In the current design, the modulation frequency for SSD is 17 GHz, and the critical dispersion requirement is slightly exceeded for a 600-line/mm grating. The 17-GHz modulator system was not available for the ILS subsystem tests, so we used a 3-GHz modulation frequency. We used an 1800-line/mm grating that exceeded the critical dispersion requirement and allowed us to clearly resolve individual FM sidebands.

Figure 8a is an image taken by the far-field camera diagnostic at the output of the four-pass amplifier. The angular dispersion produced by the 1800-line/mm grating cleanly separates the individual spots in the far field. We show a plot in Figure 8b comparing a lineout from the camera image with a power spectrum for an 81-GHz modulation bandwidth. The power spectrum, $P(t)$, is given by the Bessel series:

$$E(f) \approx \sum_{n=0}^{\infty} J_n(m)\bullet[\delta(f_0 + nf_{rf}) + (-1)^n\,\delta(f_0 - nf_{rf})] \qquad (3)$$

$$P(f) \approx |E|^2\,, \qquad (4)$$

where $E(f)$ is the laser field in the frequency domain, $J_n$ is the $n$th order Bessel function, $m$ is the modulation index, $\delta$ is the delta function, and $f_{rf}$ is the rf frequency driving the phase modulator. The locations of the peaks and their magnitudes from the image lineout accurately compare with the simulated spectral peaks. The 81-GHz FM spectrum is confirmed by the spectrometer measurements in the MOR and at the regen output.

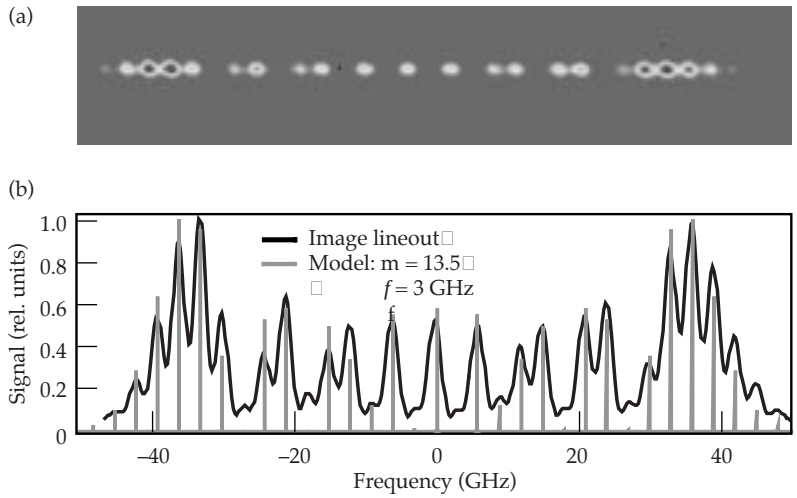


FIGURE 8. (a) The far-field camera image at the PAM output showing the beam dispersed by an 1800-line/mm grating. (b) Plot comparing a horizontal lineout from (a) and an FM spectrum where the rf frequency is 3 GHz and the modulation depth is 13.5. (70-00-0299-0363pb01)

The results from experiments on the Integrated ILS Testbed demonstrate that the PAM and MOR combined systems meet the requirements listed in Table 1. The optical layout and specifications demonstrated in the PAM development lab become the basis for the first PAM engineering prototype.

## PAM Engineering Prototype

The 48 preamplifier modules that seed the main amplifier chains in the NIF laser system reside on the preamplifier support structure (PASS), a large space frame in the main laser bay. The PAMs are designed to be line-replaceable units, or LRUs, that can slide into place on precision rails on the PASS or be quickly removed as a self-contained unit and replaced or repaired as needed.

In our laboratory we set up and assembled the first preamplifier module, an engineering prototype of the production PAMs that will form part of the ILS. Figure 9 is a photograph of the PAM prototype. We reproduced the three optical subsystems, the regenerative amplifier, the beam-shaping module, and the four-pass amplifier that were developed and demonstrated on the Integrated ILS testbed, and mounted these subsystems on the PAM prototype. The regenerative amplifier and beam-shaping module are mounted on one side of a vertical optical support structure. The larger four-pass amplifier is mounted on the opposite side.

The electronics to support the PAM include: a diode-laser power supply, stepper motor controllers, ion-pump controllers, timing modules, temperature controllers, and a VME-based embedded processor controller that provides overall electronics control of the PAM. These electronics units are mounted above the optics support structure in an electronics bay that runs the length of the PAM. A high-energy, electrical pulser that drives the six flashlamps in the 5-cm rod amplifier is housed in a separate unit, apart from the PAM.

We have operated the PAM prototype over the past several months to demonstrate the requirements listed in Table 1. In addition, we developed a high-resolution output beam diagnostic to accurately measure the wavefront, near-field contrast, and the far-field spot size at the output of the PAM prototype. Figure 10 shows processed data taken with the high-resolution out-put beam diagnostic for a 17-J shot. The information that we garner from these comprehensive tests of the PAM engineering prototype will enable us to design the 48 production PAMs.

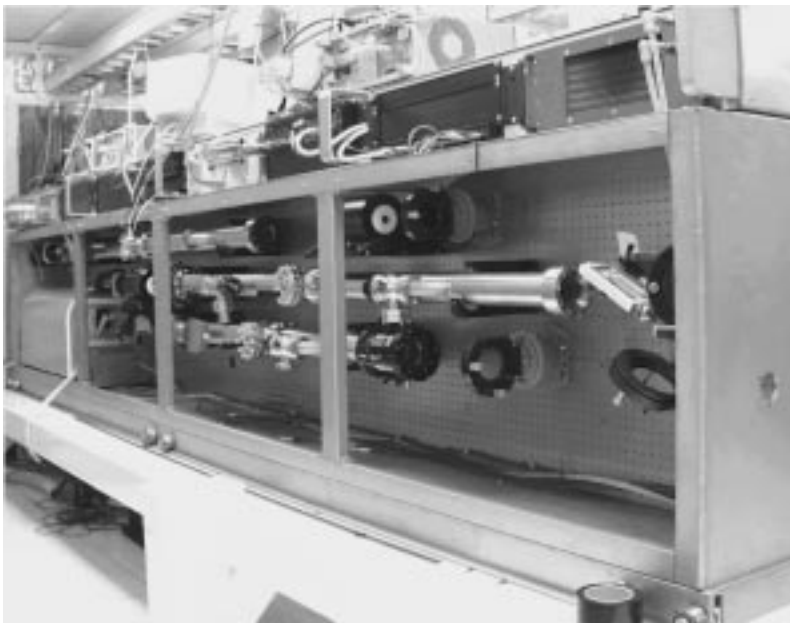

FIGURE 9. PAM engineering prototype mounted on mini-PASS structure. This view shows the four-pass amplifier.
(70-00-0299-0364pb01)

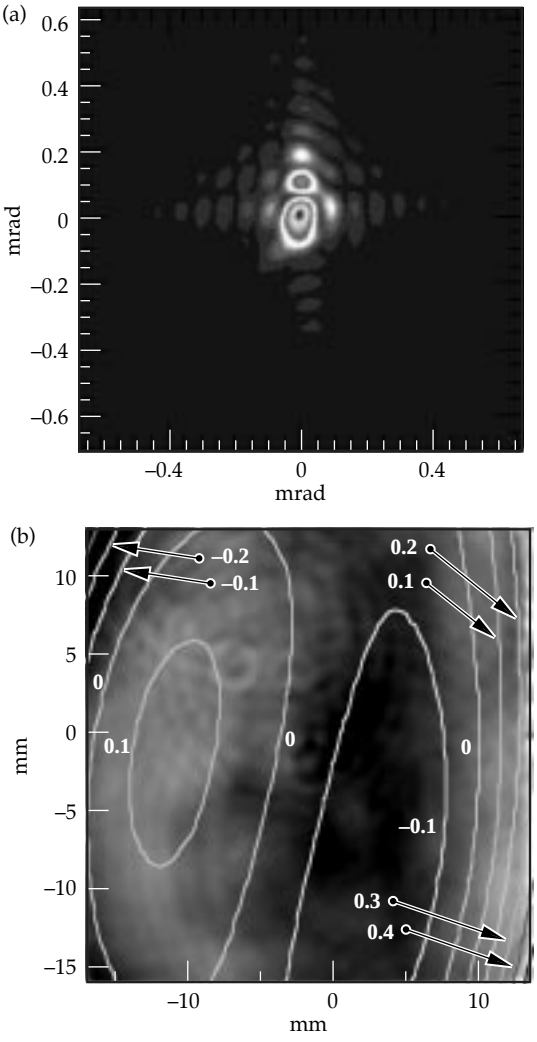


FIGURE 10. (a) Far-field image at the output of the PAM prototype taken with a high-resolution PAM output diagnostic (Strehl ratio = 0.65). (b) Phase map of the output wavefront taken with a radial shearing interferometer (peak-to-valley phase = 0.71λ).
(70-00-0299-0365pb01)

## Preamplifier Beam Transport System

The final system in the ILS, or front end, of the NIF laser is the PABTS, shown in Figure 11. The 16.9-J output from a PAM passes through an isolation module that contains a large-aperture Faraday rotator, half-wave plate, and polarizers to isolate and protect the front end from a high-energy pulse traveling backwards from the main amplifier chain.

From the isolation module, the beam enters the 1:4 split assembly, where the single beam is split into four beams that will seed four separate main amplifier chains. The four-way split and balancing of power among the four legs is accomplished using thin-film polarizers and half-wave plates.

Each of the beams passes through a six-element vacuum relay telescope that relays the beam to the input relay plane of the transport spatial filter. This zoom telescope has variable magnification from 0.95 to 1.02 and can be used to adjust the size of the beam in each of the four legs to accommodate changes in the main amplifier's optics.

Next a timing section allows for adjustment of the timing in each leg by changing the optical path length via a translating mirror. A pair of turning mirrors directs the beam either into the transport spatial filter (TSF), or a final telescope prior to the TSF, depending upon the side of the laser space frame in relation to the main amplifiers.

Detailed mechanical and optical designs of the PABTS are complete, and hardware prototyping is under way. One quad of a PABTS beamline will be built in 1999.

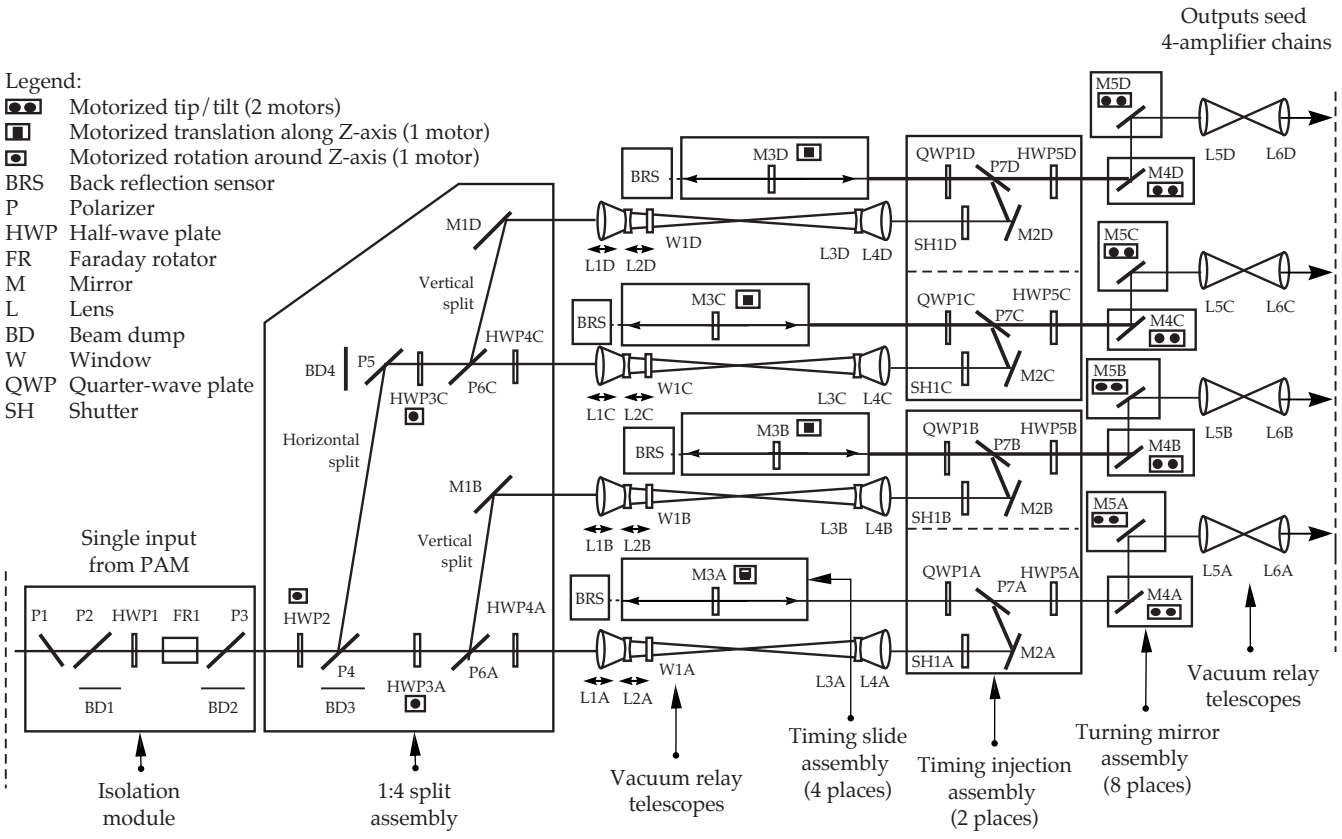


FIGURE 11. The preamplifier beam transport system (PABTS); different subassemblies are designed to be line-replaceable units. (70-00-0299-0366pb01)

## Summary

The ILS, or front end, of the NIF laser system is nearing the end of its development phase. In the past year, we performed a series of experiments that demonstrated or exceeded the performance specifications listed in Table 1 for the combined MOR and preamplifier development systems. Many of the subsystems described in this article and demonstrated in our development laboratories are now engineering prototypes. In the coming year, we will assemble an engineering prototype of the entire ILS, including MOR, PAM, and PABTS, plus the computer controls, timing, and diagnostics systems. We will then demonstrate the integrated operation and performance of the NIF laser system front end.

## Acknowledgments

We thank the important contributions made by several people in various key stages of the ILS development: Ray Beach, Scott Burkhart, Scott Mitchell, Mike Perry, Jim Davin, Brent Dane, Ralph Page, and Nick Hopps.* In addition we would like to acknowledge the scientific, technical, and design contributions of the following people: Richard Hackel, Ernesto Padilla, Ernie Dragon, Rod Lanning, Regula Fluck, Dave Young, Jim Crawford, Rob Campbell, John Braucht, Ron Tilley, Marcus Bartlow, Pete Ludwigsen, Mike Gorvad, Curt Laumann, Dave Wang, Dave Aikens, Bob Powers, Horst Bissinger, Steve Herman, Russ Jones, Brad Golick, Don Bartel, Jim Hauck, Ron Korniski, Gloria Zuleta, Don Fleming, Greg Fischer, M. Reta, Kathy Coatney, Will House, Annette Springer, Cidelia Sanchez, Lori Dempsey, and Frances Mendieta.

*Atomic Weapons Establishment, Aldermaston, Berkshire, UK

## Notes and References

1. J. A. Paisner, J. D. Boyes, S. A. Kumpan, W. H. Lowdermilk, and M. Sorem, "Conceptual Design of the National Ignition Facility," *Proceedings of the First International Conference on Solid State Lasers for Application to Inertial Confinement Fusion*, Monterey, CA, May 31–June 2, 1995, *SPIE Proceedings Series* **2633**, 2.
2. S. Skupsky et al., *J. Appl. Phys.* **66**, 3456–3462 (1989).
3. R. B. Wilcox, D. Browning, G. Dreifuerst, E. Padilla, and Frank Penko, "Development System Performance of the NIF Master Oscillator and Pulse-Forming Network," *Third International Conference on Solid State Lasers for Application to Inertial Confinement Fusion*, Monterey, CA, June 1998.
4. A. Asseh et al., *Electronics Letters* **31**(12) 969 (1995).
5. J. R. Murray et al., *J. Opt. Soc. Am. B* **6**, 2402–2411 (1989).
6. R .B. Wilcox, D. F. Browning, and R. H. Page, "Fiber DFB Lasers as Oscillators for High-Power MOPA Systems," *Conference on Lasers and Electrooptics (CLEO)*, Baltimore, MD (1999).
7. S. C. Burkhart, R. B. Wilcox, D. Browning, and F. Penko, "Amplitude and Phase Modulation with Waveguide Optics," *Proceedings of the Second International Conference on Solid State Lasers for Applications to Inertial Confinement Fusion*, Paris, France, Oct. 22–25, 1996, *SPIE Proceedings Series* **3047**, 610–617.
8. J. K. Crane et al., "Integrated Operations of the National Ignition Facility (NIF) Optical Pulse Generation Development System," *Third International Conference on Solid State Lasers for Application to Inertial Confinement Fusion*, Monterey, CA, UCRL-JC-129871 (June 1998).
9. J. K. Crane et al., *ICF Annual Report 1997*, Lawrence Livermore National Laboratory, Livermore, CA, UCRL-LR-105821-97, 246–259, (1998).
10. M. D. Martinez et al., "Optimized, Diode-Pumped, Nd:Glass, Prototype Regenerative Amplifier for the National Ignition Facility," *Proceedings on Optoelectronics and High-Power Lasers & Applications*, San Jose, CA, Jan. 24–30, 1998, *SPIE Proceedings Series*, vol. 3267, pp. 234–242.
11. N. W. Hopps et al., "Optimization of the Alignment Sensitivity and Energy Stability of the NIF Regenerative Amplifier," *Third International Conference on Solid State Lasers for Application to Inertial Confinement Fusion*, Monterey, CA, UCRL-JC-130961 (June 1998).
12. M. Henesian et al., " Diffraction Modeling of the National Ignition Facility (NIF) Optical Pulse Generation System and Integration into the End-to-End System Model," *Third International Conference on Solid State Lasers for Application to Inertial Confinement Fusion*, Monterey, CA (June 1998).
13. J. M. Auerbach and V. P. Karpenko, *Applied Optics* **33**, 3179–3183 (1994).
14. B. D. Moran et al., "Suppression of Parasitics and Pencil Beams in the High-Gain National Ignition Facility Multipass Preamplifier," *Proceedings on Optoelectronics and High-Power Lasers & Applications*, San Jose, CA, Jan. 24–30, 1998, *SPIE Proceedings Series*, vol. 3264 , pp. 56–64.
15. L. M. Frantz and J. S. Nodvik, *J. Appl. Phys.* **34**, 2346–2349 (1963).

# Main Amplifier Power Conditioning for the NIF

*M. Newton* *D. Smith** *B. Moore** *G. Ullery* *J. Hammon****
*M. Wilson** *D. Muirhead** *T. Downey** *S. Hulsey* *W. Gagnon†*
*H. Harjes** *D. Van DeValde** *P. McKay** *R. Anderson***

Design of the power conditioning system (PCS) for the NIF laser is nearing completion. Modeling predicts that the design will meet all performance requirements. A first-article NIF test module (FANTM), Figure 1, has been built at Sandia National Laboratories (SNL) in Albuquerque, New Mexico. This power conditioning module is being tested to verify the design performance and system lifetime. NIF's power conditioning system will consist of 192 modules. The final design of the module, to be built to drive the NIF first bundle consisting of eight beamlets, will be based on the information and understanding gained from the operation and testing done on the first-article power conditioning module.

The NIF PCS is being designed and built by SNL in collaboration with Lawrence Livermore National Laboratory (LLNL) and industrial partners. Its architecture is different from any laser power conditioning system previously built at LLNL and was chosen as the most cost-effective way to reliably deliver the large amount of electical energy needed for NIF.

The design of the power conditioning systems for flashlamp-pumped lasers represents an evolution that has occurred over many years and several generations of lasers.[1–3] The direction of this evolution has been to build modules that can handle larger amounts of energy with a smaller number of components. NIF's forerunners utilize small, independent modules that store less than 100 kJ. In comparison, NIF's PCS will be able to store nearly 2 MJ in a single module. The move toward fewer components was driven by the need to reduce the cost of supplying energy to drive lasers of this size.

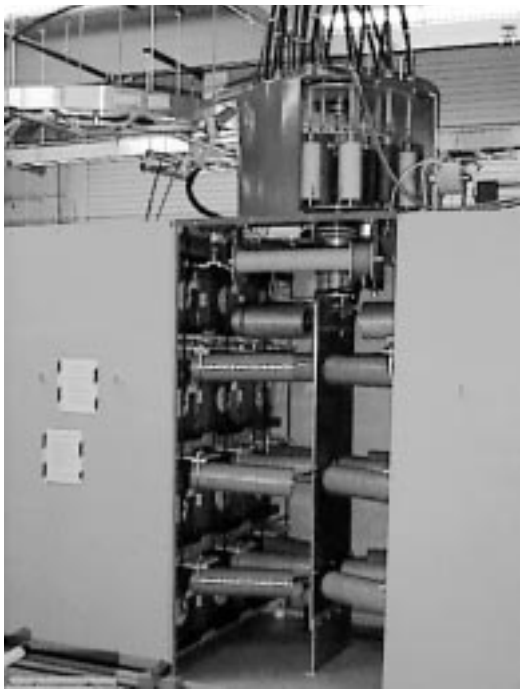

FIGURE 1. The first-article NIF test module (FANTM). (70-00-0399-0763pb01)

The specifications for the electrical performance of the PCS are derived from the

*Sandia National Laboratories, Albuquerque, NM
**American Controls Engineering
***Maxwell Physics International
†Consultant

overall performance goals of the laser system. The PCS must also meet lifetime, reliability, and maintainability requirements that are derived from the operational requirements for the NIF laser system. The overall system performance will be demonstrated through performance and reliability testing using FANTM.

## System Performance

An important measure of NIF laser performance is the gain coefficient of the amplifier. Gain coefficient is a measure of the change in light intensity vs the path length of the light through the laser glass. Gain coefficient is dependent not only on the laser glass, but also on the temporal characteristics of the light pulses generated by the flashlamps. The desired temporal characteristics of the flashlamp light translate directly into requirements on the shape, amplitude, and timing of the drive pulses supplied by the power conditioning system.

A computer model developed by Ken Jancaitis of LLNL calculates the gain coefficient of the NIF amplifier for a given electrical drive input. This code, GainCalc v1.0, is used to verify that the output waveforms of the PCS meet the gain coefficient requirement of >5.0%/cm.

## Power Conditioning Modules

NIF's power conditioning equipment will be located in capacitor bays adjacent to each of four laser clusters. Forty-eight independent power conditioning modules (PCMs) such as the one shown in Figure 2 will drive the lasers in each cluster.

Each module will shape and deliver pulses of energy to NIF flashlamps. A description of an individual module is shown in Table 1.

A schematic of the module is shown in Figure 3. Each module is nominally comprised of 20 nominally 83.5-kJ capacitors connected in parallel through damping elements to limit fault currents. The energy stored in a module is switched to the output transmission lines through a single gas-discharge switch. The peak current through this switch is approximately 500 kA.

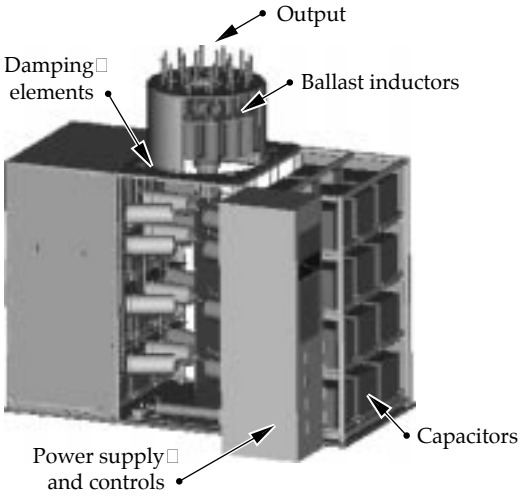


FIGURE 2. Power conditioning module (the switch is not shown) overall size is 10 ft high by 11 ft wide by 5 ft deep. (70-00-0399-0764pb01)

TABLE 1. Power conditioning module specifications.

| | |
|---|---|
| Operating voltage | 23.5 kV |
| Minimum delivered energy per lamp | 34 kJ |
| Number of lamps per module | 40 |
| Pulse duration | 360 $\mu$s |
| Peak output current | 530 kA |
| Nominal energy storage* | 1.6 to 1.9 MJ |
| Number of capacitors | 20 nominal, 24 maximum |

*Modules must each deliver a minimum of 34 kJ per flashlamp with easy expandability to approximately 40 kJ per flashlamp. To deliver 34 kJ per flashlamp, the module must store 1.6 MJ; to deliver 40 kJ per flashlamp, the module must store 1.9 MJ.

Energy is evenly distributed to the 20 parallel flashlamp circuits through the ballast inductors and transmission lines. These flashlamps are configured as 20 circuits, with each circuit having two flashlamps in series. The module will deliver nominally 68 kJ of energy to each flashlamp pair during the main discharge pulse.

Each of the 192 modules will have a maximum energy storage capacity of

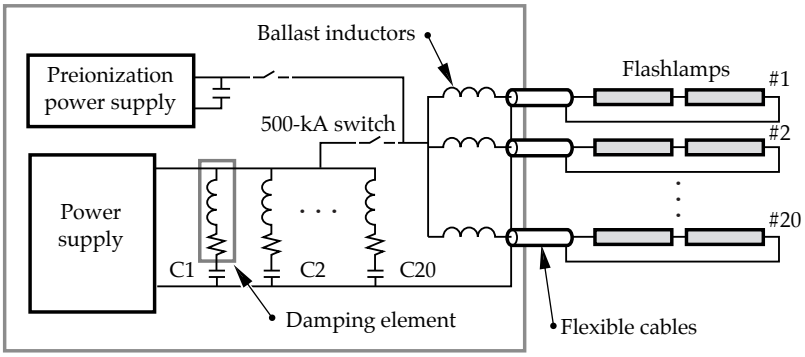


FIGURE 3. Power conditioning module schematic. (70-00-0499-0826pb01)

nearly 2 MJ. The potential for faults to cause significant damage increases as the amount of energy in a single module increases. Thus, significant investments have been made to develop components that are either robust against all known failure modes, or that fail in a well-controlled fashion and can be easily replaced. The size and configuration of the NIF power conditioning module represent an aggressive balance between cost and risk.

Each module must deliver a very specific quantity of energy and waveshape to each of the flashlamps. Each flashlamp must be preionized with a small amount of energy (500 joules) approximately 300 microseconds before the main discharge to ensure breakdown and to uniform plasma borefilling of the flashlamps. A minimum of 34 kilojoules must be delivered to each flashlamp during the main discharge. Typical current and voltage waveforms measured for energizing the flashlamps are shown in Figure 4. This pulse format shows the features for preionization and triggering in addition to the main discharge pulse.

## Capacitors

Self-healing, or metallized, dielectric capacitors are used to store the energy for driving the NIF flashlamps. Unlike film-foil capacitors used in past laser systems, the metallized dielectric capacitors have a very predictable lifetime. This characteristic allows the design of a capacitor with a mean lifetime tailored specifically to the NIF requirement of 20,000 shots, without the additional cost of excessive design margins.

A summary of the NIF capacitor requirements is shown in Table 2.

The cost of the 3,840 capacitors that NIF will require constitutes 30 to 40 percent of the total power conditioning system cost, the system's largest single cost component. Capacitor reliability will also have a significant impact on the overall system reliability. Significant resources have been invested to

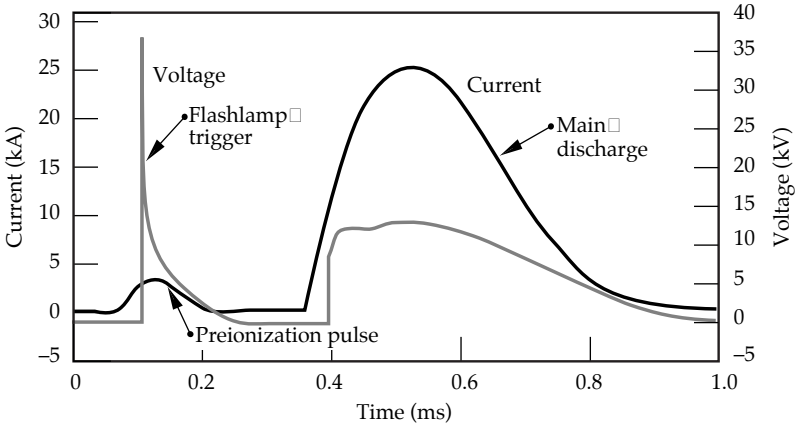


FIGURE 4. (a) Flashlamp drive current (black) and (b) voltage across flashlamp (gray). (70-00-0399-0762pb01)

TABLE 2. Capacitor specifications.

| | |
|---|---|
| Type | Metallized dielectric |
| Nominal capacitance | 290 μF (+10%, –5%) |
| Operating voltage | 24 kV |
| Peak discharge current | 30 kA |
| Voltage reversal | <10% |
| Lifetime | 20,000 shots |
| Maximum size | 36" × 18" × 18" |
| Duration of discharge | 360 μs |

develop capacitors that carefully balance reliability and cost.

Capacitor development for NIF began nearly three years ago, when LLNL began working with multiple vendors to develop capacitors that would meet NIF specifications. After multiple iterations of design, fabrication, and testing, several vendors (Thomson Passive Components, ICAR, Aerovex, and Maxwell Technologies) have built capacitors that meet the NIF requirements. Development of lower-cost capacitor designs will continue until 1999, when LLNL begins the final design-qualification testing.

## Capacitor-Charging Power Supplies

Each module will be charged by its own capacitor-charging power supply. The power supply specifications are shown in Table 3.

We have been working with three vendors (Dell Global Technologies, EMI, and Maxwell Technologies) to develop these power supplies. The specifications for these supplies are very close to those of standard off-the-shelf supplies, with the exception of the regulation and stability requirements. Prototype supplies have been built by the three vendors and have been operated and tested on the first-article power conditioning module.

Each power supply must charge its module's capacitors to 24 kV in a maximum of 80 s. This charge time was chosen because it was an acceptable compromise between capacitor lifetime, switch prefire probability, and power supply/prime power cost. Once a module is charged, it will be held at its charge voltage for a maximum of 15 s while other systems in NIF are synchronized and armed for the shot.

TABLE 3. Power supply specifications.

| | |
|---|---|
| Maximum operating voltage | 26 kV |
| Charge rate | 26 kJ/sec |
| Regulation | ±0.05% |
| Shot-to-shot stability | ±0.05% |

## Inductors

There are two different types of inductors in each module. The ballast inductor ensures an equal distribution of delivered energy to each flashlamp circuit. The damping element limits fault currents in the module resulting from capacitor failures and short circuits across the bus. The design of both inductors is driven by a general philosophy that all of the inductors must remain intact during any of the possible fault conditions. However, the individual inductor(s) affected by the fault will be replaced before the next shot. Efforts are under way to optimize both designs to minimize the cost while ensuring that the inductors will meet the fault requirements.

The stored energy is discharged through a high-power spark-gap switch (see the section on switches below) into a distribution network of 20 ballast inductors and transmission lines. The purpose of the ballast inductors is to ensure that the module's energy is delivered equally to all of the 40 flashlamps that it must power.

The two primary requirements of ballast inductors are:

- To provide current shaping over the NIF lifetime requirement of 20,000 shots.
- To withstand fault currents of 100 kA.

We have successfully demonstrated designs that will meet these requirements. Developments are continuing to lower the cost of these units.

The second type of inductor, a resistive inductor or damping element, is connected in series with each capacitor. The purpose of this damping element is to limit fault currents in the event that one of the capacitors fails internally, or in the event that the module's output bus is short-circuited. To minimize damage, the damping elements must be able to withstand a fault current of 400 kA. Considerable effort is being expended to ensure reliability of this system component. Damping element designs have been developed that will meet the requirements, but efforts are ongoing to "value engineer" this component as well.

## Switches

Each module must transfer the 2 MJ of energy stored in its capacitors to 40 flashlamps. It does this through a switch, which must meet the following criteria:

- Be highly reliable (no prefires).
- Have a relatively long lifetime.
- Conduct 530 kA.
- Operate at 24 kV.

SNL fabricated a test stand to test various types of switches to identify one that would meet these requirements. The types of switches tested include: spark-gap switch; ignition switch (a mercury-filled arc switch); rotating arc-gap switch; and two solid-state switches.

Maxwell/Physics International's Model ST300, a spark-gap switch shown in Figure 5, was selected on the basis of its performance and relatively low initial cost, even though its operating cost will be higher. Each ST300 will need to be replaced every 1,500 to 2,000 shots throughout NIF's anticipated lifetime requirement of 20,000 shots. A decision was made to utilize this switch instead of a rotating arc-gap switch, which remains an alternate. Although insufficient testing has been done on the rotating arc-gap switch, it appears that this type of switch would meet the NIF lifetime requirement. However, its cost is five to ten times that of the spark-gap switch Model ST300.

Data from SNL's multiple lifetime testing of the Model ST300 spark-gap switch, which has proven to be accurate and repeatable, was used to predict when switches would need to be replaced or refurbished.

FIGURE 5. Spark-gap switch. (70-00-0499-0827pb01)

# Controls and Diagnostics

Each of NIF's 192 power conditioning modules will have its own embedded controller, which will control module functions including:

- Charging of the main capacitors.
- Gas-purging of the switch.
- Charging the preionization circuit.
- Charging and firing of trigger circuits.

This embedded controller also serves diagnostics functions. Twelve-bit digitizers are used to collect waveform information from the module during a shot. The controller collects information, including 20 output current waveforms as well as reflector ground current and facility ground current. It collects power-supply-charging waveform information from the main

capacitor bank and the preionization capacitor bank. It monitors the waveforms to ensure that they are correct, and it informs the operator if a shot was acceptable. If there were problems inherent in the shot, the controller pinpoints the problem and alerts the operator.

Low-energy preionization lamp check (PILC) shots evaluate the health of all the flashlamps in the NIF system. The embedded controller evaluates waveform information to detect any broken flashlamps. This is a critical step that must precede flashlamp cooling, a procedure that could scatter broken glass and other debris throughout the amplifier and potentially cause significant damage to the amplifier and other laser system components. If no abnormalities are detected during the PILC, the controller will communicate the status to the supervisory control system, which will then initiate flashlamp cooling.

## The "FANTM"

The first-article NIF test module, or FANTM, represents the entire power conditioning system from "the wallplug," or AC power source, to the flashlamps. It was built in October 1998 to test and evaluate power conditioning module mechanical design and electrical performance. Since then, it has been operated and tested at SNL Albuquerque, collecting data to ensure that the module meets all NIF requirements, including fault tolerance and overall reliability. It also has been used to evaluate design improvements and to estimate time and effort required to build PCMs and install them in the NIF laser system.

Resistors initially were used to simulate flashlamp loads during activation and initial operation. In January 1999, NIF flashlamps were installed at Sandia as a load for the first-article module. Testing is under way to fully characterize module performance and reliability when driving NIF flashlamps.

## Acknowledgments

This article describes the contributions of many people, too numerous to list as co-authors. People who have made contributions to the designs and calculations described in this paper are: Jake Adcock, Gary Mower, and Dean Rovang (Sandia National Laboratories–Albuquerque); Steve Fulkerson, Doug Larson, and Chet Smith (Lawrence Livermore National Laboratory); Bob Anderson (American Controls Engineering); Jud Hammon (Maxwell/ Physics International); and Bill Gagnon (consultant).

## Notes and References

1. K. Whitham, D. Larson, B. Merritt, and D. Christie, "OVA Pulse Power Design and Operational Experience," *Pulsed Power for Lasers*, in *Proc. SPIE* (Society of Photo-optical Instrumentation Engineers, Los Angeles, CA, Jan. 13–14, 1987), **735**, 12–17.
2. D. Larson, R. Anderson, and J. Boyes, "Fault Tolerance of the NIF Power Conditioning System," in *Proc. of the First Annual Conference on Solid State Lasers for Application to Inertial Confinement Fusion* (Society of Photo-optical Instrumentation Engineers, Bellingham, WA, May 30-June 2, 1995), **2633**, 587–595.
3. W. L. Gagnon, "The Near and Long Term Pulse Power Requirement for Laser-Driven Inertial Confinement Fusion," in *Proc. of the Second IEEE International Pulsed Power Conference* (Institute of Electrical and Electronics Engineers, Lubbock, TX, June 12–14) **1979**, 49–54.

# INTEGRATED COMPUTER CONTROL SYSTEM

*P. J. VanArsdall*
*R. C. Bettenhausen*
*F. W. Holloway*
*R. A. Saroyan*
*J. P. Woodruff*

The National Ignition Facility (NIF) design team is developing the integrated computer control system (ICCS), which is based on an object-oriented framework applicable to event-driven control systems. The framework provides an open, extendable architecture that is sufficiently abstract to construct future mission-critical control systems. Supervisory software is constructed by extending the reusable framework components for each specific application. The framework incorporates services for database persistence, system configuration, graphical user interface, status monitoring, event logging, scripting language, alert management, and access control. More than twenty collaborating software applications are derived from the common framework.

The ICCS consists of 300 front-end processors (FEPs) attached to 60,000 control points coordinated by a supervisory system. Computers running either Solaris or VxWorks operating systems are networked over a hybrid configuration of switched fast Ethernet and Asynchronous Transfer Mode (ATM). ATM carries digital motion video from sensors to operator consoles. A brief summary of performance requirements follows (Table 1).

TABLE 1. Selected ICCS performance requirements.

| Requirement | Performance |
|---|---|
| Computer restart | <30 minutes |
| Postshot data recovery | <5 minutes |
| Respond to broad-view status updates | <10 seconds |
| Respond to alerts | <1 second |
| Perform automatic alignment | <1 hour |
| Transfer and display digital motion video | 10 frames per second |
| Human-in-the-loop controls response | within 100 ms |

The ICCS architecture was devised to address the general problem of providing distributed control for large scientific facilities that do not require real-time supervisory controls. The framework uses the client-server software model with event-driven communications to distribute control. The framework is interoperable among different kinds of computers and transparently distributes the software objects across the network by leveraging a Common Object Request Broker Architecture (CORBA).

## CORBA DISTRIBUTION

Past architectural approaches to distributed controls have relied on the technique of building large-application programming interface (API) libraries to give applications access to functions implemented throughout the architecture. This practice results in large numbers of interconnections that quickly increases the system complexity and make software modification much more difficult. To address this problem in the ICCS, software objects are distributed in a client-server architecture using CORBA.

CORBA is a standard developed by a consortium of major computer vendors to propel the dominance of distributed objects on local area networks and the World Wide Web. The best way to think of CORBA is as the universal "software bus." CORBA is a series of sophisticated, but standard sockets into which software objects can "plug and play" to interoperate with one another, even when made by different vendors. By design, CORBA objects interact across different languages, operating systems, and networks.

At a greatly simplified level, the major parts of CORBA are shown in the figure below. The interface types and methods provided by the server objects and used by the clients are defined by an industry standard Interface Definition Language (IDL). The IDL compiler examines the interface specification and generates the necessary interface code and templates into which user-specific code is added. The code in the client that makes use of CORBA objects is written as if the server was locally available and directly callable. Each computer on the network has an object request broker that determines the location of remote objects and transparently handles all communication tasks.

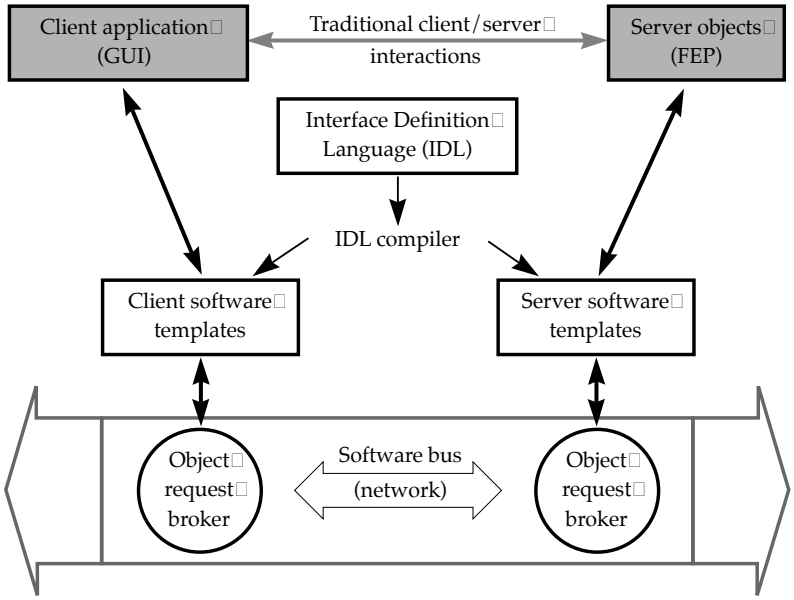


**Software bus network implementation for CORBA distribution.**
(40-00-0298-0341pb01)

Over twenty distributed software applications built from the common framework will operate the NIF control system hardware from a central control room (Figure 1). The ICCS software framework is the key to managing system complexity and, because it is fundamentally generic and extensible, it is also reusable for the construction of future projects.

## Control System Architecture

The ICCS is a layered architecture consisting of FEPs coordinated by a supervisory system (Figure 2). Supervisory controls, which are hosted on UNIX workstations, provide centralized operator controls and status, data archiving, and integration services. FEP units are constructed from VME/VXI-bus or PCI-bus crates of embedded controllers with interfaces that attach to control/monitor points (e.g., motors and calorimeters). FEP software implements the distributed services needed to operate the hardware by the supervisory system. Precise triggering of fast diagnostics and controllers is handled during a two-second shot interval by the timing system, which is capable of providing triggers to 30-ps accuracy and stability. The software is distributed among the computers and provides plug-in software extensibility for attaching control/monitor points and other software services by using the CORBA protocol.

The operator console provides the human interface in the form of operator displays, data retrieval and processing, and coordination of control functions. Supervisory software is partitioned into several cohesive subsystems, each of which controls a primary NIF subsystem such as alignment or power conditioning. Several databases are incorporated to manage experimental and operations data. The subsystems are integrated to coordinate operation of laser and target area equipment.

FEPs perform sequencing, data acquisition, process control, and data reduction. The software framework includes a standard way for FEP units to be integrated into the supervisory system by providing the common distribution mechanism coupled with software patterns for hardware configuration, command, and status monitoring functions.

A segment of the control system accommodates industrial controls for which standard commercial solutions already exist. The segment is composed of a network of programmable logic controllers that reside below the FEP and attach to field devices that functionally control, for example, vacuum systems, argon gas in the beam tubes, and thermal gas conditioning for amplifier cooling. This segment also observes the independent safety interlock system, which monitors doors, hatches, shutters, and other sensors to establish and display the hazard levels in the facility. Potentially hazardous equipment is permitted to operate only when conditions are safe. Interlocks

FIGURE 1. Photograph of the NIF computer control room. (40-00-1298-2628pb01)

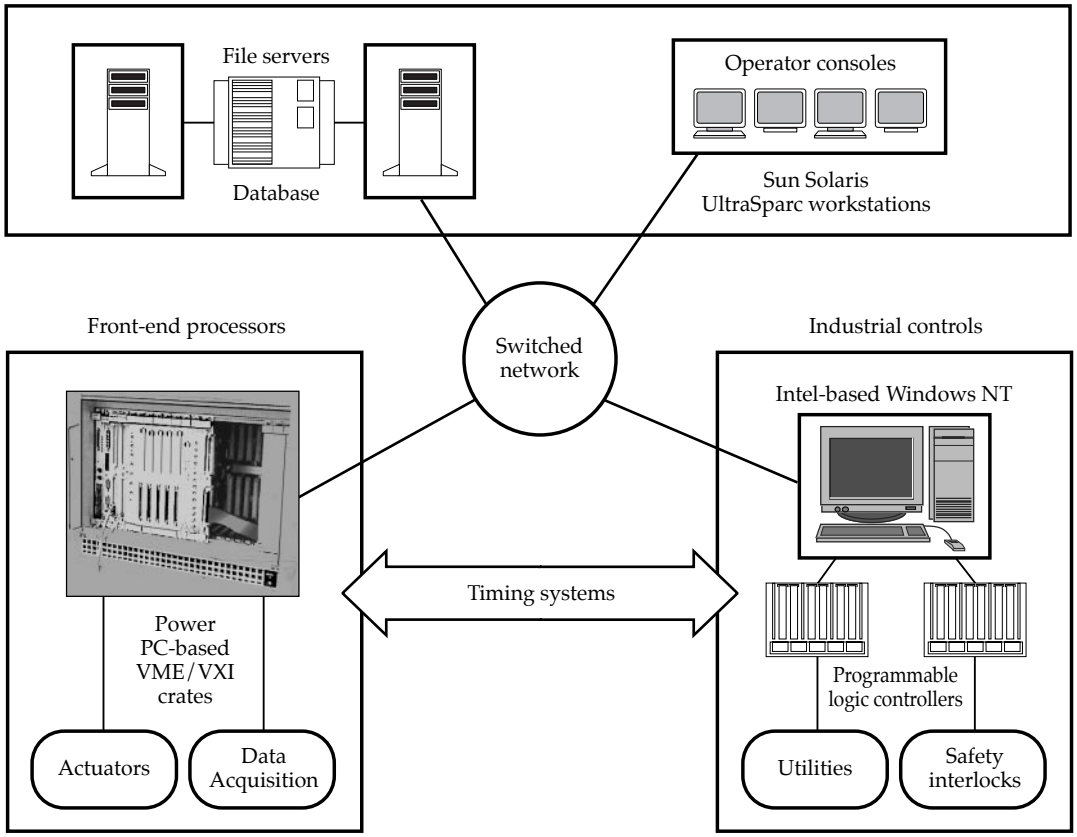


FIGURE 2. Integrated computer control system architecture. (40-00-1298-2627pb01)

function autonomously to ensure safety without dependency on the rest of the control system.

There are eight supervisory software applications that conduct NIF shots in collaboration with 19 kinds of FEPs as shown in Figure 3. The ICCS is partitioned into several loosely coupled systems that are easier to design, construct, operate, and maintain. Each subsystem is composed of a supervisor and associated FEPs. The eighth supervisor is the shot director, which is responsible for conducting the shot plan, distributing the countdown clock, and coordinating the other seven supervisory applications.

Seven subsystems comprise the primary supervisory controls. The Alignment Supervisor provides coordination and supervision of laser wavefront control and laser component manual and automatic alignment. The Laser Diagnostics Supervisor provides functions for diagnosing performance of the laser by collecting integrated, transient, and image information from sensors positioned in the beams. The Optical Pulse Generation Supervisor provides temporally and spatially formatted optical pulses with the correct energetics and optical characteristics required for each of the beams. The Target Diagnostics Supervisor coordinates the collection of data from a diverse and changing set of instruments. The Power-Conditioning Supervisor is responsible for high-level control and management of high-voltage power supplies that fire the main laser amplifiers. The Pockels Cell Supervisor manages operation of the plasma electrode Pockels cell optical switch that facilitates multipass amplification within the main laser amplifiers. The Shot Services Supervisor provides monitoring of environmental and safety parameters as well as control of programmable logic controller subsystems.

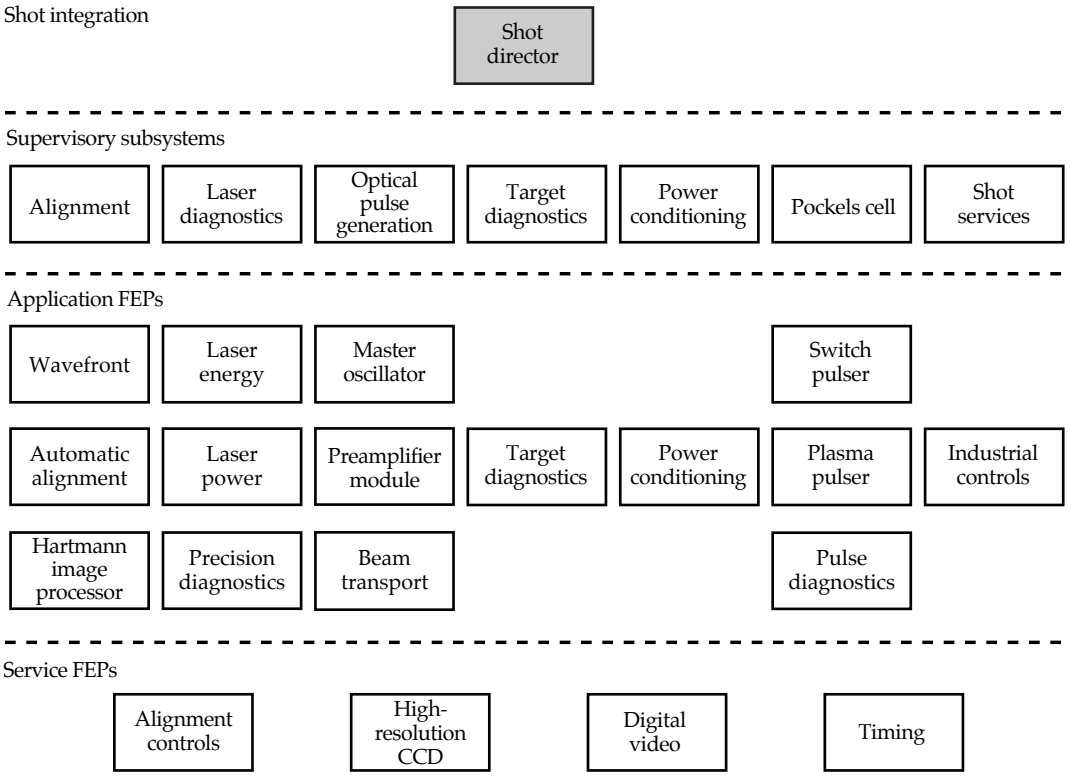


FIGURE 3. Software applications in the NIF control system. (40-00-0298-0324pb02)

## Computer System and Network

Figure 4 shows the NIF computer and network architecture, which is composed of 30 UNIX workstations, 300 FEPs, and several hundred more embedded controllers (not shown). The main control room contains seven graphics consoles, each of which houses two workstations with dual displays. The supervisors are normally operated from a primary console, although the software can easily be operated from adjacent consoles or remote graphics terminals located near the front-end equipment. File servers provide archival databases as well as centralized management services necessary for coordinating the facility operation.

The network design utilizes both Ethernet and ATM technologies to take advantage of the best features of each. ATM provides time-sensitive video transport, whereas Ethernet provides connectivity for the large majority of systems. The design utilizes 155 Mbit/s ATM and Ethernet at both 10 and 100 Mbit/s speeds, depending on expected traffic requirements. The operator consoles and file servers have both ATM and 100 Mbit/s Ethernet connections, while most FEPs have either 10 or 100 Mbit/s connections made through Ethernet switches. Given the low cost and performance advantages of Ethernet switches relative to shared Ethernet hubs, switches with 100 Mbit/s uplinks will be used.

TCP/IP (Transmission Control Protocol/Internet Protocol) is the protocol used for reliable data transport between systems, either over Ethernet or ATM. TCP provides retransmission of packets in the event that one is lost or received in error. The only traffic not using TCP will be digitized video and network triggers. Video is transferred using the ATM adaptation layer 5 (AAL5) protocol. Network triggers are broadcast to many end-nodes simultaneously using multicast protocols.

The network supports the transport of digitized motion video in addition to the more typical control, status, and shot data.

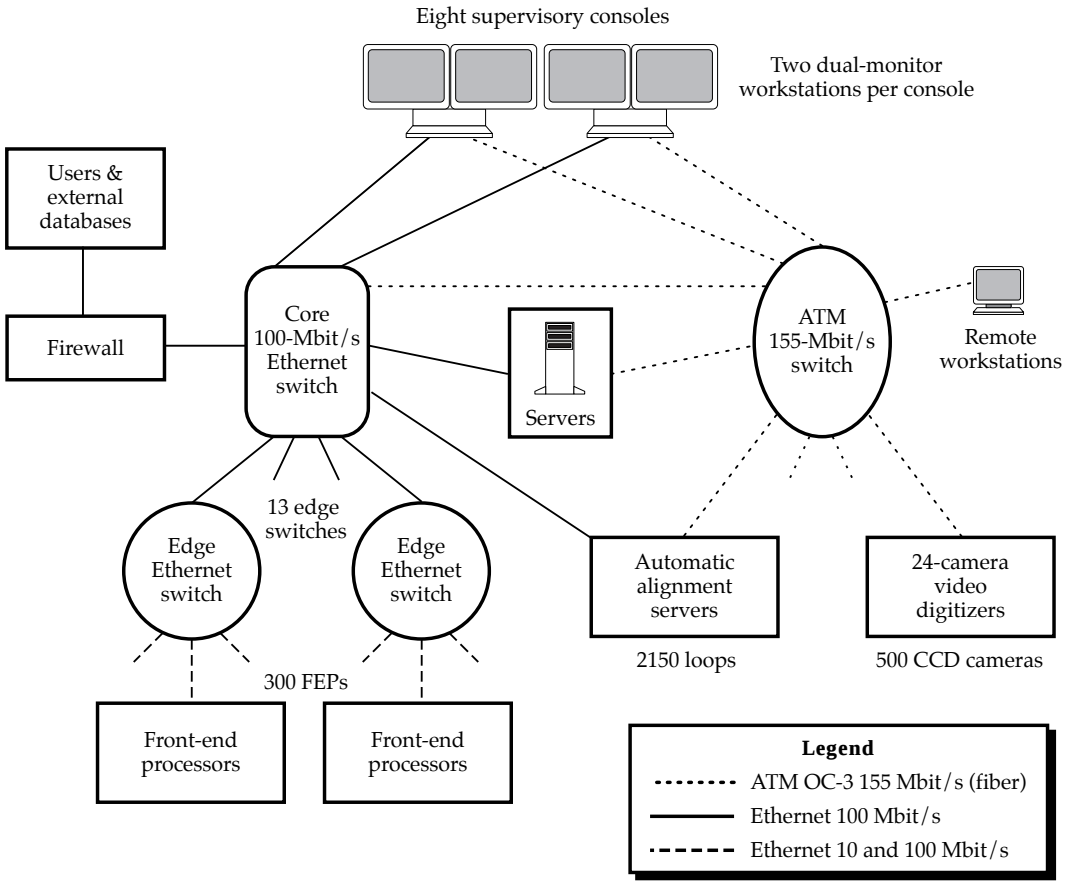


FIGURE 4. NIF computer system and network architecture. (40-00-1298-2629pb01)

The network transports video streams at 10 frames per second (about 25 Mbit/s) between special FEPs that digitize camera images and operator workstations that can display at least two concurrent streams. Video compression is not used because of the high cost of encoding the video stream.

Digitized video is sent via the ATM application program interface (API) using the ATM quality of service capabilities. The API provides an efficient method of moving large, time-sensitive data streams, resulting in higher frames/second rates with lower central processing unit (CPU) utilization than alternative approaches, which is an important consideration for the video FEPs and console workstations. Performance testing of the prototype video distribution system indicates that 55% of the FEP CPU (300-MHz UltraSparc AXI) is used to broadcast three streams, while 10% of the operator workstation CPU (300-MHz UltraSparc 3D Creator) is utilized for each playback stream.

Estimates of the peak traffic requirements for the various subsystems were analyzed as a basis for the network design. The expected peak traffic flows between subsystems in terms of messages per second and message size were specified. This data was combined and analyzed to determine peak throughputs into and out of each network-attached device.

A discrete event simulation was created to evaluate the performance of key network scenarios. For example, it was shown that "network triggers" in the millisecond regime could be reliably broadcast between computers in the network via the user datagram protocol. One application using network triggers is the arming of the video FEPs to enable digitizing the laser pulse during shots. The network trigger tactic will save $250K over a hardware implementation.

If bandwidth requirements increase in the future, the network architecture allows

the integration of Gbit/s Ethernet and 622 Mbit/s ATM technologies in a relatively straightforward manner.

## Software Framework

The ICCS supervisory software framework is a collection of collaborating abstractions that are used to construct the application software. Frameworks[1] reduce the amount of coding necessary by providing prebuilt components that can be extended to accommodate specific additional requirements. The framework also promotes code reuse by providing a standard model and interconnecting CORBA backplane that is shared from one application to the next.

Components in the ICCS framework are deployed onto the file servers, workstations, and FEPs, as shown generically in Figure 5. Engineers specialize the framework for each application to handle different kinds of control points, controllers, user interfaces, and functionality. The framework concept enables the cost-effective construction of the NIF software and provides the basis for long-term maintainability and upgrades.

The following discussion introduces the framework components that form the basis of the ICCS software.

**Configuration**—a hierarchical organization for the static data that define the hardware control points accessible to the ICCS. Configuration provides a taxonomic system

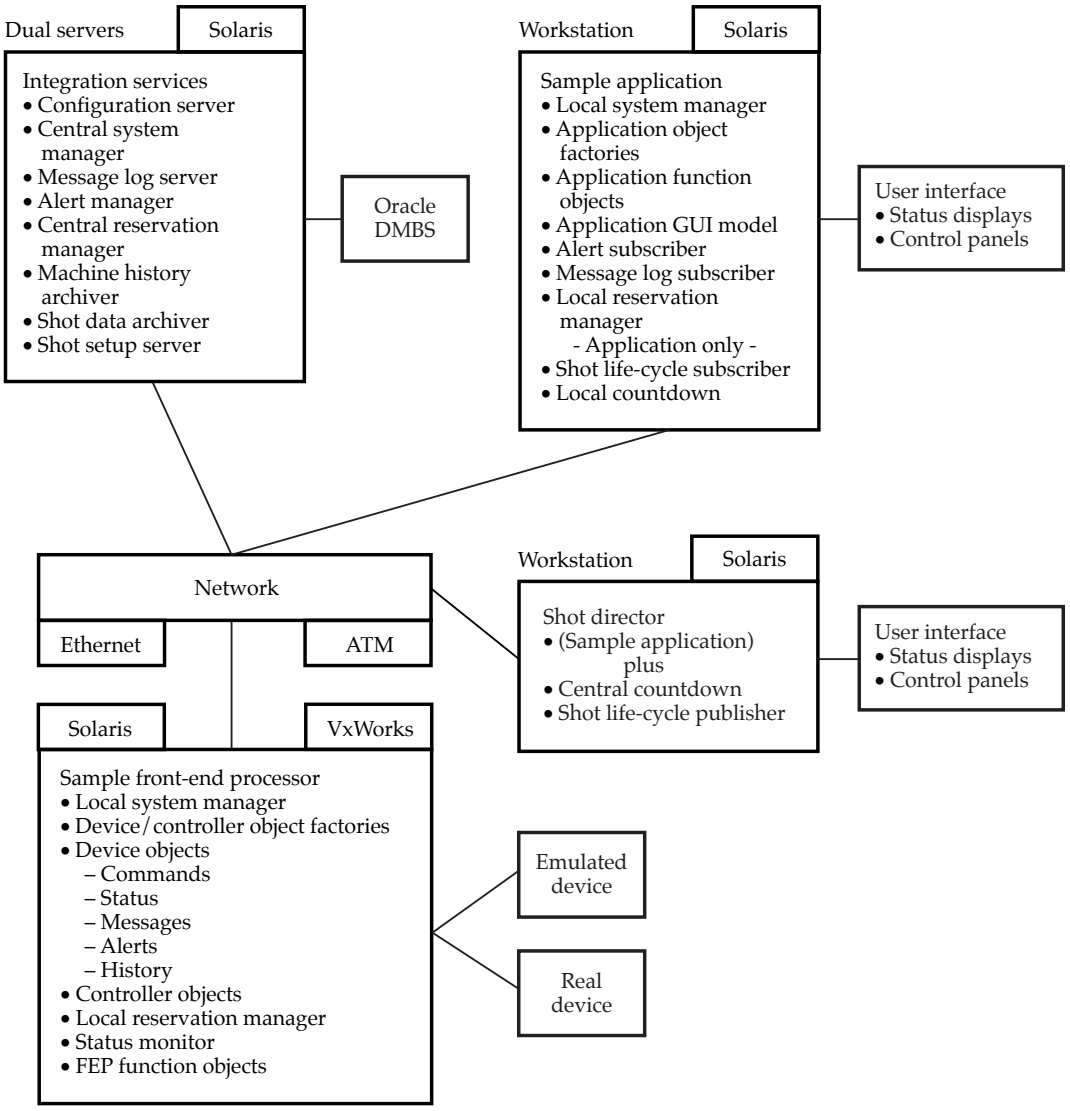


FIGURE 5. Deployment of ICCS framework objects into a sample application and FEP on networked computers. (40-00-1298-2630pb01)

used as the key by which clients locate devices (and other software services) on the CORBA bus. During normal operation, configuration provides to clients the CORBA references to all distributed objects. An important responsibility of configuration is the initialization of FEPs during start-up. Configuration data are stored in the database and describe how and where the control hardware is installed in the system. Calibration data for sensors, setpoints for alignment devices, and I/O channels used by devices on interface boards are examples of static data managed by configuration. During ICCS start-up, this framework collaborates with an object factory located in the FEP. Using the data and methods stored in the configuration database, the object factory instantiates, initializes, and determines the CORBA reference for each device and controller object in the FEP.

**Status Monitor**—a device that provides generalized services for broad-view operator display of device status information using the publisher–subscriber model of event notification. The status monitor operates within the FEP observing devices and notifies other parts of the system when the status changes by a significant amount. Network messages are only generated when changes of interest occur.

**Sequence Control Language**—a language used to create custom scripting languages for the NIF applications. The service automates sequences of commands executed on the distributed control points or other software artifacts. After full implementation of the design, operators will create and edit sequences by selecting icons that represent control constructs, Boolean functions, and user-supplied methods from a visual programming palette. The icons are then interconnected to program the sequence, and any Boolean conditions or method arguments needed are defined to complete the sequence script.

**Graphical User Interface (GUI)**—the method through which all human interaction with the ICCS will take place and which will be displayed on control room consoles or other workstations in the facility. The GUI is implemented as a framework to ensure consistency across the applications. Commercial GUI development tools are used to construct the display graphics. This framework consists of guidelines for look and feel as well as many common graphical elements.

**Message Log Server**—a device that provides event notification and archiving services to all subsystems or clients within the ICCS. A central server collects incoming messages and associated attributes from processes on the network, writes them to appropriate persistent stores, and also forwards copies to interested observers such as GUI windows.

**Alert System Manager**—a component that raises an alert for any application encountering a situation that requires immediate attention, which then requires interaction with an operator for the control system to proceed. The alert system records its transactions so that the data can be analyzed after the fact.

**Reservation Manager**—a system that manages access to devices by giving one client exclusive rights to control or otherwise alter a control/monitor point. The framework uses a lock-and-key model. Reserved devices that are "locked" can only be manipulated if and when a client presents the "key."

**System Manage**r—a component that provides services essential for the integrated management of the ICCS computer network. This component ensures that necessary processes and computers are operating and communicating properly. Services include orderly system start-up, shutdown, and watchdog process monitoring.

**Machine History Archiver**—a system that gathers information for analysis about NIF operational performance to improve efficiency and reliability. Examples of such information are component adjustments, abnormal conditions, operating service, periodic readings of sensors, and reference images.

**Generic FEP**—a component that pulls together the distributed aspects of the other frameworks (in particular the system manager, configuration, status monitor, and reservation frameworks) by adding unique classes for supporting device and controller interfacing. These classes are

responsible for hooking in CORBA distribution as well as implementing the creation, initialization, and connection of device and I/O controller objects. The generic FEP also defines a common hardware basis including the processor architecture, I/O board inventory, device drivers, and field-bus support. The FEP application developer extends the base software classes to incorporate specific functionality and control logic.

**Shot Data Archiver—**a server working in collaboration with the System Manager to assure that requested shot data are delivered to a disk staging area. The ICCS is responsible for collecting the data from diagnostics, making the data immediately available for "quick look" analysis, and delivering the data to an archive.

**Shot Setup Server**—a server working in collaboration with the ICCS shot director to manage shot setup plans. These plans contain the experimenter's goals for a shot and the hardware setup derived from the goals.

## Software Development Environment

The ICCS incorporates Ada95, CORBA, and object-oriented techniques to enhance the openness of the architecture and long-term maintainability of the software. C++ is also supported for the production of graphical user interfaces and the integration of commercial software. Software development of an expected 500,000 lines of code is managed under an integrated software engineering process (Figure 6) that covers the entire life cycle of design, implementation, and maintenance. The object-oriented design is captured in the Rose design tool in UML (unified modeling language) notation that maintains schematic drawings of the software architecture.

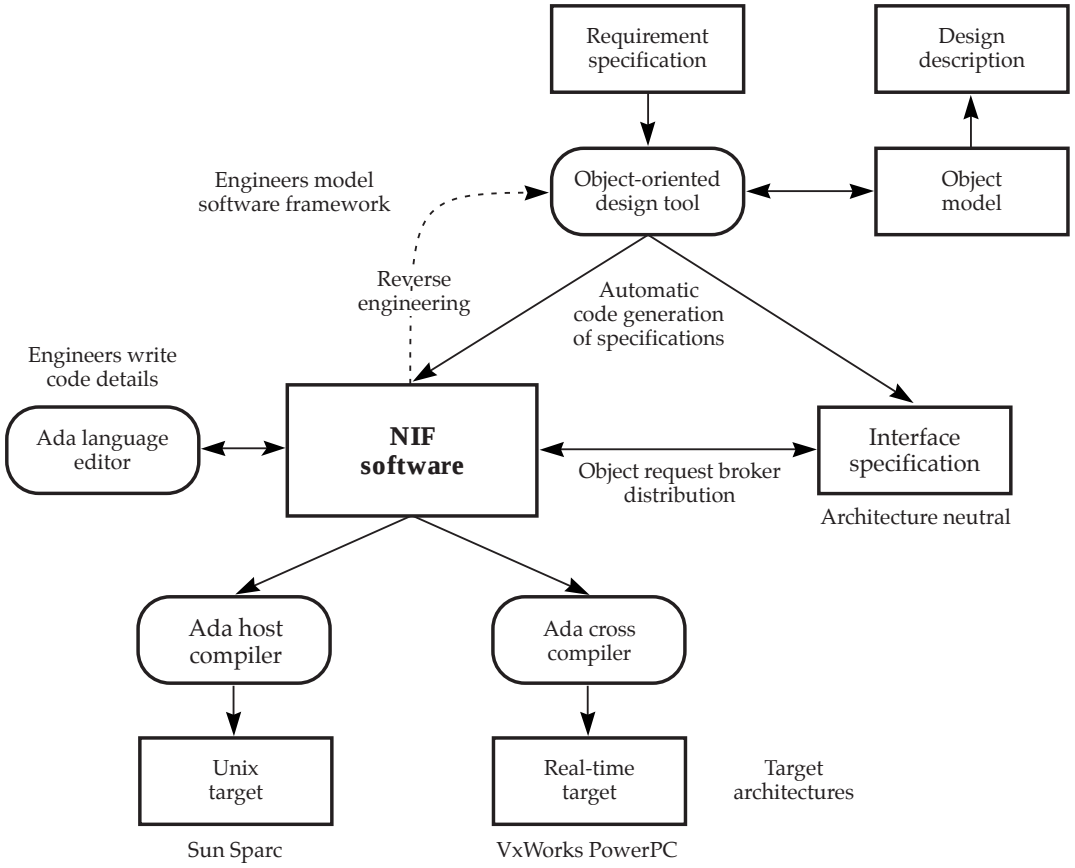


FIGURE 6. Flowchart of the ICCS software engineering process incorporating model-driven design techniques. (40-00-1298-2631pb01)

Developers analyze detailed requirements and express them as scenarios that help determine how the software will be organized. In essence, the Rose tool is used to model the public interfaces and interactions between major software entities (i.e., the classes). Rose automatically generates Ada code specifications corresponding to the class interface and type definitions. The developer fills in the detailed coding necessary to implement the private contents of each class. Rose generates IDL for classes that are distributed, which is passed through the IDL compiler to generate Ada or C++ skeleton code as before. The design description is a narrative document that explains the object-oriented model and contains other information necessary for implementation and maintenance.

Source code is compiled for a variety of target processors and operating systems. Current development is either self-hosted to Solaris on Sparc processors or cross-compiled for VxWorks on PowerPC processors. The models, sources, binaries, and run-time images are version-controlled by the Apex configuration management system, which allows the frameworks and applications to be independently developed by different engineers, each having a protected view of the other components.

## Summary

The ICCS is being developed using the iterative approach to software construction[2] that is proven effective for projects whose requirements continue to evolve. Five iterations in the "Light" series (Figure 7) are planned leading to facility deployment in 2000 when the first 8 of the 192 beams will be operated. Each new release will follow an updated plan addressing the greatest risks to the architecture while increasing the functionality delivered to the Project.

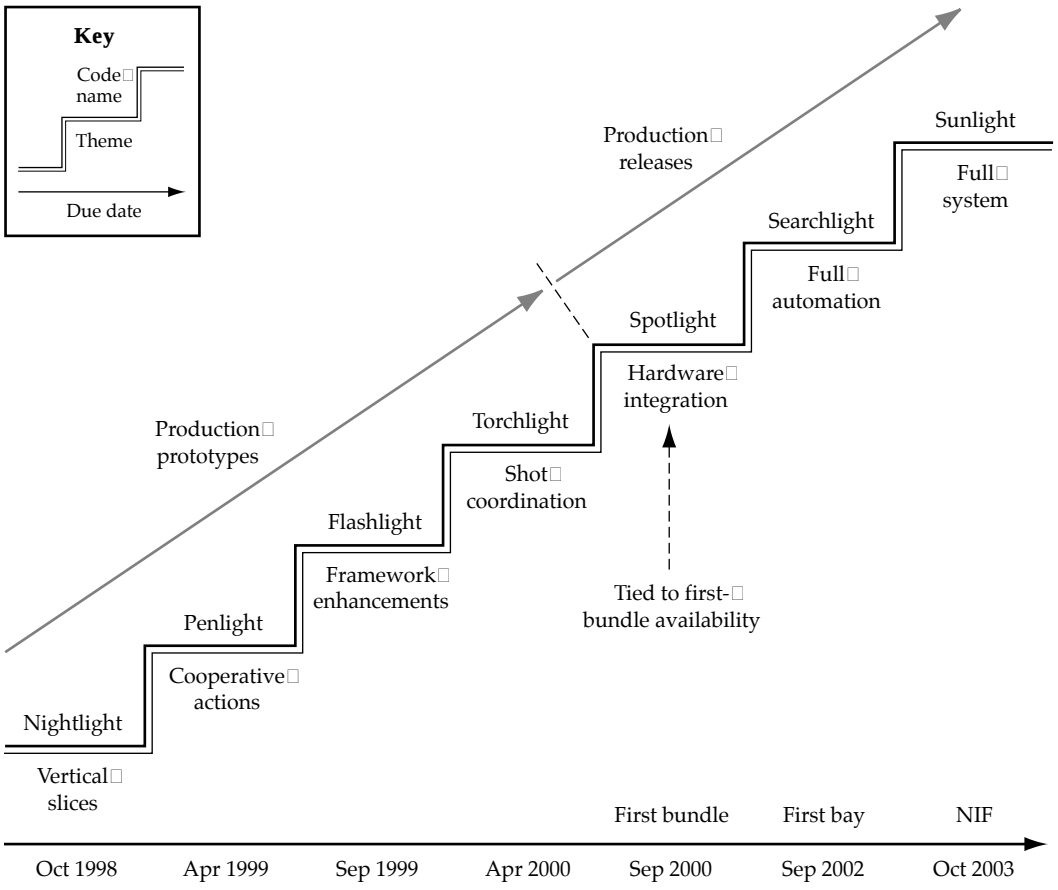


FIGURE 7. Light series of NIF software construction. (40-00-1298-2632pb01)

The first release, "Nightlight," was completed this fall and submitted to independent test. Nightlight delivered 120,000 source lines of tested code—about 20% of the anticipated total—which exercised the framework in initial vertical slices of all supervisory and FEP applications. Nightlight also established an independent test process and the procedures by which quality software could be assured.

Construction of the ICCS incorporates many of the latest advances in distributed computer and object-oriented software technology. Primary design goals are to provide an extensible and robust architecture that can be maintained and upgraded for decades. Software engineering is a managed process utilizing model-driven design to enhance the product quality and minimize future maintenance costs. The ICCS framework approach permits software reuse and allows the system to be constructed within budget. As an added benefit, the framework is sufficiently abstract to allow future control systems to take advantage of this work.

## Acknowledgments

The authors wish to acknowledge the contributions of the following colleagues without whose efforts this work would not be possible: G. Armstrong, R. Bryant, R. Carey, R. Claybourne, T. Dahlgren, F. Deadrick, R. Demaret, C. Estes, K. Fong, M. Gorvad, C. Karlsen, B. Kettering, R. Kyker, L. Lagin, G. Larkin, G. Michalak, P. McKay (Sandia National Laboratories, Albuquerque, NM), M. Miller, V. Miller Kamm, C. Reynolds, R. Reed, W. Schaefer, J. Spann, E. Stout, W. Tapley, L. Van Atta, and S. West.

## Notes and References

1. V. Swaminathan and J. Storey, *Object Magazine*, April 1988, pp. 53–57.
2. B. Boehm, *IEEE Computer*, May 1988, pp. 61–72.

# Multiaperture Optical Switch for the NIF

*M. Rhodes* *C. Ollis*

*R. Bettenhausen* *J. Trent*

*P. Biltoft*

This article discusses the optical switch system for the National Ignition Facility (NIF). The NIF laser architecture is based on a multipass power amplifier to reduce cost and maximize performance. A key component in the laser design is an optical switch that "closes" to trap the optical pulse in the amplifier cavity for four gain passes and then "opens" to divert the optical pulse out of the amplifier cavity. The optical switch consists of a full-aperture Pockels cell that provides voltage control of the beam polarization and a reflecting–transmitting polarizer.

Figure 1 shows one of NIF's 192 beamlines. During a NIF shot, an optical pulse enters the cavity from the transport spatial filter by reflecting off the polarizer. After the optical pulse passes through the Pockels cell, a precisely timed voltage pulse is applied to the Pockels cell so that the beam polarization is rotated 90° when it returns after reflecting from the LM1 mirror. The optical pulse then passes through the polarizer, reflects off the LM2 mirror, and passes back through the polarizer. Because voltage is still applied to the Pockels cell, the beam polarization is rotated back to its original polarization on this third pass through the Pockels cell. After the optical pulse passes, the voltage pulse starts to turn off. By the time the optical pulse returns again, no further rotation occurs. The beam reflects off the polarizer and exits the cavity, having passed through the main amplifier four times.

Optical switches are common in many types of lasers, such as Q-switched lasers and regenerative lasers. However, the size (40 × 40 cm), shape (square), and energy density (5 J/cm$^2$) of the NIF beams require an optical switch of unprecedented proportions. Commercially available, conventional Pockels cells do not scale to such

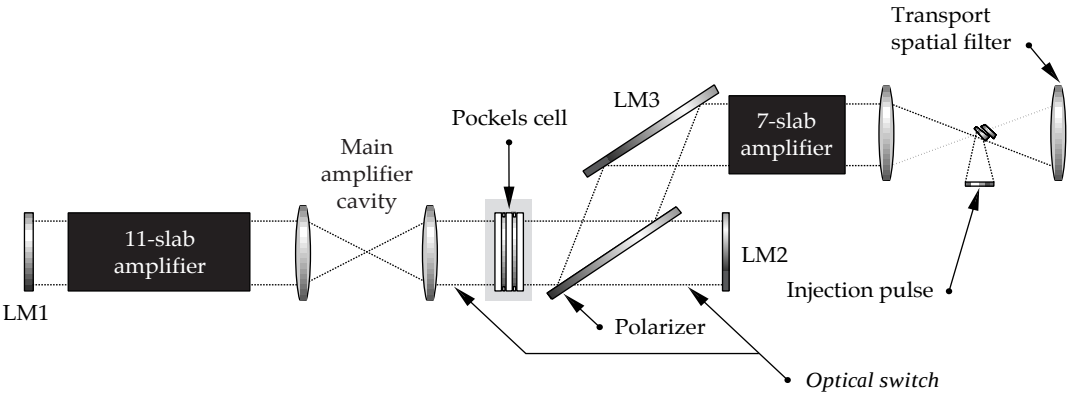


FIGURE 1. One of 192 beamlines of the NIF, showing the location of the optical switch system. (70-00-0299-0367pb01)

large apertures or the square shape required for close packing. The NIF optical switch is based on the plasma-electrode Pockels cell (PEPC). This article first reviews PEPC technology, then discusses the details of the NIF optical switch system, including the line replaceable unit (LRU), support structure, vacuum and gas systems, required assembly hardware, electronic systems required to operate the optical switch, and the computer control system.

## Plasma Electrode Pockels Cell Technology

In any Pockels cell, polarization rotation of a transmitted laser beam occurs when an electric field is applied to an electro-optic crystal, inducing birefringence. In a conventional "ring-electrode" Pockels cell, the electric field is applied to a cylindrical rod of crystal via rings of metal deposited on the end faces of the rod. To obtain sufficient field uniformity across the active aperture, the length of the rod must be one to two times the diameter. This requirement poses a problem for Pockels cells with apertures larger than about 10 cm.

In a PEPC, the electric field is applied in a different way. A cloud of ionized gas (plasma) is formed by electric discharge on both sides of the crystal. The plasma is electrically conductive and transparent to the incoming laser beam. The plasma coats both sides of the crystal, allowing direct application of the required voltage (about 17,000 V in our case). The electric field is uniform across the entire aperture regardless of aperture shape or size.

PEPC technology was first invented at LLNL in the 1980s, but focused development of a PEPC to be used on a high-energy laser began in 1990. We progressed from a 27-cm-aperture PEPC to a 32-cm PEPC, then to the 37-cm PEPC that became a working part of the Beamlet laser (the scientific prototype for NIF). With the success of Beamlet and the Beamlet PEPC, we began working on a PEPC for NIF in 1995. The focus was to find a way to closely pack multiple apertures to meet the goals of the NIF conceptual design. Our work culminated in the NIF PEPC shown in Figure 2.

## NIF PEPC Line Replaceable Unit

As with many other NIF components, the NIF PEPC is designed as a line replaceable unit (LRU) to enable rapid replacement and off-line repair. This is the smallest subarray of apertures that will be installed or removed from the NIF beamline. The PEPC LRU, shown in Figure 2, is a 4 × 1 module (four apertures high by one wide). A total of 48 PEPC LRUs will be required to provide optical switching for the 192 beamlines in NIF. Although the LRU integrates four apertures into one module, electrically it is divided into a pair of two-aperture PEPCs, one of which is shown in cross section on the right side of Figure 3. Also shown are the pulse generators that operate the PEPC. Each plasma pulser drives a pulse of current (~1000 A) through the low-pressure helium (~65 mTorr) on either side of the KDP crystals forming the plasmas. Once the plasmas cover both sides of the KDP, the switch pulser fires, applying the exact voltage (~17 kV) across the crystals required for 90° of polarization rotation.

The NIF PEPC is a complex piece of electro–mechanical–optical hardware that integrates various elements, including a four-aperture PEPC, a high-vacuum pumping system, a feedback-controlled gas-feed system, a support frame, and a three-point kinematic mounting system. Each of the four apertures in an LRU requires three large-aperture optical components: two fused silica windows and one plate of KDP. Each LRU contains eight windows and four KDP plates.

## The Operational Core: A Four-Aperture PEPC

The operational core of the PEPC LRU is a four-aperture PEPC whose design is based on nine years of development and testing. All the PEPCs we have built have essentially the same construction. They are a sandwich structure made of an insulating midplane between a pair of housings. The midplane acts as a carrier for the KDP crystals. The housings, in conjunction with the windows, form sealed volumes covering

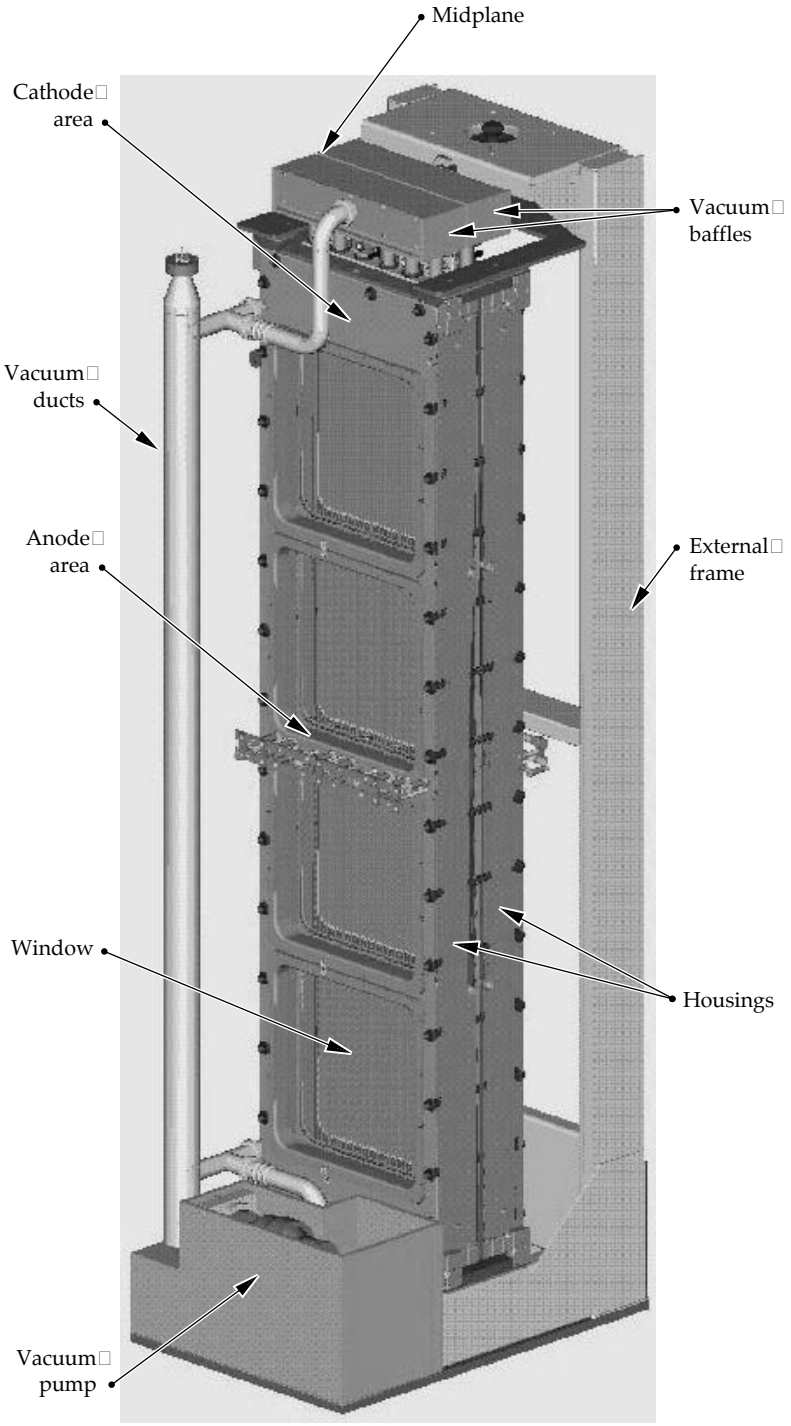


FIGURE 2. Each NIF PEPC line replaceable unit (LRU) is a 4 × 1 module.
(08-00-1198-2240pb01)

the KDP surfaces. The plasma discharges required for PEPC operation are formed within these sealed volumes. The housings also act as mechanical members that support the midplane and allow for mounting of cathode-electrode assemblies, anode-electrode assemblies, vacuum baffle assembly, and silica windows.

An important difference between the Beamlet PEPC and the NIF PEPC is the choice of housing material. Housings in the Beamlet PEPC were fabricated from solid polyethylene. Although this material provided excellent insulation properties, the polyethylene proved difficult to machine to close tolerances. For NIF, the

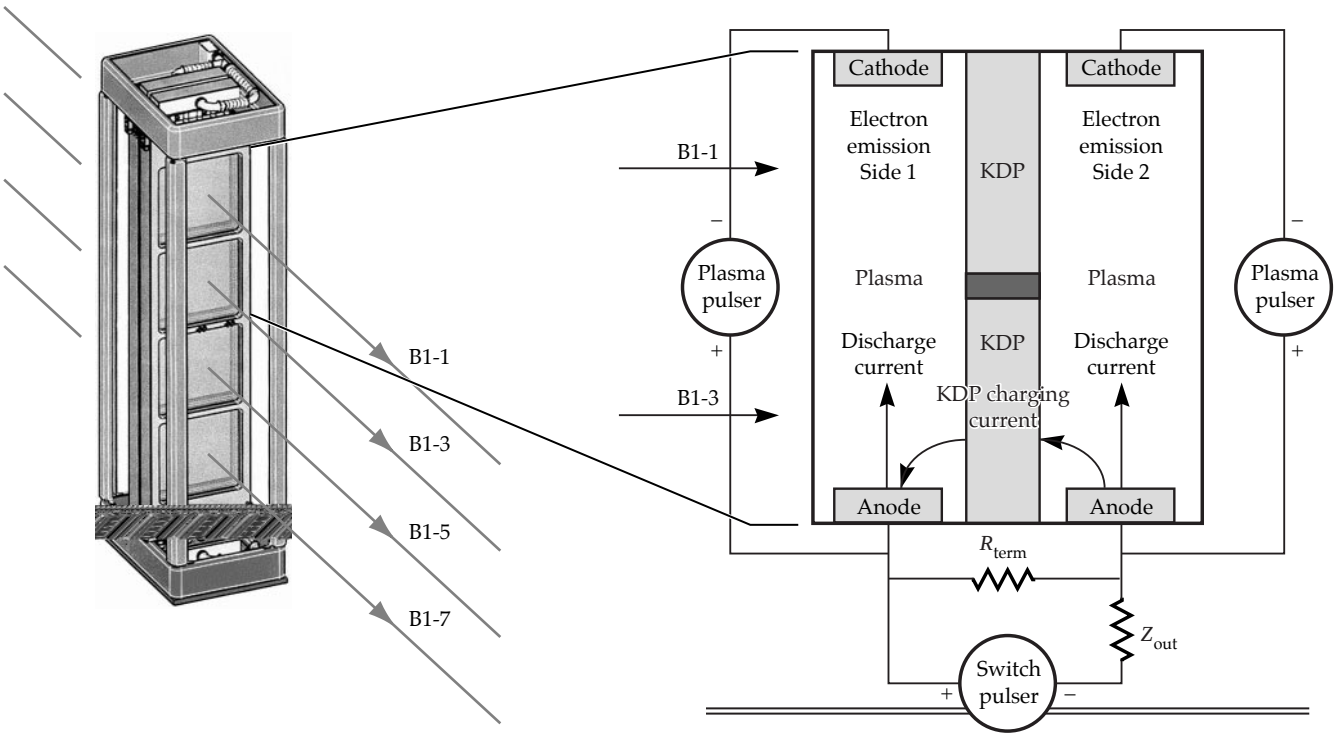


FIGURE 3. The LRU is electrically divided into a pair of two-aperture PEPCs, one of which is shown in cross section on the right. Also shown are the pulse generators that operate the PEPC. (70-00-0299-0368pb01)

PEPC housings are made from aluminum. Compared to polyethylene (or any other plastic), aluminum has superior strength and machinability. We take advantage of the higher strength by reducing the housing wall thickness enough to meet the aperture packing requirements for NIF. However, aluminum does not provide the required insulation between the discharge anode and cathode structures. They are insulated from the housing with plastic, and plasma is insulated from the aluminum walls by an anodic coating on the aluminum ($Al_2O_3$ insulator).

We have tested our design of the operational core by constructing an operational prototype shown in Figure 4. This device forgoes the external frame described below, but otherwise is a fully operational NIF 4 × 1 PEPC. We have tested the switching performance of the operational prototype in a four-beam polarimeter that illuminates each aperture with a low-fluence NIF-size laser beam. The experimental apparatus measures the fraction of light in two orthogonal polarizations, from which we can determine switching efficiency. If all the light is perfectly rotated exactly 90°, then the switching efficiency is 100%. In practice, there are always factors that cause less than perfect switching. Some examples are strain in the crystal, variations in applied voltage, and strain in the vacuum windows. Switching efficiency only includes losses due to polarization errors and does not include absorption in the crystal (about 5% per cm) or reflective losses from the optic surfaces. The NIF requirements are that the average switching efficiency across an entire aperture must be better than 99%, and that the minimum switching efficiency of any small spot must be greater than 98%. Results from the prototype show that each of the four apertures has an average switching efficiency of at least 99.8%, and the lowest small-area switching efficiency is 99.5%. Thus, the NIF requirements are easily met. We have determined that the dominant factor causing polarization error in our prototype is strain in the vacuum windows. Such strain is unavoidable because

FIGURE 4. Photograph of the prototype used to test our design of the operational core. This device has no external frame, but otherwise is a fully operational NIF 4 × 1 PEPC. (08-00-1198-2242pb01)

of the atmospheric pressure difference across the windows. However, ensuring the flatness of the window support shelf in the housings can minimize the resulting polarization error.

## Vacuum and Gas Feed System

The vacuum and gas feed system is required for plasma-discharge production. The vacuum system consists of a hybrid turbomolecular-drag pump. A single pump evacuates the entire LRU interior to the $10^{-6}$-Torr range. The discharge volume is pumped through ports built into the cathode bases. These ports connect to the vacuum baffle structure. The baffles are insulators that keep the switch pulse from shorting out through the common vacuum system. The baffles connect to the turbo pump with a series of ducts. All turbo pumps in a cluster exhaust to a mechanically pumped foreline manifold.

The gas feed system injects the discharge gas near the anodes so the gas flows across the crystal faces. A constant pressure is maintained with a feedback-control system. We determined the operating pressure experimentally to optimize plasma uniformity, and the value is typically 65 mTorr in the NIF PEPC LRU. A group of gauges mounted on the vacuum ducting measures the pressure over various ranges. The high-vacuum base pressure is measured with a cold-cathode ionization gauge. The pumpdown from atmosphere is measured with a 0- to 1000-Torr capacitance manometer. The operating pressure is measured with 0- to 1-Torr capacitance manometer. This gauge provides feedback to the pressure controller that varies the output of a mass flow controller.

## Support Frame and Kinematic Mounts

In the PEPC LRU, the operational core mounts into an L-shaped frame, as shown in Figure 5. The bottom of the support frame is an interface plate that incorporates all of the interfaces required between the PEPC LRU and the rest of the PEPC system. The interface plate includes feedthroughs for 4 plasma-pulse cables, 16 switch-pulse cables, 2 switch-pulse voltage monitors, gas input, foreline vacuum exhaust, vacuum gauge feedthroughs, and access to the turbo pump. The interface plate also seals to the NIF periscope structure after LRU insertion.

The PEPC LRU attaches to the periscope structure by a three-point kinematic mounting system that allows for safe, precise, ultraclean, repeatable positioning of the PEPC in the NIF beamline.

FIGURE 5. Prototype of the PEPC LRU mounted to a mockup section of periscope structure. (70-00-0299-0369pb01)

A ball mounted to the top of the LRU, as shown in Figure 6, is one of the three mounting points. When inserted into the periscope, the ball mates with a cone attached to the periscope frame. A closing "clamshell" mechanism captures the ball and keeps it in contact with the cone. The LRU essentially hangs from this device. The other two mounting points are a pair of V grooves, attached to each side of the LRU near the bottom, that mate with a pair of balls attached to the periscope frame.

The mounting system provides for precise and repeatable placement of an LRU in a NIF beamline. Each LRU must be interchangeable to any other location in the beamline. The requirement for positioning is ±1 mm in translation and ±120 μrad in rotation about the vertical axis. We have verified that our design meets these requirements by performing tests with the prototype assembly. Test results show that we achieved ±0.04 mm in translation and ±55 μrad in rotation about the vertical axis. The results are well within the NIF requirements.

## Assembly Fixtures

The PEPC LRUs will be assembled in the NIF Optical Assembly Building (OAB). A dedicated area in the OAB will be configured specifically for PEPC assembly and testing. Because the PEPC LRUs contain

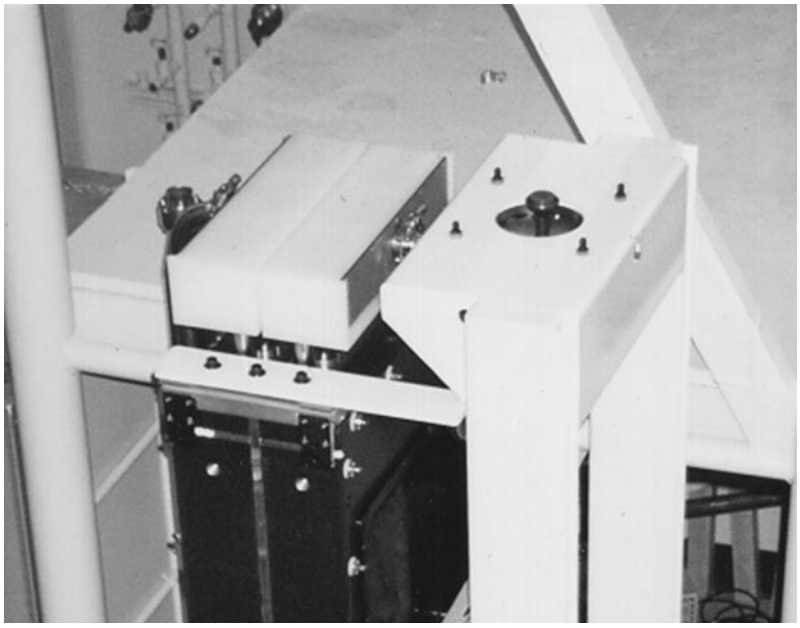

FIGURE 6. A ball mounted to the top of the LRU is one of the three mounting points by which the PEPC LRU attaches to the periscope structure. (70-00-0299-0370pb01)

optics (windows and KDP crystals), the assembly procedure is designed to minimize contamination of optical surfaces.

We have designed and built a PEPC assembly fixture to facilitate assembly of PEPCs in a safe, ultraclean, and ergonomic manner. This device, shown in Figure 7, will be used in conjunction with an Ergotech motorized positioner. The Ergotech lifts and rotates the assembly fixture while the assembly fixture facilitates integration of the housings, midplane, and support frame.

The potting fixture, shown in Figure 8, is designed to control integration of KDP switch crystals into the glass midplane. The midplane has four apertures for crystals, which must be precisely positioned

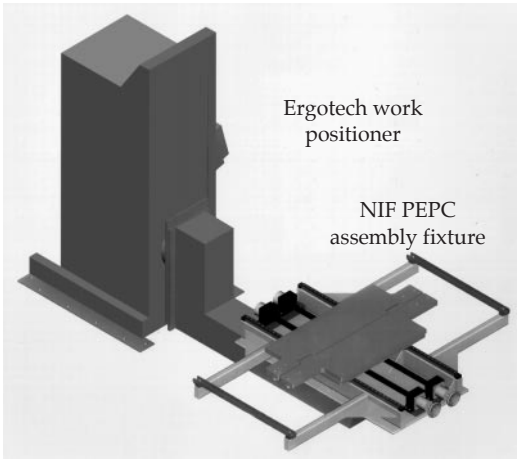


FIGURE 7. The PEPC assembly fixture will be used with an Ergotech motorized positioner to assemble PEPC LRUs in the Optical Assembly Building. (70-00-0299-0371pb01)

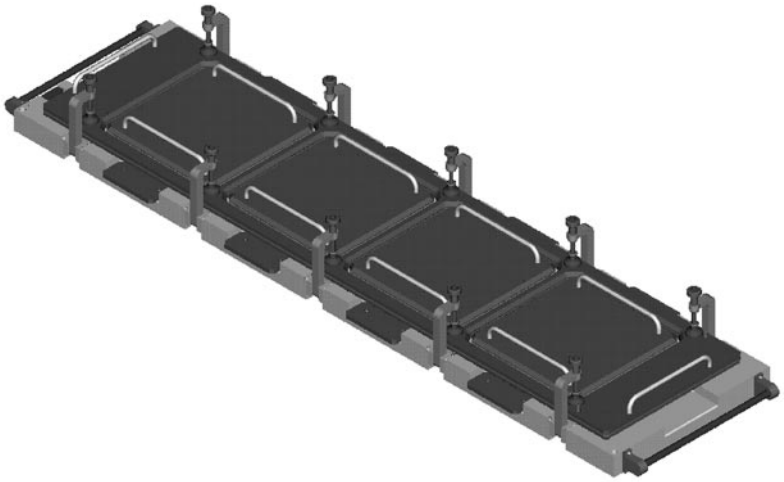

FIGURE 8. The potting fixture controls integration of KDP switch crystals into the glass midplane. (70-00-0299-0372pb01)

with respect to the midplane. Four gaskets that hold the crystals in the potting fixture are custom shaped to achieve precise positioning and provide a seal while potting. The crystals are potted with very-high-grade silicone rubber. The crystals are fragile and will fracture with minimal mechanical or thermal shock. The fixture and potting process minimize both mechanical and thermal loading of crystals.

## PEPC Control System

The function of the PEPC control system is to provide remote control and monitoring of the PEPC subsystem during NIF operation. The system will control all the components of the PEPC system, including plasma pulsers, switch pulsers, vacuum and gas gauges, valves, and turbo and roughing pumps.

As with other segments of the NIF control system, the PEPC control system is based on front-end processors (FEPs) that connect upstream to supervisory software modules and downstream to input/output interfaces, as shown in Figure 9. Each cluster of 12 PEPC LRUs will require 3 FEPs. Because there are 4 clusters in NIF, the PEPC control system will have a total of 12 FEPs. The 3 FEPs per cluster divide the control duty for the PEPC subsystems. The first FEP controls the switch pulsers. The second FEP controls the plasma-pulser controls, monitors the individual gas and vacuum system on each LRU, and monitors the cluster-wide vacuum roughing system. The third FEP controls pulse diagnostics. It contains high-speed waveform digitizers for the acquisition of switch-pulse voltage and plasma-pulse current.

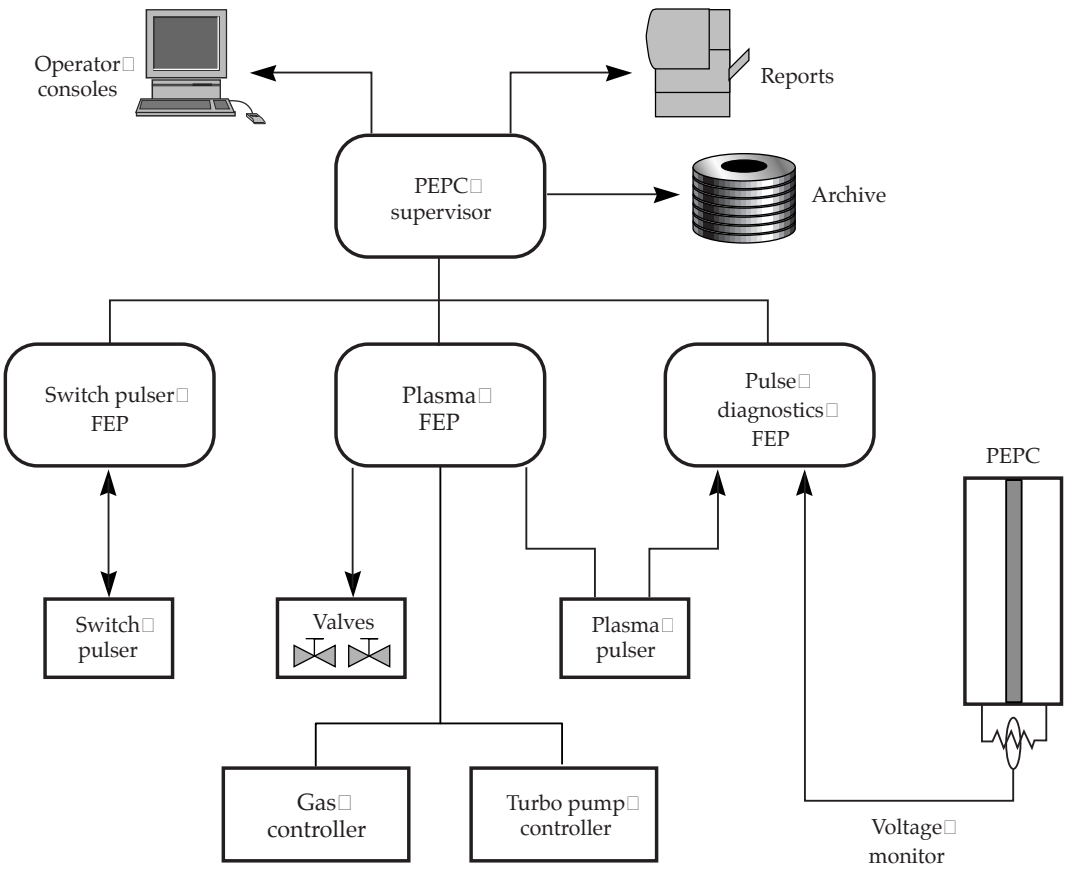


FIGURE 9. The PEPC control system. (70-00-0299-0373pb01)

During a NIF shot, the PEPC control system turns on the PEPC system, checks for normal operation of each LRU, fires the PEPC system every 5 s until a NIF shot occurs, and then turns the PEPC system off. The control system determines whether an LRU is firing properly by comparing the switch-pulse voltage waveform with a reference waveform, as shown in Figure 10. The actual waveform is subtracted from the reference. Any deviation in pulse timing or shape leads to a difference signal that is larger than the noise tolerance. The control system detects the difference and alerts the shot-control operators that a PEPC LRU is not working properly.

# Conclusion

This article describes the NIF optical switch system, which enables multipass operation of the NIF laser amplifier. The NIF optical switch is based on a novel electro-optic device called the plasma electrode Pockels cell (PEPC). With PEPC technology, it is possible to construct Pockels cells with very large apertures. After proving the viability of large-aperture, PEPC-based optical switches on the Beamlet laser, we have designed and successfully tested a four-aperture PEPC for the NIF.

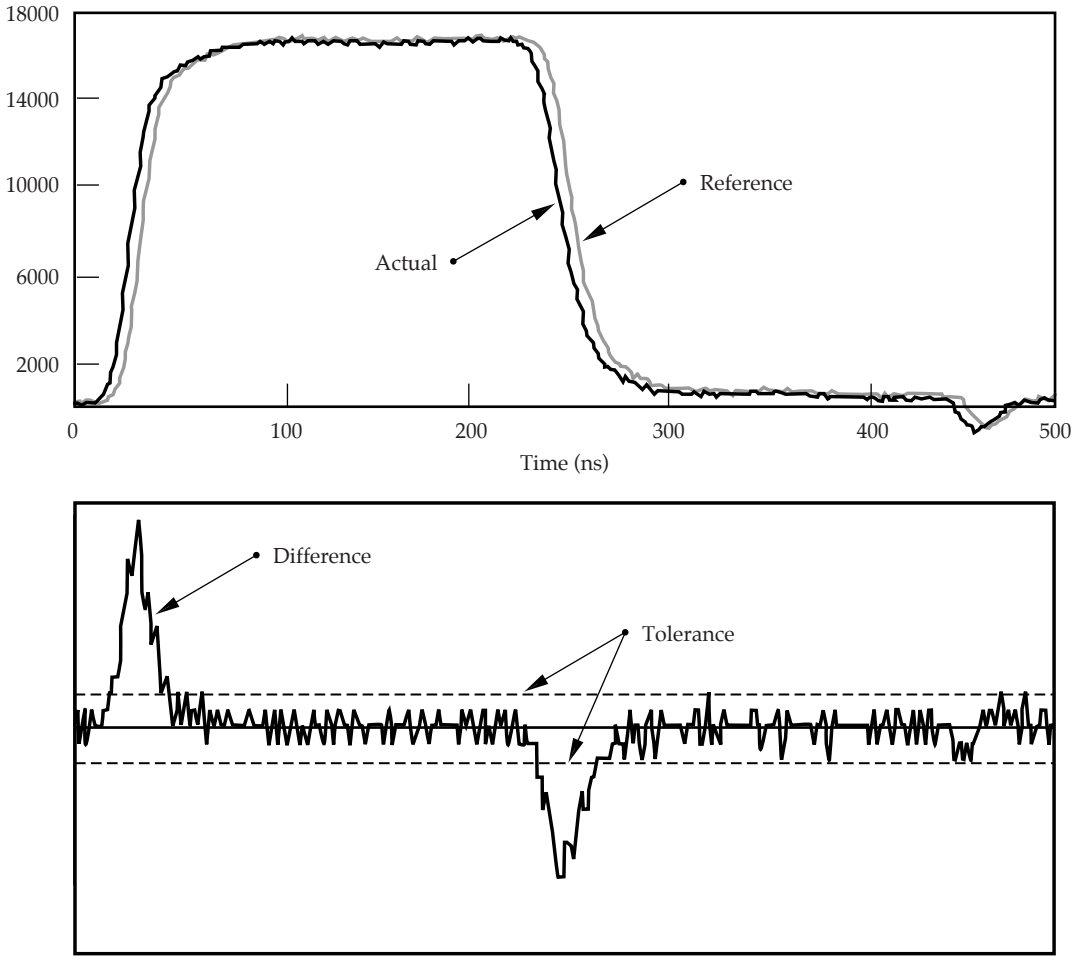


FIGURE 10. The PEPC control system determines whether an LRU is firing properly by comparing the switch-pulse voltage waveform with a reference waveform. (70-00-0299-0374pb01)

# BEAMLET EXPERIMENTS

*P. Wegner* *B. Van Wonterghem*

*S. Burkhart* *C. Widmayer*

*J. Murray*

The Beamlet laser is a single-aperture, nearly full-scale physics prototype of the 192-beam Nd:glass laser driver for the National Ignition Facility (NIF).[1] It employs a multipass amplifier architecture similar to the design of a single NIF beamline. As shown in Figure 1, the laser system consists of a preamplifier followed by two large amplifier stages: a four-pass cavity amplifier and a single-pass booster amplifier. The cavity amplifier contains eleven side-pumped Brewster's angle slabs situated at one end of a 36-m-long image-relayed cavity formed by a spatial filter and two end mirrors. The pulse from the preamplifier is injected near the focal plane of the spatial filter and makes four passes through the slabs before being ejected from the cavity by a full-aperture plasma-electrode Pockels cell and polarizer. The five-slab-long booster amplifier provides additional amplification and delivers typically 12 kJ in 3 ns, the Beamlet design point. The beam is then spatially filtered and relayed to the final optics, where it is frequency-converted to the third harmonic and focused to an equivalent NIF target plane. Comprehensive diagnostics at the input and output of the main amplifier provide beam data for gauging system performance at both 1.053-$\mu$m (1$\omega$) and 0.351 (3$\omega$) wavelength.[2,3]

(a)

(b)

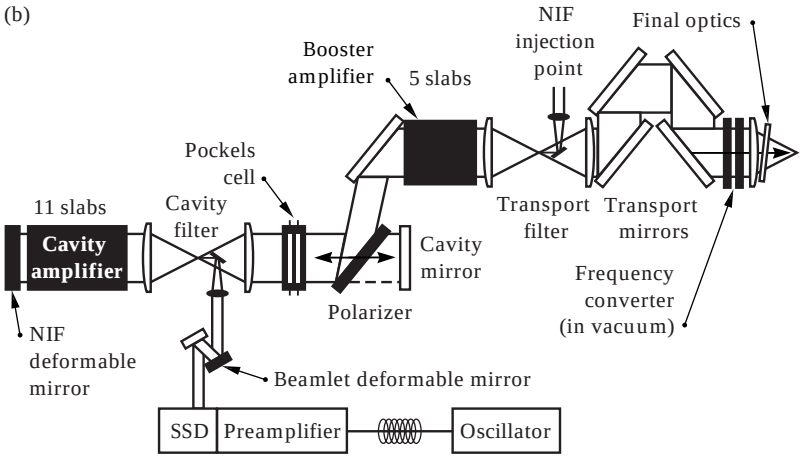


FIGURE 1. (a) Photo of the Beamlet facility taken from the output end of the laser, showing the test mule and focal-plane diagnostic (foreground) used for third-harmonic experiments. (b) Diagram of the Beamlet prototype laser showing relative locations of major components. (70-50-1297-2574pb01)

Beamlet's design diverges from the NIF's in three important and quantifiable ways:

1. A smaller clear aperture (36 vs 40 cm).
2. Injection of the Beamlet pulse into the 18-m-long cavity filter (vs injection of the NIF pulse into the 60-m-long transport filter).
3. An adaptive optics system that utilizes a 7-cm deformable mirror at the output of the preamplifier (vs the 40-cm deformable mirror that will be deployed at the cavity first-mirror position on NIF).

In addition, the Beamlet master oscillator and preamplifier are non-prototypical of NIF, although they share certain modern design features. Nonetheless, Beamlet has proven to be an essential test bed for evaluating laser physics and component engineering issues related to the NIF.

The primary mission for Beamlet has been the integrated testing of NIF laser technologies. Since its activation milestone in September 1994, Beamlet has produced over one thousand full-system shots in over twenty experimental campaigns addressing a broad range of technical issues relating to high-power beam propagation, high-energy temporally shaped pulses, spatial filtering, wavefront control, final optics, and frequency conversion. Experiments in high-power beam propagation established NIF *B*-integral limits and spatial-filter requirements for controlling nonlinear ripple growth and beam breakup. Experiments in pulse shaping produced the high-contrast, high-fluence 20-ns shaped 1ω pulses required for the NIF ICF mission. Experiments addressing spatial-filter issues established the pressure limits for NIF spatial filters, and demonstrated new pinhole designs that are effective in mitigating closure and back reflections under NIF operating conditions. Experiments in wavefront control demonstrated ability to meet NIF focusing requirements and provided a baseline for establishing finishing specifications for NIF optical components. Final optics experiments evaluated prototype UV components in NIF-like configurations at high fluence and demonstrated high-efficiency frequency conversion to the third harmonic using crystals fabricated with both conventional and rapid-growth technology. The following sections describe each of these activities.

## High-Power Pulse Propagation

The control of nonlinear ripple growth leading to beam breakup is an essential part of the design and operation of high-power solid-state lasers.[4] The mechanism of concern is the intensity-dependent refractive index in the laser components, which enables a weak ripple wave copropagating with a strong pump wave to couple and scatter a third wave conjugate in angle to the ripple.[5–7] Subsequent interaction of the conjugate wave with the pump feeds back and amplifies the ripple wave leading eventually to the unstable generation of higher-order ripple modes, self-focusing, and beam breakup.

Methods of mitigating ripple growth are limited, but critical for producing high-quality beams with safe modulation levels. Optical components must comply with stringent specifications for homogeneity and surface finish to limit the source of phase perturbations, which cause small-scale amplitude modulation. Growth of these source terms depends on the *B*-integral, or intensity-dependent phase retardation allowed between spatial-filter pinholes ($\Delta B$), and is limited by pinhole sizing.

Near-field modulation experiments were conducted on Beamlet to establish the *B*-integral limits and spatial filtering requirements for the NIF. By propagating 200-ps pulses through the laser under conditions equivalent to those expected during a 20-ns ICF ignition pulse, we obtained "snap shots" of beam quality that might otherwise be masked by temporal integration effects in the diagnostics. The reduced gain and high *B*-integral that occur during the most stressful period near the end of the ignition pulse were simulated by conducting the majority of the tests with the

booster amplifiers turned off. This configuration mimics the most severe condition in which the pulse has extracted all the energy from the booster amplifiers.

A metric for evaluating beam quality is the beam contrast, defined as the standard deviation of the near-field irradiance divided by the mean. Contrast was measured for various pinhole sizes as a function of the *B*-integral accumulated between the Pass-4 pinhole in the cavity spatial filter and the pinhole plane of the transport spatial filter, $\Delta B$. Initial tests were conducted without a pinhole in the transport spatial filter to evaluate beam contrast at the input lens of the spatial filter, where the risk of 1ω damage is highest. Figure 2 shows examples of the resulting near-field irradiance data obtained at low and high *B*-integral. The dependence of contrast on $\Delta B$ is plotted in Figure 3a for two different cavity pass-4 pinhole sizes corresponding to acceptance angles of ±200 μrad and ±130 μrad. Open points in the plot represent shot data, and solid points are the result of numerical simulation. The onset of rapid deterioration in beam quality occurs at lower $\Delta B$ with the larger pinhole. At a $\Delta B$ of approximately 2 rad, the 200-μrad data has begun a rapid ascent towards beam breakup while the 130-μrad data is still in the slowly varying region of the curve. Thus for $\Delta B < 2$, cavity pinhole sizes of 200 μrad or smaller are acceptable, but with smaller pinholes the margin for error is substantially increased.

Figure 3b plots the contrast that results at the output relay plane of the laser when a pinhole is used in the transport spatial filter. In this case there is discrepancy between the test data and the simulations that is attributed to incomplete characterization of the noise fields in the preamplifier. Nonetheless, both show that the beam contrast should remain small for $\Delta B$ as high as 3 rad if the pinhole size in the filters is reduced from 200 to ~100 μrad. Reducing pinhole size is a challenge because it increases the risk of closure for long pulses (see the section Spatial Filtering on p. 47). For $\Delta B < 1.8$ rad, the contrast is < 0.08 and, within error, is independent of pinhole size below 200 μrad. This result is the origin of the 0.1-contrast specification and 1.8-rad $\Delta B$ limit for the NIF.

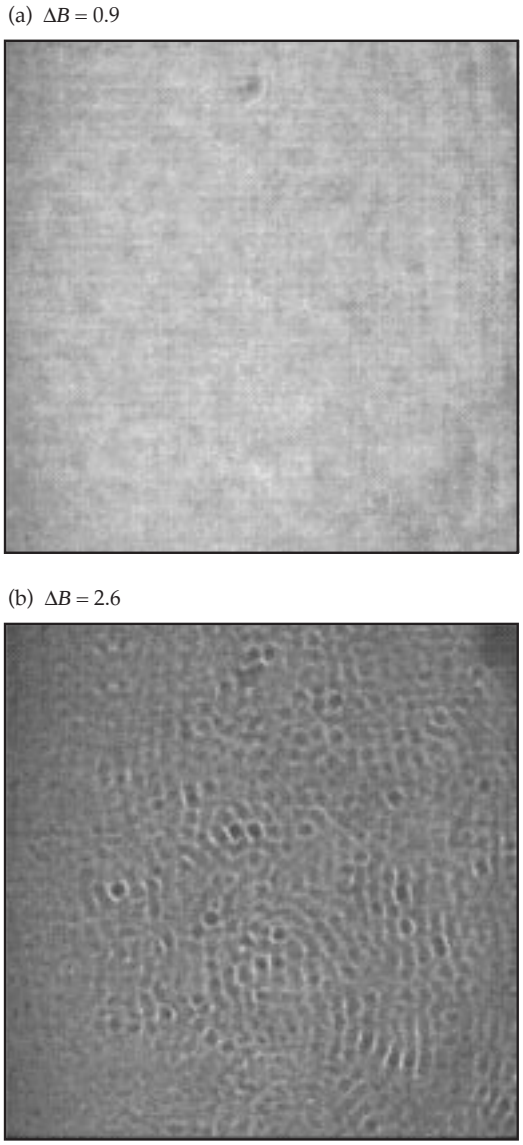


FIGURE 2. 1ω near-field beam modulation at (a) low and (b) high *B*-integral through the booster amplifiers. Images show the central 24.4 cm of the beam and were obtained with output sensor looking through the transport spatial filter with the pinhole removed. (70-00-0499-0781pb01)

## High-Energy Shaped Pulses for ICF

Temporal pulse shaping will be achieved on the NIF using low-voltage waveguide electrooptic modulation techniques in integrated optical circuits.[8] This technology has been used on Beamlet to produce 20-ns, NIF-like ignition pulses with a pulse-shaping system consisting of two arbitrary waveform generators (AWGs) in series. A 20-ns AWG with 1-ns resolution formed the electrical signal corresponding to the long,

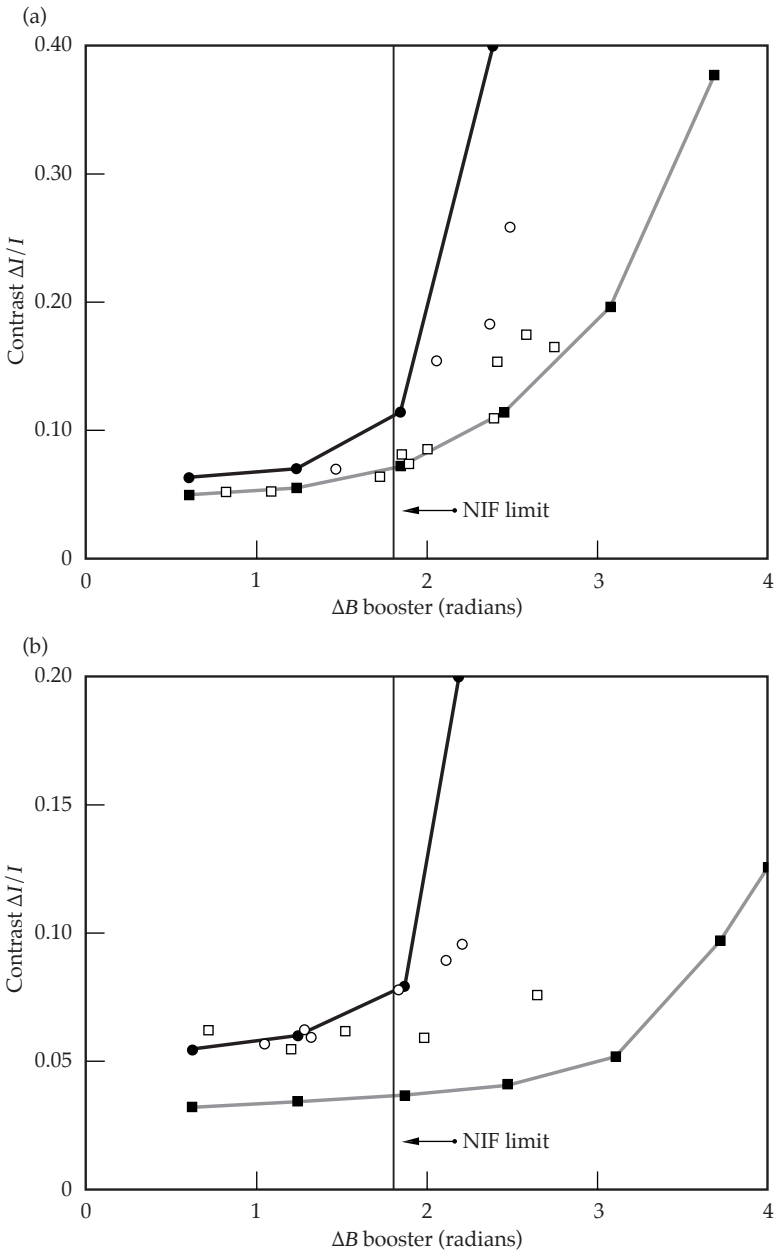


FIGURE 3. (a) Near-field irradiance contrast ratio vs *B*-integral for two cavity/transport pinhole configurations: 130 μrad/open (squares) and 200 μrad/open (circles). Measurements and simulations are denoted by open and filled symbols, respectively. (b) Results obtained with a pinhole in the transport spatial filter: 130 μrad/100 μrad (squares) and 200 μrad/200 μrad (circles). (70-00-0499-0782pb01)

low-intensity foot of the pulse, and a 7-ns fast (250-ps) AWG appended the high-bandwidth features of the complex pulse shape to the end of the foot. The resulting driver voltage signal controlled the light amplitude propagated through a $LiNbO_3$ modulator.

The required optical pulse shape at the modulator was calculated from the desired pulse shape at the laser output using empirical lumped-gain models for the various Beamlet amplification stages. The relatively small amount of saturation in the regenerative amplifier and preamplifier was well approximated by energy gains *G* that decreased linearly with extracted energy at the rate of 1.4%/mJ and 16%/J, respectively. The gain model for the main amplifier was based on the curve fit to the data shown in Figure 4, which plots measured input energy vs output energy for shots spanning approximately one year. The data was best approximated with two polynomials: 2nd order below 6583 J and 3rd order above. The resulting composite curve produces a better fit than could be

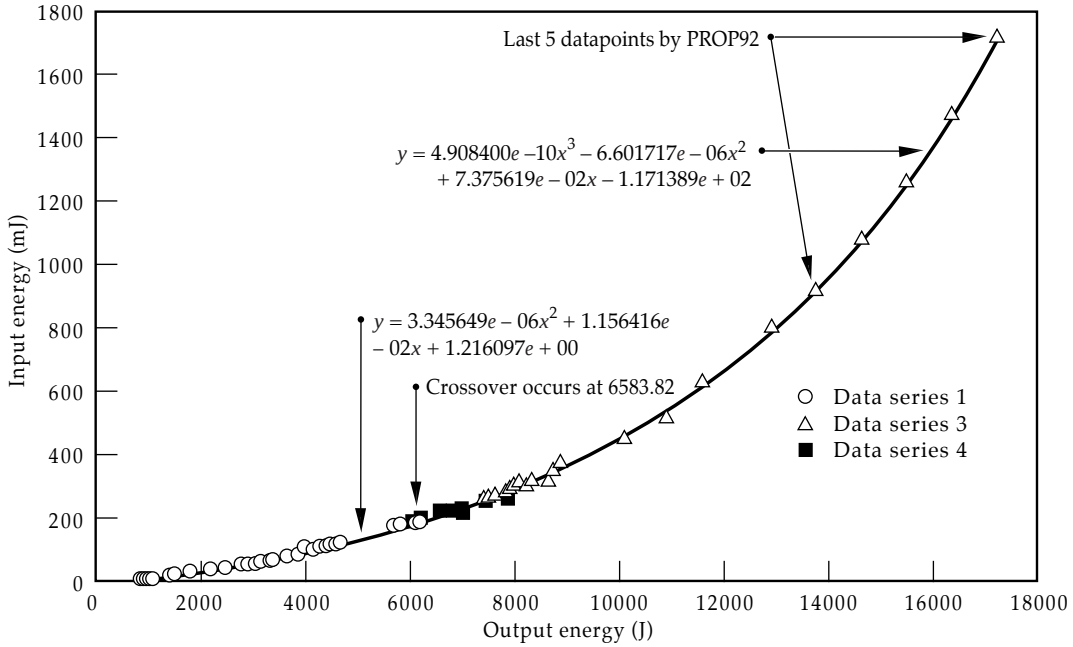


FIGURE 4. Gain of the main amplifier plotted as input energy required to produce a given output energy. Curve denotes best fit used for pulse shaping. (70-00-0499-0783pb01)

achieved with a simple single-gain-element Frantz–Nodvik calculation, and has proven adequate for pulse shaping.

With predictions based on these models, we produced the 15.5-kJ, 1ω NIF ignition pulse shown in Figure 5. Scaled for beam size, the energy and peak power of this pulse fall on the NIF red-line performance curve for square pulses shown in Figure 6, demonstrating the primary 1.05-μm laser requirement for inertial confinement fusion. Successful propagation of this pulse required advances in spatial filtering, described in the following section.

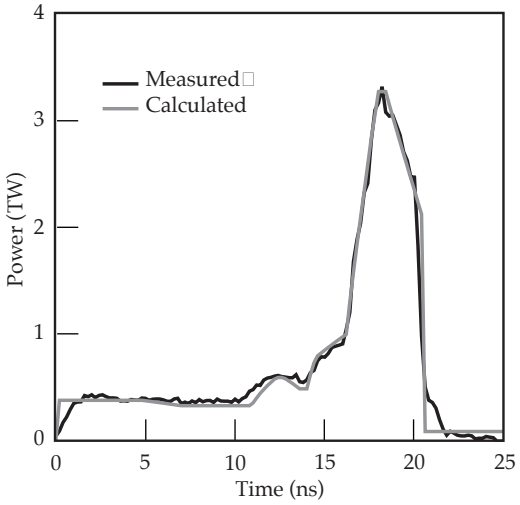


FIGURE 5. Measured temporal profile of a 15.5-kJ, 1ω ignition pulse produced on Beamlet. Data is in good agreement with predictions based on the pulse shaping model (gray profile). (70-00-0499-0784pb01)

# Spatial Filtering

Spatial filter issues of importance for the NIF fall into three categories:

1. Pinhole closure—the problem of keeping the required small pinholes open for the full duration of the NIF ignition pulse.
2. Back reflections—the need to avoid back reflections from pinholes that can damage the injection optics.
3. Background pressure—the question of maximum safe operating pressures for NIF cavity and transport spatial filters (CSFs and TSFs, respectively).

Beamlet experiments addressed each of these areas in turn.

## Pinhole Closure

Three types of pinholes were tested for closure on Beamlet, as shown in Figure 7. The first type is a washer design consisting of a hole in a flat plate oriented at approximately normal incidence to the beam. The second type is a leaf design consisting of four azimuthal segments displaced along

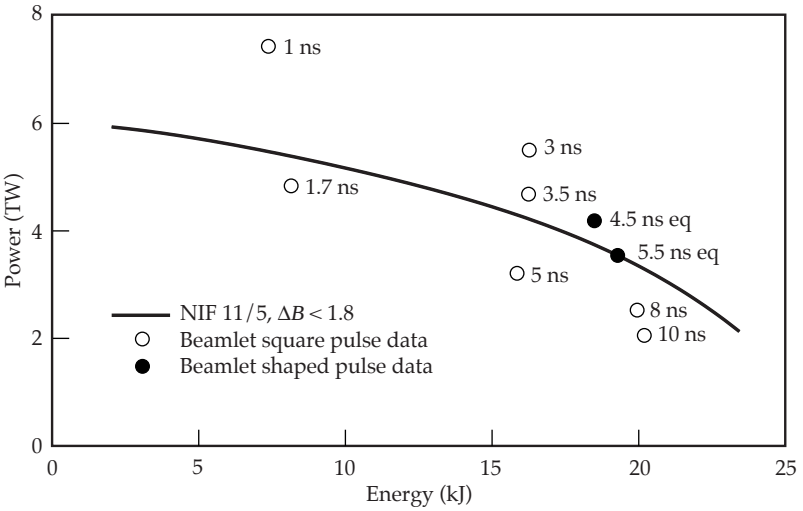


FIGURE 6. NIF 11-5 amplifier configuration safe performance limit, with Beamlet experimental data points scaled to the NIF beam area. Square pulse data is plotted as open circles. Shaped pulse data (filled circles) is characterized by an equivalent pulse duration defined as the energy divided by peak power.
(70-00-0499-0785pb01)

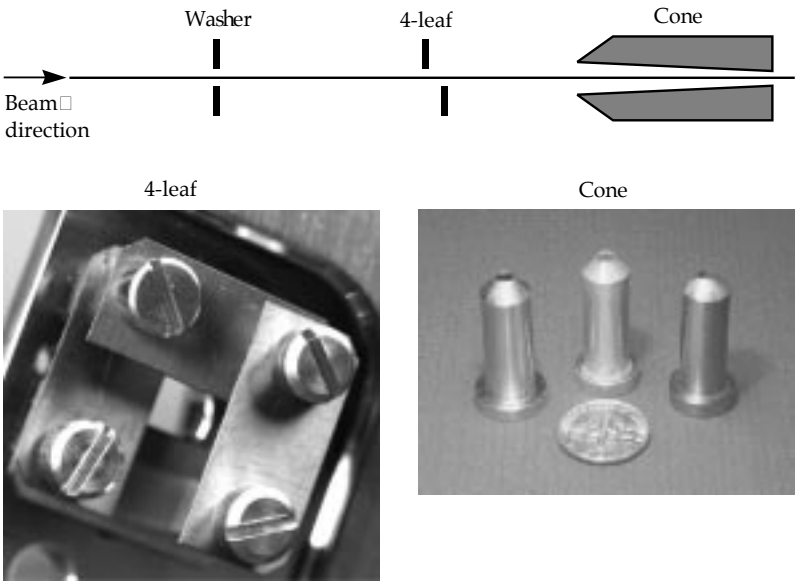


FIGURE 7. The three types of pinholes tested on Beamlet.
(70-00-0499-0786pb01)

the beam axis to eliminate the possibility of plasma convergence at the center of the pinhole. The third type is a conical pinhole, designed such that low-density plasmas on the surfaces reflect or refract the incoming light rather than absorb it.[9] The design of the cone pinhole is parameterized by the cone angle $\alpha$ and the cone length $L$. For the Beamlet tests we set $\alpha = 1.3\ \alpha_{min}$ and $L = 0.7L_{max}$, where $\alpha_{min}$ equals the $f$-number of the spatial filter divided by 2 and $L_{max} = 2R_0/(\alpha + \alpha_{min})$.[10] Here $R_0$ is the radius of the pinhole aperture, which when divided by the focal length of the spatial filter input lens gives the cutoff angle of the pinhole.

Pinhole performance was evaluated with a specialized set of diagnostics. A pulsed Mach–Zender interferometer was used to measure the phase shift of a 532-nm probe beam passing through the pinhole during the passage of the main laser pulse. The fringe pattern from the interferometer was recorded on a streak camera and a 120-ps rise-time gated optical imager to obtain time-resolved phase maps in $x$-$t$ and $x$-$y$ that could be correlated with electron density in the pinhole (see Reference 11 and article by Feit on p. 63 of this *Quarterly Report*). A second gated optical imager measured the transmitted near-field beam

irradiance during the last nanosecond of the pulse. Because pinhole closure affects the trailing edge of the pulse first, this diagnostic gave the most definitive indication of closure at near-threshold conditions. A second streak camera was configured to image a central strip of the transmitted near-field beam irradiance and measure the time variation of the modulation in that strip. This diagnostic was used to determine when the increased modulation associated with closure occurred during the pulse.

The majority of the tests were conducted with 20-ns square pulses to simulate the leading foot of a shaped ignition pulse. To compare shots of different energies $E_{pulse}$ and closure times $t$, we adopted a figure of merit $E_{closure}$ defined as the energy needed to close a pinhole at the end of a 20-ns square pulse. Because the closure time is inversely proportional to the plasma expansion velocity, which in turn is proportional to the laser irradiance at the edge of the pinhole,[11] $E_{closure}$ is simply $E_{pulse}t(\text{ns})/20$, the validity of which has been confirmed by measurement. Applying this analysis to the test data for ±100-$\mu$rad pinholes with 20-ns square pulses yields the results summarized in Figure 8, which plots $E_{closure}$ as a function of atomic mass for the three pinhole types and four different materials. Conical pinholes outperformed washer and four-leaf pinholes in all cases. In general, performance was also better for higher-Z pinholes which produce shower closure velocities, with the exception of the Au cone, which did not perform as well as the Ta cone. It is believed that an inadequate finish on the interior surface of the Au cone caused its lower-than-expected performance.

The conical pinhole design was also tested using 20-ns shaped ignition pulses. The required ignition pulse at the input to the NIF frequency converter has an energy of 19.4 kJ and a contrast of 10:1 (Figure 5). However, simple scaling laws for pinhole closure show that the pinhole most susceptible to closure is not the output pinhole in the $f/80$ TSF, but the Pass-4 pinhole in the $f/31$ CSF, where the pulse energy is 14.8 kJ and the contrast is 21:1. Tests with this pulse shape closed a ±100-$\mu$rad stainless-steel (SS) cone pinhole at 3× the energy of the corresponding 20-ns foot-only pulse, suggesting that the closure energy for ignition pulses can be obtained by multiplying $E_{closure}$ in Figure 8 by 3. In this case, none of the ±100-$\mu$rad pinholes tested would work for the NIF ignition pulse. The ±100-$\mu$rad Ta cone comes close based on this simple 3× scaling, but additional margin would be needed for the increased angular divergence associated with beam smoothing by spectral dispersion (SSD) and for finite alignment tolerances.

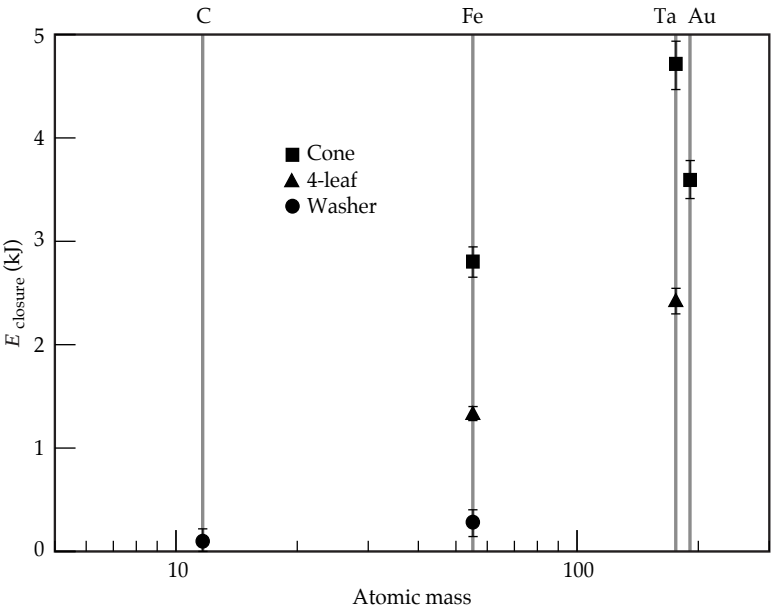


FIGURE 8. Closure energies for three types of ±100-$\mu$rad pinholes plotted vs atomic mass. (70-00-0499-0787pb01)

On the other hand, a ±150-μrad SS cone pinhole meets NIF requirements with ease, passing a 15.5-kJ, 10:1 ignition pulse with ±7.5 μrad of added SSD divergence with no sign of closure. The 10:1 ignition pulse is harder to keep open than the required 21:1 pulse with the same total energy because the intensity in the foot is larger by 2×. Figure 9 shows the interferometry data for this shot. The interferogram recorded by the streak camera is shown on the left. Analysis of the fringe pattern at the time indicated gives the phase shift of the probe pulse as a function of position in the pinhole, plotted on the right. A second curve in this plot shows how the phase shift would look at closure based on data from a different shot. The large separation between the curves indicates that the ±150-μrad SS cone pinhole was quite far from closure at end of the pulse. This pinhole is currently our baseline choice for NIF.

## Back Reflections from Pinholes

Back reflections have been a problem for staged pinhole geometries, in which the pinhole angular acceptance is gradually decreased from the input to the output of the laser. Because pinhole staging results in the best output beam quality, it remains the preferred mode of operation, and thus a solution for back reflections is required. All of the pinhole tests were performed in this configuration and generated measurable back reflections for pulses greater than about 1 TW into the transport spatial filter. However, the energy reflected from the cone pinholes was down by at least an order of magnitude from the energy reflected by the other pinhole geometries. Furthermore, its back reflection increased approximately linearly with power, whereas the back reflection for both leaf and washer pinholes increased nonlinearly, indicating a stimulated scattering process at the pinhole. Imaging of the back-reflected light (Figure 10) showed unambiguously that the back reflections originate from the surfaces of the pinhole rather than from an on -axis plasma, confirming the advantages of the cone geometry over the planar washer and leaf designs.

## Maximum Background Gas Pressure

Residual gas in the spatial filters at pressures above a certain maximum $p_{th}$ causes increased modulation in the near-field irradiance of the transmitted pulse, similar to the modulation observed above the threshold for pinhole closure. Threshold pressure is known to depend strongly on spatial filter *f*-number,[12] and as a result the Beamlet gas-pressure tests were conducted with both $f/26$ and $f/78$ geometries to determine values for $p_{th}$ applicable to the NIF CSF ($f/31$) and TSF ($f/80$), respectively. Figure 11 shows the results plotted as pressure vs peak intensity at the focus of the spatial filter. Three types of points are plotted for each *f*-number to distinguish whether the data came in above, at, or below $p_{th}$ as gauged by the modulation level in the transmitted near-field beam irradiance. Best-fit $p_{th}$ for the $f/26$ data is indicated by the upper curve,

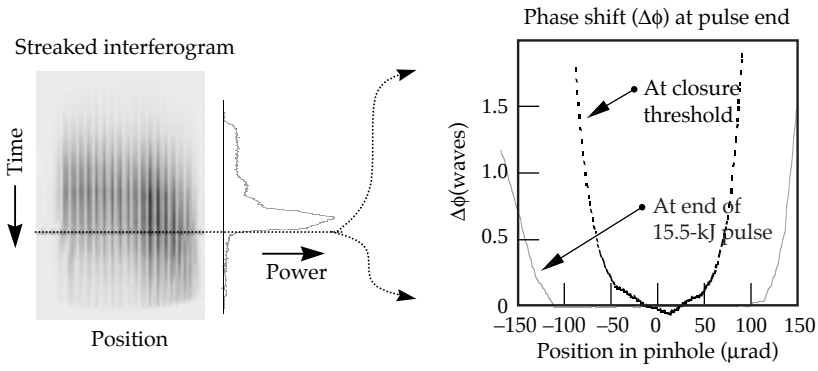


FIGURE 9. Interferometric data showing the phase shift of a probe pulse at the pinhole during passage of a 15.5-kJ, 10:1 contrast ignition pulse with ±7.5 μrad of added SSD divergence. The pinhole was a ±150-μrad SS cone. (70-00-0499-0788pb01)

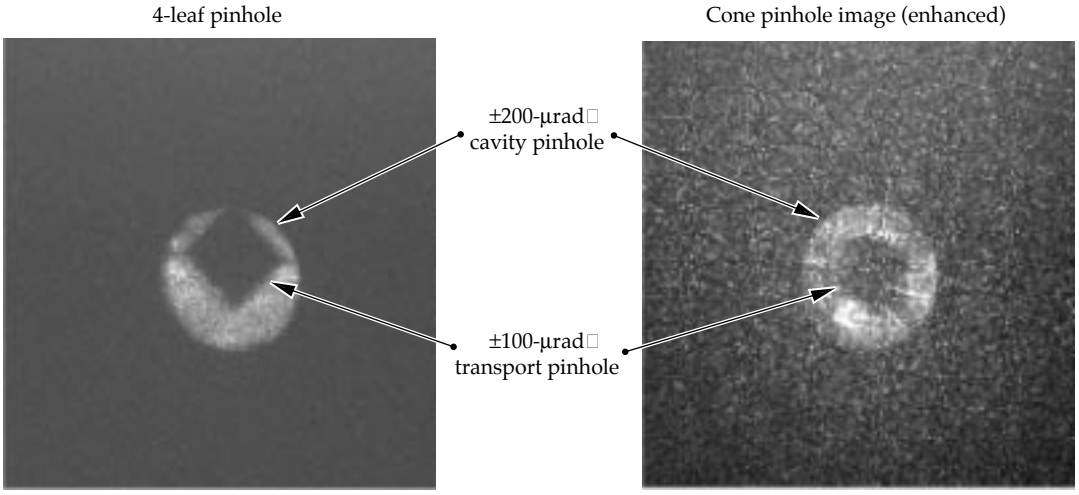


FIGURE 10. Back-reflected laser light from TSF pinholes, as imaged through the pinholes in the CSF. Back-reflected energy from the 4-leaf pinhole was 180 mJ at 2.0 TW, as measured at the input sensor, while that from the cone was only 10 mJ at 3.5 TW. (70-00-0499-0789pb01)

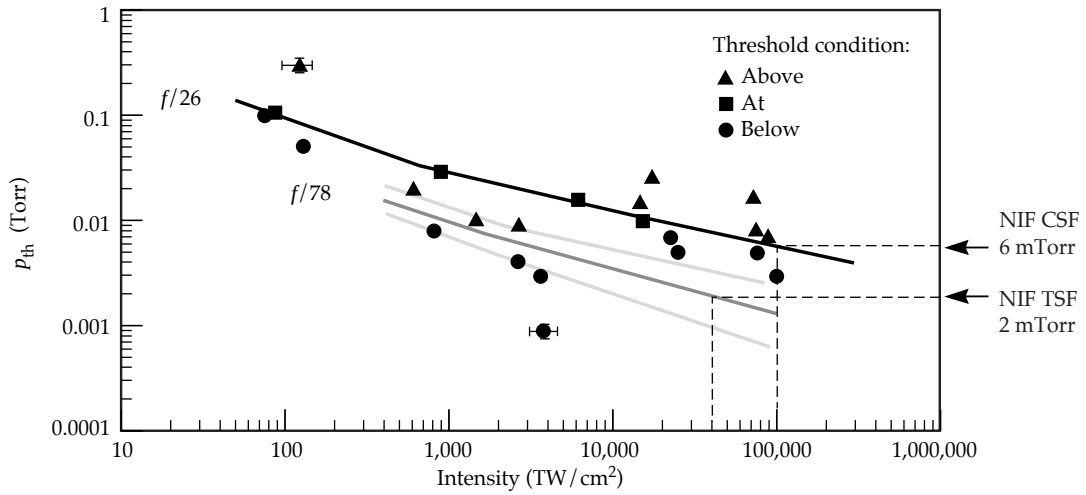


FIGURE 11. Data for determining threshold pressure $p_{th}$, at which residual spatial filter pressure disturbs the transmitted pulse. Filled triangles and squares denote data that was above or at threshold, respectively. Data below threshold is indicated by circles. Dashed lines show predicted thresholds at expected NIF filter intensities (70-00-0499-0790pb01)

which is well defined out to the maximum intensity expected for the NIF CSF. The $f/78$ data, however, was obtained by reducing the aperture of the beam by 3×, which also reduced the maximum power output by 9×. Consequently, the $f/78$ data ends well short of the expected intensities for the NIF TSF. Maximum and minimum credible extrapolations are indicated by the two gray curves, with the dark gray intermediary curve corresponding to our current best estimate. The results give $p_{th}$ values of 6 mTorr for the NIF CSF and 2 mTorr for the TSF. There is roughly a factor of two uncertainty in the $f/78$ data, because the beam quality was significantly better for the central subaperture of the beam used in those tests, and better beam quality has been observed to give lower values of $p_{th}$. Safety considerations dictate that the maximum allowed NIF operating pressures be roughly an order of magnitude below these values.

Measurements with both residual gas and a pinhole in the spatial filter showed no interaction between the effects of the residual gas and pinhole closure. $E_{closure}$ remains essentially constant for pressures from well below to 3× above $p_{th}$. The reason there is no interaction is that the two phenomena affect different temporal parts of the pulse. Data from the streaked near-field diagnostic

showed that pressures at or slightly above $p_{th}$ affect mainly the leading edge of the pulse, whereas near-threshold pinhole closure affects the trailing edge.

## Wavefront Control and Beam Focusability

Effective wavefront control is essential for achieving the high-brightness focal-spot conditions specified for NIF targets. For example, certain NIF weapons physics target requirements call for delivery of 500 TW of 3ω radiation inside a 250-μm-diam focal spot.[13] For the 7.7-m focal-length lenses on the NIF target chamber, this spot size corresponds to a half angle of 16 μrad, which sets a stringent upper limit for the divergence of the laser.

There are several sources of divergence in the laser, primarily in the 1ω section, that can significantly degrade the quality of the focal spot unless mitigated or otherwise controlled. These sources fall readily into four categories:

1. Static phase errors related to the finishing, mounting, and alignment of the optical components.
2. Prompt phase errors related to a deformation of the amplifier slabs during pumping.[14]
3. Thermally induced phase errors related to heat accumulation in the amplifiers, including gas turbulence effects.[15,16]
4. Nonlinear phase errors associated with the intensity-dependent ripple growth and whole-beam self-focusing.

At a given power level, minimum divergence and maximum beam brightness are achieved when the system is cold and thermally induced phase errors are absent (see Figure 12). In this case, performance is primarily limited by the fraction of prompt and static phase errors that remain uncorrected by the wavefront-control adaptive optic system (AOS) as a result of its limited spatial resolution.

The active component in the Beamlet AOS is a 7-cm-square deformable mirror (DFM) with 39 independent actuators;[17] the number of actuators and their arrangement is similar in design to the 40-cm mirror that will be deployed on the NIF.[18] The mirror resides at the output of the preamplifier (see Figure 1) and conditions the wavefront of the pulse before it is injected into the cavity amplifier. Wavefront data for closed-loop control of the mirror is provided by either of two 77-element Hartmann sensors located in diagnostic packages situated at the input and output of the main amplifier. Closed-loop control allows the figure of the mirror to be updated continuously (~1 Hz response) to maintain a predefined wavefront at the Hartmann sensor, which is typically specified to be either "flat" or a compensating figure determined from the wavefront error measured on a previous shot (termed "prefigure"). Additional diagnostics, including radial shear interferometers, were used to independently check the operation of the AOS and quantify beam quality.[19] Measurements of system

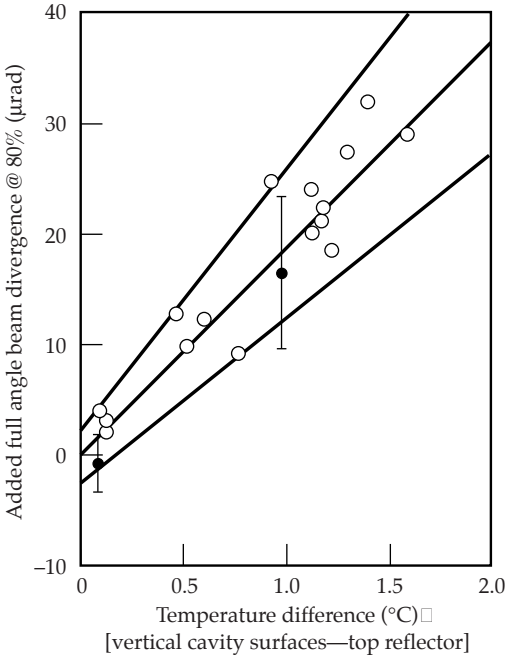


FIGURE 12. Beamlet measurements correlating 1ω laser divergence with amplifier temperature. The AOS is unable to correct for gas-density fluctuations of high spatial frequency caused by amplifier heating. (02-30-1093-3491pb01)

wavefront and beam quality both with and without an optimized AOS are presented in the following subsections.

## Preamplifier Wavefront Quality

The output of the Beamlet preamplifier is very close to diffraction-limited. Continuous-wave measurements showed that the AOS improves the wavefront of the preamplifier by ~0.25 waves to achieve a residual error of 0.32 waves peak to valley, 0.06 waves rms, and a Strehl ratio of 0.87. Firing the 5-cm rod added ~0.2 waves of prompt phase error that was not readily evident unless the AOS was actively correcting the static error. With the rod pumped, wavefront measured with and without the DFM was qualitatively different but similar in peak-to-valley and rms error. The 80% spot size was equivalent for the two cases (4.3-$\mu$rad half angle), but the DFM improved the brightness of the focal spot by ~30%. These results are consistent with those of Reference 20.

## Output Wavefront Quality

Beam quality at the output of the system is approximately 2.5× the diffraction limit with the AOS optimized to correct both prompt and static wavefront errors in the main amplifier, meaning that 80% of the energy is in a diameter 2.5× the 80% diameter of a diffraction-limited beam. With the preamplifier pumped and the main amplifiers static (rod shot condition), the residual wavefront error at the output of the system was ~1 wave peak to valley, 0.2 waves rms, and the 80% half angle of the focal spot was 10.5 $\mu$rad (Figure 13a). The measurement was made with the AOS operating closed-loop to maintain a flat wavefront at the output Hartmann sensor up until 1 s prior to the shot. Data obtained under similar conditions, but with the main amplifiers pumped, yielded an output wavefront error of ~3 waves peak to valley, 0.6 waves rms, and a much-degraded focal spot (Figure 13b). The difference between these two wavefronts gives the prompt distortion caused by

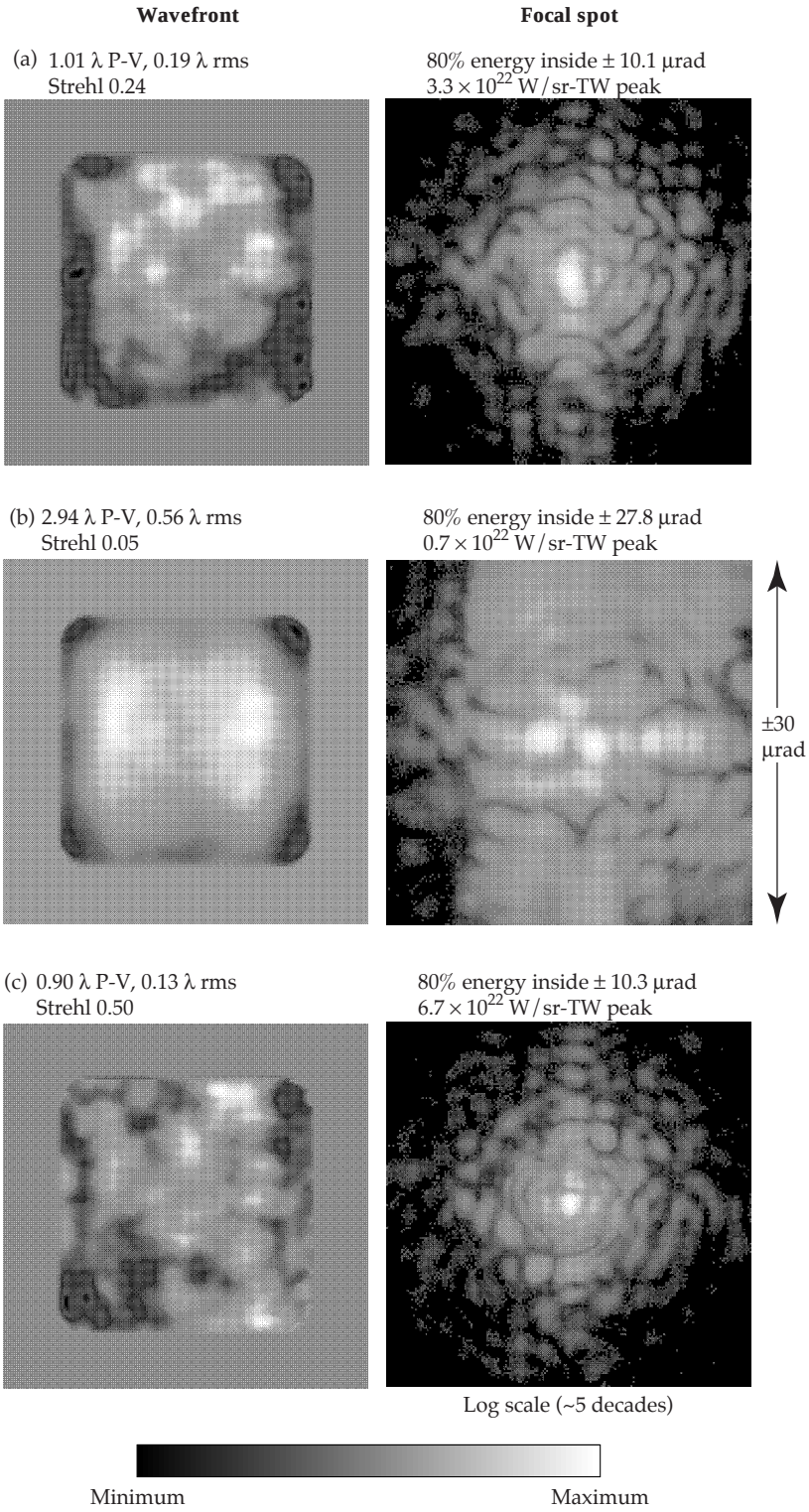


FIGURE 13. 1ω wavefront and focal spot measured at the output of the main amplifier for (a) rod shot with the AOS maintaining a flat wavefront up until 1 s prior to the shot, (b) same AOS condition as (a) but with the main amplifiers pumped, and (c) main amplifiers pumped with the AOS maintaining an optimized prefigured wavefront up until 1 s prior to the shot. (70-00-0499-0791pb01)

pumping the large amplifiers. With an appropriate prefigure of the DFM based on this measurement, it was possible to achieve an output wavefront and focal spot on a low-power system shot that were equivalent in quality to the data obtained on rod shots (Figure 13c).

These results demonstrate that the 39-actuator design of the DFM is highly effective at correcting the prompt wavefront distortions incurred in the main amplifier, and that, as a result, the focusability of the laser is primarily limited by the static errors in the main amplifier that are not correctable with the AOS. In the case of Beamlet, this residual error has been shown to meet the NIF high-brightness focal-spot requirements at both low and high power. Table 1 summarizes the results of high-power focal spot measurements conducted with an optimized AOS at output powers of up to 5.3 TW (1ω) and 3.1 TW (3ω) in a 200-ps pulse. Amplifier configuration is denoted 11-0 or 11-5, depending on whether the booster amplifier was pumped. Maximum power was achieved with the 11-5 configuration, for which the total *B*-integral accumulated in the amplifiers was 2.6 rad ($\Sigma B$), and the corresponding 80% power half angles of the 1ω and 3ω focal spots were 12 and 15 μrad, respectively. Scaling the power in the 3ω focal spot (0.8 × 3.1 TW) by the ratio of NIF to Beamlet beam sizes (1240 $cm^2$/1050 $cm^2$) and multiplying by the number of beams (192) and the transmission of the final optics (0.94) results in a NIF-equivalent performance of 540 TW inside ±15 μrad. Thus if the quality and associated static errors of the NIF optics are held to Beamlet levels, and the NIF AOS behaves equivalently, the NIF focusing requirements will be achievable.

## Static Errors and Optics Finishing Specifications

The static wavefront errors in the Beamlet amplifier were quantified by calculating the difference between the input and output wavefronts, as measured on a rod shot with a flat mirror in place of the DFM. The result, shown in Figure 14, has proven useful for correlating optics-finishing specifications with focal-spot performance. For the central core of the focal spot, corresponding to divergence angles less than ~30 μrad, the finishing effects of importance are long-wavelength figure errors, for which the appropriate specification is the rms gradient of the transmitted wavefront.[21] Applying a low-pass filter with a cutoff frequency of 0.03 $mm^{-1}$ to the difference data in the figure and calculating the rms gradient of the result yields a value of 1300 Å/cm for all

TABLE 1. Results of high-power focal spot measurements conducted with an optimized AOS at output powers of up to 5.3 TW (1ω) and 3.1 TW (3ω) in a 200-ps pulse.

| | | | | | 1ω focal spot | | | 3ω focal spot | | |
|---|---|---|---|---|---|---|---|---|---|---|
| Shot | Amplifier | $\Sigma B_{1\omega}$ (rad) | $P_{1\omega}$ (TW) | $P_{3\omega}$ (TW) | 50% half angle (μrad) | 80% half angle (μrad) | Peak intensity* | 50% half angle (μrad) | 80% half angle (μrad) | Peak intensity* |
| B7082005 | 11-0 | 1.3 | 1.3 | 0.6 | 5.4 | 11.7 | 3.7 | 8.0 | 13.6 | 0.67 |
| B7082103 | 11-0 | 2.0 | 2.0 | 1.2 | 5.4 | 11.5 | 3.9 | 7.4 | 12.8 | 0.73 |
| B7082205 | 11-0 | 2.1 | 2.2 | 1.3 | 5.7 | 11.8 | 3.0 | 8.1 | 13.7 | 0.70 |
| B7082501 | 11-0 | 2.8 | 2.8 | 1.8 | 5.1 | 11.6 | 3.8 | 8.4 | 14.1 | 0.67 |
| B7082601 | 11-5 | 1.6 | 3.4 | 2.3 | 5.3 | 12.3 | 3.3 | 7.7 | 12.5 | 0.92 |
| B7082702 | 11-5 | 1.8 | 3.8 | 2.2 | 4.6 | 11.7 | 3.9 | 6.7 | 12.3 | 0.83 |
| B7082802 | 11-5 | 2.6 | 5.3 | 3.1 | 4.4 | 12.1 | 4.7 | 6.5 | 14.9 | 0.82 |
| B7082902 | 11-5 | 2.4 | 5.0 | 3.2 | 4.0 | 11.6 | 4.8 | 7.3 | 15.4 | 0.77 |

* $10^{22}$ W/sr-TW. Divide by the square of the lens focal length in cm to obtain irradiance (W/$cm^2$-TW)

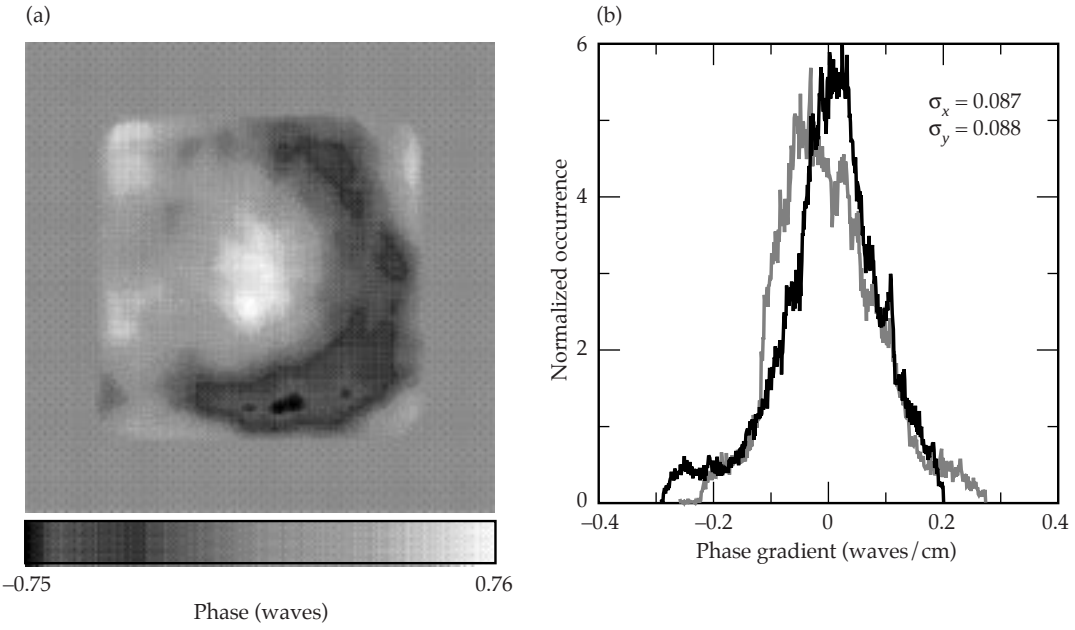


FIGURE 14. (a) Static wavefront distortion of the main amplifier. measuring 1.51λ P-V, 0.34λ rms. (b) Horizontal (gray) and vertical (solid) gradient distributions after filtering with a cutoff frequency of 0.03 $mm^{-1}$. Total rms gradient is the rss of $\sigma_x$ and $\sigma_y$. (70-00-0499-0792pb01)

of the optics combined. Assuming incoherent addition of phase between different elements, and accounting for multiple coherent passes through sections of the amplifier, the average rms gradient per optic is estimated to be 1300/17.2 = 75 Å/cm. Simulations using an average gradient distribution based on this result, and nominal power spectral densities for the high-frequency aberrations[22] predict focal spots that are consistent with the Beamlet measurements.[23] Thus, to ensure focal-spot performance equivalent to Beamlet, specifications for NIF optics currently limit the rms gradient of the transmitted wavefront to 70 Å/cm for spatial scale lengths >33 mm.

## Final Optics and Frequency Conversion

The NIF final optics perform several critical functions in a compact assembly:

1. Frequency converting the 1ω pulse from the laser amplifier to 3ω with high efficiency.
2. Focusing the 3ω energy onto the target.
3. Diverting the unconverted energy away from the target.
4. Providing a full-aperture sample of the 3ω beam for diagnostics.
5. Randomizing the spatial coherence of the laser energy at the target.
6. Shielding upstream optics from debris and high-energy x rays and neutrons emitted from the target.

The designs of the components that accomplish these tasks have been described elsewhere.[24,25]

To test and validate various aspects of the final optics design on Beamlet, we constructed a "test mule" (term borrowed from the auto industry describing a flexible prototype) at the output of the main laser amplifier that allowed us to field 37-cm-aperture versions of the optical components in a NIF-like configuration without the cost and complexity of activating a complete final optics assembly (FOA). A NIF-like 1ω window at the input to the test mule isolated the vacuum environment of the final optics from the main amplifier, allowing safe operation at full 3ω fluence without risk of damage and potential fracture of the input window. Temperature-controlled water flowing through heat exchangers on the surface of the test mule maintained a constant thermal environment of 20.0 ± 0.1°C for the frequency converter; similar passive cooling will be used for the NIF FOA. Beam alignment into the test mule and the 3ω diagnostics package was accomplished

using four 45° high-damage threshold 1ω mirrors. The requirement for slight out-of-plane orientation of the mirrors resulted in mixed "s'" and "p" reflections and the associated risk of beam depolarization, which could negatively impact frequency conversion. Fractional depolarized energy was measured both with and without the mirrors and found to be acceptable at less than 1%. Test mule experiments addressing frequency conversion and high-fluence operation of the final optics are described in the following subsections.

## Frequency Conversion

Experiments conducted with the test mule played an important role in proving the design of the NIF frequency converter and validating the physics model on which a detailed error analysis of its performance is based. The model is the most comprehensive yet developed for the converter, including details such as spatially varying birefringence in the crystals that has only recently been quantified using orthogonal polarization interferometry techniques.[26] Several Beamlet test configurations, summarized in Table 2, were used to evaluate both second-harmonic generation (SHG) and third-harmonic generation (THG), with converters consisting of both conventionally grown and rapidly grown potassium dihydrogen phosphate/potassium dideuterium phosphate (KDP/KD*P) crystals.[27] The crystals were tested in a prototype 37-cm-aperture final optics cell (FOC), which also contained the final focus lens, as shown in Figure 15a. Precision-machined surfaces in the FOC supported the optics around their perimeter and registered them with microradian tolerance. Compliant clamps held the optics in place; a load of 0.6 lb/in. was found to adequately constrain the crystals while providing good surface figure (Figure 15b). The configuration of the 1ω laser was the same for all tests: eleven cavity amplifiers, five booster amplifiers, a 200-μrad C pinhole in the Pass-4 cavity spatial filter pinhole, and a 150-μrad SS cone pinhole in the transport filter. Pulse format was 1.5 ns square. Estimated accuracy of the energy-conversion efficiency measurements was ±6% (3ω).

SHG efficiencies measured with a conventionally grown Type-I doubler from a NIF production boule are plotted in Figure 16a. Maximum energy efficiency was 73% (aperture-averaged, time-integrated) at an input 1ω irradiance of approximately 4 GW/cm$^2$ (aperture-averaged, peak-in-time). Similar tests of a rapidly grown Type-I doubler achieved 70.5% efficiency at similar drive irradiance. The measured performance of these crystals was in good agreement with modeling based on measured 1ω pulse parameters and measured crystal refractive-index variations. The effects of the latter were verified by measuring the 2ω near-field fluence distributions with the crystal tilt biased well away from exact phase matching, a configuration very sensitive to phase mismatch. As shown in Figure 17, the resulting nonuniformities in the data were well reproduced in the model.

THG efficiencies measured with a rapidly grown doubler and tripler are plotted in Figure 16b. Maximum energy

Table 2. Beamlet test configurations used to evaluate both SHG and THG, with converters consisting of both conventionally grown and rapidly grown KDP/KD*P crystals.

| | Conventional | | Rapid growth | |
|---|---|---|---|---|
| Parameter | SHG | THG | SHG | THG |
| 1ω laser | | | | |
| Beam size (cm) | 34 | 34 | 34 | 30 |
| Doubler | | | | |
| Serial number | 345-1 | 345-1 | RG8B-2 | RG8B-2 |
| Thickness (mm) | 11.09 | 11.09 | 11.10 | 11.10 |
| Δθ distribution (μrad int, 1 σ) | 22.3 | 18.8 | 17.5 | 27.8 |
| Surface loss (% before/after) | | | | |
| $S_1$ (1ω) | 0.91/– | –/1.49 | 1.03/– | 1.64/1.67 |
| $S_2$ (1ω) | 0.91/– | –/1.49 | 1.03/– | 1.64/1.67 |
| $S_2$ (2ω) | 1.70/– | –/2.53 | 1.48/– | 2.85/3.30 |
| Tripler | | | | |
| Serial number | – | LL1-37-1 | – | RG8A-1 |
| Thickness (mm) | – | 9.48 | – | 9.41 |
| Deuteration level (%) | – | 70 | – | 85 |
| Δθ distribution (μrad int, 1σ) | – | 36.2 | – | 67.7 |
| Surface loss (% before/after) | | | | |
| $S_1$ (1ω) | – | 0.60/– | – | 2.75/3.05 |
| $S_1$ (2ω) | – | 1.82/– | – | 1.30/2.20 |
| $S_2$ (3ω) | – | 0.10/– | – | 0.37/2.21 |
| Measured performance | | | | |
| Maximum energy efficiency | 73 | 75 | 70.5 | 73.5 |
| At 1ω irradiance (GW/cm$^2$) | 4.0 | 3.8 | 3.9 | 3.6 |

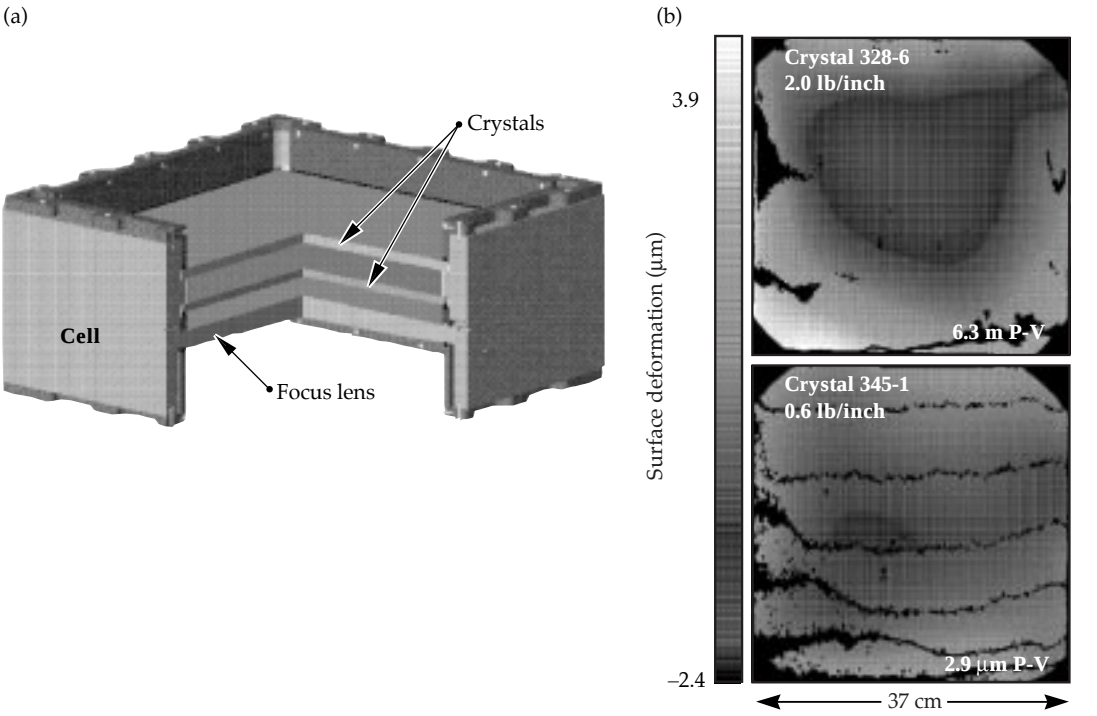


FIGURE 15. (a) Cutaway view of the final optics cell showing mounting scheme for the crystal and focus lens. (b) Measured surface figure of a mounted doubling crystal. Dark bands are caused by interference of the reflections from the near-parallel front and back surfaces of the crystal. (70-00-0499-0793pb01)

efficiency was 73.5% at an input 1ω irradiance of approximately 3.6 GW/cm$^2$. In comparison, the model, with an input field based on near-field 1ω irradiance data and an eleven-time-slice approximation of the measured 1ω pulse shape, predicted an energy conversion efficiency of 77%, and a peak-power conversion efficiency of 79.5%. Including the 30-GHz bandwidth of the drive pulse and the measured depolarization in the Beamlet laser lowers the calculated energy efficiency to 75%. Incorporating the additional losses caused by the degradation of the sol-gel antireflection coatings over the course of the experiment further reduces the efficiency to 71.5%, suggesting that the model is accurate to within the uncertainty in the component transmissions. Calculated and measured near-field fluence distributions for both the third-harmonic and residual second-harmonic fields were in fairly good agreement as a result of having the orthogonal-polarization interferomery data incorporated in the model. The energy balance in the model (the ratio of total energy out of the converter to total energy into the converter) was ~3% higher than observed, consistent with the actual transmissions of the components in vacuum being lower than the initial values modeled. Based on these results, peak-power 3ω conversion efficiencies approaching 80% should be achievable at NIF ICF drive irradiances, provided that high-quality antireflection coatings are maintained on the frequency-converter optics.

## High-Fluence Operation

High-energy operation of the final optics was investigated as high-damage-threshold fused-silica components became available. Third-harmonic fluences of up to 8 J/cm$^2$ and NIF-equivalent energies of up to 9.6 kJ in 3-ns square pulses were tested in a series of three campaigns (Figure 18) that produced valuable data for extrapolating component performance and lifetime for the NIF.[28] The tests culminated in a limited number of full-fluence shots through an integrated final optics configuration, including frequency-conversion crystals, focus lens, and a diffractive optics package containing a color separation grating (CSG) and beam sampling grating (BSG) on a single silica plate, a kinoform phase plate (KPP), and a debris shield. Time constraints imposed by Beamlet shutdown allowed

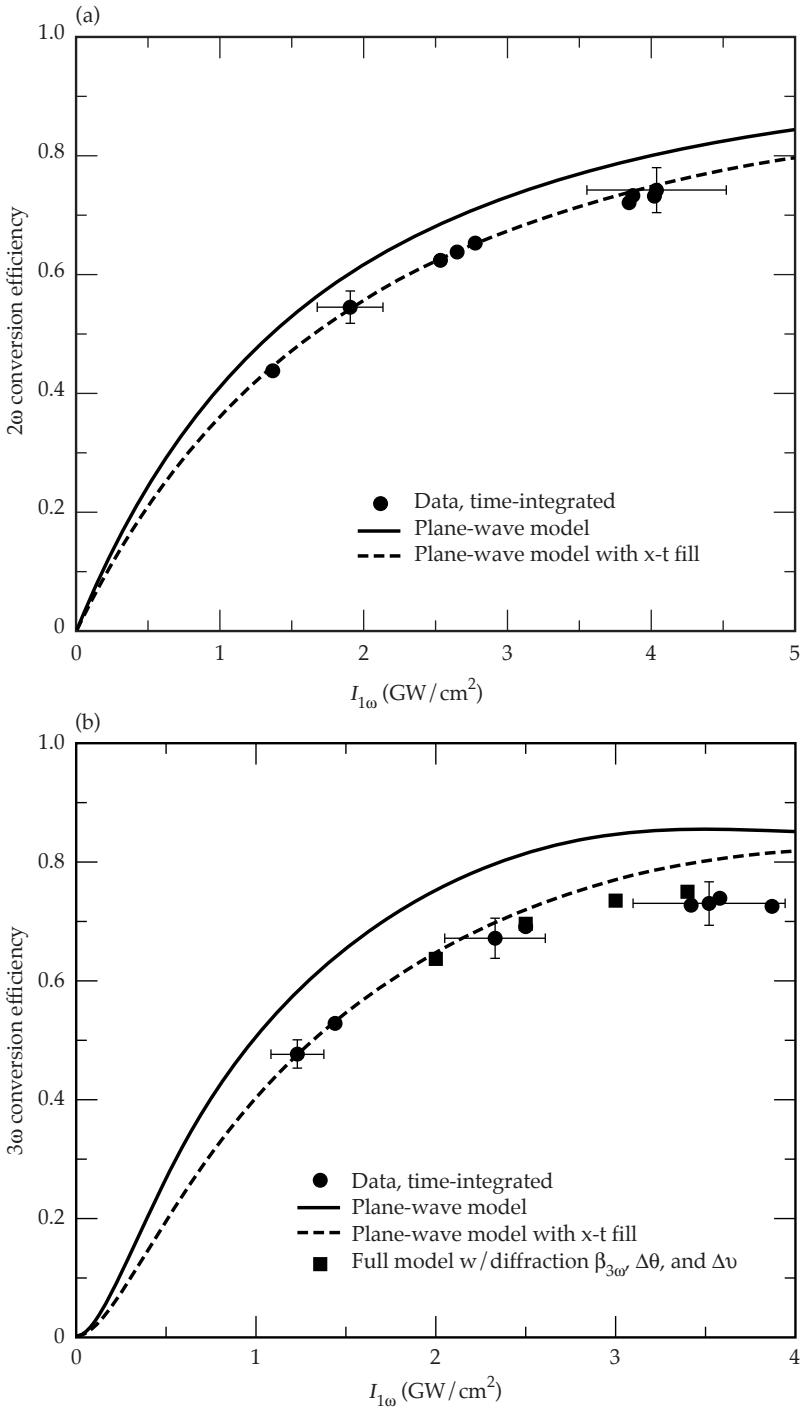


FIGURE 16. (a) Plot comparing measured and calculated SHG efficiency versus 1ω irradiance for conventional-growth doubler #345-1. (b) Comparison of measured and calculated THG efficiency for rapid-growth doubler #RG8B-2 and tripler #RG8A-1.
(70-00-0499-0794pb01)

very little on-line characterization of the individual diffractive optics prior to the integrated test. A low-damage-threshold version of the KPP was tested previously and its performance reported elsewhere.[29] The CSG concept was used successfully at low fluence in an experiment conducted for the French Commissariat a l'Energie Atomique. Results of the high-fluence tests revealed problems with CSG-induced beam modulation and damage associated with the sol-gel coating being thicker than $\lambda/4$ near the step edges, an effect previously identified as being responsible for reducing CSG diffraction efficiency. Improved CSG designs under development are expected to eliminate this problem.

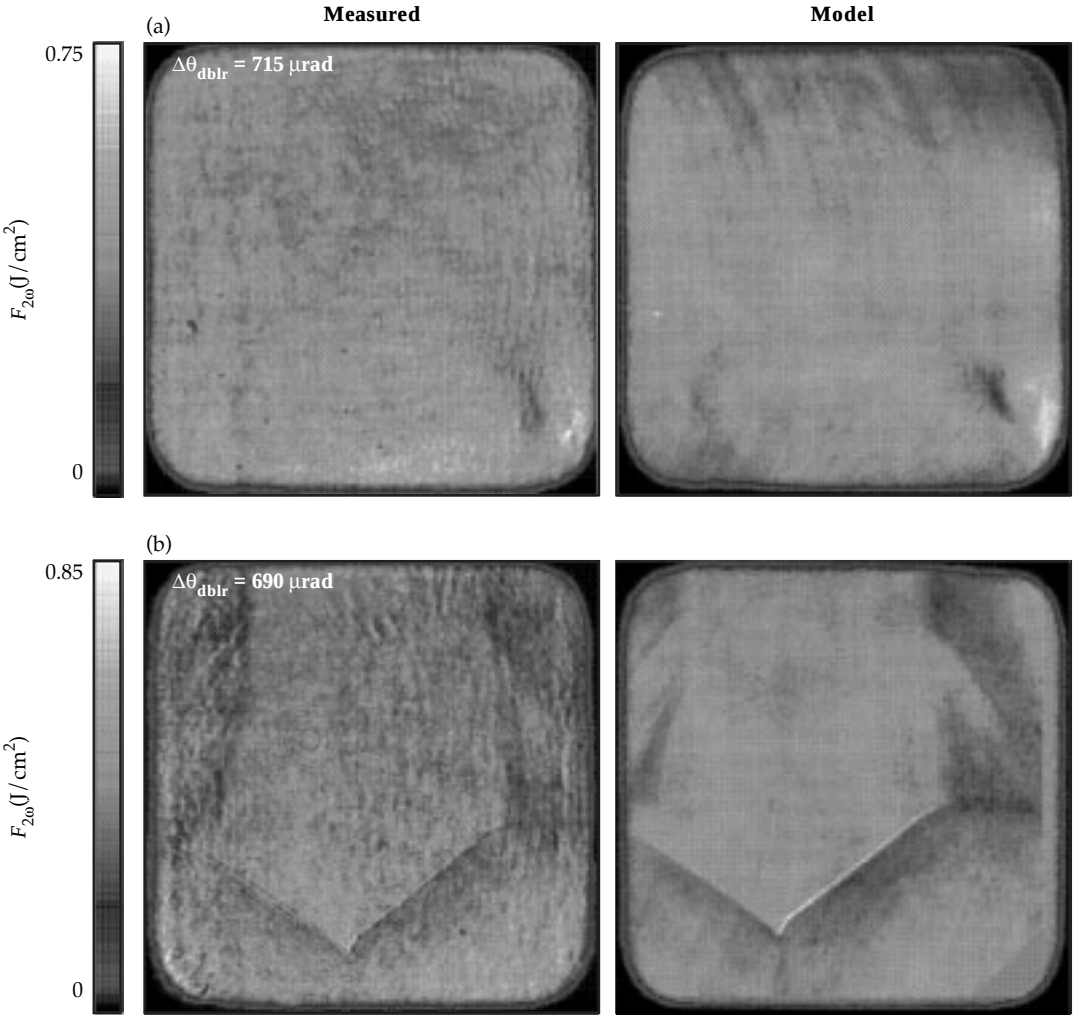


FIGURE 17. (a) Comparison of measured and modeled 2ω near-field distributions for conventional-growth doubler #345-1 at a drive irradiance of 3.9 GW/cm$^2$. Measured and modeled conversion efficiencies were 6.7% and 6.5% respectively at an angular detuning of 715 μrad (internal angle). (b) Similar comparison for rapid-growth doubler #RG8B-2 at a drive irradiance of 4.2 GW/cm$^2$. Measured and modeled conversion efficiencies were 6.6% and 7.0% respectively at an angular detuning of 690 μrad. Sharp features in (b) are the boundaries between {101} (pyramidal) and {100} (prismatic) growth regions in the crystal; conventional growth material is all pyramidal.
(70-00-0499-0795pb01)

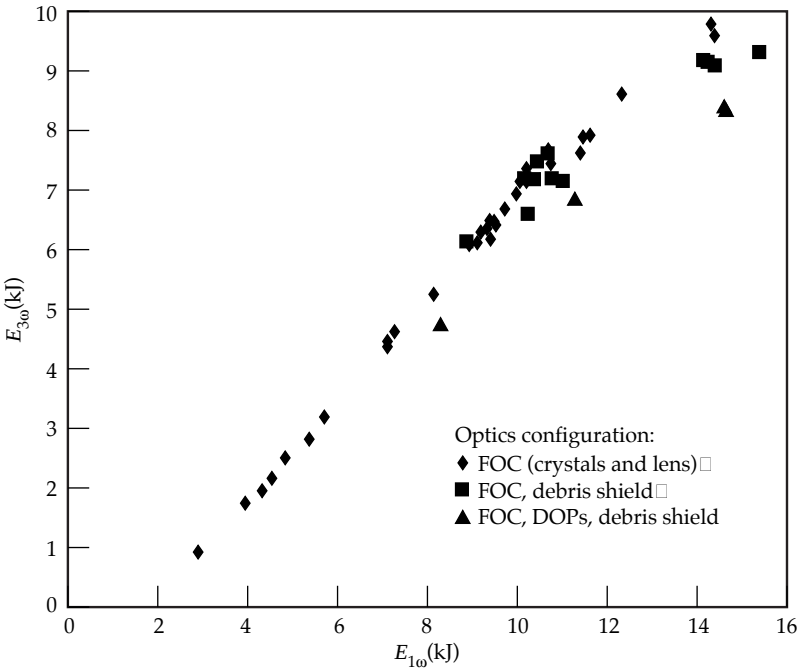


FIGURE 18. 3ω energy at the output of the final optics vs 1ω energy at the output of the laser amplifier, based on data obtained during the Beamlet high-energy test mule campaigns scaled to a NIF beam size of 1240 cm$^2$. Pulse duration was 3 ns square.
(70-00-0499-0796pb01)

## Summary

Beamlet has contributed to NIF technology development in many areas and demonstrated important aspects of the NIF design. Near-field modulation experiments at high power have established the *B*-integral limits and spatial-filter pinhole sizes needed for controlling nonlinear ripple growth at high power and assuring safe operation without damage. High-contrast 20-ns pulses have been demonstrated at NIF-equivalent energy and power using prototypical pulse shaping technology. Pinhole designs have been developed and tested for spatial filtering. These experiments resulted in a ±150-$\mu$rad SS cone baseline pinhole for the NIF, operating with neither closure nor back reflection. Detailed wavefront and far-field irradiance measurements demonstrated (1) that the Beamlet 3ω pulse meets spot-size criteria for NIF high-brightness missions, and (2) have provided a baseline for validating NIF propagation codes and establishing NIF optics specifications. In addition, efficient frequency conversion to the third harmonic was demonstrated with conventional and rapid-growth KDP/KD*P crystals in a prototypical NIF final optics configuration.

## Acknowledgments

The authors gratefully acknowledge the many contributions from the large team of technicians, scientists, engineers, and administrative staff who made this work possible.

## Notes and References

1. B. M. Van Wonterghem et al., *Appl. Opt.* **36**, 4932 (1997).
2. S. C. Burkhart, W. C. Behrendt, and I. Smith, *ICF Quarterly Report* **5**(1), 68, Lawrence Livermore National Laboratory, Livermore, CA, UCRL-LR-105821-95-1 (1994).
3. J. A. Caird et al., "Beamlet focal plane diagnostic," *Proc. Soc. Photo-Opt. Instrum. Eng.* **3047**, 239 (1996).
4. J. B. Trenholme, *Laser Program Annual Report*, Lawrence Livermore National Laboratory, Livermore, CA, UCRL-50021-75, 237 (1975).
5. V. I. Bespalov and V. I. Talanov, *JETP Lett.* **3**, 307 (1966).
6. R. L. Carman, R. Y. Chiao, and P. L. Kelley, *Phys. Rev. Lett.* **17**, 1281 (1966).
7. E. S. Bliss, D. R. Speck, J. F. Holzrichter, J. H. Erkkila, and A. J. Glass, *Appl. Phys. Lett.* **25**, 448 (1974).
8. S. C. Burkhart, R. Wilcox, D. Browning, and F. Penko, "Amplitude and phase modulation with waveguide optics," *Proc. Soc. Photo-Opt. Instrum. Eng.* **3047**, 610 (1996).
9. P. M. Celliers et al., *Appl. Opt.*, **37**, 2371 (1998).
10. J. E. Murray, D. Milam, C. D. Boley, and K. G. Estabrook, "Spatial filter issues," presented at Solid State Lasers for Application to Inertial Confinement Fusion, Monterey, CA (1998).
11. D. Milam et al., "Pinhole closure measurements," presented at Solid State Lasers for Application to Inertial Confinement Fusion, Monterey, CA (1998).
12. J. E. Murray et al., "Spatial filter issues," *Proc. Soc. Photo-Opt. Instrum. Eng.*, **3047**, 207 (1996).
13. J. Murray et al., *ICF Quarterly Report* **7**(3), 99, Lawrence Livermore National Laboratory, Livermore, CA, UCRL-LR-105821-97-3 (1997).
14. A. C. Erlandson, M. D. Rotter, D. N. Frank, and R. W. McCracken, *ICF Quarterly Report* **5**(1), 18, Lawrence Livermore National Laboratory, Livermore, CA, UCRL-LR-105821-95-1 (1994).
15. M. D. Rotter, R. W. McCracken, A. C. Erlandson, and D. Brown, "Thermal recovery measurements on multi-segment amplifiers," *Proc. Soc. Photo-Opt. Instrum. Eng.* **2633**, 70 (1995).

16. R. Hartley et al., "Wavefront correction for static and dynamic aberrations to within 1 second of the system shot in the NIF Beamlet demonstration facility," *Proc. Soc. Photo-Opt. Instrum. Eng.* **3047**, 294 (1996).
17. J. T. Salmon et al., "An adaptive optics system for solid state lasers used in inertial confinement fusion," *Proc. Soc. Photo-Opt. Instrum. Eng.* **2633**, 105 (1995).
18. C. La Fiandra, P. Mehta, G. Goldstein, R. A. Zacharias, and S. Winters, "NIF deformable mirror," presented at Solid State Lasers for Application to Inertial Confinement Fusion, Monterey, CA (1998).
19. P. J. Wegner et al., "Wavefront and divergence of the Beamlet prototype laser," presented at Solid State Lasers for Application to Inertial Confinement Fusion, Monterey, CA (1998).
20. B. M. Van Wonterghem et al., "A compact and versatile pulse generation and shaping subsystem for high energy laser systems," *Proc. Soc. Photo-Opt. Instrum. Eng.* **1870**, 64 (1993).
21. J. K. Lawson et al., "NIF optical specifications—the importance of the RMS gradient," presented at Solid State Lasers for Application to Inertial Confinement Fusion, Monterey, CA (1998).
22. J. K. Lawson, D. M. Aikens, R. E. English Jr., and C. R. Wolfe, "Power spectral density specifications for high-power laser systems," *Proc. Soc. Photo-Opt. Instrum. Eng.* **2775**, 345 (1996).
23. W. H. Williams et al., "Modeling characterization of the National Ignition Facility focal spot," presented at LASE '98, San Jose, CA (1998).
24. R. E. English Jr., J. Miller, C. Laumann, and L. Seppala, *ICF Quarterly Report* **7**(3), 112, Lawrence Livermore National Laboratory, Livermore, CA, UCRL-LR-105821-97-3 (1997).
25. V. Karpenko et al., *ICF Quarterly Report* **7**(3), 166, Lawrence Livermore National Laboratory, Livermore, CA, UCRL-LR-105821-97-3 (1997).
26. P. J. Wegner et al., "Frequency converter development for the National Ignition Facility," presented at Solid State Lasers for Application to Inertial Confinement Fusion, Monterey, CA (1998).
27. N. P. Zaitseva et al., *J. Cryst. Growth* **180**, 255 (1997).
28. M. Kozlowski et al., "Laser damage performance of fused silica optical components measured on the Beamlet laser at 351 nm," Symposium on Optical Materials for High Power Lasers, Boulder, CO (1998).
29. P. J. Wegner et al., "Third-harmonic performance of the Beamlet prototype laser," *Proc. Soc. Photo-Opt. Instrum. Eng.* **3047**, 370 (1996).

# Modeling the Interaction of the NIF Laser Beam with Laser Components

*M. D. Feit*

*C. D. Boley*

Large laser systems with high peak power, such as the National Ignition Facility (NIF), contain a great variety of optical components. These include lenses, mirrors, potassium dihydrogen phosphate (KDP) crystals, spatial filters, diffractive optics plates, debris shields, and so forth. The NIF beam has sufficient intensity to produce adverse effects either on these components themselves or on their functionality as part of the laser. Laser-interaction modeling like that normally used in treating ICF targets plays an important role in ameliorating these adverse effects.

We illustrate such modeling here with two examples. These arise from the need to avoid pinhole closure in the spatial filters and the need to avoid laser-induced damage to optical elements such as lenses.

Spatial filters remove high spatial frequency noise from the beam[1] by focusing it through a pinhole. The material forming the pinhole removes the most divergent rays, which are found at the outermost part of the focused beam. At NIF intensities (see below), the laser intensity at the pinhole edge can be sufficiently large to create a plasma that can expand into the pinhole and degrade the quality of light passing through the pinhole later in the pulse. This degradation, called pinhole closure, is examined below for various pinhole designs.

To contain cost, large laser systems like NIF necessarily operate near laser-induced damage thresholds for some optical elements. On the other hand, because of the very large number of components, it is necessary to establish safe operational limits and tolerable levels of damage risk. It would be difficult to establish such limits from experimentation alone because of the large number of materials, coatings, and environments, and the need to scale from results of small-scale experiments to full-sized optical elements. Thus, it is useful to establish theoretical models of laser-induced damage to aid understanding, interpretation, and application of empirical results; for example, there exists a good understanding of the deleterious effects of intensification due to nonlinear propagation (self-focusing).[2] In this article, we discuss mechanisms of laser damage initiation on fused silica. (Except for the frequency-doubling and -tripling crystals, all optics in the NIF Final Optics Assembly will be fabricated from fused silica.) The results presented here are part of an extensive experimental-theoretical effort to understand 3ω fused silica damage, in order to ameliorate it and to devise quality assurance tests of damage vulnerability suitable for NIF.[3] This 3ω fused-silica laser damage effort, led by M. R. Kozlowski, has been documented in numerous Boulder Damage Symposium papers during the past few years.

## Pinhole Modeling

In a spatial filter, a pinhole subtending a half-angle $\alpha$ removes incoming rays misdirected beyond this angle, as illustrated schematically in Figure 1. Equivalently,

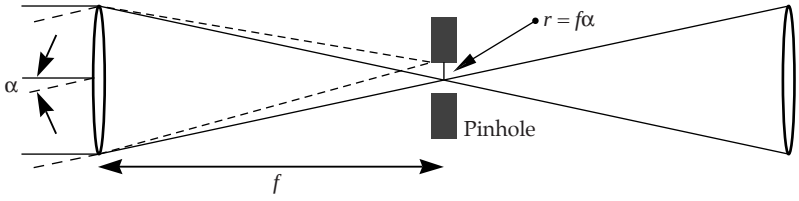


FIGURE 1. Schematic geometry of a spatial filter (not to scale), showing incoming rays misdirected by a given angle brought to a common point in the focal plane.
(70-00-0499-0960-pb01)

the pinhole removes noise of spatial wavelength shorter than $\lambda/\alpha$. If the angle is too small, however, the wings of the beam at focus can deposit substantial energy on the pinhole material.[4] For typical NIF pulses, the intensities near the pinhole edge will range from several GW/cm$^2$ to several TW/cm$^2$, depending on the pinhole size, the pulse shape, and the beam alignment. At these intensities, the material will generate a plasma that expands into the pinhole and that can cause difficulties. At lower electron densities, the plasma will induce aberrations on the beam, while at higher electron densities, the plasma will deflect and absorb the beam.

We have modeled two types of pinholes, shown in Figure 2. The first type, which we have treated more extensively than the second, consists of four azimuthally spaced blades, staggered in the longitudinal direction (parallel to the beam), with the blades successively rotated by 90°. The use of staggered blades avoids plasma convergence at the centerline, in contrast to a circular "washer" type pinhole. The longitudinal separation of adjacent blades (typically 2.4 mm) is sufficient to minimize interactions among the plasmas during the passage of the beam. At the same time, the blades are close enough so that each filters the beam in the far field. This is possible because an aberrated beam has an extended range near focus. The blades can be situated either horizontally/vertically ("square" orientation) or at a 45° angle ("diamond" orientation) relative to the far-field pattern of the square laser beam. The latter orientation performs better than the former, because it allows more room for the diffractive lobes of the beam at focus, which extend horizontally and vertically from the central spot.

The second type of pinhole has a conical shape, which is designed to refract the filtered light away from the beam rather than to absorb it.[5] Experiments have shown that this design is superior to the blade design.[6] Cones pass at least twice the energy of blades, and they also avoid a back reflection problem encountered with blades. However, they are more difficult to model than blades. One reason is that their longitudinal length is 3 to 4 times that of the blade design, with the result that the intensity distribution at the entrance differs significantly from that at focus. In the work described here, cones are treated via a comparatively primitive model, which also applies to blades.

FIGURE 2. Typical 4-leaf and cone pinholes. The size of the square opening in this 4-leaf pinhole is 2.7 mm.
(70-00-0499-0961pb01)

We expect the fourth-pass pinhole in the NIF cavity spatial filter (CSF) to present the greatest problems. To compare this with the pinhole on the NIF transport spatial filter (TSF), we employ simple scaling arguments.[6] Assuming that the plasma closure speed is constant, one can show that the closure time is sensitive to the *f*-number of the spatial filter, scaling approximately as $f^3$, and that it also scales roughly with the inverse of the beam power. On NIF, the CSF and TSF have *f*-numbers of 31 and 80, respectively, while the power into the TSF is at most three times that into the fourth pass of the CSF. Applying the anticipated scaling, we expect the fourth-pass CSF pinhole to have a closure time about 1/6 that of the TSF pinhole. The former pinhole, therefore, should present more serious problems than any other NIF pinhole. Its behavior was simulated by experiments on Beamlet, which has two spatial filters of *f*-number 26, close to the value of the NIF CSF. The Beamlet TSF was chosen because of its higher beam power and its proximity to output diagnostics. The pinhole experiments were performed during 1997 and 1998 (Ref. 6).

In addition to experiments on Beamlet, pinhole-related experiments were conducted with the Optical Sciences Laser (OSL)[7] to understand the dependence of plasma speed on irradiance and material composition. Here a blade was illuminated with a pulse of intensity similar to that expected on pinhole edges, and the electron density of the ablated plasma was probed in time via interferometry. This allowed for the study of phenomena in an off-line setting. We used the results to explore parameter dependencies and to test our numerical models.

In the following discussion, we consider first the OSL experiments and then the Beamlet experiments.

## Modeling OSL Experiments

In the OSL experiments,[7] a strong pulse of peak intensity 50–600 GW/cm$^2$ and duration 5 to 15 ns struck a material blade (knife edge) at a right angle. The materials of interest for pinholes were stainless steel and tantalum (Ta). These were chosen because we found that high-Z materials generally exhibit slower closure rates than low-Z materials. The geometry is illustrated in Figure 3. A probe beam was passed over the blade and through the main beam, and its phase shift was measured as a function of distance above the blade and time. In modeling this experiment,[8] we set up the two beams and the blade, with many thin zones near the surface of the blade. These zones, which followed the material, expanded into the vacuum as the material vaporized.

To describe the plasma, we employed LASNEX, a 2D Lagrangian radiation hydrodynamics code typically used in ICF

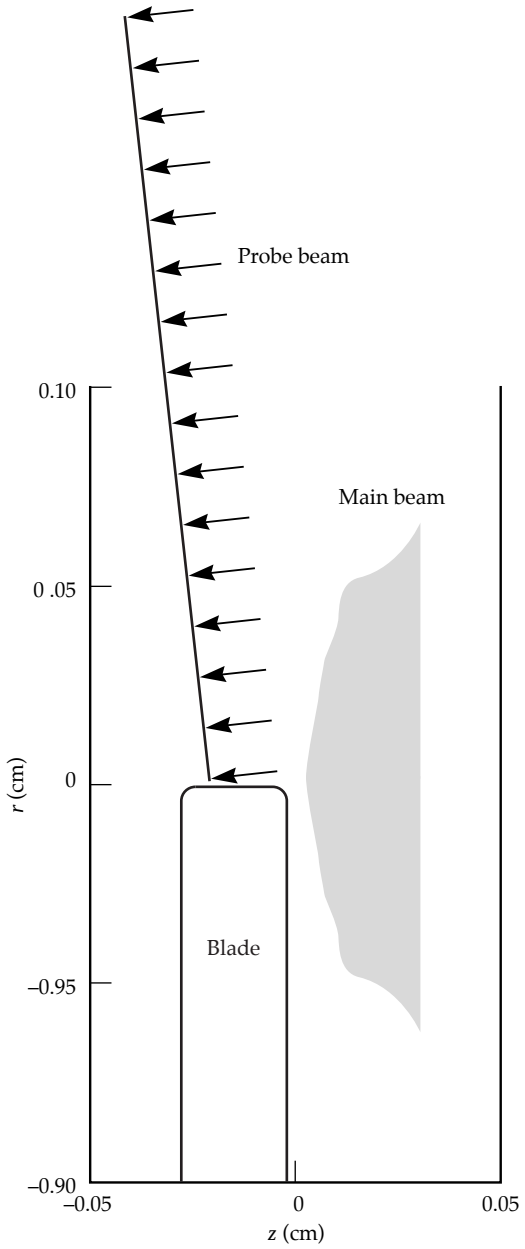


FIGURE 3. Schematic illustration of knife-edge experiments on OSL. The intensity profile of the main beam is indicated. Both this beam and the probe beam have circular profiles. (70-00-0499-0962pb01)

target calculations.[9,10] LASNEX calculates the absorption and refraction of the rays and the plasma properties. While it is believed to be the best available code for the present purposes, this application represents a low-energy extrapolation of its normal range. The code does not treat in detail, for example, the thermodynamics of vaporization. Of primary interest here is the electron density, which produces phase shifts in the probe beam by decreasing the local index of refraction according to

$$n(\mathbf{x}) = \left[1 - n_e(\mathbf{x}) / n_c\right]^{1/2} , \quad (1)$$

where $n_c$ is the critical density (about $10^{21}$ cm$^{-3}$ for light of wavelength 1053 nm). The optical path difference in waves along a ray path is proportional to the line integral of the change in the index of refraction:

$$\phi = -\int (n-1)\frac{dl}{\lambda} , \quad (2)$$

with the sign chosen to make $\phi$ positive.

Figure 4 shows typical LASNEX predictions for the electron density midway through a pulse of maximum intensity 175 GW/cm$^2$, incident on a Ta blade. Note that the expansion is nearly symmetrical about the tip of the blade. The electron density decreases almost exponentially with distance, with the critical electron density located a few micrometers from the surface. The maximum electron temperature is about 40 eV, while the maximum ionization state is about 19. Each of these quantities is moderately uniform within the bulk plasma but decreases sharply near the blade.

To find the phase change of the probe beam, we employed the postprocessing code HOLOX.[11] For typical plasma sizes at the midpoint of a pulse, an electron density of about $10^{18}$ cm$^{-3}$ produced a shift of a single wave with insignificant deflection. Note that this is three orders of magnitude below the critical density.

In both experiment and simulation, the phase profile exhibited a regular behavior as a function of distance above the blade and time. At a given time, the phase decreased exponentially with distance above the blade. As time increased, the phase profiles flattened out in a regular manner. This is illustrated in Figure 5, which shows the phase profiles at particular times for a stainless-steel blade, which we model as iron. Note that the calculated phase change generally

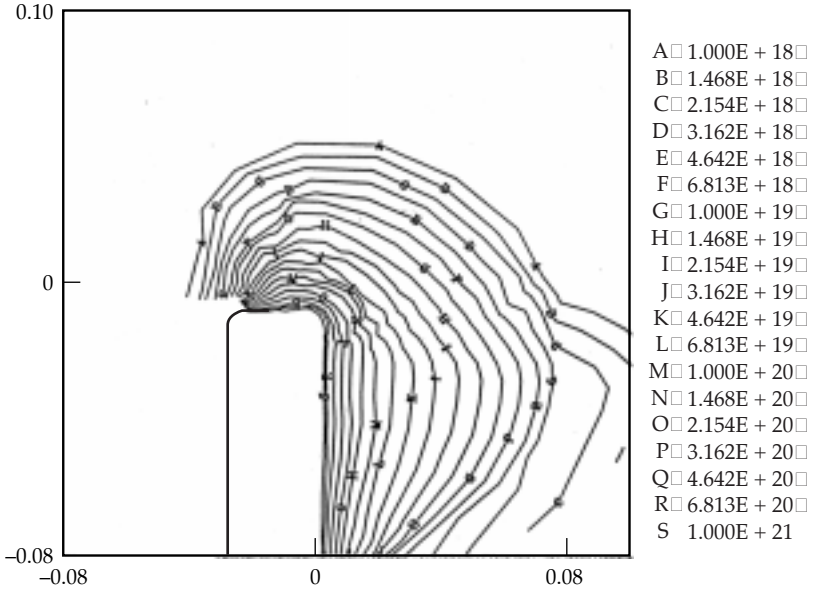


FIGURE 4. Electron density at $t$ = 10 ns, for a pulse of maximum intensity 175 GW/cm$^2$ on a Ta blade on OSL, as calculated by LASNEX. The contour labels give the electron density in cm$^{-3}$. Dimensions are in cm. (70-00-0499-0963pb01)

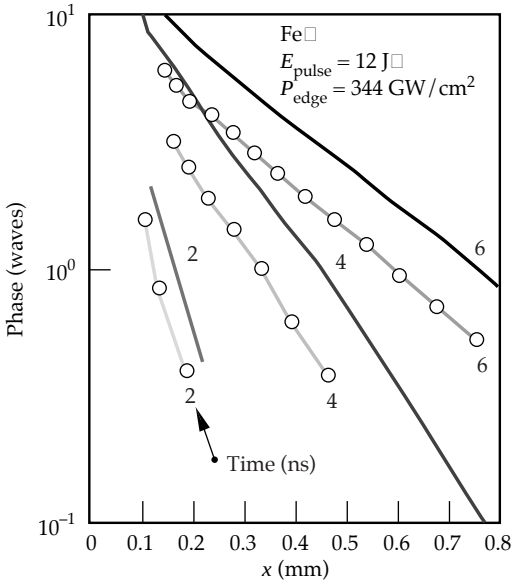


FIGURE 5. Phase profiles versus distance from the blade, for a pulse of peak intensity 345 GW/cm$^2$ illuminating a stainless-steel blade on OSL. The points denote measurements, while the lines give calculations. (70-00-0499-0964pb01)

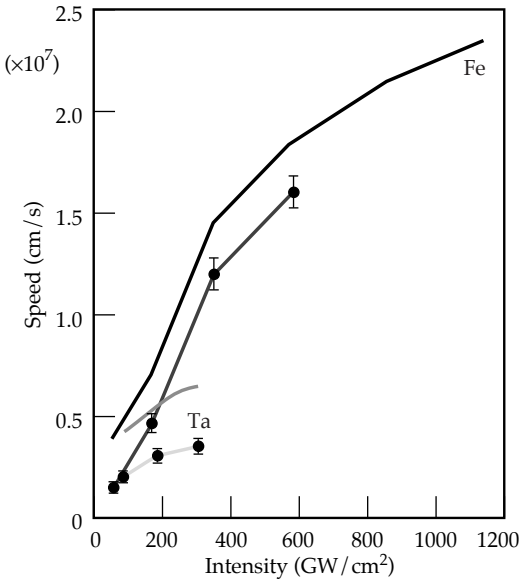


FIGURE 6. Speed of the 1-wave contour on OSL, for blades of stainless steel and Ta. The points denote measurements, while the lines give calculations. (70-00-0499-0965pb01)

exceeds the measured phase change, but that the trends are similar. For both experiment and model, the overall behavior is summarized by a function of the form

$$\phi(x,t) = \exp\frac{c_1(t-t_0)-x}{c_0(t-t_0)}\ , \qquad (3)$$

where $x$ is the distance above the blade. The parameters depend on intensity and material. This functional form is valid for times greater than $t_0$, the time required for the electron density to reach an exponential profile, which typically is a few nanoseconds. Setting the numerator to zero, we see that $c_1$ is the "1-wave speed" (the speed of the point with $\phi = 1$). The speed $c_0$ is related to the rate at which the profiles flatten with respect to position. We always have $c_1 > c_0$. The speed of the $n$th wave is $c_1 - c_0 \ln n$ (valid as long as it is positive, which typically holds for $n \le 10$).

Figure 6 shows the calculated and measured 1-wave speeds for a range of edge irradiances. For stainless steel, the calculated speed reaches approximately $2.3 \times 10^7$ cm/s at 1200 GW/cm$^2$. This exceeds experiment by a constant offset of about $0.2 \times 10^7$ cm/s. The data for Ta cover a more limited range of intensities, reaching only 300 GW/cm$^2$, and the speeds are smaller because of the larger atomic weight. Again the calculated speeds exceed experiment by a fixed offset. Because of the offsets, the calculated speeds do not appear to aim toward zero at low intensities, which is clearly nonphysical. Indeed, LASNEX was not intended to model this regime.

From the OSL experiments, we learned that the plasma model gives results of about the right magnitude. Although the calculated phase speeds exceed experiment, they do so in a systematic way. Thus the model is conservative, in the sense that it overstates the plasma effects.

## Modeling Beamlet Experiments

We extended the plasma calculations to 4-leaf pinholes,[8] using a beam profile appropriate to Beamlet. Since the far-field range of the beam exceeded the longitudinal

length of the pinhole, the plasma calculated for a single blade was replicated and rotated to describe four blades. For a given pinhole size, the electron density in the square orientation was markedly more peaked than that in the diamond orientation, because the far-field lobes intercepted the blades at a higher power level.

To find the effects on the beam, a separate propagation calculation was necessary. We propagated a beam through the entire spatial filter, including the plasmas, via the code PROPN1 (Ref. 12). The plasmas were used to set up phase screens for the code, and the edge of each blade defined a transmission mask. While this scheme should be iterated, the first iteration gave interesting and useful results.

Figure 7 shows lineouts of the calculated near fields, at the image plane located a distance twice the focal length from the output lens, for a Ta pinhole of half-angle 100 $\mu$rad in the square orientation. The calculation is for a 20-ns pulse of energy 1 kJ. One sees that the high-frequency noise visible on the incoming wavefront is indeed removed for early time slices (less than 10 ns), when the blades filter the beam without generating significant plasmas. The intensity has been filtered to the expected scale of $\lambda/\alpha \sim 1$ cm. For later time slices, though, the beam breaks up into successively larger regions, and the beam contrast (the normalized variance of the intensity) steadily increases. The characteristic size of the regions also increases, reaching about 5 cm at 19 ns. This trend is also seen in experiment. Closure, defined as a 20% increase in contrast, was observed at about 10 ns, which is close to the calculated time of 11 ns.

When calculations are done for this pinhole in the diamond orientation, however, the pinhole remains open. Such a trend would be expected from the considerations given earlier. In experiment, the pinhole also remaind open at this energy. It finally closed for a pulse of energy between 2 and 3 kJ.

If Ta is replaced by stainless steel, then the diamond pinhole is predicted to close rapidly after 10 ns, in about the same manner as the Ta square orientation. The contrast rises by an order of magnitude between 10 ns and 19 ns. The reason for the adverse behavior is the increased plasma speed. Experimentally, stainless steel also was observed to close more rapidly than Ta.

Although the calculations for 4-leaf pinholes are instructive and reveal trends similar to experiment, they are not readily extended to cone pinholes. In addition, we are interested in describing misalignment effects, for which the plasma and propagation calculations are even more burdensome than those described above. Hence a simple pinhole model has been devised that applies to both 4-leaf and cone pinholes and that can also describe misalignment.[6] The model was developed wth

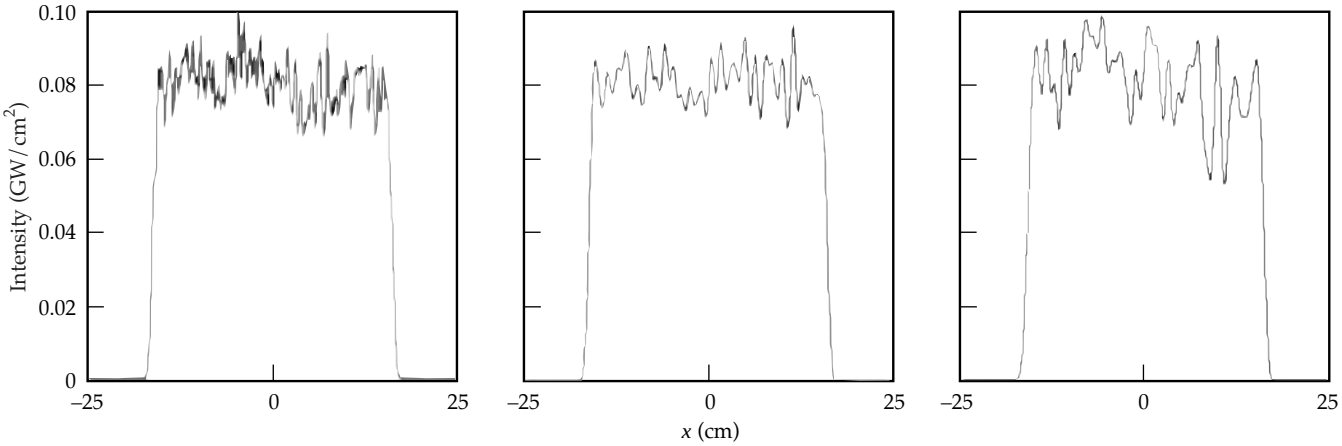


FIGURE 7. Horizontal lineouts, along the beam center, of the calculated near field for a 100-$\mu$rad Ta pinhole, in the square orientation. The pulse duration is 20 ns, and the beam energy is 1 kJ. The lineouts give the incoming pulse (left) and the outgoing pulse at 8 ns (center) and 13 ns (right). The horizontal dimension is in cm. (70-00-0499-0966pb01)

J. E. Murray. A schematic view of the focal plane, as pictured in the simple model, is shown in Figure 8. We envision a round beam within a round pinhole, with the center of the beam displaced a distance $r_{mis} = f\alpha$ from the center of the pinhole, where $f$ is the focal length and $\alpha$ is the misalignment angle. The radius $r_b$ of the beam is arbitrarily chosen to enclose 99% of the azimuthally averaged energy. To apply the model to a 4-leaf pinhole, we choose an effective pinhole radius. For the square orientation, this is the pinhole half-width, while for the diamond orientation it is the average distance of a blade from the beam center.

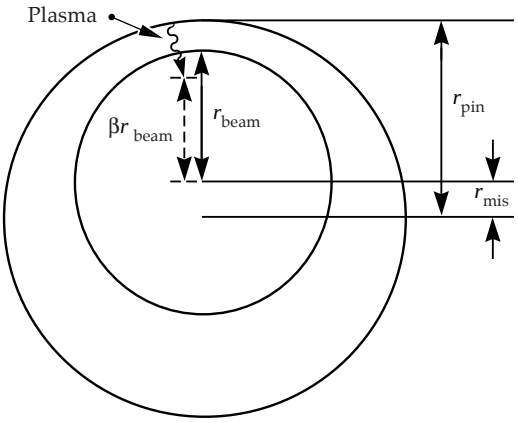


FIGURE 8. Schematic geometry of beam and pinhole, as envisioned in the model of Eq. (4).
(70-00-0499-0967pb01)

We suppose that the pinhole closes when the plasma ablated from the nearest edge, traveling at a particular speed, penetrates to a fraction $\beta$ of the beam radius. The choice of this speed is somewhat arbitrary. It might seem reasonable to choose the 1-wave speed, but the model works more satisfactorily with a faster speed, corresponding to a smaller wave index. In practice, we have chosen the 0.1-wave speed. From these assumptions, we can write the closure time in the form

$$\tau = \frac{r_{pin} - r_{mis} - \beta r_b}{\gamma c_n \left[ I\left(r_{pin} - r_{mis}\right)\right]}, \qquad (4)$$

with $r_{pin}$ the pinhole radius. In the denominator, note that the speed $c_n$ depends on the intensity, which in turn depends on the pinhole radius and misalignment. The dependence of speed on intensity was obtained from OSL measurements, as described above, supplemented with LASNEX results. Since the speed is not known for the glancing angle appropriate to a cone pinhole, we assume that it is the 90° speed, multiplied by a parameter $\gamma$. Thus the model has two parameters: $\beta$ and $\gamma$ (with $\gamma = 1$ for a 4-leaf pinhole).

Figure 9 shows the closure predictions for a diamond Ta pinhole of half-angle 100 $\mu$rad. The upper and lower lines correspond to beam powers of 135 GW and 160 GW, respectively, for a temporally constant pulse shape. The closure time decreases with misalignment, with the sharpest rate of decrease occurring for the smallest misalignment. Also shown are three data points from the Beamlet TSF, with powers in the range 135 to 160 GW. These closure times decrease from 20 ns at 2.5 $\mu$rad to about 13 ns near 12 $\mu$rad, although the error bars are appreciable. The model matches this behavior and predicts a closure time of about 7 ns at a misalignment of 20 $\mu$rad. In the fit we use $\beta = 0.9$, which follows from a fit to all data for 4-leaf pinholes.

Closure times for the stainless-steel cone, of half-angle 100 $\mu$rad, are displayed in Figure 10. The lines give predictions for beam powers of 140 GW and 195 GW, with $\beta = 0.9$ and $\gamma = 0.1$. The data are

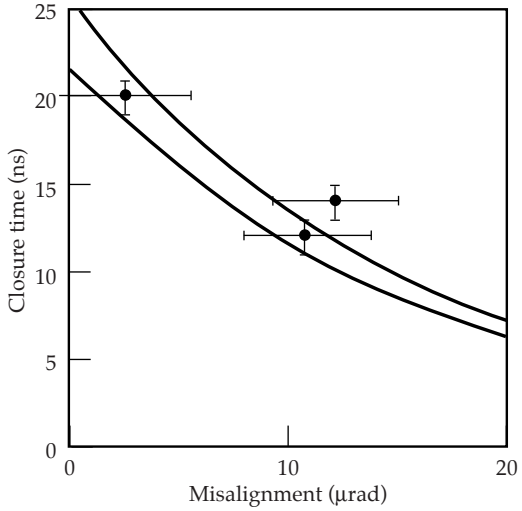


FIGURE 9. Closure time vs misalignment for a diamond Ta pinhole of half-angle 100 $\mu$rad, according to model and Beamlet experiment, for a beam power in the range 135–160 GW. The pulse is constant in time. Since the experimental points vary somewhat in beam power, the model curves are given for the largest and smallest powers.
(70-00-0499-0968pb01)

distributed within this range. As in the previous case, the calculated closure time decreases most rapidly at small alignments. Again the model is comparable with experiment, although it is unfortunate that the data tend to congregate near a common point. Additional data would be desirable to test the model more generally.

Finally, we use the model to predict closure as a function of both pinhole size and misalignment for a stainless-steel cone pinhole. Here we attempt to simulate a temporally shaped ignition pulse (Haan pulse) of 14.8 kJ on NIF. On Beamlet, a Haan pulse of 8.3 kJ was observed to close (i.e., barely pass) at 20 ns. For the same misalignment, a temporally flat pulse closed at 2.2 kJ. Assuming simple scaling, we suppose that a 14.8-kJ Haan pulse can be simulated by a flat pulse of 3.9 kJ. Figure 11 shows how the closure time increases as the pinhole half-angle is increased from 100 to 150 μrad. With no misalignment, closure occurs after 20 ns (the point is barely visible in the corner). NIF specifications allow for 10% misalignment, based on the pinhole radius. The calculation indicates that a 120-μrad pinhole provides ample margin for a closure time of 20 ns. In this case, the edge power is 34 GW/cm$^2$. On the basis of experiments and this modeling, the current NIF design calls for a 150-μrad stainless-steel cone pinhole.

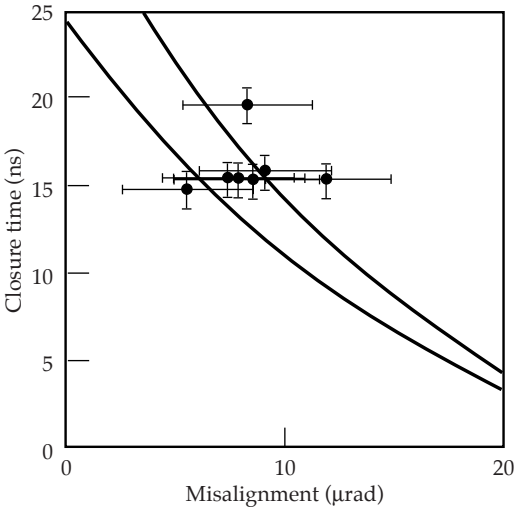


FIGURE 10. Closure time versus misalignment for a stainless-steel cone of half-angle 100 μrad, according to model and Beamlet experiment. The beam power is in the range 140 to 195 GW. (70-00-0499-0969pb01)

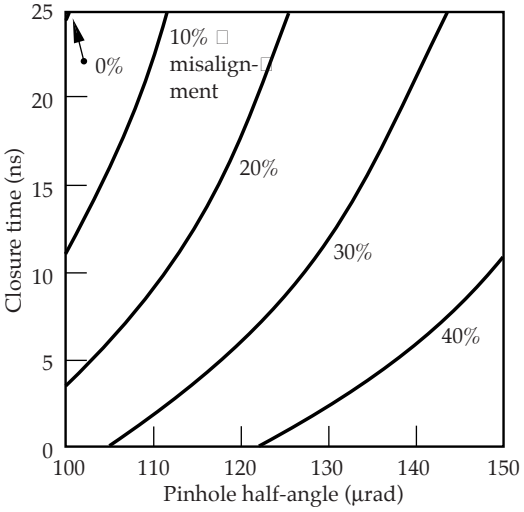


FIGURE 11. Calculated closure time versus pinhole half-angle, as calculated for various fractional misalignments, for a stainless-steel cone. The closure time for a 100-μrad pinhole with perfect alignment is about 25 ns. The pulse simulates a 14.8-kJ ignition pulse. (70-00-0499-0970pb01)

## Initiation of Surface Laser Damage

The NIF final optics will operate at a wavelength of 351 nm (3ω or third harmonic of 1-μm light). Optical damage at 3ω is a more severe problem than at first-harmonic wavelength. Damage in fused silica is typically initiated on the surface or in a near-surface layer, usually most visible on the exit side of the optical element for reasons discussed below. Experiments indicate that damage is initiated at subwavelength-sized sites. Local heating of absorbing nanoparticles can result in material fracture due to thermal-induced stress. Also thermal explosion, in which the absorbing region grows in size with heating, can play a role. Damage in fused silica due to bulk defects, e.g., bubbles or inclusions, can also occur but is expected to be ultimately less significant than surface damage because these defects are expected to be relatively rare.

This section discusses our effort to understand quantitatively the interaction of high-power lasers with damage-initiating defects. Our theoretical description must include optical propagation, absorption and ionization of material, hydrodynamics and shock wave propagation, thermal and radiation transport, elastic-plastic material response and material failure. No computational model at present contains all of the necessary physics. However, we have

used several powerful computer codes with numerical diffraction and scattering models to extend our understanding of the initiation of laser damage.[13] In combination with carefully designed experiments, modeling can identify significant physical effects and scaling behavior.

First, we discuss several important physical effects accompanying laser interaction with metallic surface contaminants. Comparing the results of experiment and modeling, we address the following questions. What difference does it make if the contaminant is on the entrance or exit surface? What is the connection between plasma generation and damage? What is the effect of the surrounding environment? We then discuss damage initiation at subsurface absorbing nanoparticles embedded by the finishing process. Finally, we point out the danger posed by even nonabsorbing bulk defects.

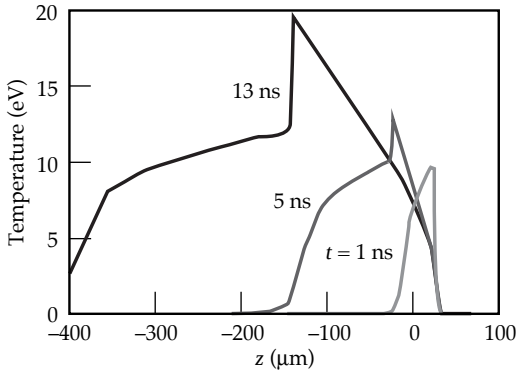


FIGURE 12. Temperature resulting from absorbing front-surface metallic particle on fused silica in air (8.5-ns pulse on 1-$\mu$m-thick Al). Air interface at $z = 0$. Air (to left of expanding metallic plasma) is heated by absorption of ultraviolet radiation from plasma. (70-00-0499-0971pb01)

## Surface Contaminants

Optical surfaces can be contaminated by small particles, say from tens of nanometers to hundreds of micrometers in size. These arise, for example, from dust, condensation, or debris from light interaction with chamber walls and targets. Various types, sizes, and shapes of contaminant have been studied. The simulations presented here refer to artificial "particles" deposited onto a silica substrate. These 1-$\mu$m-thick particles of C, Al, or Ti were sputter-deposited through a mask and were either round or square. Damage initiation experiments were carried out in the 3ω Laser Damage group labs and at the OSL.

For metallic particles, laser light is absorbed in a thin skin depth leading to strong heating and plasma formation. The temperature of the resulting plasma can be as high as 20eV resulting in multiple ionization of the material. Such a hot plasma is a strong radiator of UV and soft x rays. In this case, radiation transport dominates thermal conduction as a means of transporting energy. This radiation is strongly absorbed in any surrounding air, causing heating and further ionization. In this case, the ionization front in the air can expand supersonically. Figure 12 shows our results for irradiating a front-surface absorber in air. The hot "shoulder" seen at the left at late times is air that has been heated through absorption of UV radiation. UV emission from the plasma can also be absorbed in the substrate, creating color centers that increase absorption seen by subsequent pulses.[14] The strongly localized energy deposited in the substrate produces strong shock waves that can cause mechanical damage. Finally, the plasma radiation can induce electronic defects in the glass that permanently change its characteristics and decrease the damage threshold for subsequent pulses.

Laser damage usually is easier to induce on the exit surface. Conventional wisdom points to Fresnel reflection and interference inside the material as the source of this asymmetry.[15] However, the predicted ratio of thresholds does not always hold, and this effect should vanish for antireflection-coated optics. Another difference between contaminated entrance and exit surfaces is that with absorption on the entrance surface, the plasma formed expands and shields the particle from the incoming laser light; that is, further laser energy is absorbed in the plasma itself. Consequently, the pressure pulse launched into the substrate is on the order of 10 kbar. With the absorber on the exit surface, however, the plasma is formed at the interface of two solid materials and confined. The high density of the plasma means higher heat capacity, lower temperature, and much higher pressures (say, 60 kbar) leading to a lower laser damage threshold. Figure 13 compares these two cases.

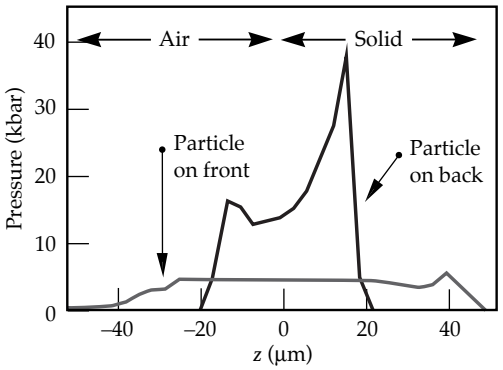


FIGURE 13. Pressure profiles resulting from front- or rear-surface contaminants are different due to plasma confinement for the rear-surface case. Higher temperatures were also calculated for the rear-surface case.
(70-00-0499-0972pb01)

## Subsurface Absorbing Nanoparticles

Experimental observation shows that micropit damage spots appear near the laser damage threshold, particularly on the exit side of nominally clean fused silica samples (see Figure 14). All micropits have comparable sizes, with depth comparable to the width. Pits tend to be elongated, and cracks open preferentially normal to the electric field polarization direction.

It is natural to think that such pits are initiated by subwavelength particulate absorbers in the subsurface layer. Such an absorber might be a small contaminant particle, for example, due to the polishing process. Polishing a brittle surface can result in a thin layer of nearly invisible mechanical damage (microcracks). These cracks can serve as damage initiation centers, particularly if some absorbing material is trapped in them. This appears to be the case for certain ceria-containing polishing compounds. Because ceria is strongly absorbing at 3ω, we will consider ceria nanoparticles here. Heating the material around the absorber can result in further absorption increase, thermal explosion, material ejection, and crater formation.

## Heating

The absorption cross section σ for a particle small compared to an optical wavelength is given in Refs. 16 and 17. The fraction of light incident on the geometric cross section that is absorbed is given by $\alpha = \sigma/\pi a^2$. Starting from a very small radius $a$, α will initially grow faster than linearly with $a$, and then, if the absorber's dielectric coefficient is of large magnitude, tends to saturate at large particle size. Because of diffraction, this absorption fraction can actually be larger than unity, i.e., more laser energy is absorbed than that intercepted by the particle's geometric cross section.

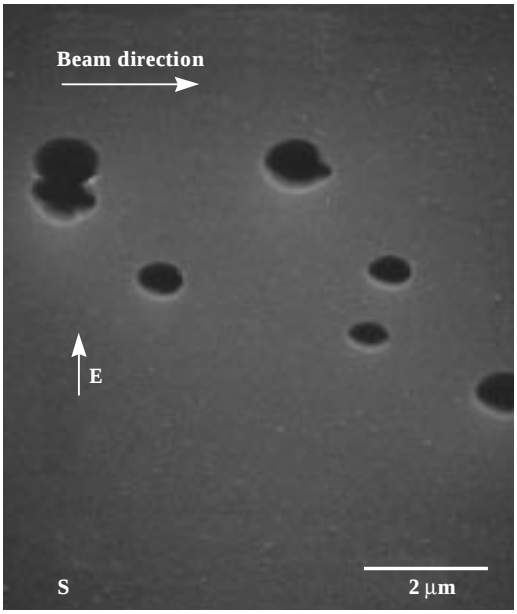


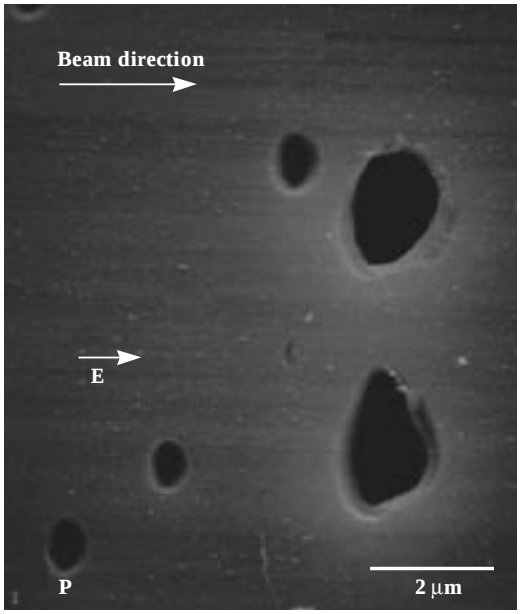


FIGURE 14. Micropit laser-induced damage observed on initially pit-free fused silica surface shows characteristic subwavelength size and orientation with respect to polarization of laser electric field (courtesy of F. Génin).
(70-00-0499-0973pb01)

The size of the absorber is also typically much smaller than a thermal diffusion length. This simplifies treatment of the temperature in the surrounding material, which can be treated as stationary. In Figure 15 we present the peak temperature $T_0$ for a ceria particle with refractive index $n = 2 + 0.2i$. The light intensity was assumed to be 3 GW/cm$^2$, and the pulse duration was taken as 3 ns. The thermal conductivity was taken as 0.014 W/cm K. In the figure, $ka = 0.5$ corresponds to a ceria particle with radius about 28 nm. Here $k = 2\pi/\lambda$ is the wave number of the light, and $a$ is the radius of the particle. The peak temperature grows as the square of the particle size divided by the wavelength for small particles. This result demonstrates why the NIF third-harmonic light is more dangerous than the fundamental. The absorption efficiency depends on the particle size measured in wavelengths, so it is effectively three times as large at the third harmonic.

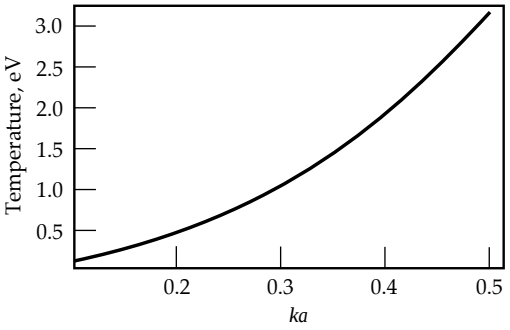


FIGURE 15. Calculated peak temperature increases at a ceria particle of radius $a$ embedded in fused silica. Laser fluence was 9 J/cm$^2$ at 3ω. (70-00-0499-0974pb01)

## Thermoelastic Stress

When the temperature distribution is known, the thermoelastic stresses can be calculated.[18] For example, Figure 16 shows the **xx** component of stress for a spherical ceria particle embedded in fused silica. The peak temperature was assumed to be 1000 K, and the coordinates are given in terms of the particle radius. Notice that the radial stress (equatorial in the figure) is compressive while the tangential or hoop stress (at the poles) is tensile. For an infinite medium, the stress distribution is symmetric as shown. For a near-surface particle, the presence of the free surface modifies the distribution, and material failure most likely occurs initially around the equator of the particle (the "pole" is directed toward the surface).

## Glass Damage

The DYNA2D time-dependent mechanical response code[13] was used to model the damage to fused silica due to heating of a near-surface subwavelength ceria particle. A tensor damage model was used to describe the mechanical damage of brittle material. For low loading, elastic waves can propagate. At higher loads, plastic deformation and tensile and compressive failure can occur. The fact that material strength is larger for loads applied only a short time is taken into account using parameters determined from experiments on high-velocity projectile impacts on glass.

We considered a ceria particle embedded in glass. It was assumed that the glass outside the particle is nonabsorbing. The ceria particle was described with the same type of damage model as the glass, but with different parameters.

In the runs presented below, we consider 100-nm-radius particles at distances of 300 nm and 150 nm from the surface. Energy was deposited at a constant rate for 3 ns, which corresponds to a laser fluence of 10 J/cm$^2$. Figure 17 shows the damage distribution in ceria and glass for particles placed 300 nm under the surface at 1, 2, and 2.5 ns, respectively. The figure indicates the

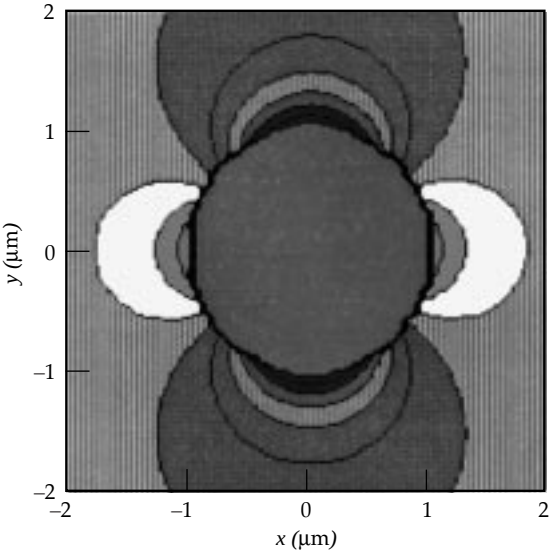


FIGURE 16. Variation of **xx** component of stress near embedded ceria particle in silica. Peak temperature is 1000 K and drops off as $1/r$ outside particle. Radial stress is compressive and hoop stress is tensile at particle substrate interface. (70-00-0499-0975pb01)

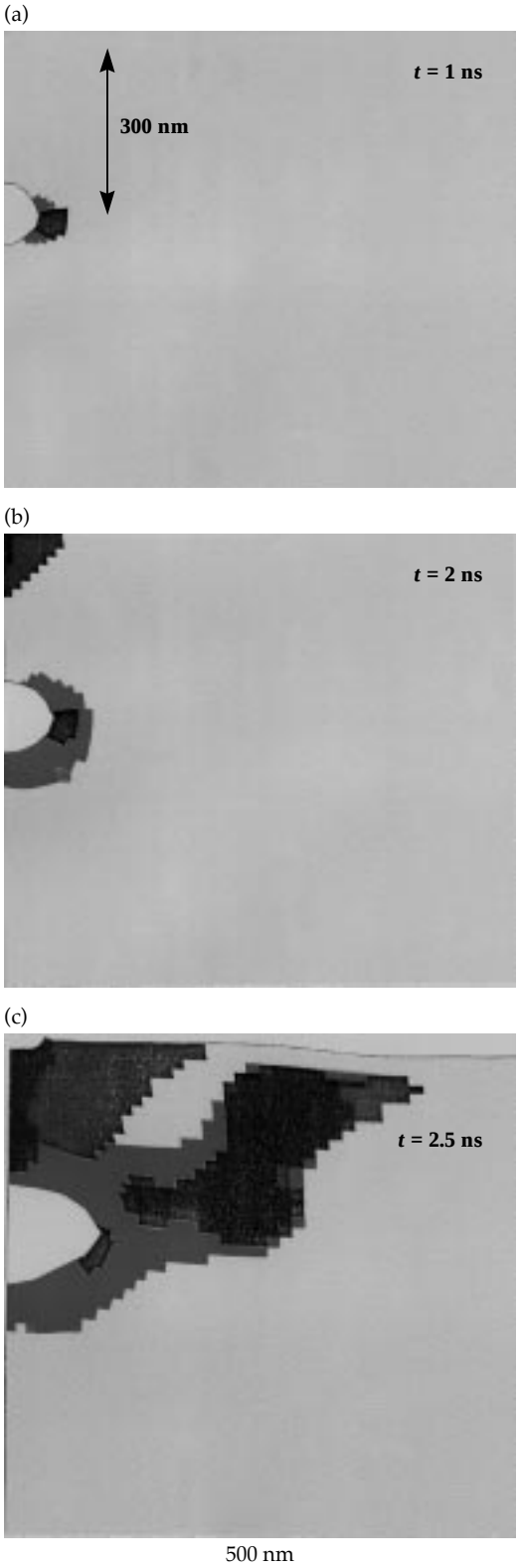


FIGURE 17. Growth of material damage in fused silica due to buried 100-nm ceria particle 300 nm below the surface. Damage initiates near the particle equator and grows to the surface to form a conical region (a) after 1-ns irradiation, (b) 2-ns, (c) 2.5-ns. The material inside the conical region is eventually completely crushed and ejected (calculation by D. Faux). (70-00-0499-0976pb01)

amount of damaged material. Because thermal expansion in ceria is much larger than that of fused silica ($130 \times 10^{-7}$ $K^{-1}$ vs $7 \times 10^{-7}$ $K^{-1}$), thermal expansion generates the initial stresses and damage in the surrounding material. Simultaneously, the shock reaches the free surface and reflects back, generating tensile stresses that easily damage the material. As noted above, because of the free surface, fracture propagates from the equator toward the free surface as additional material fails as stresses are redistributed. The damaged region forms a characteristic conical shape. At the closest and farthest parts of the region, the particle stresses are mainly compressive and initially do not damage the material. Later increases in pressure and arrival of the reflected wave crush most of the material within the cone. All mechanical resistance to shear is destroyed within the cone. The crushed material is finally ejected, forming a conical pit similar to that observed in experiments. The velocity of ejection is not high, only 150 to 200 m/s. It takes a comparatively long time to evacuate the pits. If the completely damaged material is taken as the eventual pit boundary, the estimated pit diameter is about 800 nm and the depth about 400 nm.

This model assumed fixed absorption and does not take into account thermal explosion, i.e., growth of absorption with contaminant heating. We estimate this effect in the next section.

## Thermal Explosion

When the temperature around the inclusion reaches a critical value, a thermal explosion takes place.[19,20] This involves the rapid expansion of the heated region into the glass, which is then ionized. It occurs because the plasma produced by the initially absorbed light radiates UV, which is strongly absorbed in the matrix resulting in heating and an increase in the absorption coefficient of the glass. The situation is very similar to laser-supported ionization waves,[20,21] the main difference being that absorption occurs in a volume instead of just at a front.

Our analysis shows that the radius of the absorbing region tends to grow exponentially: $a = a(0) \exp G$, where the growth factor $G$ is given by

$$G = 10\frac{F\omega}{n_e I_0 c}\,\mathrm{Im}\frac{1}{\varepsilon+2} \tag{5}$$

For absorption at 3ω, solid-state density electron $n_e$, ionization potential $I_0$ of 10 eV, fluence $F$ of 10 J/cm$^2$, and a scattering rate 0.5 of the optical frequency, the growth factor $G$ is about 10. The plasma ball will rapidly grow to a size comparable to a wavelength, after which exponential growth ceases. For the parameters used above, this final radius $a$ is about 500 nm. Any nanoparticle strong absorber will initiate damage of at least this size.

## Nonabsorbing Bulk Defects

The danger posed by absorbing defects in a transparent substrate has long been recognized and understood.[22] Such defects absorb energy, and they heat and expand, thereby thermally and mechanically stressing the surrounding material. It is also known that pure diffractive effects (e.g., clipping at the pinhole) in high-power laser systems can lead to laser-induced damage by causing intensity modulations that seed nonlinear self-focusing.[23,24] In this case, nonlinear refraction increases the local beam intensity level above the damage threshold.

For high-power laser systems, intensity modulations due to purely transparent defects may be capable of inducing damage without invoking any nonlinear effects. Both negative index defects (e.g., voids) and positive index defects (e.g., high-refractive-index inclusion) scatter light strongly, causing strong localized intensity modulation. High-refractive-index inclusions are especially dangerous since they act like efficient focusing lenses.

The situation of interest here is in the borderline area of wave optics and geometric optics. Very small defects (size comparable to a wavelength) with refractive index not very much different from that of the surrounding material can be treated by perturbative methods (Born approximation, WKB method, etc.) or treated by paraxial wave propagation. In the present case, we are interested in defects up to many wavelengths in size with very large differences in refractive index (e.g., –0.5 for a void up to +0.6 for a pure zirconia inclusion). This situation cannot be treated by paraxial optics since it involves strong reflections including total internal reflections inside an inclusion.

The vector theory of electromagnetic scattering was worked out by Mie; it is described in the classic book of Van de Hulst.[17] To be definite here, we choose to model spherical defects for which the solution can be calculated in a convenient form. In the case of larger (compared to wavelength) spheres, it is adequate to use the scalar approximation familiar from spherical scattering in the Schroedinger equation. That is, we wish to solve the scalar wave equation

$$\nabla^2 E + k_0^2 \eta(r)^2 E = 0 \tag{6}$$

where $k_0$ is the free space wave number $2\pi/\lambda$, and $\eta(r)$ is the spatially dependent refractive index. The refractive index is assumed to have the value $\eta_1$ inside a sphere of radius $a$, and the value $\eta_2$ outside this sphere. For convenience, we define the material wave numbers $k_{1,2} = k_0\,\eta_{1,2}$. Then, the solution can be written as a superposition of spherical waves of the form

$$E = \sum_{l=0}^{\infty}(2l+1)i^l \exp(i\delta_l) \times\left[j_l(k_2 r)\cos(\delta_l) - n_l(k_2 r)\sin(\delta_l)\right] \times P_l(\cos\theta) \tag{7}$$

Here $j_l$ and $n_l$ are spherical Bessel functions and $P_l$ is a Legendre polynomial. The effect of the scatterer centered at $r = 0$ is given by the phase shifts $\delta_l$, which vanish identically for no scatterer. The phase shifts are determined from a transcendental eigenvalue equation

$$\tan(\delta_l) = \frac{k_2 j_l'(k_2 a) - \gamma_l j_l(k_2 a)}{k_2 n_l'(k_2 a) - \gamma_l n_l(k_2 a)} \tag{8}$$

where

$$\gamma_l = \frac{k_l j_l'(k_l a)}{j_l(k_l a)} \tag{9}$$

and the primes denote differentiation with respect to argument. Although there are an infinite number of terms in the summation in Eq. 7, the number of partial wave phase shifts $\delta_l$ appreciably affected by the scattering is proportional to the size of the scatterer, i.e., roughly equal to $ka$. This is why it is computationally difficult to treat very large defects.

The calculations reported here are for small defects (wavelength scale and less) since these are most likely to occur. The intensifications important for damage initiation only become larger and persist over longer distances for larger defects. On the other hand, spherical defects probably exhibit the largest magnitude effect, especially for large refractive index inclusions. Actual defects need not be perfectly spherical, of course. Our results serve to point out the large intensifications, thus the serious consequences, which can result from transparent defects.

## Voids

The distribution of intensity around a typical small spherical void (refractive index unity) in fused silica is shown in Figure 18. A plane wave of intensity unity is incident from above. Because the refractive index in the void is lower than that of fused silica, the void acts like a thick diverging lens. From a geometric optics picture, light rays are bent strongly away from the axis, leaving a "shadow" region behind the void. It is the intensity modulations on the edge of this shadow that concern us here. Intensity maxima of twice the incident intensity occur in the vicinity of the void. Further away, these maxima tend to die out. These modulations die out more slowly for larger voids (over a distance comparable with the Rayleigh range $ka^2$).

## Inclusions

Defects with larger refractive index than the surrounding material are more dangerous since they act as concentrating lenses. These are not simple lenses, of course, because they are "thick," i.e., there is a large variation in optical path length over the incoming beam. Consider a spherical inclusion of radius $a$. The phase variation experienced by straight-ahead rays passing through the sphere is given by

$$\Delta\phi = 2Ka(\Delta n / n)[1 \pm (x / a)^2]^{1/2} \qquad (10)$$

at transverse position $x < a$. Here $\Delta n/n$ is the relative change in refractive index. Expanding the square root yields a simple estimate for the effective focal length as $a/(2\Delta n/n)$. This estimate is reasonably borne out by the wave-optical calculations, especially in that the focal length is proportional to the size of the sphere. The full calculation has to be carried out, however, to determine the intensity at the (aberrated) focus.

The intensification factor can be large, even when the change in refractive index is small. For example, the peak axial intensity (in units of the input intensity) downstream from a 4-$\mu$m sphere of index 1.51 in a silica ($n = 1.5$) substrate is about 1.5. A modest increase in refractive index of the inclusion to 1.6 increases the maximum intensity to 10 times the initial intensity.

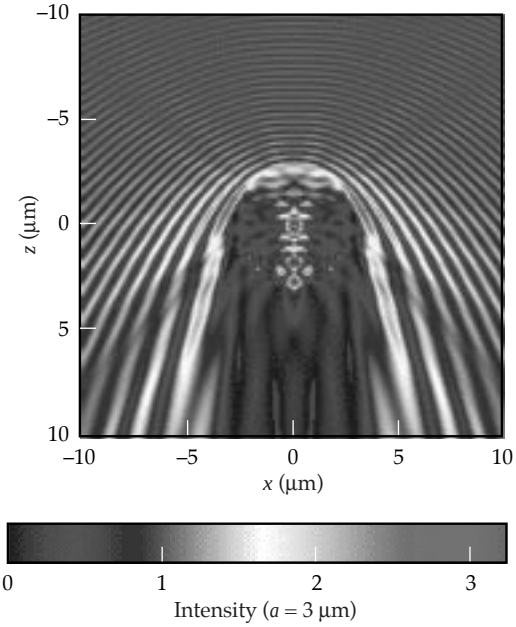


FIGURE 18. Distribution of intensity in vicinity of small spherical void in glass. Light incident from top. Note shadow region behind void and intensity modulations. (70-00-0499-0977pb01)

For a high-index inclusion, e.g., $ZrO_2$, a refractory used in fabrication of fused silica, the intensification is nearly 1000 (Figure 19). Bulk inclusions of high refractive index are thus expected to lead to damage even though they are unlikely to be perfect spheres. Because of the high vulnerability of surfaces, bulk damage produced by inclusions may be accompanied by associated exit surface damage.

# Conclusions

In this paper, we have discussed models that describe two of the ways in which the NIF beam can interact adversely with laser components. These interactions can lead to pinhole closure in the spatial filters and laser-induced damage to optical elements such as lenses. We have discussed a complex model for 4-leaf pinholes and a simple model for pinholes in general, including the cone design. The models have been tested via data taken on OSL and Beamlet and appear to be adequate to make projections for NIF. For the description of laser-induced damage, our modeling has demonstrated the importance of very small absorbing particles as well as nonabsorbing particles in initiating the damage. We expect that such laser-interaction modeling, which involves a number of areas of physics and extensive numerical codes, will continue to contribute to the development of advanced laser technology.

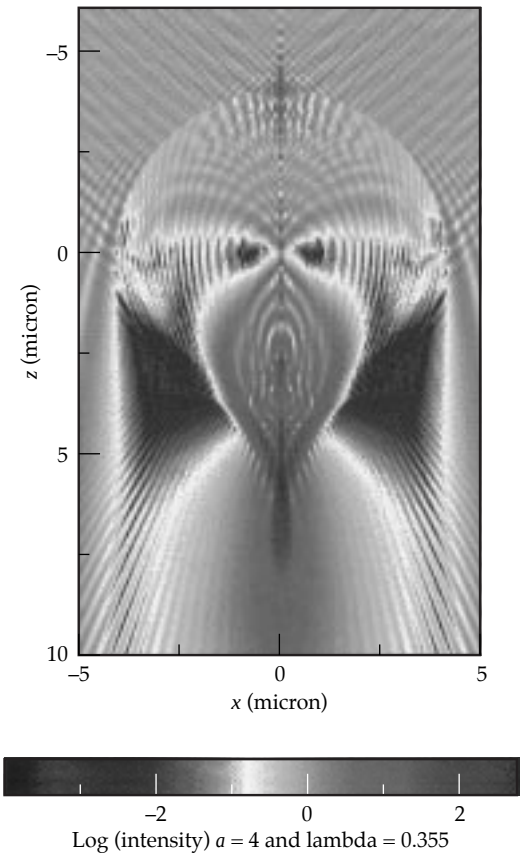


FIGURE 19. Light intensification near zirconia sphere ($n$ = 2.1) in fused silica. Laser incident from top. (70-00-0499-0978pb01)

# Acknowledgments

It is a pleasure to acknowledge the contributions of our colleagues to the work presented here. These colleagues include J. M. Auerbach, K. G. Estabrook, D. R. Faux, F. Y. Génin, M. R. Kozlowski, D. Milam, J. E. Murray, A. M. Rubenchik, S. Schwartz, and L. M. Sheehan.

## Notes and References

1. J. T. Hunt, J. A. Glaze, W. W. Simmons, and P. A. Renard, *Appl. Opt.* **17**, 2053–2057 (1978).
2. See, e.g., J. T. Hunt, K. Manes, P. A. Reynard, *Appl. Opt.* **32**, 5973–82 (1993); for assessments for the 1ω chain, see M. D. Feit, C. C. Widmayer, W. H. Williams, R. A. Sacks, P. A. Renard, and M. A. Henesian, "NIF's assessment of the optical damage threat for flat in time pulses," and M. D. Feit, W. H. Williams, C. C. Widmayer, R. A. Sacks, and P. A. Renard, "Assessment of the damage threat for the two baseline ICF shaped temporal pulses," both in *NIF Laser System Performance Ratings*, Lawrence Livermore National Laboratory, Livermore, CA, UCRL-ID-131115 (July 1, 1998).
3. M. R. Kozlowski, R. P. Mouser, S. M. Maricle, P. J. Wegner, and T. L. Weiland, "Laser damage performance of fused silica optical components measured on the Beamlet laser at 351 nm," p. 428; S. Schwartz, M. D. Feit, M. R. Kozlowski, and R. P. Mouser, "Current 3ω large optic test procedures and data analysis for the quality assurance of National Ignition Facility optics," p. 314; M. D. Feit, A. M. Rubenchik, M. R. Kozlowski, F. Y. Génin, S. Schwartz, and L. M. Sheehan, "Extrapolation of damage test data to predict performance of large-area NIF optics at 355 nm," p. 226; all in *SPIE* **3578**: XXX Annual Symposium on Optical Materials for High Power Lasers, Boulder, CO, Sept. 28–Oct 1, 1998.
4. J. M. Auerbach, N. C. Holmes, J. T. Hunt, and G. J. Linford, *Appl. Opt.* **18**, 2495–2499 (1979).
5. P. M. Celliers et al., "Spatial filter pinhole for high-energy pulsed lasers," *Appl. Opt.* **37**, 2371–78 (1998).

6. J. E. Murray, D. Milam, C. D. Boley, and K. G. Estabrook, "Spatial filter pinhole development for the National Ignition Facility," in preparation.
7. D. Milam et al., "Pinhole Closure Measurements," Third Annual International Conf. on Solid State Lasers for Application to Inertial Confinement Fusion, Monterey, CA, June 7–12 (1998).
8. C. D. Boley, K. G. Estabrook, J. M. Auerbach, M. D. Feit, and A. M. Rubenchik, "Modeling of Laser Knife-Edge Experiments," Third Annual International Conf. on Solid State Lasers for Application to Inertial Confinement Fusion, Monterey, CA, June 7–12 (1998).
9. G. B. Zimmerman and W. L. Kruer, *Comments in Plasma Physics and Controlled Fusion* **2**, 51–61 (1975).
10. J. A. Harte, W. E. Alley, D. S. Bailey, J. L. Eddleman, and G. B. Zimmerman, *ICF Quarterly Report* **6**(4), 150–164, Lawrence Livermore National Laboratory, Livermore, CA, UCRL-LR-105821-96-4 (1997).
11. M. K. Prasad et al., *Phys. Fluids* **8**, 1569–1575 (1992).
12. J. M. Auerbach, Lawrence Livermore National Laboratory, Livermore, CA, internal communication (1998).
13. Laser absorption, ionization, and hydrodynamics were modeled with the HYADES code; cf. J. T. Larsen, "HYADES—A Radiation Hydrodynamics Code for Dense Plasma Studies," in *Radiative Properties of Hot Dense Matter*, edited by W. Goldstein, C. Hooper, J. Gauthier, J. Seely, and R. Lee (World Scientific, Singapore, 1991). Mechanical strength was modeled with Lawrence Livermore National Laboratory's DYNA code; cf. R. G. Whirley, B. E. Engelmann, and J. O. Hallquist, *DYNA2D—A Nonlinear, Explicit, Two-Dimensional Finite Element Code for Solid Mechanics User Manual*, Lawrence Livermore National Laboratory, Livermore, CA, UCRL-MA-110630 (1992).
14. A. P. Gagarin, L. B. Glebov, and V. G. Dokuchaev, *Kvant. Electron.* **4**, 1996 (1977); English translation in *Sov. J. Quant. Electr.* **7**, 1136 (1977).
15. N. L. Boling, M. D. Crisp, G. Dube, *Appl. Opt.* **12**, 650–60, (1973).
16. L. D. Landau and E. M. Lifshitz, *Electrodynamics of Continuous Media* (Pergamon Press, New York, 1960).
17. H. van de Hulst, *Light Scattering by Small Particles* (Dover Publications, New York, 1981).
18. A. P. Boresi, *Elasticity in Engineering Mechanics* (Prentice Hall, New Jersey, 1965).
19. M. F. Koldunov, A. A. Manenkov, I. L. Pokotilo, Sov. *J. Quant. Electr.* **18**, 345 (1988).
20. S. I. Anisimov and V. A. Khokhlov, *Instabilities in Laser–Matter Interaction* (CRC Press, Boca Raton, Florida, 1995).
21. M. von Allmen and A. Blatter, *Laser Beam Interactions with Materials* (Springer, Berlin, 1994).
22. See, e.g., "Modeling laser damage caused by platinum inclusions in laser glass," J. H. Pitts, *Laser Induced Damage in Optical Materials: 1985*, Boulder Damage Symposium, *NBS Special Publication 746* (1986).
23. J. A. Fleck, Jr., and C. Layne, *Appl. Phys. Lett.* **22**, 467–9 (1973).
24. N. B. Baranova, N. E. Bykovskii, B. Ya. Zel'dovich, and Yu. V. Senatskii, *Kvant. Electr.* **1**, 2435–49 (1974), translated in *Sov. J. Quant. Electr.* **4**, 1354–61 (1975).

# Beam Control and Laser Diagnostic Systems


*E. S. Bliss* *A. A. Grey* *R. D. Kyker*
*F. R. Holdener* *R. D. Demaret* *T. J. McCarville*
*J. T. Salmon* *C. M. Estes* *V. J. Miller Kamm*
*J. R. Severyn* *M. Feldman* *R. A. Sacks*
*R. A. Zacharias* *A. J. Gates* *C. E. Thompson*
*S. A. Boege* *W. E. Rivera* *R. L. Van Atta*
*R. D. Boyd* *C. F. Knopp* *S. E. Winters*


The beam control and laser diagnostic systems for the National Ignition Facility (NIF) align the laser beam, diagnose the beam, and control the beam's wavefront. Accomplishing these tasks requires approximately 12,000 motors and other actuators, 700 cameras and other detectors, and 192 wavefront sensors and deformable mirrors.

System control components are located throughout each beamline as illustrated in Figure 1. Each of NIF's numerous laser control systems serves one or more of the following three functions: laser beam alignment, beam diagnostics, or wavefront control. We designed many of the systems to perform multiple functions and share components to reduce the costs and space requirements for NIF. For instance, the input sensors both align and diagnose the initial laser pulse.

The specific requirements for alignment include positioning the 192 beams within the 40-cm apertures of the laser components, focusing them accurately through the far-field pinholes of the amplifier-chain spatial filters, and delivering them to the precise locations specified on the target. All alignment functions are accomplished automatically by recording video images of reference light sources and beams, calculating what adjustments will achieve the desired relative positions of the imaged objects, and sending the corresponding commands to system motors.

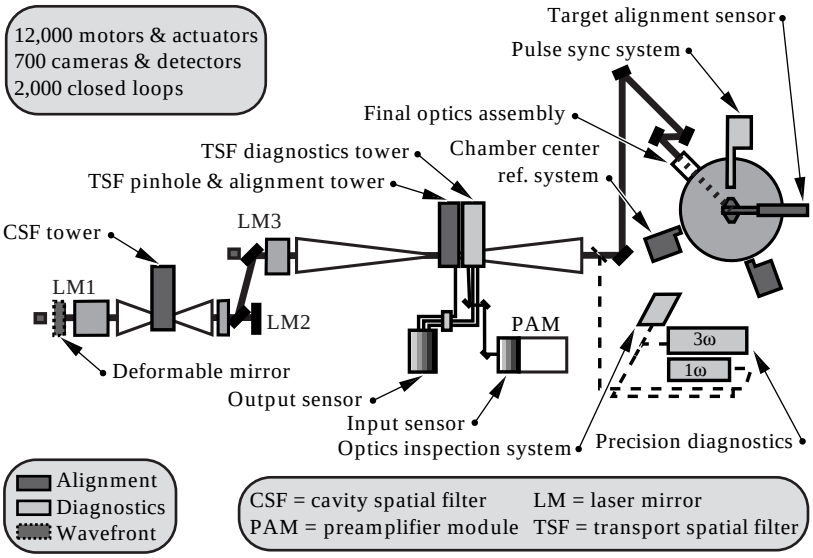


FIGURE 1. Major beam control components for a single NIF beamline. (40-00-1097-2260pb02)

The laser diagnostic systems measure the beam energy, power vs time, and the near-field transverse profile. The detectors that monitor these parameters are calorimeters, fast photodiodes, streak cameras, and charge-coupled device (CCD) video cameras. Requirements for accuracy and reliability are very high.

Wavefront systems measure optical aberrations on the laser output beams and use a deformable mirror in the four-pass amplifier of each beamline to compensate. The resulting improvement in beam quality leads to higher frequency-conversion efficiency and provides better focusing characteristics in the target chamber.

For the sake of clarity, this article is organized by function—laser beam alignment, beam diagnostics, and wavefront control. The input sensor components that handle alignment are described in the laser beam alignment section, whereas the input sensor's diagnostic components are described in the following section on beam diagnostics. Discussion of the front-end processors, another important element of laser control, appears in the "Integrated Computer Control System" article (see p. 21).

## Laser Beam Alignment

In the NIF, laser beam alignment is performed in the following areas:

- Input sensor.
- Spatial filter towers.
- Output sensor.
- Target area.

We discuss the design of the alignment components in each of these areas below.

### Input Sensor

The input sensor is located at the output of the preamplifier module (PAM) of the optical pulse generator. For alignment purposes, the input sensor must measure beam pointing and centering, provide alignment references, and provide a beam for alignment through the rest of the system. The sensor must monitor the output at three points within the PAM: the regenerative amplifier, the beam shaping module, and the multipass amplifier (for the design of these components, see "The NIF Injection Laser System" article (p. 1). The optical design for this alignment system was driven by three factors: (1) resolution and field-of-view requirements, which are directly related to performance of the sensor's function; (2) cost, which limited the number of optical elements and control points; and (3) space, which required that the sensor package fit within the preamplifier transport-optics design footprint. Figure 2 is a photograph of the instrumentation side of a prototype input sensor with beam paths highlighted. The main beam passes on the other side of the package.

The sensor includes a CCD camera that measures both the near-field and far-field intensity profile of the beams. For the far field, the camera measures beam pointing and provides a pointing reference for the PAM control points. The same camera is used to produce a near-field image for

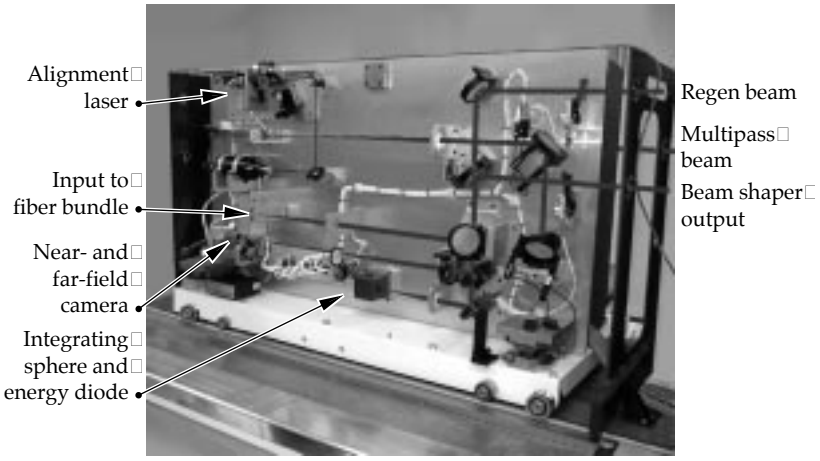


FIGURE 2. Photograph of a prototype of the NIF input sensor package that is being tested in the laboratory. Instruments and indications of beam paths have been labeled. (40-00-0499-0879pb01)

beam-centering alignment. We designed this camera to perform its near-field imaging without disrupting the far-field pointing reference by adding insertable lenses to the fixed far-field lens element and camera.

The continuous-wave (CW) alignment light source shown in Figure 2 is used to align the rest of the system. It provides a beam of the same wavelength and size as the regenerative amplifier (regen) beam. Although the regen beam itself can also be used, it is not always available between shots, and then only at the rate of one pulse per second. The CW alignment beam goes through the input-sensor beam shaper, where it is shaped into a 27.5-mm-square beam.

## Spatial Filter Towers

The spatial filter towers are line-replaceable units (LRUs) that are installed from above at the center of the cavity spatial filter (CSF) and transport spatial filter (TSF) (Figure 3). These towers hold multiple components that serve several functions for each beam, as shown in Figure 4. Platforms holding the components for two beams are mounted at each of the four levels in the towers. They provide a stable base for injection optics, diagnostic optics, pinhole assemblies, and beam dumps. Figure 5 is a photo of a prototype alignment tower platform with some of the components for one beam mounted. This prototype has been shown to meet precision requirements.

Each platform in the CSF and each alignment platform in the TSF has a pinhole assembly that rotates around an axis parallel with the beam propagation direction to accurately position one of the multiple sets of pinholes in the focal plane of the corresponding spatial filter lenses. The same platforms also carry pointing references to which the alignment beam from the input sensor is aligned between shots. In the CSF, the reference takes the form of a reticle that is positioned by selecting a particular position of the rotating pinhole assembly. A local illuminator, also mounted on the platform, provides light for viewing the reticle directly with a camera on the same platform. In the TSF, as shown in Figures 4 and 5, the pointing references are provided by fiber-optic light sources moved into the pinhole plane by their own precision translation stage. Images of the TSF references are viewed in the output sensor. Baffles, one of which is shown in Figure 5, control stray light. Fixed and prealigned beam dumps absorb energy

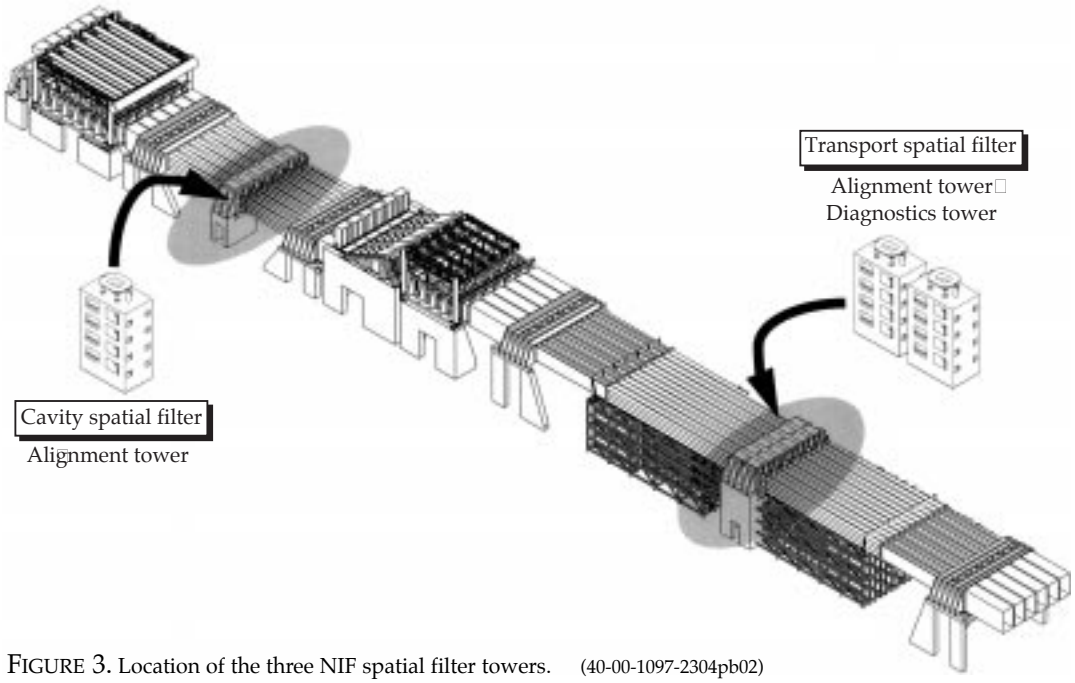


FIGURE 3. Location of the three NIF spatial filter towers. (40-00-1097-2304pb02)

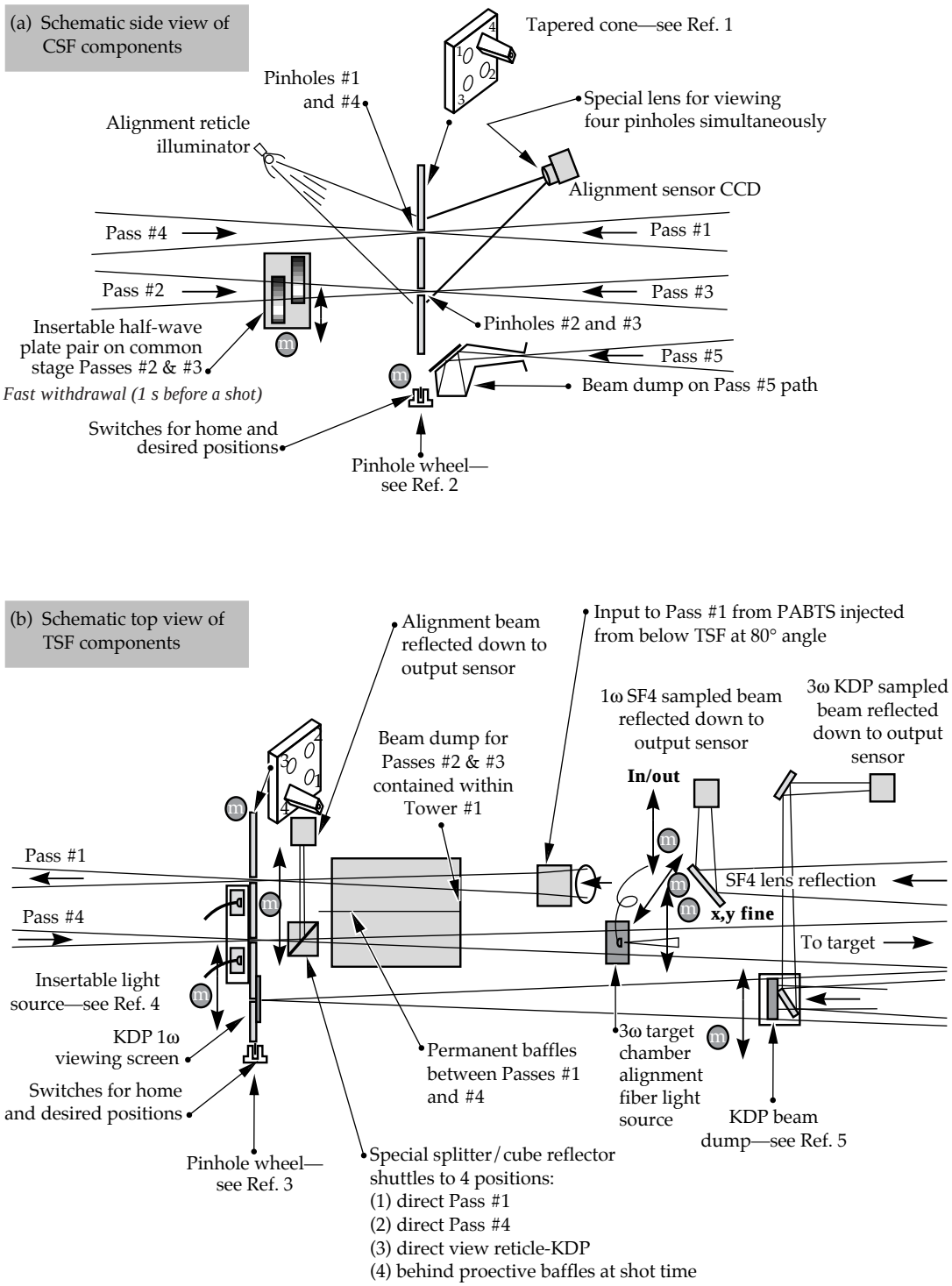


FIGURE 4. Schematic views of the (a) CSF tower and (b) TSF alignment and diagnostic tower components for one beam. (40-00-0499-0880pb01)

from faults or leakage from the Pockels cell and from target back reflections. The pointing references and other alignment optics identified in Figure 4 are removed from the beam path to fire the laser.

## Output Sensor

The output sensor and relay optics packages are located beneath the TSF center vessel, as shown in Figure 6. The sensor

FIGURE 5. A prototype alignment tower platform with the principal components for one beam. (40-00-0499-0881pb01)

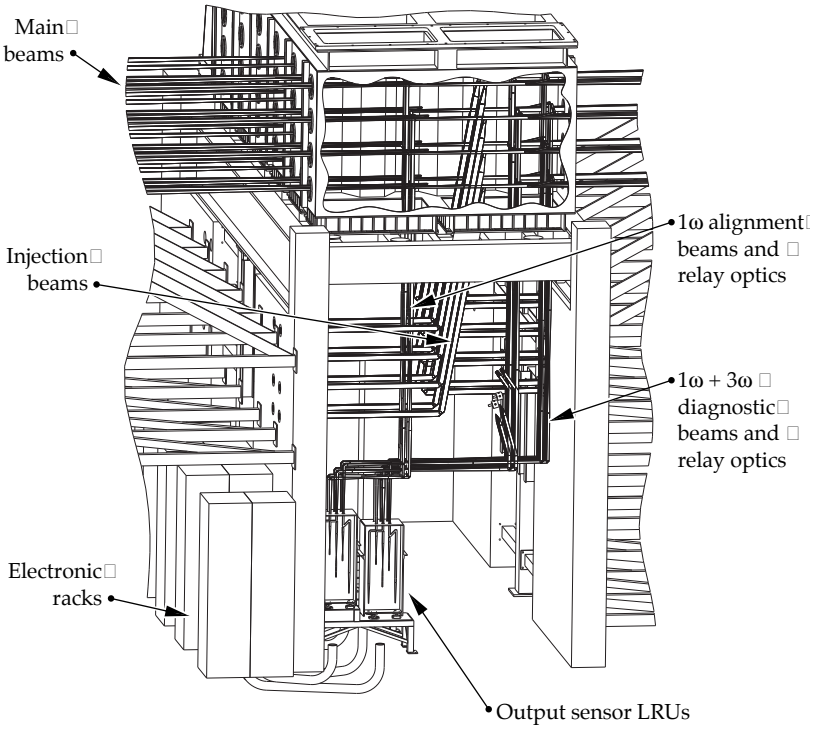


FIGURE 6. The output sensor packages and associated relay optics are located below the center part of the TSF. (40-00-1097-2249pb02)

and relay optics view the following, for alignment purposes:

- Injection beam at Pass 1 for injection pointing.
- Pass 1 in near field for beam centering at the final optics.
- Pass 4 in far field for output pointing.
- Pass 4 in near field for beam centering.
- Reflection from the final optics at the pinhole plane to adjust the angle of the KDP frequency conversion crystals.

These systems are required to center beams within 0.5% of the beam dimension, locate the focused beams on shot pinholes within 5% of the pinhole diameter, position beams on target within 50-$\mu$m rms, and adjust the KDP crystal angle within ±10 $\mu$rad over a field of view of ±200 $\mu$rad. Light for these tasks is intercepted by a moving beamsplitter cube pickoff near the TSF pinhole plane on the alignment tower (see Figure 4b).

Light for all these functions is then directed down to the output sensor along a single path per beam. The pickoffs, relay optics, and transport mirrors are staggered to multiplex the eight beams spatially for each bundle. Two beams per bundle "time share" each output sensor, using beam splitters and shutters in the transport paths. The nominal beam size in the relays is 20 mm.

Figure 7 is a photograph of the prototype NIF output sensor package with beam paths added for illustration. Only the 1ω camera is used for alignment. It has two lens systems for near-field and far-field viewing and a motorized focus adjustment. The near-field lens system is shared with diagnostics (see the diagnostics discussion on p. 85), and the far-field lens system performs focused beam and reticle viewing functions. Both cameras have motorized continuously variable attenuators.

## Target Area

We have two main alignment systems in the NIF target area: the chamber center reference system (CCRS) and the target alignment sensor. Figure 8 shows the layout of these two systems within the target chamber. The target alignment sensor inserter uses the same positioner design as the target inserters. These inserters, the CCRS modules, and target diagnostics are mounted on the same platform to minimize the relative motion among them. At

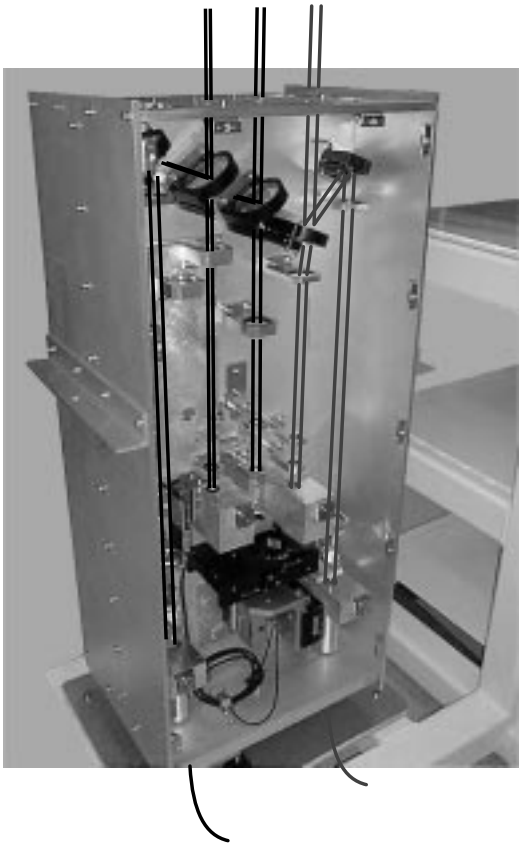

FIGURE 7. This photograph shows the principal components and beam paths of the prototype NIF output sensor package being tested in the laboratory. The output sensor performs both alignment and diagnostic functions. (40-00-0499-0882pb01)

shot time, the alignment sensor is removed and protective baffles are positioned in front of the CCRS port windows.

The CCRS must provide a stable position reference system in the target bay and be able to position targets repeatably within the narrow field of view (FOV) of the target diagnostics. Its long-term stability must be ≤30 $\mu$m, and its FOV must be ±5 cm from the target chamber's center.

The system has two identical viewing instruments that have been adjusted to identify a common position in the center of the target chamber, and each has two simultaneous modes of operation. One mode measures a component's target chamber position by imaging the position of a reticle on the component. The other mode measures the component's orientation by monitoring the direction of light reflected from the reticle.

The target alignment sensor collects images of alignment beams in the target plane and provides data for controlling beam

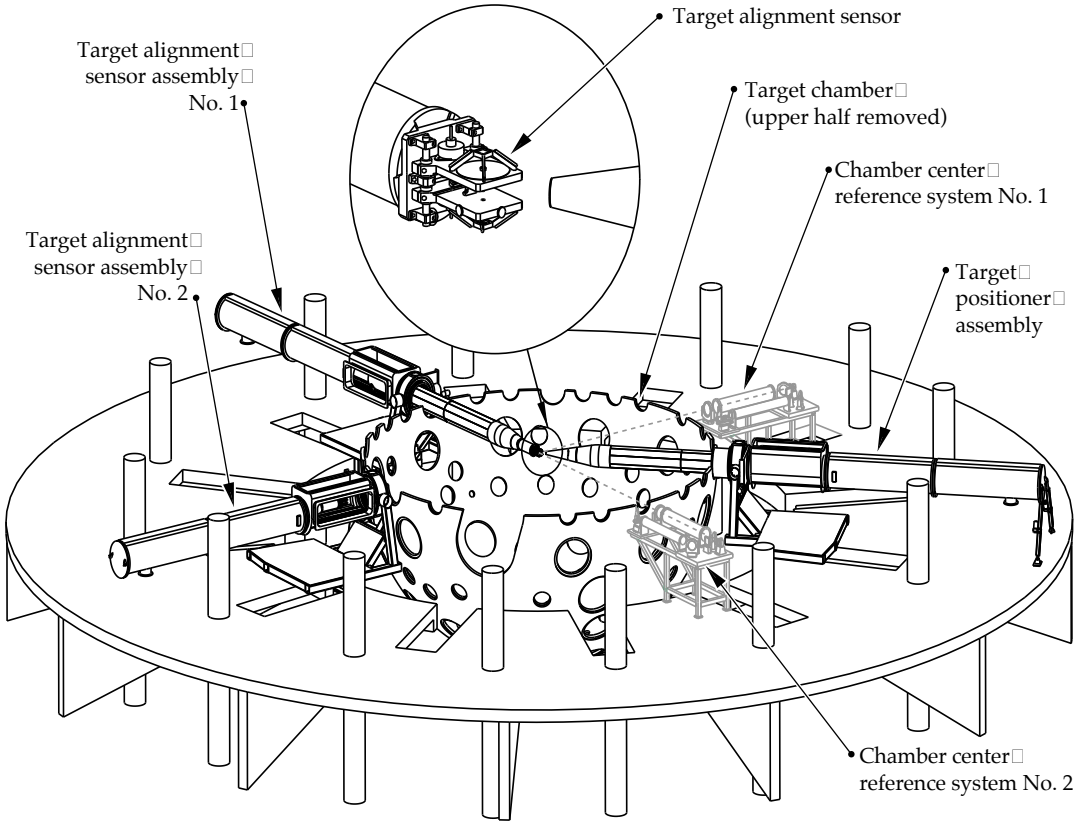


FIGURE 8. Layout of the target area alignment systems. (40-00-1097-2251pb02)

positions and spot size. The total deviation for all beams must be ≤50 μm rms; a single beam must deviate no more than 200 μm; and the sensor must achieve a specified central lobe size to ±50 μm. The sensor must operate everywhere within 5 cm of the target chamber center. Figure 9 shows a schematic of the setup for the target alignment sensor and a photo of the prototype. The sensor has two CCDs, which see both the target and the beams. The assemblies that reflect the beams were designed for minimal deflection and high natural frequency.

# Beam Diagnostics

NIF's beam diagnostics characterize the beam at key locations in the beamline (Figure 10). These systems include the:

- Input sensor.
- Output sensor.
- Calibration calorimeters and final optics diagnostics.
- Temporal diagnostics.
- On-line optics inspection system.
- Target chamber diagnostics.
- Supplemental diagnostics:
  - Roving assemblies.
  - Trombones.
  - Precision diagnostics.

We briefly discuss the requirements and design activities of each of these diagnostic systems below.

## Input Sensor

The input sensor, in addition to providing certain alignment functions (see p. 80 and Figure 2), characterizes the PAM by sampling at the output of the regenerative amplifier, the beam shaping aperture, and the multipass rod amplifier. The sensor measures beam energy, near-field images, and temporal pulse shape. The imaging resolution is 1% of the beam dimension and 2% of the maximum fluence.

Diagnostic samples are obtained from a 1% partial reflector for the regenerative amplifier and through leaky mirrors for the beam shaper and multipass amplifier. The coatings on these mirrors provide adequate signal levels to the energy diagnostics, as well as to the alignment diagnostics.

The energy from the regen, beam shaper, or four-pass amplifier is measured with an integrating sphere and photodiode followed by a charge integrator and digitizer. Shutters select which sample is measured and a CCD camera obtains near-field images for each beam prior to or during a shot. An optical fiber bundle sends a sample of the multipass output to the power sensor (see Figures 10 and 13), where it is time multiplexed with other signals. The PAM output beam can also be diverted to a calorimeter to periodically calibrate the multipass energy diagnostic.

## Output Sensor

The output sensor performs many diagnostic tasks in addition to its alignment functions (for alignment discussion, see p. 82). The sensor characterizes the 1ω output (energy, near-field fluence profile, temporal pulse shape, and wavefront) and 3ω output (near-field fluence profile and temporal pulse shape). The 1ω output energy

(a)

- CCDs see both the target and the beams
- The target is viewed from three sides
- No light hits the target
- Design will vary for different targets

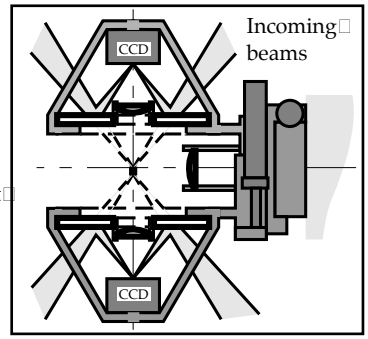


(b)

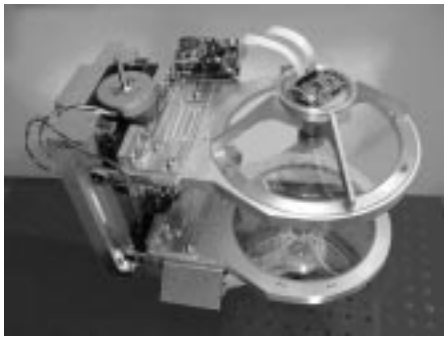

FIGURE 9. (a) A schematic illustrating the setup concept for target alignment. (b) Photograph of the prototype target alignment sensor currently under test. (40-00-0499-0883pb01)

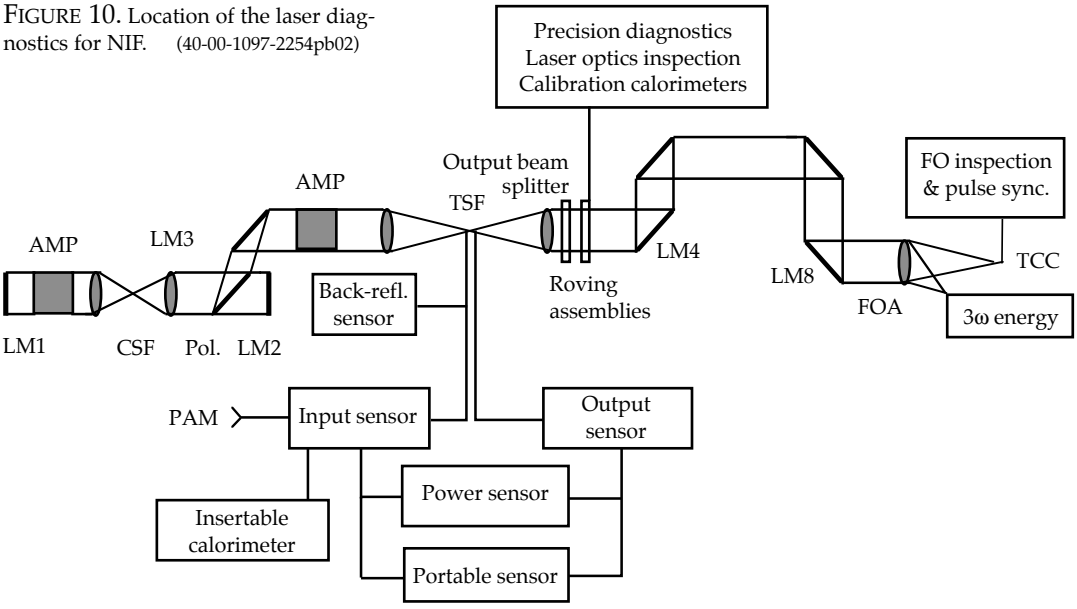


FIGURE 10. Location of the laser diagnostics for NIF. (40-00-1097-2254pb02)

must be measured within 3%, and the 1ω and 3ω temporal pulse shape must be measured within 2.8%. The 1ω beam wavefront must be measured within 0.1 wave, and the 3ω output beam must be imaged at the plane of the conversion crystal with a spatial resolution of 3.2 mm. Figure 7 shows the output sensor's principal components and beam paths, and Figure 11 shows a schematic for the output sensor's diagnostic functions.

Reflections from optics in the main beam supply samples of the 1ω and 3ω beams. The 1ω sample reflects from the front surface of a beam splitter at the output of the TSF. This surface is coated with a solgel antireflection coating (nominally 0.1% *R*), and the splitter is tilted by 0.8 mrad to offset the reflected sample from the path of the existing beam. The 3ω sample reflects from the flat entrance surface of the target chamber lens in the final optics assembly. This lens is also tilted by 0.6 mrad to the opposite side to offset the reflected sample beam from the exit path, and its coating is similar to that on the SF4 lens sampling surface. Pickoffs for the beam samples are near the focus in the TSF. Pickoff optics for

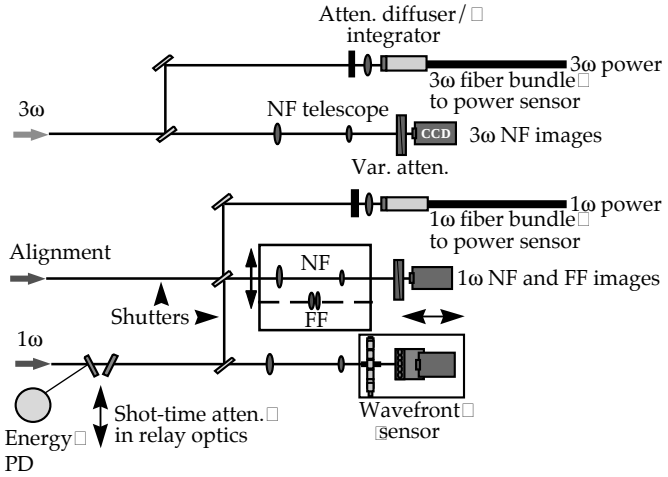


FIGURE 11. Output sensor schematic for beam diagnostics. NF and FF mean near field and far field, respectively. PD means photodiode. (40-00-1097-2256pb01)

1ω and 3ω sample beams are located on TSF Tower #2, as shown in Figure 4. Relay optics transport the beams from the TSF to the output sensors beneath the TSF center vessel. Each side of the output sensor collects data for two beams as illustrated in Figures 7 and 11.

The output sensor has three CCD cameras, each with continuously variable attenuators. One camera—shared with the alignment functions—images the 1ω near-field profile, the second images the 3ω near-field profile, and the third is the detector array for a Hartmann wavefront sensor (see p. 93 for a discussion of the Hartmann sensor). The 1ω energy is measured by an integrating sphere with a time-integrated photodiode, which is inserted at shot time. Power samples are sent to the power sensor (see Temporal Diagnostics at right column) using two optical fiber bundles.

## Calibration Calorimeters and Final Optics Diagnostics

Calorimeters, which measure beam energy, are used in three areas of NIF: the input sensor, the output sensor, and the final optics diagnostics. Each input sensor has a port for manual mounting of a 5-cm calorimeter to calibrate the sensor's energy diode without opening the beamline (Figure 2). The output energy diodes are calibrated using two groups of eight roving bundles of 50-cm calorimeters—one for each laser bay. Each group can be remotely positioned to intercept the outputs from one eight-beam bundle at a time. Finally, 192 10-cm calorimeters in the final optics diagnostics measure a fraction of each beam's 3ω energy as it propagates toward the target.

We use calorimeters similar to those on Nova. The 5-cm calorimeters are an off-the-shelf design, and the 50-cm and 10-cm calorimeters are scaled versions of the 40-cm ones used in the Nova target chamber. These calorimeters can meet the NIF requirements.

The final optics diagnostics uses a diffractive splitter to obtain a sample for the 3ω calorimeter (Figure 12). This calorimeter calibrates the 3ω power for each shot. It must operate in a vacuum, and have a damage threshold >3 J/cm$^2$ at 351 nm, a 10- × 10-cm aperture, a 1- to 60-J energy range, a repeatability of <1% at the 30-J level, and a linearity of <1% over a range of 50:1. The sampling grating on the flat surface of the focus lens diverts <1% of the 3ω energy and focuses the sample in front of the calorimeter.

## Temporal Diagnostics

Temporal diagnostics includes two portable sensors, rack-mounted power sensors near the input and output sensors, and a back-reflection sensor. NIF will have two portable streak cameras, mounted on carts, which can each be used in place of a normal power sensor for one beam at a time. The streak cameras must have a time resolution of 10 ps, a dynamic range of 1000:1, and multiple channels, and be easily movable among the other sensor packages. Each camera

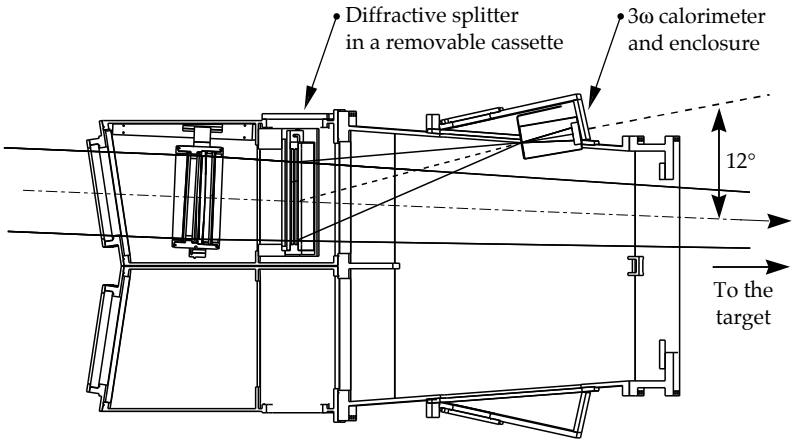


FIGURE 12. The final optics diagnostics uses a diffractive splitter and volume-absorbing calorimeter. (40-00-1097-2257pb02)

can handle 19 sample inputs—1ω or 3ω—through fiber-optic bundles. One of four sweep times can be selected—1.5 ns, 5 ns, 15 ns, or 50 ns—with resolutions from 10 ps (for 1.5 ns) to 250 ps (for 50 ns).

Each power sensor must have a dynamic range of 5000:1, a record length of 22 ns, an accuracy of 2.8% averaged over a 2-ns interval, and a rise time of 450 ps. It takes samples on fiber bundles from the output and input sensors, and time multiplexes signals as shown in Figure 13 to minimize costs. The transient digitizer in the sensor is a commercial technology with a long record length. Each 1ω photodiode receives signals from four input sensor fiber bundles and eight output sensor fiber bundles. Each 3ω photodiode receives signals from four output sensor fiber bundles. Time separation is achieved using the propagation time through the laser and optical fiber delay lines for signals close in time. The dynamic range of the eight-bit digitizer is extended using four channels, each with a different sensitivity.

## On-Line Optics Inspection System

One on-line optics inspection system is located in each switchyard, and one more at target chamber center. These systems have access to each beamline through a set of translatable mirrors described later (see Supplemental Diagnostics on p. 90). The requirement for main-beam optics is to detect flaws ≥3 mm. Our goal is that these systems detect defects ≥0.5 mm so that the optics can be removed for refinishing while defects are still small. We considered a number of issues when designing these systems. First, we selected dark-field imaging since damage spots appear best against a dark background. This allows us to detect spots below the resolution limit. Our imaging scheme is to backlight the large optics with apodized and collimated laser illumination sources. Undisturbed light is intercepted by a stop in the dark-field optics, but light diffracted from damage spots is imaged onto a CCD camera. Second, the systems' resolution will be limited by one of two factors: the far-field aperture in the TSF or the number of pixels in the cameras' CCD arrays. We must properly account for these limitations in the design. Third, depth of field will be short enough to isolate all but the most closely spaced optics. Fourth, use of different pinhole combinations in the CSF and careful image processing can "strip away" any overlaid images.

The laser bay optics are inspected with the high-resolution cameras located in each switchyard. Figure 14 shows the layout of a switchyard inspection package. For optics in the main laser, the illumination source is the alignment laser located in the input sensor. This alignment beam is injected into the TSF along Pass 1, and LM1 is aligned to return the beam along Pass 4.

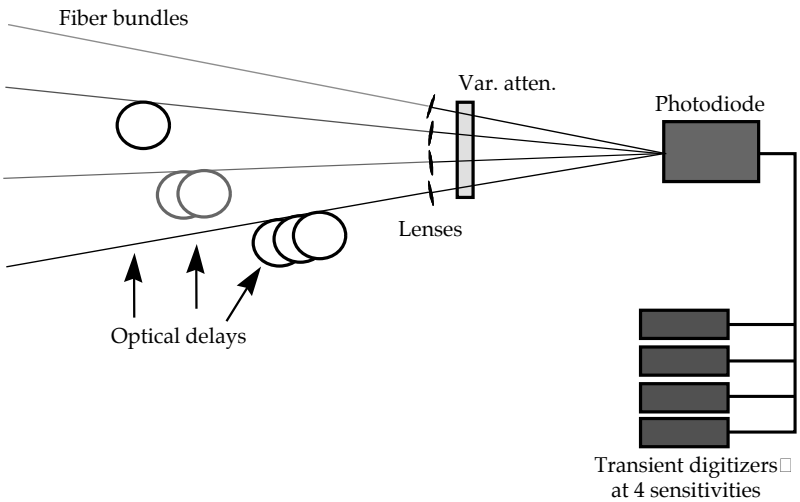


FIGURE 13. Schematic diagram of a power sensor in which time-multiplexed optical pulses are combined on a common photodiode, and the electrical outputs drive multiple channels in transient digitizers.
(40-00-1097-2258pb02)

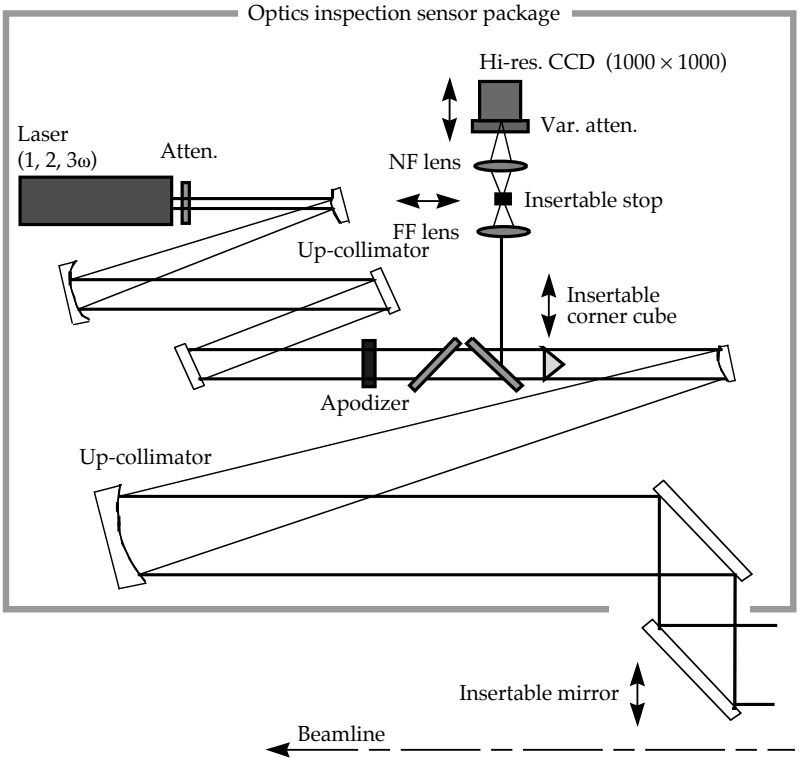


FIGURE 14. Inspection package used for all but the final optics. One such inspection system resides in each switchyard. NF and FF mean near field and far field, respectively. Light is directed into or from the package by an insertable mirror.
(40-00-1097-2259pb02)

The inspection package captures dark-field images at each plane containing an optic. Image subtraction software will help detect the changes from previous inspections.

For inspecting switchyard and target optics up to the first surface of the final focus lens, the switchyards' 1ω source will be injected toward the target using the outward-looking roving mirror (p. 91). The first surface of the final focus lens will be aligned to retroreflect a portion of this beam. Dark-field images will be captured by the inspection system in the switchyard at each plane containing an optic.

For inspecting the final optics, we will image through the kinoform phase plate at 3ω using a damage inspection package inserted at the target chamber center (described further in the next section). This viewer will have a sufficiently short depth of field to discriminate between the closely spaced final optics elements.

## Target Chamber Diagnostics

Target chamber diagnostics include the pulse synchronization detector module and the target optics inspection system. Both are located at the center of the target chamber at the end of the diagnostic instrument manipulator, as shown in Figure 15a. Similar adjustments are required for both the pulse synchronization and final optics inspection modules. They can be oriented to any beam position. Translation commands for the diagnostic manipulator and angle commands for the modules come from the CCRS (see Target Area on p. 83). The maximum move time to intercept light from a different four-beam quad is 5 s; the typical time is <0.8 s.

Figure 15b shows the components of the synchronization module. The pulse arrival times at target chamber center must be set with 20-ps relative accuracy. The module must simultaneously capture signals from the four beams of a final optics assembly quad and position each focused beam on the end of a separate fiber bundle with an accuracy of <100 $\mu$m. The fiber bundles carry the optical signals to a streak camera where their relative times of arrival are compared. The signal is obtained by firing a rod shot and capturing the leakage of 1ω radiation through the conversion crystals.

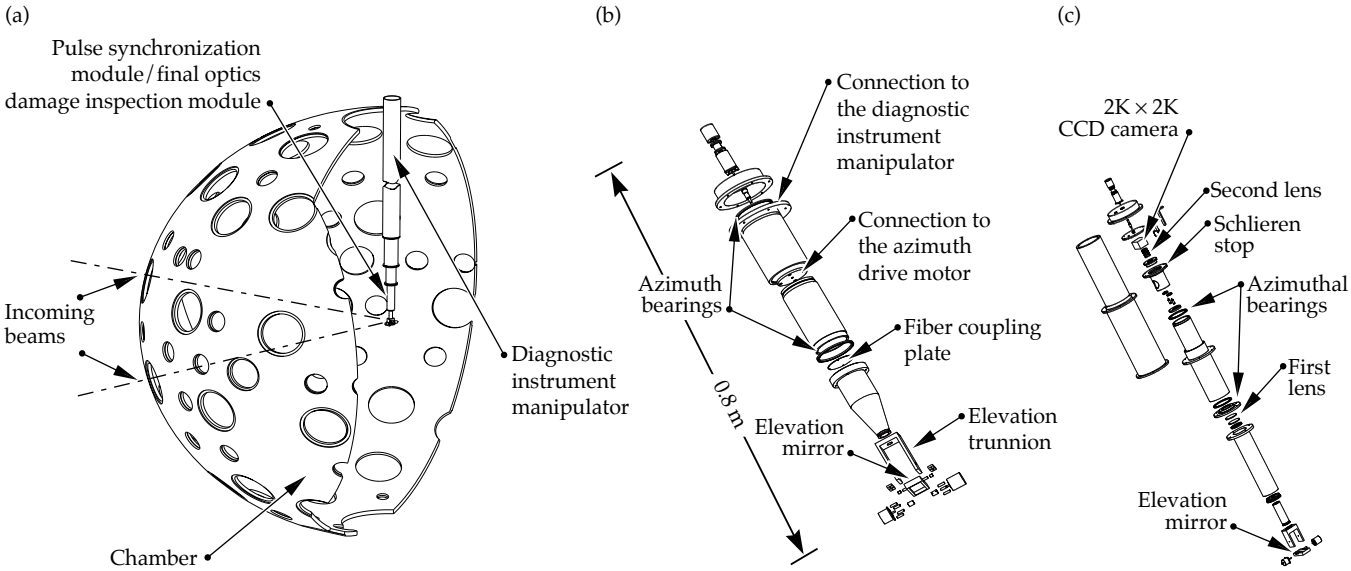


FIGURE 15. (a) The pulse synchronization detector module and final optics damage inspection module can be attached to the end of the diagnostic instrument manipulator and inserted into the center of the target chamber; (b) exploded view of the pulse synchronization module; (c) exploded view of the final optics damage inspection module. (40-00-1097-2261pb02)

The final optics damage inspection module, also located at target chamber center, is shown in Figure 15c. The module examines the closely spaced final optics that are not observable by other means. The final optics are backlit with collimated 3ω radiation. A high-pass filter, with a central schlieren stop placed at the focus, removes those rays that are not deviated by flaws. A CCD camera captures data from the full-aperture image. The camera, lenses, schlieren stop, and filters rotate as a unit in the azimuthal direction.

## Supplemental Diagnostics

As described above, the NIF design includes significant diagnostic capabilities on each beamline. However, it will be important to be able to calibrate some of these measurements, to verify that they are operating correctly, or to collect more detailed information. For this purpose, additional diagnostics that can be used on one or a few beams at a time are located in each switchyard. They include full-aperture calibration calorimeters and a suite of precision diagnostics.

Figure 16 shows the layout of components related to supplemental diagnostics in one of the switchyards. An array of eight calorimeters, the "roving calorimeter assembly," travels on horizontal rails to any of the 12 bundle locations. If desired, each of the eight calorimeters can collect the output from the corresponding beam in that bundle. However, any of the eight calorimeters can also be rotated toward the laser on its outside vertical edge so that it allows the beam to pass. Beams that are allowed to pass continue on to the target chamber or are directed to the precision diagnostics as described below.

The optical-mechanical system designed to intercept any one beam in each switchyard and send it toward the precision diagnostics is called the "roving mirror system." It comprises an additional pair of parallel horizontal rails, two pair of parallel vertical rails, and three translatable mirrors. The x-y top mirror (Figure 17a) in combination with the y mirror picks off a beam and diverts it toward the precision diagnostics and optics inspection package. The x-y bottom mirror, combined with the y mirror, provides a path from the optics inspection package to the target chamber (Figure 17b). Both roving systems are inside of a large enclosure through which the laser output beams pass.

Each of the roving calorimeter and x-y mirror assemblies weighs about 1000 lb. The horizontal motion of the assemblies is

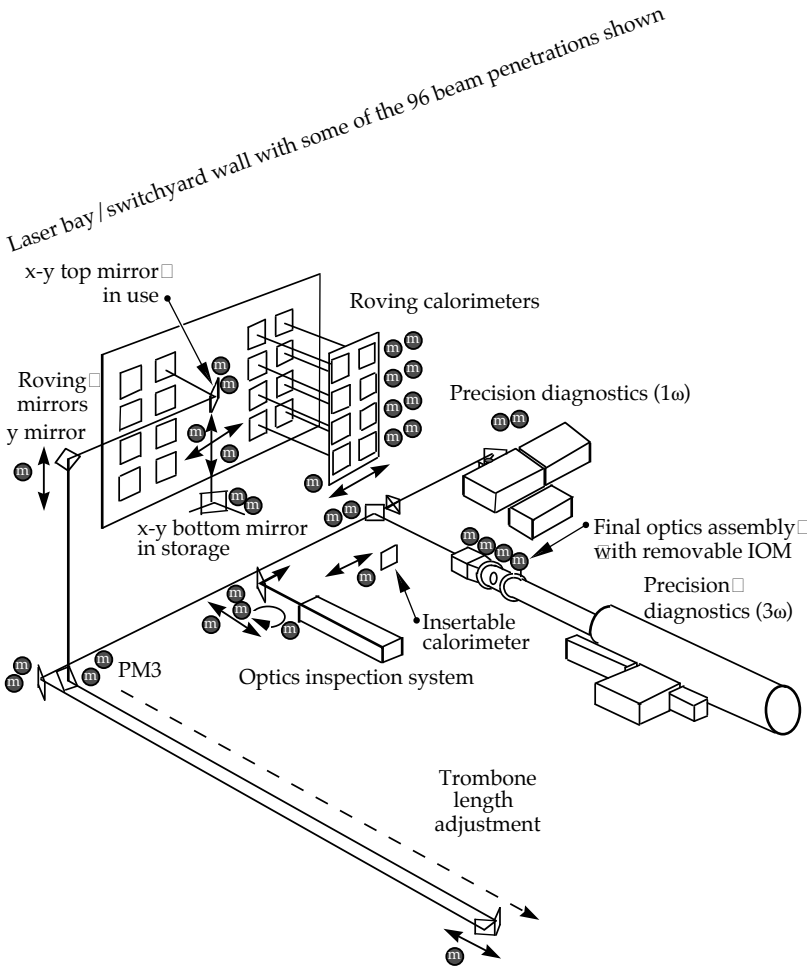


FIGURE 16. Supplemental diagnostics for calibration and for a variety of detailed measurements are located in the switchyard.
(40-00-1097-0381pb02)

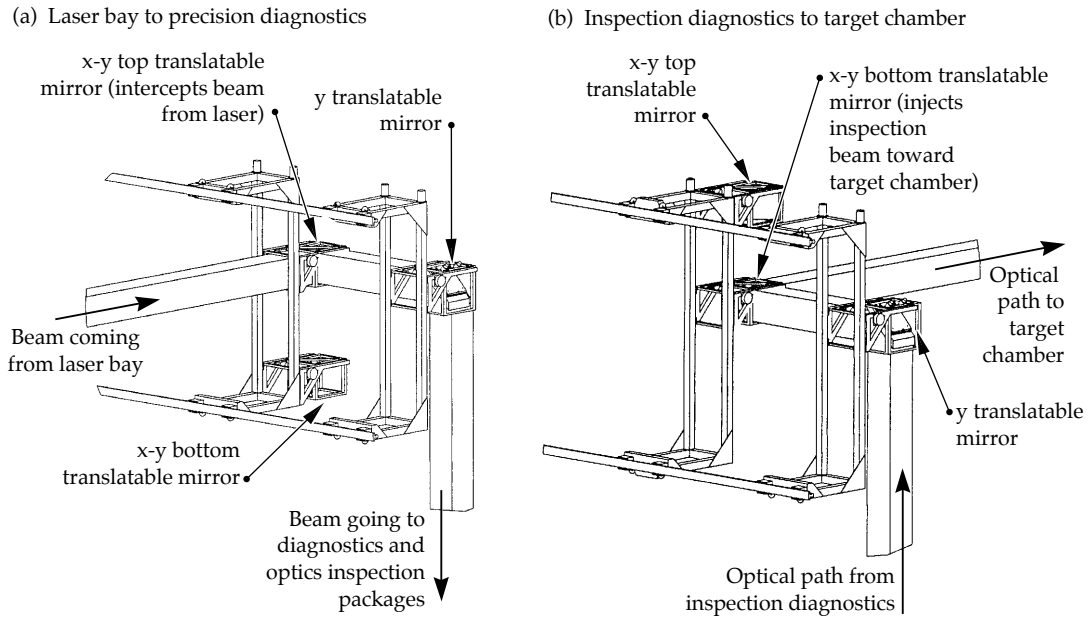


FIGURE 17. Two roving mirror system configurations provide (a) a path from the laser bay to the precision diagnostics station and (b) a path from inspection diagnostics to the target chamber.
(40-00-1097-2262pb03)

belt driven by motors fixed at one end of the enclosure. The average time to move from one beam to an adjacent beam is estimated at 16 s. The enclosure maintains an argon gas environment, and the mechanisms must be designed to avoid production of particles that might contaminate the nearby optics. The path length from the roving mirror to the precision diagnostic stations for each beam is matched to that beam's path length to the target chamber by adjustment of an optical "trombone."

The precision diagnostic stations are shared diagnostics that measure laser output performance one beam at a time using more extensive instrumentation than that found in the output sensors (Table 1). During installation and activation, the precision diagnostics will be used to verify the performance of each beam, including its dedicated diagnostic packages. The 3ω precision diagnostics, illustrated in Figure 18, will measure frequency conversion characteristics of the selected beam using a separately selected integrated optics module (IOM). Each IOM comprises the set of optics, including frequency conversion crystals and final focus lens, that is normally mounted at each beam's entrance to the target chamber. The precision diagnostics provide the only capability for simultaneously measuring high-power 3ω beam properties at the full 40-cm near-field aperture and in a far-field plane equivalent to the target chamber focus. Once NIF is operational, the station will be available for diagnosing beamline and component problems and for performing laser science experiments.

The precision diagnostic station will be able to measure the following aspects of the 3ω laser pulse:

- Energy, with an accuracy of 2.7%.
- Power vs time, with an accuracy of 3.1% and a rise time of 450 ps for all parts of a 22-ns pulse having a 50-to-1 contrast ratio.
- Focused spot size and smoothness, with 30-$\mu$m spatial resolution and 20-ps temporal resolution for a selected 1.5-ns period.
- Near-field spatial profile in the frequency conversion crystal plane, with resolution as high as 300 $\mu$m.

TABLE 1. The 1ω measurement capabilities of the precision diagnostic station compared to those of the output.

| Measurement | Precision diagnostic | Output sensor |
|---|---|---|
| Energy | | |
| Range | To 22 kJ | To 22 kJ |
| Accuracy | Better than 1.5% | 3% |
| Power resolution | <40 ps or 100 ps | 450 ps |
| Far-field imaging FOV | ±180 $\mu$rad (best) | None |
| Near-field imaging resolution (in main beam) | ~1.4 mm and/or ~300 $\mu$m | 3.2 mm |
| Wavefront | | |
| Hartmann precision | Better than $\lambda/20$ | $\lambda/10$ |
| Radial shearing interferometer precision | –0.1 $\lambda$ (16× reference) | None |
| Schlieren | | |
| Energy balance | Better than 15% | None |
| Power resolution | <40 ps or 100 ps | None |
| Far-field imaging FOV | ±500 $\mu$rad | None |
| Near-field imaging resolution | ~1.6 mm (in main beam) | None |
| Prepulse sensitivity | $2 \times 10^4$ W/beam for 200 ns preceding foot pulse | None |
| Potential added measurements | Versatile | Fixed |

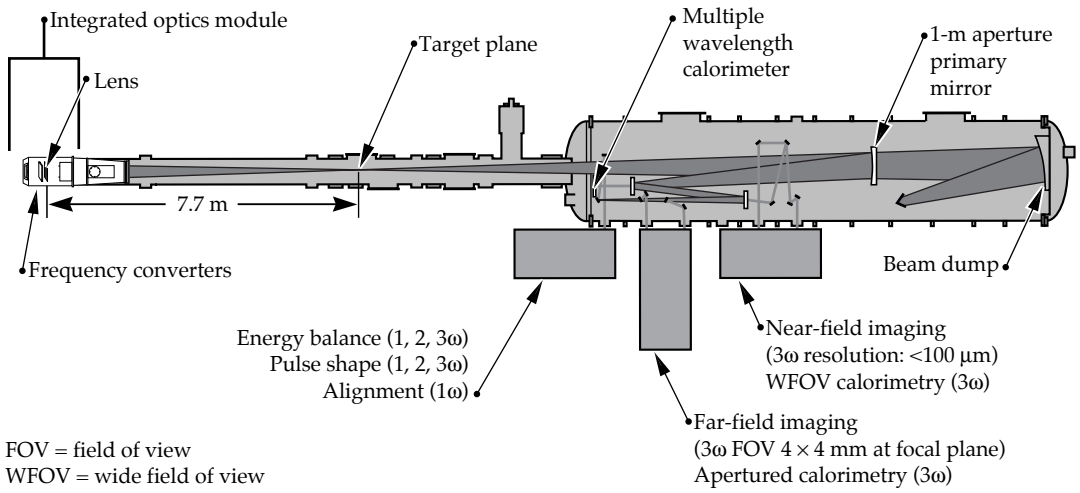


FIGURE 18. The precision diagnostics measure the characteristics of a full-power NIF beamline. The larger vacuum chamber is necessary to avoid high-intensity air breakdown and to expand the beam enough that it doesn't damage beam-splitting optics.
(70-00-0796-1536pb02)

# Wavefront Control

The three main components of the wavefront control system are the:

- Hartmann wavefront sensor.
- Deformable mirror.
- Computer controller.

The use of lasers as the driver for inertial confinement fusion experiments and weapons physics applications is based on their ability to produce high-energy short pulses in a beam with low divergence. The focusability of high-quality laser beams far exceeds that of alternate technologies, and the challenge for NIF is to ensure that the potential of high output beam quality is realized. Although considerable effort has been expended to minimize aberrations due to beamline components, other design constraints, including cost, have caused the residual error to be significant. A wavefront correction system is required to compensate for these errors.

During preparations for a pulsed shot, the wavefront control system monitors the wavefront of each alignment laser at the beamline output and automatically compensates for measured aberrations using a full-aperture deformable mirror. In the last few minutes before a shot, the controlled wavefront is biased to include a precorrection for the estimated dynamic aberrations caused by firing the flashlamp-pumped amplifiers. One second before a shot, closed-loop operation is interrupted, and the Hartmann wavefront sensor is configured to measure the pulsed wavefront. The measured pulsed wavefront error provides additional information for setting precorrection wavefronts prior to the next shot.

Requirements for the system include operation at 1 Hz closed-loop bandwidth, reduction of low spatial frequency angles in the beam to less than 20 $\mu$rad, and a range of at least 15 waves for correction of simple curvature measured at beamline output. Figure 19 shows the location of system components.

## Hartmann Sensor

The Hartmann sensor includes a 2D array of lenslets and a CCD video camera. The output sensor (Figure 7) delivers a demagnified image of the output beam to the lenslet array. Each lenslet collects light from a specific part of the beam and focuses it on the CCD. The focal length must correspond accurately to the distance from the lenslet to the CCD; this result is obtained using an index-matching fluid sealed between the lenslets and an optical flat. The lateral position of the focused spot is a direct measure of the direction of the light entering the lenslet. Directional data from the 77 hexagonally packed lenslets of the NIF sensor are processed to determine the output wavefront with an accuracy of ≤0.1 wave averaged over the

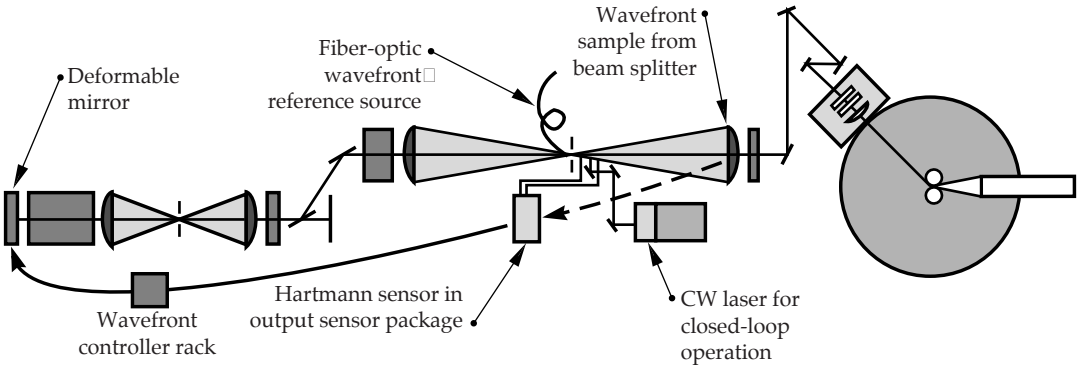


FIGURE 19. General location of the primary wavefront control components—the Hartmann sensor, the deformable mirror, and the wavefront controller. A diagnostic beam splitter immediately following the spatial filter output lens provides a wavefront sampling surface. (40-00-1097-2265pb02)

lenslet spacing and a spatial resolution of 43 mm when mapped into the 400-mm beamline aperture.

## Deformable Mirror

Each NIF beam includes a large-aperture deformable mirror for wavefront control in the main laser cavity. The required optical clear aperture is approximately 400 × 400 mm square. The mirror shape is determined by small push and pull displacements of 39 actuators spaced 74 mm apart on the back side of the mirror. After three deformable mirror designs were built and tested, including two from commercial sources, an LLNL design was judged to offer the best performance. Its PMN (lead magnesium niobate) actuators can be replaced in the event of failure, and the epoxy joints used to attach the actuators are protected from flashlamp light. The ceramic part of each actuator is kept under compression by preloading to minimize the growth of microcracks.

Figure 20 is a photograph of the prototype mirror built from the chosen design. It has a BK7 glass substrate with a hard dielectric coating having a reflectivity of ≥99.5% and a 1ω transmission of >0.2%.

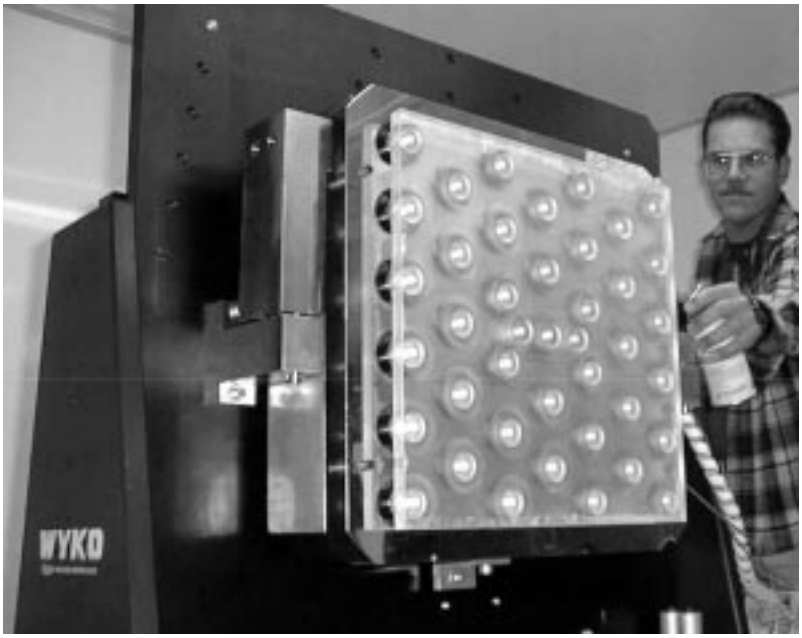


FIGURE 20. An LLNL 40- × 40-cm prototype deformable mirror has been successfully assembled and tested. (40-00-0499-0886pb01)

The transmission is required to allow viewing of centering references located behind each mirror.

When installed in the laboratory for testing, the LLNL prototype mirror had sufficiently low residual error at nominal drive voltages that response functions were readily measured, and subsequent modeling of the deformable mirror in a NIF beamline has used the measured functions. The mirror was also operated in closed-loop mode and was able to match the nominally flat interferometer reference mirror to within 0.3 $\mu$m peak-to-valley and 0.03 $\mu$m rms. Subsequently, with an aberrated optic in the beam to simulate some of the general features of a NIF beamline, the closed-loop system was able restore a flat wavefront to similar accuracy. Although additional testing will be done on the LLNL mirror, it is now considered to be NIF qualified.

Figure 21a shows the predicted long spatial-wavelength aberration of a NIF beamline resulting from a combination of thermal distortions of the amplifier slabs, inaccuracies in optics fabrication, alignment errors, optic distortions due to coating stress, and the bending of parts due to mounting and gravity effects. The properties of the focused 3ω spot that would result from such a wavefront were calculated using the extensive modeling capabilities developed for the NIF system over the last several years. The results are presented in Figures 21b and 21c. The beam focuses very poorly, with a 37-$\mu$rad spot radius required to include 80% of the beam energy.

When a deformable mirror with the measured characteristics of the LLNL prototype mirror is included in the beamline model as part of a wavefront correction system, the mirror assumes the shape of the surface in Figure 22a, and the focus characteristics change to those presented in Figures 22b and 22c. The 80% spot radius is reduced by more than 3.5× to 10.5 $\mu$rad, which means an increase in the focused fluence of more than an order of magnitude. Of course, system aberrations that have higher spatial frequencies than the deformable mirror can address will degrade this result, but the wavefront correction capability plays an essential role in achieving NIF performance goals.

## Wavefront Controller

The wavefront controller function is accomplished by systems that are modular at the eight-beam-bundle level. Each wavefront controller comprises computer hardware and software to periodically calibrate the associated Hartmann wavefront sensors and deformable mirrors, operate the automatic wavefront correction loops during preparations for a shot, and capture pulsed wavefront measurement data during a shot. In the moments immediately prior to a shot, the system is generally operated under closed-loop control to an

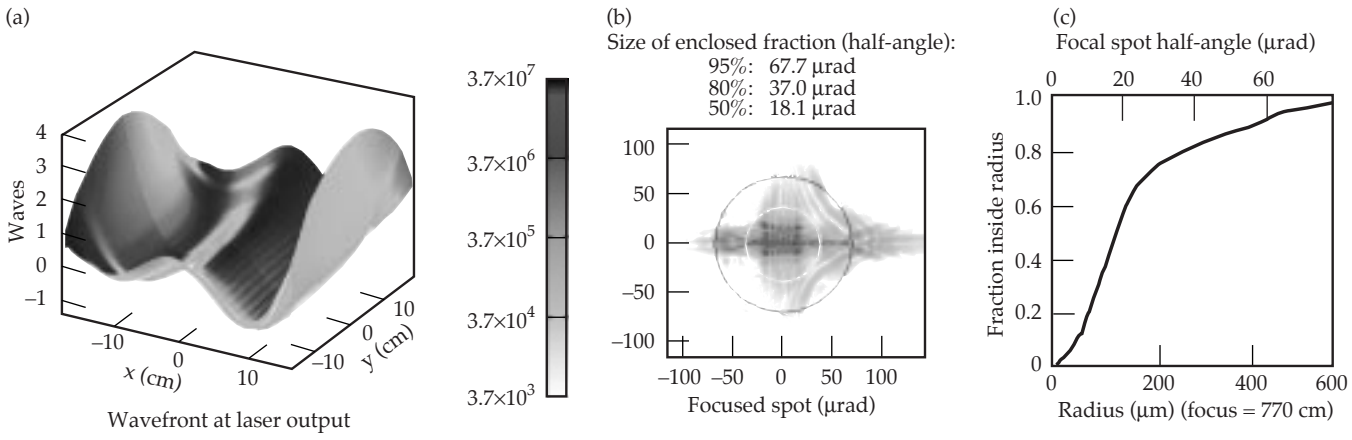


FIGURE 21. Performance of a NIF beamline is degraded by optical aberrations: (a) uncorrected output wavefront, (b) focal spot corresponding to these aberrations, and (c) radial distribution of energy. (40-00-0499-0884pb01)

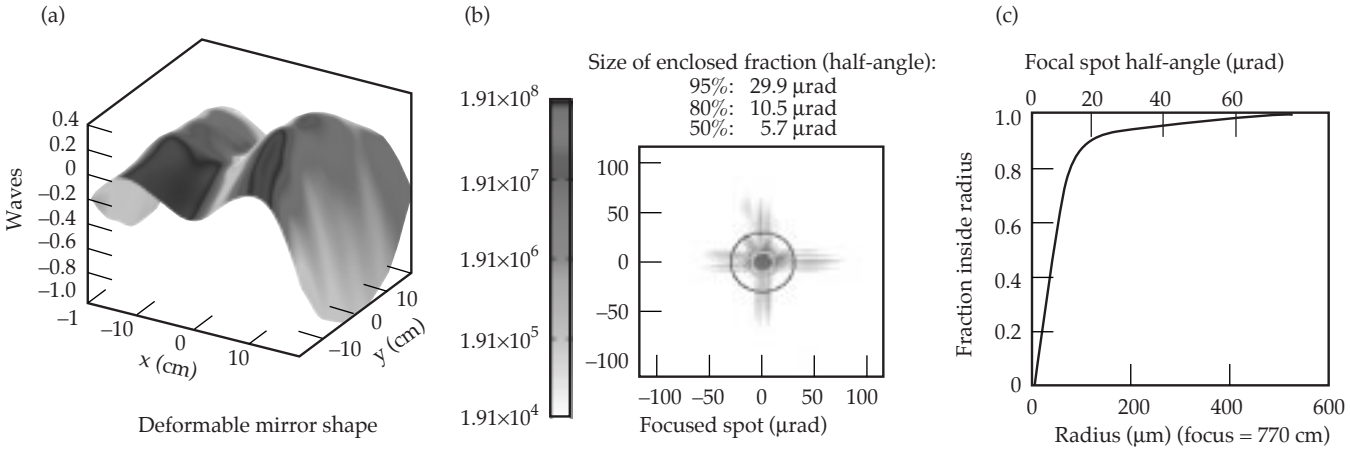


FIGURE 22. Performance of a NIF beamline when the wavefront correction system is in operation: (a) shape of the deformable mirror, (b) improved focal spot, and (c) radial distribution of energy. (40-00-0499-0885pb01)

offset wavefront value. This is because the flashlamp-pumped amplifiers introduce a dynamic wavefront change when they are fired, and the wavefront system must be set to anticipate that change.

Since the Hartmann sensor data is in video format, the controller incorporates image processing capabilities appropriate for recognizing and tracking the position of the 77 focused spots from each Hartmann image. The image processing code attains maximum accuracy by automatic adjustment of software parameters for gray scale and brightness. The controller also measures and applies the influence matrix for the deformable mirror actuators and the amplifier precorrection file in accordance with the mirror control algorithm. When operating in closed-loop, the controller is intended to maintain a closed-loop bandwidth of approximately 1 Hz on each beam.

The NIF wavefront controller hardware will use the VME industrial computer bus and multiprocessor architecture, which is designed to make maximum use of standard components and to accommodate replacement of modular elements as microprocessors and other computer electronics continue to evolve. The system will be attached to the integrated computer control system network using CORBA (see p. 21).

## Summary

All of the laser control systems have completed 100% design reviews, and we are proceeding with prototype testing, Title III design, and procurement. Activities are now shifting to completion of detailed drawings and ordering of production hardware. As this hardware arrives, it will be thoroughly tested before installation in the laser, switchyard, and target bays of the NIF facility. The beam control and laser diagnostics systems will be among the first to be activated so that their functionality can be used to control and monitor subsequent additions to each beamline. When NIF is completed, these systems will operate in conjunction with the integrated computer controls to provide the level of automatic operation that is essential for successful facility operation.

## Acknowledgments

The authors specifically acknowledge the significant contributions of the talented technology associates, technicians, and designers in beam control and laser diagnostics to the designs described above. In addition, because the NIF Project is now in its fifth year, the design has benefited from the efforts of some who are no longer on the staff, but whose contributions are not forgotten.

## Notes and References

1. Present baseline design uses a tapered cone on Pass #4 only preventing pinhole closure for a 20-ns pulse. Passes #1, #2, and #3 use stainless-steel washer-type pinholes.
2. The CSF pinhole wheel rotates to multiple precision set points to locate an alignment reticle, a selection of the shot pinholes, several optics inspection pinholes, or a 35-mm clear aperture.
3. The TSF pinhole wheel positions multiple shot pinholes or an 80-mm clear aperture.
4. Two insertable light sources mounted on a common translation stage provide references for beam alignment and wavefront calibration.
5. Insertable 45°reflector with attached dump for 3ω diagnostic beam is withdrawn from beam for alignment and optical inspection.

# Design and Performance of Flashlamp-Pumped Nd:Glass Amplifiers for the NIF*


*A. C. Erlandson* *C. Marshall* *M. Rotter* *O. Carbourdin*** *G. LeTouze***

*T. Alger* *E. Moor* *S. Sutton* *E. Grebot*** *X. Maille***

*J. Horvath* *L. Pedrotti* *L. Zapata* *J. Guenet*** *S. Seznec***

*K. Jancaitis* *S. Rodriguez* *J. Beullier*** *M. Guenet***


The National Ignition Facility (NIF) will use a 192-beam, 1.8-MJ laser for inertial confinement fusion (ICF) experiments.[1] A major laser component of the NIF, the flashlamp-pumped Nd:glass amplifiers must provide sufficient gain and stored energy to meet requirements for laser energy and power while adding minimal wavefront distortion to the laser beams. The NIF amplifiers differ from those used in previous ICF laser systems mainly in their overall scale and packaging. Figure 1 shows a two-slab-long, 4 × 2 NIF amplifier module, where the n × m designation denotes the number (height × width) of parallel amplifying channels or beam apertures that are combined. The NIF amplifiers use 40-cm-square apertures, which approximate the practical size limit imposed by amplified spontaneous emission (ASE) that depumps the laser slabs and limits gain. Large-aperture size reduces system costs by reducing the number of laser beams needed to produce the required energy on target. Previously, the largest amplifiers constructed were the 2 × 2 Beamlet amplifiers, which combined only four 40-cm-square apertures.[2]

Amplifiers with combined beams were first proposed by Lawrence Livermore National Laboratory (LLNL) in 1978 as a way of reducing the cost of MJ-class fusion laser systems.[3] Combining beams in a single enclosure reduces costs in three ways: (1) by making amplifiers more compact, thereby reducing the size and cost of the building; (2) by increasing pumping efficiency, thereby reducing the size and cost of the power-conditioning system; and (3) by reducing the number of internal amplifier parts. The NIF design achieves considerable cost savings by making the NIF amplifiers larger than the Beamlet amplifiers. Similar amplifiers will be used in the Laser Megajoule (LMJ), a 240-beam laser system now being developed and designed by the French Commissariat a l'Energie Atomique (CEA). Much of the development work for the LMJ amplifiers resulted from collaborative efforts between scientists and engineers at LLNL and the French CEA.

FIGURE 1. A two-slab-long, 4 × 2 NIF amplifier module. (70-00-0199-0056pb02)

*This article also appears in the Vol. 8, No. 4 issue of the *ICF Quarterly Report*; it is included in this issue for completeness.
**Commissariat a L'Energie Atomique (French Atomic Energy Commission)

This article describes the design and performance of the NIF amplifiers. First, we describe the NIF amplifier design. Next, we describe the prototype amplifier we tested and discuss the equipment used to measure its optical performance. We then compare model predictions with measurement results, and show performance predictions for the NIF amplifiers that are based on our test results and validated models.

# NIF Amplifier Design

## Pump Cavity Design and Performance

The NIF amplifiers provide optical gain at the 1.053-$\mu$m wavelength by using neodymium-doped, phosphate glass, rectangular laser slabs oriented at Brewster's angle with respect to the beam, to eliminate reflection losses. The slabs have absorbing glass edge claddings to prevent internal parasitic laser oscillation. Each slab holder supports four slabs, one stacked above the other. Central flashlamps cassettes pump slabs in both directions, while side flashlamp cassettes with large silver reflectors pump slabs in one direction. The glass blastshields between the flashlamps and the laser slabs serve three purposes: (1) they prevent acoustic waves generated by the flashlamps from propagating into the beam path and causing wavefront distortion; (2) they provide a contamination barrier between the flashlamp cavity and the critical slab cavity; and (3) they form one wall of the channel used for flowing cooling gas around the flashlamps. Figure 2 shows a plan view of a single NIF amplifier slab column that illustrates the arrangement of the slabs, flashlamps, blast shields, and reflectors.

The NIF amplifiers must meet requirements for gain, gain uniformity, wavefront distortion, and thermal recovery rate. High gain is required for the laser to meet its output energy and power requirements, especially because of the limited injected-energy from an affordable pulse generation system. At the same time, the amplifier must achieve its gain requirements efficiently to reduce the size and cost of the power-conditioning system used to drive the flashlamps. Accordingly, the NIF amplifiers use several features to increase efficiency. The side flashlamp arrays use silver reflectors

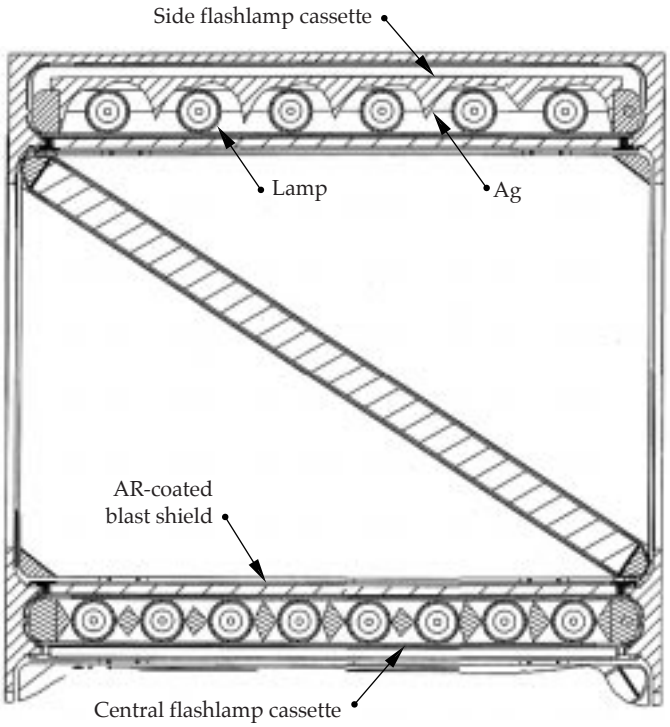


FIGURE 2. Plan view of the NIF amplifier pump cavity. (70-00-0199-0057pb02)

with involute reflector shapes. They are designed to reflect flashlamp light toward the laser slabs, while returning little flashlamp light back to the absorbing flashlamp plasma.[4] Compared with flat reflectors, the involute reflectors reduce the flashlamp electrical energy required to meet the gain requirement by ~15%. Additional reductions in flashlamp electrical energy are achieved by using sol-gel antireflective (AR) coatings on both sides of the blast shields (7%) and by preionizing the flashlamps with weak electrical pulses delivered several hundred microseconds before the main pulse (10%). Preionization causes the flashlamp arc to develop more uniformly, and it increases the electrical-to-optical conversion efficiency of the flashlamp plasma. Overall, the predicted storage efficiency of the NIF amplifiers is 3.8%, which is significantly higher than those in previous ICF lasers (3.0% and 1.8% for the Beamlet and Nova amplifiers, respectively).[2] Storage efficiency is defined as the total extractable energy stored in the laser slabs divided by the electrical energy delivered to the flashlamps.

In addition to the above criteria, we want the amplifiers to produce uniform gain distributions across their apertures, so that uniform beam output fluence can be readily obtained. Uniform output fluence is essential for maximizing output energy while maintaining acceptable optical damage risk. With significant gain variations, it becomes necessary to compensate by increasing the input fluence distribution in regions of the aperture with lower gain, as was done on the Beamlet laser. In large slabs, such as the 4.1- × 45.8- × 80.9-cm slabs used in the NIF amplifiers, the transverse gain uniformity is determined not only by the distribution of flashlamp light across the slab, but also by internal amplified spontaneous emission. ASE preferentially depletes gain near the slab's ends because this position has the longest path length for internal amplification.[2,5] The skewed diamond-shaped reflectors in the central flashlamp arrays reduce gain variations in the NIF pump-cavity design by directing flashlamp light preferentially near the slab ends.

We used a 3D ray-trace code to evaluate reflector shapes and to predict gain distributions across the aperture. The 3D code calculates pump rates for the neodymium-ion inversion by using a reverse ray-trace technique where rays were propagated backward from the point of interest in the slab to the flashlamp plasma. The ray-trace model tracked the change in the spectral content of each ray as it interacts with various reflecting and transmitting media present in the pump cavity. The absorption and reflectance properties of cavity components and the emission properties of the lamp plasma were determined experimentally.[6] Once the pump distribution was calculated as a function of flashlamp power, the peak gain-coefficient distribution was calculated by solving the differential equation for stored energy density as a function of time at each point in the slab. In addition to radiative and nonradiative spontaneous decay processes, the model also tracked spatially and temporally dependent ASE decay rates throughout the volume of the laser slabs. Both the physical assumptions in the model and the calculational techniques used in the computer programs that implement the gain model have been described in detail in earlier publications.[7,8,9]

Wavefront distortion is produced by waste heat deposited in the laser slabs by flashlamp pumping processes. Wavefront distortion has a prompt component that is caused by the flashlamp heating the laser slabs during the shot; it also has a residual thermal component that is caused by thermal energy remaining in the pump cavity from previous shots. The prompt component is primarily caused by the uneven heating of the two sides of the slab. This causes the slab to warp before the laser beam passes through the slabs when peak gain is attained.[10] Residual thermal distortions are caused by thermal gradients in the laser slabs themselves, as well as thermal gradients in the gas that is convectively heated by the laser slabs. The residual slab distortions, like the prompt pump-induced distortion, tend to be low order. The deformable mirror system now planned for the NIF is expected to correct the residual slab distortions. The gas distortions, however, have higher spatial frequencies and are more rapidly varying, making them difficult to correct.

To accelerate the recovery from residual thermal distortion, the NIF flashlamps will be actively cooled by flowing gas. Flashlamp cooling is effective because some 60% of the pump waste heat resides in the flashlamp envelopes immediately after a shot. Although water cooling has been successfully used to accelerate the shot rate of the OMEGA Laser at the University of Rochester,[11] gas cooling was chosen for the NIF to eliminate water-jacket tubes and to leave more room for efficiency-enhancing reflectors. NIF flashlamp cooling system will provide gas flow rates of up to 20 cubic feet per minute per flashlamp, with the gas flow direction alternating between flashlamp cassettes as shown in Figure 3. The inlet temperature of the cooling gas will be controlled over a ±5°C range centered about the ambient temperature with ±0.3°C accuracy.

We used several computer codes to calculate the wavefront distortion induced by flashlamp pumping processes. The prompt temperature rise, which was assumed to be proportional to the time-integrated local pump rate, was calculated using a 2D ray-trace code, which was a precursor to the 3D ray-trace code described above.[12] The residual temperature component was calculated using a finite-element heat transfer program, with starting temperatures set equal to values measured on a test amplifier shortly after firing the flashlamps.[13] The calculated temperature distributions were used as input for finite-element calculations of the deformation and stress in the laser slabs.[14] The final step in the calculation sequence was to use the calculated temperature, deformation, and stress distributions in a ray-trace algorithm to evaluate the optical path length variations across the aperture.[15] The effects of refractive index responses to temperature and stress were included in the calculations.

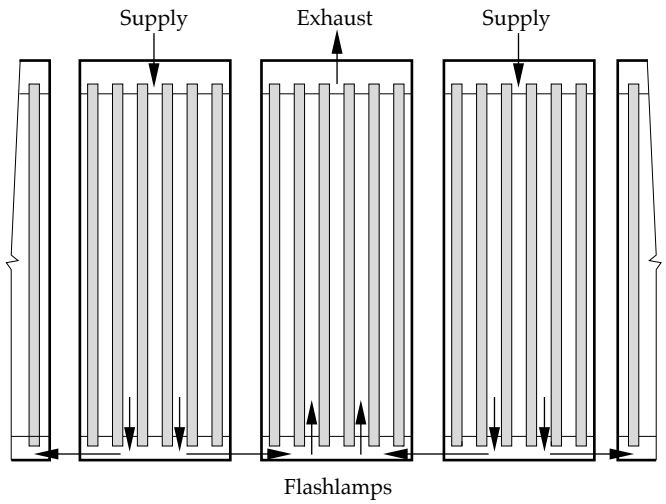


FIGURE 3. Alternating the direction of cooling gas flow through the flashlmp cassettes enabled us to put cooling-gas connections at the top of the amplifier, thereby simplifying the amplifier mechanical design. (70-00-0199-0058pb02)

## Mechanical Design

The large scale of the NIF amplifiers requires new mechanical designs that allow convenient assembly and maintenance. Accordingly, the NIF amplifiers use a modular design in which the most critical components, including the flashlamps, laser slabs, and reflectors, are mounted in line-replaceable units or cassettes that can be readily inserted or removed without disturbing their neighbors.[16] See Figure 4.

The design uses sealed maintenance carts that access the bottom of the amplifiers in order to install and remove flashlamp cassettes and four-high slab cassettes. The cassettes are inserted and removed from their enclosure, called the frame assembly unit, which is supported by top plates mounted to an overhead support structure. Plenums distribute electricity and cooling gas to the flashlamps from the top, through holes on the top plate.

Each NIF 4 × 2 beam bundle uses an 11-slab-long main amplifier that the beam passes four times, and a five-slab-long power amplifier that the beam passes twice. Assembly of these amplifiers begins in an off-line clean room, where the frame assembly units are cleaned and the top plates and blast shields with antireflective coatings are installed. A flashlamp-light-resistant polymer is used to bond the blast shields to a metal frame, and silicone inflatable seals are used to seal the metal frame to the inside of the frame assembly unit. These seals reduce leak rates between the flashlamp cavity and the slab cavity. After the blast shields have been installed, frame assembly units are bolted together to form 5- and 11-slab-long units that are

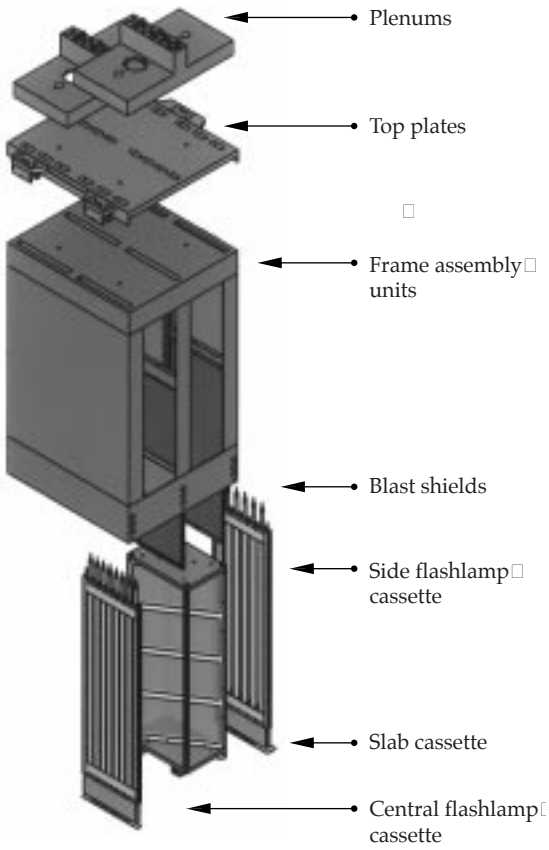


FIGURE 4. The NIF amplifiers use a modular design. (70-00-0199-0059pb02)

transported to the laser bay where they are mounted to an overhead support structure by their top plates.

The laser slabs, reflectors, and metal parts that comprise the slab cassettes are spray-cleaned and assembled in an elevated, class-100 clean room. We have to maintain high cleanliness levels because small particles resting on the laser slabs can cause damage when heated by flashlamp and laser light. Current specifications call for the laser slabs and metal surfaces to be maintained at cleanliness levels of 50 and 100, respectively. The levels correspond to particle-size distributions in which there are only one 50- or 100-$\mu$m particle per square foot of surface area, respectively. Following assembly, the slab cassettes are lowered into a specialized clean cart. Once the cart has been moved to the laser bay, it docks to the bottom of a frame assembly unit and establishes a hermetic seal to maintain cleanliness. After the top cover of the cart and the bottom cover of the frame assembly unit have been pressed together to trap residual particles, the cover pair is moved to the side to open a passageway for the slab cassette to be raised into the frame assembly unit. Rollers mounted in the corners of the cassette guide the cassette during insertion and prevent metal-on-metal rubbing, which generates particles. A fail-safe mechanism in the cart activates latches that hold the slab cassette in place. Slab cassettes can be removed for occasional refurbishment by reversing this installation process. Figure 5 shows a prototype slab cassette cart, which has successfully completed some 50 slab-cassette transfers in our laboratory. Similar carts will be used to install and remove the NIF flashlamp cassettes and blast shields.

FIGURE 5. The prototype slab cassette cart shown inserting a slab cassette into the NIF prototype amplifier. (70-00-0199-0060pb02)

## NIF Prototype Amplifier Design

We have built and tested a prototype amplifier at LLNL to validate key requirements prior to deployment in NIF. This prototype amplifier was extremely close to the NIF amplifier design, as it used the same size flashlamps and laser slabs and nearly the same reflector shapes. The prototype amplifier was slightly more compact in the direction transverse to the laser beam because the insertion clearances between the slab cassettes and the frame assembly units are smaller, and the blast shields are thinner. In addition, the prototype was slightly more compact in the direction parallel to the beam due to smaller gaps between frame assembly units. Ray-trace codes that we have developed to predict amplifier gain show that the differences in gain and storage efficiency between the prototype amplifier and the NIF amplifiers are negligible.

The prototype amplifier was tested as a one- , two- , and three-slab-long amplifier. Both the "diamond" and "X" configurations of the two-slab-long amplifier were tested. Amplifiers of different lengths were tested in order to infer the gain and wavefront distributions of the interior slab; this was important because the 5- and 11-slab-long NIF amplifiers have many interior slabs in addition to X and diamond end slabs. Figure 6 shows the diamond, X, and three-slab-long amplifier configurations we tested.

To measure temperatures at approximately 80 different locations inside the amplifier, we used thermocouples. They were placed on three laser slabs in one of the slab cassettes with holes drilled through the slabs to establish good thermal contact. Thermocouples were also placed on flashlamps, blast shields, and reflectors near the slab cassette. The purpose of the temperature measurements was to determine the initial temperature rise of the pump cavity components and to determine cooling rates after shots.

The laser slabs in the prototype amplifier were finished from LG-770 glass made by Schott Glass and LHG-8 glass made by Hoya. Both types of laser glass had Nd ion concentrations of $4.2 \times 10^{20}$ ions/cm$^3$. The flashlamps were made by EG&G and ILC Technology.

## Apparatus for Gain and Wavefront Measurements

We constructed an optical diagnostic system to perform time-resolved gain and wavefront measurements over the entire aperture of our prototype amplifier. Measurements were performed using a pulsed, injection-seeded, single-longitudinal mode, Nd:YLF probe laser operating at 1.053 $\mu$m. This laser produced 80-mJ, 20-ns-long pulses at a repetition rate of 13 Hz. The probe laser beam was expanded and image relayed by a series of telescopes. After passing through the amplifier once, the beam reflected back through the amplifier and telescopes a second time. After returning from the amplifier, a portion of the beam was sampled with a beam splitter and reflected to scientific-grade charge-coupled device (CCD) cameras for gain and wavefront measurements. Figure 7 shows a schematic of our equipment.

Amplifier gain distributions were determined by calculating the ratio of the images produced by two CCD cameras (the gain reference camera and the gain

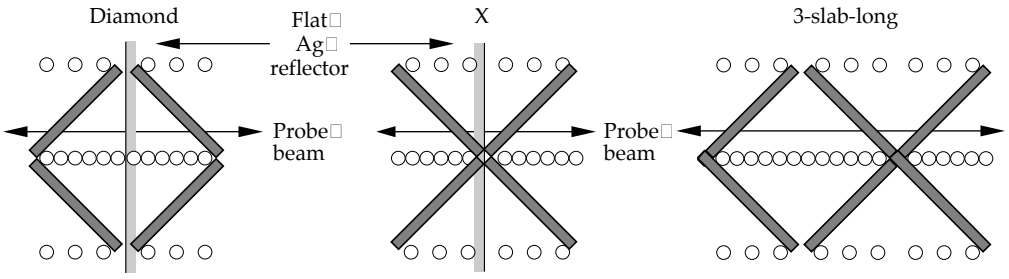


FIGURE 6. Plan view of the prototype amplifier in the diamond, X, and 3-slab-long configurations. (70-00-0199-0061pb02)

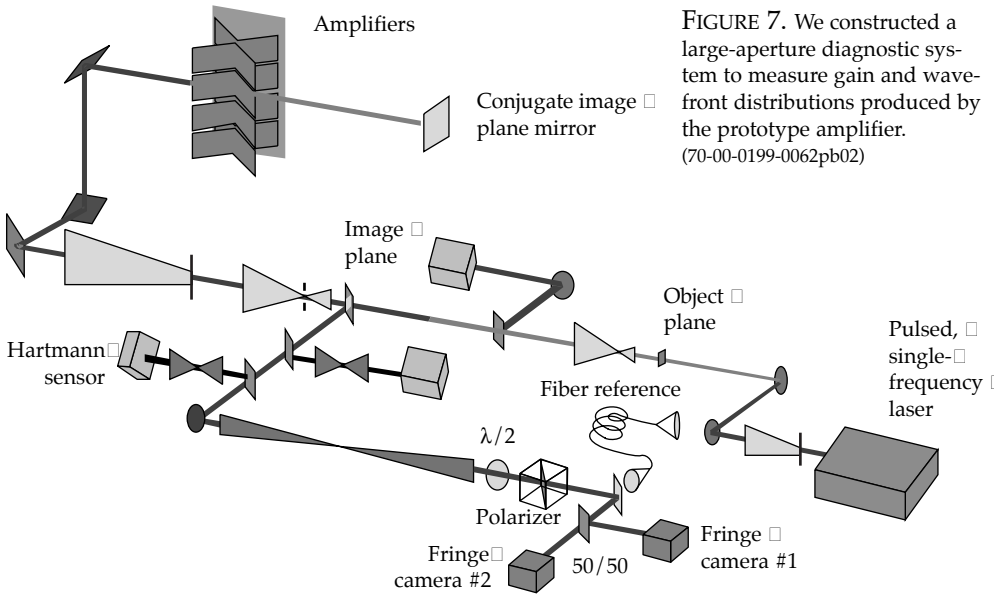


FIGURE 7. We constructed a large-aperture diagnostic system to measure gain and wavefront distributions produced by the prototype amplifier. (70-00-0199-0062pb02)

probe camera); they recorded the laser beam intensity before and after the beam passed through the amplifier. Measured background contributions from the flashlamp light and amplified spontaneous emission were subtracted from the gain camera image. A correction factor for passive transmission losses was determined by firing the probe laser without firing the amplifier flashlamps. Crosshair images were used to ensure proper registration of the gain and reference camera images.

Wavefront distributions were measured by interfering the probe beam with a reference beam, which was generated with an ~25-m-long single-mode optical fiber cut so that its optical length approximately matched the probe laser path length. To increase the fringe contrast ratio, a half-wave plate and a polarizer were used to attenuate the probe laser to approximately the same intensity as the reference beam. Two cameras were used to record interferograms on successive pulses of the 13-Hz probe laser. A Fourier-transform technique was used to calculate wavefront distributions from the interferograms.[17] We checked the calibration of the interferometer by measuring the wavefront of a known lens. From this check, we estimate the accuracy of our wavefront measurements to be ±0.02 waves rms, for both cameras. Prompt pump-induced wavefront distortion was determined by subtracting the wavefront measured at the time of peak gain from the wavefront measured 75 ms earlier.

## Measurement Results and Comparison with Model Predictions

Gain measurements were in close agreement with model predictions. For example, Figure 8 shows measured and predicted gain-coefficient distributions for the two-slab-long X configuration, with the flashlamp pulses close to the 34-kJ per lamp, 360-$\mu$s-long pulses anticipated for the NIF. Although the distributions in Figure 8 characterize the aperture next to the bottom, distributions measured in the other apertures were nearly the same, due to the vertical translation symmetry of the pump cavity. Gain was lower on the right-hand side of the aperture because the right-hand sides of both slabs were close to the ends of the amplifier where pump-light fluences were lower. Differences between the model predictions and measurements were less than 1% rms for all other combinations of apertures and configurations (diamond, X, and 3-slab-long). This agreement was achieved with a single value of the adjustable parameter used in the model to scale the flashlamp pumping rate.

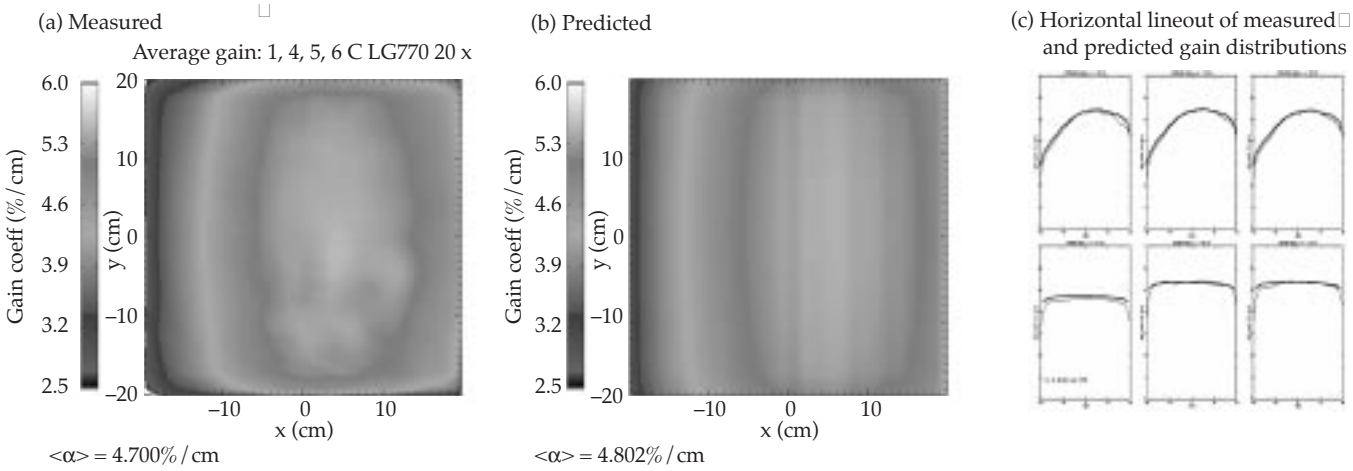


FIGURE 8. Measured and predicted gain distributions for the two-slab-long X configuration, with flashlamps energized with 34-kJ-per-lamp, 360-μs-long pulses. Measurements were made in the next-to-bottom aperture. (70-00-0199-0063pb02)

Prompt pump-induced wavefront distortion measurements were also in close agreement with model predictions. Figure 9 compares the measured and predicted prompt pump-induced wavefront distortion for the X configuration and for the standard flashlamp energy of 34 kJ/lamp. The results have been normalized to a single-slab pass. The close agreement between measurements and predictions was obtained using a scaling factor that adjusts the prompt temperature rise in the slab relative to the calculated pumping rate. Equally close agreement was obtained for other apertures and for time delays of up to 1 ms after the time of peak gain, using a single value for the scaling factor.

In addition to the optical characterizations, we also performed temperature measurements to determine the efficacy of the flashlamp cooling system. Figure 10 shows average slab temperature versus time after a flashlamp shot, for two cases: (1) with flashlamp gas set at ambient temperature; and (2) with the flashlamp cooling gas set 0.5°C below ambient temperature. Our data show that the average slab temperature recovers to within ~0.1°C of

FIGURE 9. (a) Measured and (b) predicted prompt pump-induced wavefront distributions for the two-slab-long "X" configuration, with flashlamps energized with 34-kJ-per-lamp, 360-μs-long pulses. Measurements were made in the next-to-bottom aperture. (70-00-0199-0064pb01)

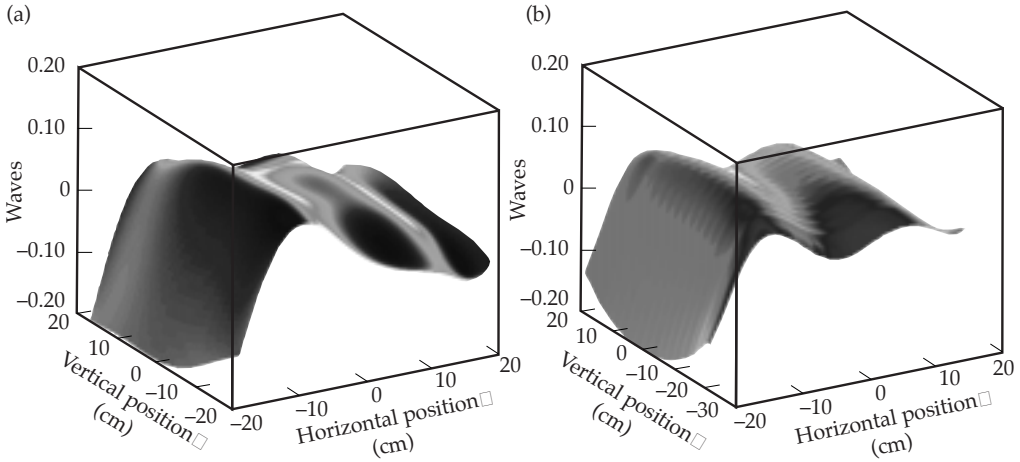

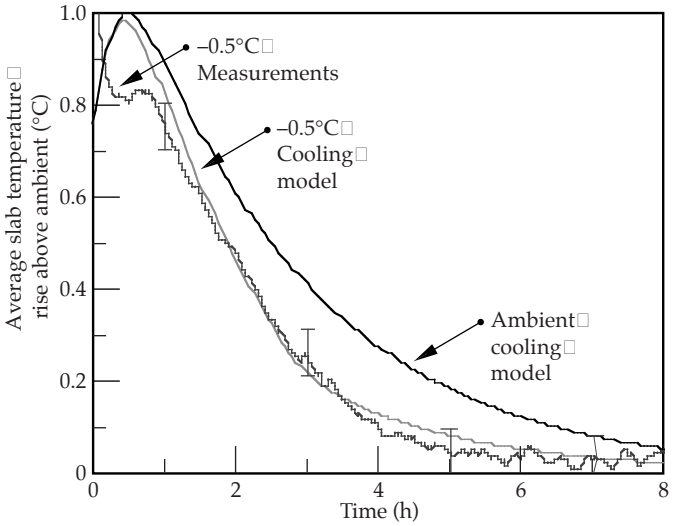


FIGURE 10. Using slightly chilled (–0.5°C) cooling gas accelerates slab thermal recovery rates. (70-00-0199-0065pb02)

the ambient temperature in about eight hours using ambient-temperature cooling gas, and in about four hours using slightly chilled gas. Measured gas distortions had high frequency components, with the rms amplitude varying linearly with the difference between the average slab temperature and the ambient temperature. Measured slab distortions were low order and recovered to less than 0.04 waves (peak-to-valley) per slab per pass within 3–4 hours after each shot. This measurement is consistent with the magnitude of the slab distortions, which we expect to correct with a deformable mirror on NIF.

## Performance Predictions for the NIF Amplifiers

Figure 11 shows the beamline-averaged gain-coefficient distribution for a NIF laser beam, predicted by our validated 3D ray-trace code. The code took into account several features of the NIF amplifiers that were different from the prototype amplifier: protectively coated Ag reflectors with stable, higher reflectances; improved, two-layer sol-gel antireflective coatings on the blast shields; use of equal numbers of LG-770 and LHG-8 laser slabs; and slight reflector-shape differences. The predicted aperture-averaged gain coefficient was 5.3%/cm, and the distribution shows the expected gain roll-off near the edges due to ASE. Propagation code modeling of the NIF beamline shows that the gain has sufficient magnitude and uniformity for the NIF laser to meet its beam power and energy requirements. To achieve a uniform output fluence distribution and maximum beam output energy, however, the input fluence distribution of the injected laser beam has to be tailored to compensate for the anticipated gain variations.

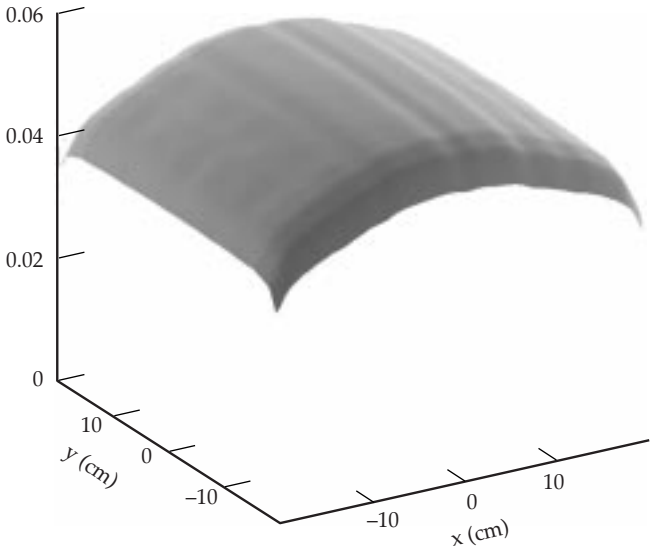


FIGURE 11. NIF beamline-averaged gain-coefficient distribution predicted with the 3D ray-trace code. (70-00-0199-0066pb02)

Figure 12 shows the total prompt pump-induced wavefront distortion for a NIF beamline, predicted with our codes using the source-term scaling factor derived from AMPLAB experiments. The distribution is a low-order "M" shape, with a peak-to-valley value of 5.9 waves. This distribution possibly overestimates the prompt pump-induced wavefront distortion that the NIF beamlines will actually produce, because it is conceivable that stray flashlamp light may have distorted the optics, which are part of the diagnostic. Nonetheless, the predicted distortions are within the range that now appears to be largely correctable with the NIF deformable mirror.

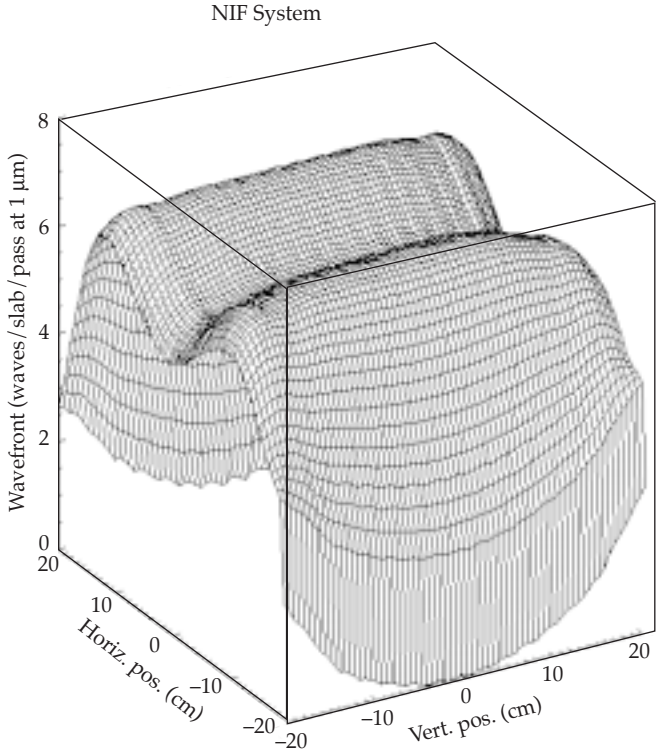


FIGURE 12. NIF beamline prompt pump-induced wavefront distortion predicted with ray-trace and finite-element codes (70-00-0199-0067pb02)

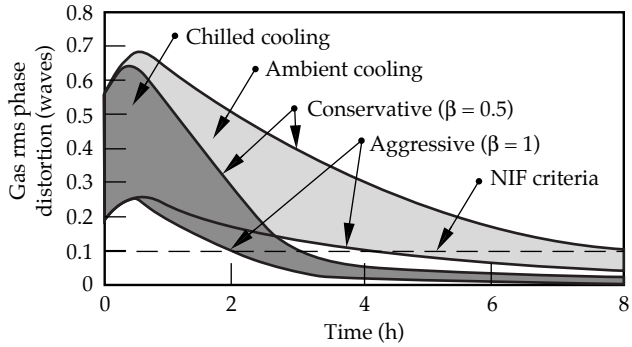


FIGURE 13. Predicted gas-distortion phase distrubances in NIF for ambient and chilled gas cooling. Aggressive and conservative assumptions are used to bracket the problem. (70-00-0199-0068pb02)

To estimate the effect of the gas distortions on the NIF laser beams, we scaled the gas distortions measured on the prototype amplifier to account for the greater path length and greater number of slabs in the NIF amplifiers. In addition, we used a beam propagation code to calculate the beam focal spot. Our estimate shows that the gas distortions will meet the NIF requirement (less than 5 $\mu$rad added beam divergence) within 3 hours after the shot, provided the temperature of the flashlamp cooling gas is ~1°C below the ambient temperature. Figure 13 shows model results for flashlamp cooling with gas at ambient temperature and at 1°C below ambient temperature. The conservative and aggressive estimates correspond to scaling the AMPLAB results by length (for aggressive estimates) and by number of laser slabs (for conservative estimates).

## Conclusion and Summary

Advances in amplifier technology developed for the NIF include a modular design and bottom-access carts to improve maintenance; features to improve storage efficiency that reduces the size and cost of the power conditioning; and active gas cooling to accelerate the laser shot rate. Further, gain, wavefront, and thermal recovery measurements performed on the NIF prototype amplifier are consistent with meeting NIF performance requirements.

## Acknowledgments

We thank numerous contributors to our design, analysis, and experimental efforts: Richard McCracken, Charles Petty, Lawrence Smith, Alex Drobshoff, Ian M. Thomas, John Trent, Drew Hargiss, Randy Aceves, Jerome Hall, Rene Neurath, Joe Smith, Wil Davis, Jean Marie Morchain,* Beatrice Bicrel,* Patrick Manac'h,*

Thierry Adjadj,* Gary Ross, John Toeppen, Larry Morris, Jean Lobit,* Douglas Swort, Ronald Bettencourt, Michael Weddle, Loretta Kleinsasser, Dzung Nguyen, John H. Campbell, Daniel Walmer, William Steele, Jerry Britten, Curly Hoagland, Gregory Rogowski, Steve Letts, Cindy Alviso, Irving Stowers, Joe Menapace, Douglas Larson, Scott Hulsey, Phil Test, Steve Fulkerson, George Pollock, Andy Hinz, Anthony Lee, Janice Lawson, Wade Williams, Mark Newton, Ken Manes, Richard London, Yuri Zakharenkhov, Peter Amendt, Jean-Francois Mengue, Fabrisse Laniesse,* John Hunt, John Murray, Richard Hackel, Jeff Paisner, Steve Payne, and Howard Powell.

*Commissariat a L'Energie Atomique (French Atomic Energy Commission)

## Notes and References

1. W. H. Lowdermilk, *Second Annual Conference on Solid State Lasers for Application to Inertial Confinement Fusion*, in *Proc. SPIE*, Bellingham, WA, Vol. 3047, p. 16–37 (1997).
2. A. C. Erlandson, M. D. Rotter, D. N. Frank, and R. W. McCracken, *ICF Quarterly Report* **5**(1), 18–28, Lawrence Livermore National Laboratory, Livermore, CA, UCRL-LR-105821-95-1 (1995).
3. W. F. Hagen, *Laser Program Annual Report–1977*, Lawrence Livermore National Laboratory, Livermore, CA, UCRL-50021-77, pp. 2-228 to 2-231 (1978).
4. W. T. Welford and R. Winston, *High Collection Nonimaging Optics,* Academic Press, New York, NY, p. 266 (1989).
5. A. C. Erlandson, K. S. Jancaitis, R. W. McCracken, and M. D. Rotter, *ICF Quarterly Report* **2**(3), 105–114, Lawrence Livermore National Laboratory, Livermore, CA, UCRL-LR-105821-92-3 (1992).
6. H. T. Powell, A. C. Erlandson, and K. S. Jancaitis, Conference on Flashlamp-pumped Laser Technology, in *Proc. SPIE*, Bellingham, WA, Vol. 609, pp. 78–94 (1986).
7. H. T. Powell, A. C. Erlandson, K. S. Jancaitis, and J. E. Murray, *High-Power Solid State Lasers and Applications,* in *Proc. SPIE,* Bellingham, WA, Vol. 1277, pp. 103–120 (1990).
8. K. S. Jancaitis, S. W. Haney, D. H Munro, G. LeTouzé, and O. Cabourdin, in *Proc. SPIE*, Vol. 3047, pp. 106–111 (1997).
9. G. LeTouzé et al., "3-D Gain Modeling of the LMJ and NIF Amplifiers," *Solid State Lasers for Application to Inertial Confinement Fusion*, Third International Conference 1998 (to be published).
10. J. E. Murray, W. F. Hagen, and B. W. Woods, *Laser Programs Annual Report*, UCRL-50021-82, Lawrence Livermore National Laboratory, Livermore, CA, p. 7–72, (1982).
11. J. H. Kelly, M. J. Shoup III, M. D. Skeldon, and S. T. Bui, *Solid State Lasers III*, edited by G. J. Quarles, in *Proc. SPIE*, Bellingham, WA, Vol. 1627, p. 252–259 (1992).
12. G. LeTouzé, O. Cabourdin, J. F. Mengue, M. Rotter, and K. Jancaitis. "Shaped Reflectors for Pump Cavities," *2nd Annual Conf. Solid State Lasers for Application to ICF*, Limeil, France (1996).
13. A. Shapiro, *TOPAZ3D—A 3-D Finite Element Heat Transfer Code*, UCID-20484, Lawrence Livermore National Laboratory, Livermore, CA (1985).
14. B. N. Maker, *NIKE3D—A Nonlinear, Implicit 3-D Finite Element Code for Solid and Structural Mechanics*, UCRL-MA-105268, Rev. 1, Lawrence Livermore National Laboratory, Livermore, CA (1995).
15. S. Doss and R. Gelinas, *Laser Program Annual Report*, UCRL-50021-86, Lawrence Livermore National Laboratory, Livermore, CA, p. 7–132 (1986).
16. A. C. Erlandson et al., *Second Annual Conference on Solid State Lasers for Application to Inertial Confinement Fusion*, in *Proc. SPIE*, Bellingham, WA, Vol. 3047, p. 16–37 (1997).
17. M. Takeda, H. Ina, and S. Kobayashi, *J. Opt. Soc. Am.*, **72**, 156–160 (1982).

# NOVA UPDATE
# OCTOBER–DECEMBER 1998

Nova Operations performed 216 experiments, which surpassed our goal for the quarter. These experiments supported efforts in Inertial Confinement Fusion (ICF), Defense Sciences, university collaborations, Laser Science, and Nova facility maintenance.

The process of planning the decommissioning of the Nova facility continued. In December, a notice appeared in the *Commerce Business Daily* to advertise the availability of Nova components. After the February 1999 deadline for proposals, a committee organized by the Department of Energy will determine the disposition of Nova components. It has already been decided that parts of Nova will be reused in the National Ignition Facility (NIF). For example, inspections have indicated that the FR5 rotator glass in the Nova Faraday rotators meets the specifications required for use on NIF.

The Petawatt project continued to innovate with the installation of a preformed plasma beamline. The center 15 cm of Beamline 8, which is unused by Nova, is already being used as a 4ω probe in the ten-beam target chamber. Hardware was installed in December that will permit this beam to be diverted to the Petawatt target chamber to create a preformed plasma in which the Petawatt beam will interact.

Hardware was installed and tested to allow the use of cryogenic targets in the Nova ten-beam target chamber for equation-of-state experiments that will be conducted next quarter. The ten-beam experiments will follow the two-beam cryogenic campaign, which served to map out the single-shock Hugoniot for deuterium from 200 kbar to 3 Mbar. The NIF will use multiple shocks to compress the hydrogen fuel to much higher density than can be achieved with a single shock, and there is no fundamental theory that allows us to calculate a priori what shock compression will be achieved for a given drive. In the cryogenic ten-beam experiments, we are developing diagnostic capability to tune multiple shocks for NIF ignition implosions and measuring the equation of state of hydrogen after two shocks. We are also simulating the plasma conditions that will occur in a NIF hohlraum with cryogenic dense He–H gas.

# National Ignition Facility Update October–December 1998

## Overall Assessment

Overall progress on the NIF Project remains satisfactory for the first quarter of FY99. The current top-level assessment of Project status remains similar to that stated at the end of the fourth quarter 1998: that there will be no change to the fourth quarter 2001 Level 2 milestone for the End of Conventional Construction, nor to the fourth quarter 2003 Project Completion date. However, the NIF Project Office now anticipates that based upon the status of Conventional Facilities, CSP-4, work on the Laser Bay Core, and the status of Special Equipment design and procurement, there could be an impact of 6 to 8 weeks in the fourth quarter 2001 completion of the Level 4 milestone for start-up of the first NIF bundle. The impact of current field conditions on this important milestone, which is to be completed in three years, continues to be evaluated on a weekly basis.

The first quarter 1999 was a productive quarter on the NIF site as the total Conventional Facilities work completed approached 42%. With the completion of Phase I work by Nielsen Dillingham Builders (NDBI), CSP-4, in December, the coordination between prime subcontractors on site has been reduced significantly. Hensel Phelps (CSP-9) now has unrestricted access and sole occupancy of the Laser Building. NDBI (CSP-6/10) has sole possession of the Target Building, and NDBI (CSP-5) has sole possession of the Optics Assembly Building (OAB). Coordination of access to the work areas, laydown space, and coordination of interface between subcontractors in the OAB Corridor are now the focus of the overall site coordination.

In Special Equipment, overall progress is satisfactory. Ten 100% reviews were conducted in the quarter, bringing the total percentage complete to 89%. In addition to the ongoing work to close out the Special Equipment design reviews and the continuation of procurement efforts, an expanded effort has been under way in the planning area. The primary focus is improving the ability to summarize the Integrated Project Schedule (IPS), providing easier methods to focus on particular areas or functions, and validating the installation logic. In addition, all Special Equipment procurement contract awards greater than $100K in the NIF Planning System must have equivalent contract milestones in the IPS. The Special Equipment part of the IPS has been reviewed and updated to ensure this compliance.

In Optics, facilitization is complete at Hoya and Schott with all contracts placed and pilot activities already started. Hiring and training for pilot runs is mostly completed. Both laser glass vendors are doing a great job in supporting the NIF schedules. The Zygo facility was completed in first quarter 1999 and first-bundle optics (LM3) are now being shaped. Pilot production contracts were finalized at two potassium dihydrogen phosphate (KDP) vendors and the first pilot runs were started, and six 1000-L crystallizers continued to operate at Lawrence Livermore National Laboratory (LLNL).

Key Assurance activities to support the Project are all on schedule, including construction safety support, litigation support to the Department of Energy (DOE) for the settlement of 60(b) (e.g., quarterly reports), and the *Final Safety Analysis Report* (FSAR).

At the end of FY98 there were 10 of 95 DOE/OAK (Oakland Office) Performance Measurement Milestones remaining to be completed, and by the end of first quarter 1999, were completed. The only remaining FY98 milestone is the "Cooling Towers Operational," which will be accomplished, as projected last quarter, in March 1999.

The FY99 DOE/OAK Performance Measurement Milestone plan includes 124 milestones. In the first quarter 1999, 11 milestones were due, and seven were completed. The cumulative variance for FY99 is four milestones. It is anticipated that two of the open first-quarter 1999 milestones will be completed in January and the remaining two in February.

In Special Equipment, three 100% reviews were conducted in October including Alignment Control, Target Area Alignment, and Final Optics Assembly. Two 100% reviews were conducted in November, including Wavefront Control Systems and Roving Mirror Diagnostic Enclosure. Five 100% reviews were conducted in December including Electronic Rack Cooling, Timing System, Pulse Generator Alignment, Precision Diagnostics, Laser Optics Damage Inspection, Roving Mirror and Roving Assemblies.

Table 1 lists Engineering Change Requests (ECRs) that were resolved by the Level 4 and Level 3 Change Control Boards during the quarter. No ECRs were over $250K. The cost impact of these ECRs and all other changes (i.e., Cost Transfer Requests) are reported in the change log at the end of each quarter. Schedule impacts are described in the individual ECRs. There are no impacts to any Level 0, 1, 2, 3 milestones.

In system integration, the following accomplishments were achieved during the first quarter 1999.

- Final preparations were completed for the design review of the rack cooling system in December, and detailed preparations began for the overall cable plant design review. Development of interface control documents (ICDs) defining cable plant requirements made some progress, but was not completed as required. Preparations for procurement of electrical racks and cable plant also continued.
- Precision Survey staff is completing the applicable Design Basis Book templates in preparation for the design review. Working reviews have been scheduled to review the draft and final viewgraphs and Design Basis Book inputs. Integrated Contractor Orders (ICOs) are being placed with Argonne, Fermi, and Lawrence Berkeley to fund their attendance and participation in the review. Stanford Linear Accelerator Center (SLAC) is already funded under an existing ICO.

TABLE 1. ECRs resolved by the Level 4 and Level 3 Change Control Boards during the first quarter 1999.

| ECR | Title | Resolution |
|---|---|---|
| 325 | Replacement of TBD in Angular Positioning | Approved |
| 337 | Increase Size of TB Fire Sprinkler Ring | Approved |
| 298 | SDR 003 Title II Update | Approved |
| 209 | SSDR 1.8.7 Rev. D from C - FOA | Approved |
| 344 | SSDR Changes for Beam Control and Laser Diagnostics | Approved |
| 376 | Additional Laser Bay Embedded Grounding Plate | Approved |
| 402 | Revise Conduit Routing to MOR Panel | Approved |

- All cable tray design and length drawings for the Laser Bays are complete except for the preamplifier support structure (PASS) area. These drawings are being recorded in the Project Database Management (PDM) system. The PASS structure area design effort began in December. Switchyard cable trays for 0′0″, 50′, and –21′9″ levels are complete. The 7′10″ level has been completely modeled to determine possible interference problems, but final tray layouts have not been completed.
- The Special Equipment rack cooling Design Review was presented in December. Comments and considerations offered at the Design Review are being discussed, and points of concern are being addressed. Heat exchanger fans have been ordered for planned lifetime tests. Reliability, availability, and maintainability (RAM) analysis efforts have begun to determine the reliability figures for the overall design. A letter of intent has been mailed to five vendors; no responses have been received at this time.

## Site and Conventional Facilities

Despite the holidays, December was another busy and productive month on the NIF site as the total Conventional Facilities work completed approached 42%.

With the completion of Phase I work by NDBI, CSP-4, in December, the coordination between prime subcontractors on site has been reduced significantly. Hensel Phelps (CSP-9) now has unrestricted access and sole occupancy of the Laser Building. NDBI (CSP-6/10) has sole possession of the Target Building, and NDBI (CSP-5) has sole possession of the OAB. Coordination of access to the work areas, laydown space, and coordination of interface between subcontractors in the OAB Corridor are now the focus of the overall site coordination.

The decision to close up the hold-opens along grid 28 and at the capacitor bays, after the laser bay mat slabs are poured, will allow a significant amount of work to be completed this winter that was originally scheduled for next winter. Most of the girts and siding, plenum wall, and rack piping work can now be completed before turning each laser bay over to Special Equipment forces.

The Laser Building core continues to be the area of the project where the schedule delays are the major concern. The cast-in-place concrete walls and roof in the core from Grid 12 to 14 are scheduled to be completed in January (see Figure 1.) The installation of the air handlers between Grid 12 and 14 are the first units that must be placed in the Laser Building, and until these units are placed, the remaining units cannot be installed. Unfortunately, these air handlers contain the largest fans, which to date have not met the specified requirements for vibration testing.

Laser Bay 2 overhead and underground work has progressed well and is basically back on schedule. Laser Bay 1 is getting off to a slow start but should be completed faster than originally planned based on the experience from Laser Bay 2. Capacitor Bay 4 slab on grade placement and fine grading of Capacitor Bay 2 and 3 slabs were completed in December, which will open up significant areas for overhead rough-in to start. The building is dried-in to the extent possible considering the hold-opens required, and the site is ready for the upcoming winter weather.

FIGURE 1. Reinforcing for the concrete walls in the Laser Building mechanical mezzanine.
(40-60-1198-2218#5Apb01)

The OAB is on schedule (see Figure 2), and the variances in the Target Building will be remedied when NDBI concentrates its resources on the critical areas of the building.

## Laser Systems

The past quarter represents a shift in the emphasis for most of Laser Systems from design to procurement. Several large procurement actions were initiated (Frame Assembly Units [FAUs] and plasma electrode Pockels cell [PEPC] assembly fixture), and documentation was prepared for numerous others (flashlamps and main capacitor charging supplies, for example). Subsystem prototype testing continued to provide valuable information for value engineering and procedure development as well as design validation. Detailed planning documentation was completed for FY99.

- Oscillator stability measurements at the input to the Regenerative Amplifier were completed using prototype optical pulse generation (OPG) hardware. The results show an rms instability of 3.1%, compared with 5% required. However, these tests do not include the smoothing by spectral dispersion (SSD) modulator, which is expected to increase the instability. The high-frequency variations are due to the unstabilized laser relaxation oscillations as well as contributions from other components. A feedback control loop is being fabricated to suppress these. The low-frequency variation is a result of several sections of polarization-maintaining fiber in the system that have a polarization-state temperature dependence. This slow variation will be minimized with the polarizing fiber system in the design for the NIF. This prototype oscillator system has been used during the past quarter to conduct integrated tests including the oscillator and preamplifier module (PAM). The PAM was operated over a range of output energies spanning 0.07 to 22.1 J in a spatially shaped beam. This surpasses the energy performance requirements for the NIF system. Future tests will include SSD, steady-state operation, and demonstration of the temporal pulse-shaping capabilities of the integrated Master Oscillator Room (MOR)/PAM system. The drawings for the long-lead preamplifier beam transport components were completed and checked during the past quarter and are in the process of being procured for the integrated testing scheduled for late this calendar year.
- The amplifier effort remained on schedule during the first quarter of the Title III effort. Two large amplifier procurements were issued for bids in November as planned: frame assembly units (FAUs) and the Euclid alignment system. Bids are currently under evaluation for the FAU procurement. The amplifier team has also made progress in developing an improved correlation between observed cleanliness levels in the amplifier and component processing. This effort will lead to improved cleanliness procedures and component cleanliness specifications for the NIF amplifier.
- The PEPC assembly fixture was procured during the past quarter, and the parts have arrived at LLNL. The fixture will be assembled for functional tests beginning in January. A value-engineering effort was initiated in an attempt to simplify and reduce the cost of the PEPC line-replaceable unit (LRU) and controls

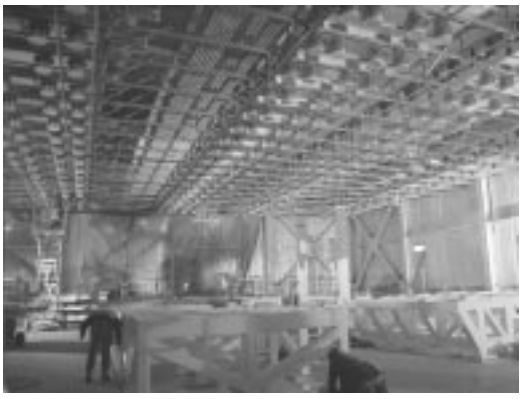

FIGURE 2. Optics Assembly Building interior, showing special equipment installation at floor level and duct work at the ceiling level. (40-60-1198-2279#15Apb01)

hardware. Several cost-reducing and reliability-enhancing features have been evaluated on the prototype cell during the past quarter. Examples include a smaller, lower-cost vacuum pump, circuit boards to mount electrical components on the LRU housing, a cold-cathode vacuum gauge to replace the hot cathode ionization gauge, and numerous improvements in the controls design and packaging. Procurement packages are currently being prepared for the PEPC LRUs for the first bundle.

- The primary focus of the power conditioning effort over the past quarter was validating the design of the power conditioning system module through testing of the first-article prototype at Sandia. Over 7000 shots have been accumulated to date. Data indicates that the module meets specifications when firing into the resistive dummy load, and simulations predict performance will meet requirements when driving flashlamps. The lifetime tests uncovered problems with the design of the commercially available energy dump resistor, which will be corrected in the NIF design. Analysis of the several catastrophic failures revealed problems with the design of the module enclosure. The design is being modified to contain any shrapnel associated with electrical faults, while reducing the pressure pulse contained within the enclosure. Capacitor qualification tests are now under way with samples from four suppliers. Tests have now been completed on at least five samples from each supplier.

## Beam Transport System

Fabrication contracts proceeded into full production, and first deliveries of finished structures have arrived at LLNL. The Switchyard 2 structure contract was awarded, and the Laser Bay concrete request for proposals (RFP) was released for bid. In the next quarter, a convoy of truck-borne structures and vacuum vessels will begin to arrive at LLNL and occupy the staging areas. Remaining design activities are nearing completion. The intensity and level of detail of installation planning will continue to increase.

- Production and shipment of all spatial filter stainless plate is complete. Vacuum vessel fabrication of end vessels is proceeding at Ranor. Fabrication and welding of the first four vessels is complete and awaiting the start of machining. Fabrication of weldments is progressing on schedule with the next group of four vessels. Stadco work on the center transport spatial filter (TSF) has the first vessel in machining and the second vessel in finish welding. The first vessel completion is expected in March, and the final unit is scheduled in late May. March metal work on the center cavity spatial filter (CSF) has the first vessel at Allied for machining, and the second vessel is in final welding.
- Initial design development and detailing is complete on the Laser Bay interstage docking frames of the spatial filter (SF) end vessels. Engineering review and design checking is progressing with the assistance of personnel from the newly integrated Infrastructure Group. Completion of design, engineering, analysis and specifications is in progress to support procurement review and release in February.
- Review of the drawings for the Vacuum System was completed, and required changes are in progress. It is expected the drawings will go into PDM by the end of February. Development of the Beam Transport System vacuum control screens has begun.
- Tests were completed on a method of precisely controlling pressure in the amplifier slab cavities. This method used weight balanced on top of a flexible bellows to maintain even pressure. Results showed that there is too much spring in the bellows to meet the delta-P requirements. Test equipment is being retooled for another candidate method.

- The Switchyard 2 structure procurement RFP was issued for bid. All prospective contractors attended a prebid conference and construction site visit at LLNL. The contract was awarded in December to AGRA Coast Ltd. in Vancouver, BC. The design team is now continuing on Switchyard 1 drawing details. Switchyard 1 is similar, but not identical to Switchyard 2. A completely new set of drawings is required, equivalent in size to the Switchyard 2 set.
- The Laser Bay concrete pedestal support structure design drawings and analyses are complete. The specification is completed and has been incorporated into the bid package that has been sent out to the bidders. A bidders site visit has been scheduled for January. Trial assemblies were accomplished on all power amplifier lower structures, which were subsequently shipped to LLNL.
- The transport mirror mount design validation team made good progress toward resolving the Title II action item regarding the mounting-induced wavefront effects of transport mirrors. Preliminary analysis of a new design approach was completed in October. Hardware for the new design was received in mid-November; and assembly of the test mirror in the mount began. Testing of the new mount then began in December The effect of gravity- and mount-induced aberrations (predicted from detailed finite-element analysis) on propagation for six beamlines was assessed. The combination of finite-element analysis and beam propagation analysis indicates that the new design will meet the requirements for laser system performance. The interferometric measurements under way are intended to validate the finite-element analysis. Preliminary results are encouraging, but show discrepancies that are not fully understood. Additional on-line and off-line tests were done in late December (and planned to continue during January) to resolve these discrepancies.

## Integrated Computer Control System

All baseline Title II design reviews, concluding with the 100% review of the Integrated Timing System in December, are complete. "Nightlight," the first of seven planned incremental releases of control system software, is complete. Nightlight was a confidence builder. The engineering team felt that they gained crucial experience and that the release successfully met planned goals. Independent testing of the software has also been completed. Sixty-nine test incidents were reported, of which twenty-one are categorized as software defects; the testing program is proving its worth at improving the quality of NIF software. The contract for the design and fabrication of the timing distribution subsystem was placed.

- Seven incremental releases of software (the "Light" series) are planned during NIF construction. A repeatable engineering process is used within each stage to ensure that the product is being correctly built and meets requirements. To begin the cycle, a portion of the product's requirements is selected for implementation. Each release will be measured against this documented set of goals. As the release is delivered, a demonstration is held, and the source code is placed under configuration management. The software is then subject to a 6-week period during which it is formally tested by the independent test team, which also provides for "ad hoc" testing by additional users. Defects that are found result in test incidents that are traced to determine the root cause. A thorough assessment of results and the engineering process is made and documented by the implementation teams. Targeting specific goals, a software implementation plan is written for the next release, which also estimates work needed in future increments. Measurements are taken on the source code, package count, and number of public methods in order to assess software complexity and rate of progress. Using this incre-


UCRL-LR-105821-99-1

mental process, a new part of the NIF software is delivered about every six months. After each release, the results are analyzed to determine corrective actions.

- The Nightlight software delivery and test are complete. In a few cases, some software tasks were deferred until the next release so that assessment and planning for Penlight could be completed for maximum benefit. Nightlight testing goals were to verify that planned features operate as expected, to establish an independent test process, and to develop the repeatable processes by which the development and independent test teams could effectively work together. Nightlight established testing activities consistent with industry standards, including: test readiness reviews, implementation of a test incident tracking system, adoption of standard software defect severity levels, standardization of documentation methods for test procedures and checklists, and configuration management of test products such as procedures and results.
- The planning process for the second release of the Penlight software was completed, culminating in reviews of the software applications and supporting frameworks. A detailed planning document was prepared that contains a review of the Nightlight release followed by sections describing each application subsystem and a section covering the supervisory framework. In addition, the plan coordinates device support, controller support, graphical user interfaces, database coverage, and framework coverage.
- A procedure for informal code walkthroughs (a line-by-line review of software) was developed after a pilot effort was completed late last year. The primary purposes of the walkthroughs are early error detection, promotion of a team programming style, and dissemination of techniques. The procedure involves assigning two or three people as reviewers, having reviewers meet informally with the code developer, and using a simple, but managed, reporting mechanism.
- Automatic alignment software demonstrated concurrent alignment of 96 beams using software to emulate the time required to execute every controlled action. Under the normal conditions emulated (i.e., no commanded actuator failed to perform its nominal requirement), the entire 96-beam laser completed alignment in just over 11 minutes.
- The video front-end processor (FEP) delivered for Nightlight exceeded performance goals of three simultaneous streams of video, each at 10 frames per second. The performance of the newly coded Ada software exceeded the C language prototypes even though the new code is object-oriented. These results help allay concern that object-oriented software might not have adequate performance over past approaches.
- The 100% review of the integrated timing system was completed in December. The meeting went very well and included a presentation by the target physics users that concluded the timing system specifications will lead to a system that can meet NIF performance requirements.
- In the integrated safety system, life testing of the fiber-optic permissive transmitters and receivers to be used in the capacitor bays has made good progress. The units have currently completed over 20,000 simulated charging cycles.
- A new version of programmable logic controller communications software was obtained from Rockwell Software that was directed at fixing a previously reported incompatibility problem. Initial testing of this version indicates that the problem has been resolved.

# Optical Components

**Optomechanical Systems.** Emphasis in all areas has shifted to preparing procurement packages and awarding contracts for first-bundle hardware. Awards were made for fused silica blanks for polarizers and

lenses for the OPG system, the CSF lens cassettes, and major procurements for the line-replaceable unit (LRU) assembly verification system.

The team assembled to resolve the optical mounts action item regarding validation of the transport mirror mount design made good progress. The specification of optical components for the OPG optical system was completed in December (48 optical component drawings). The 100% review Title II Design Review was held in November.

- The optical component drawings are awaiting check-off in Sherpa (the DOE/OAK Performance Measurement Mile-stone will be completed in January). Subsystems include the fiber launch/ regenerative amplifier and multipass amplifiers (both are part of the PAM), the input sensor telescope, the 1:4 split, the preamplifier beam transport system, and the injection system. This accomplishment resolves a previously reported problem.
- Excellent progress was made on the redesign and documentation of the preamplifier beam transport system (PABTS). The main part of this design is a six-element, adjustable telescope to accommodate the various path lengths, timing, magnification, relay plane, and collimation requirements of the part of the system just prior to injection in the TSF. The nominal configuration required for the OPG demonstration has been specified; final analysis and specification of the configurations and sensitivities for the other bundles are in progress.
- The 1ω and 3ω diagnostic relay telescope systems (eight per bundle) were redesigned for lower cost. The new designs have fewer elements but more aspheric surfaces. In addition to reducing cost, these new designs greatly simplify the ghost and stray light management for the system.
- The Title II design review was held in November for the KDP crystals. The review focused on the ability of rapid and conventional KDP growth to meet performance specifications and progress towards facilitization and demonstration of the KDP finishing equipment and processes. The reviews demonstrated that DKDP (deuterated) grown by conventional growth meets third-harmonic laser damage specifications and that rapid-growth processes can produce KDP of the size and quality required for Pockels cells and second-harmonic generators. There were no significant issues raised during the review.
- Castings of first-cluster polarizer material occurred in November with an expected delivery of annealed and shaped parts at the end of FY99. The first-cluster BK7 transport mirror material was ordered in December. The material will be stored at the vendor's warehouses in the United States until the blanks are needed. Pilot material for first-bundle laser mirror LM3 is currently being formed and shaped with the first set of blanks sent from overseas in December.
- An evaluation of the suitability of the current sol coating process for production of the NIF 1ω diagnostic beam-splitter reflecting surface was completed. The analysis indicated that current coating materials and practices will likely meet NIF requirements.

An ammonia-treated spatial filter (SF7/input) lens was installed in a Nova beamline. This lens is a full-scale demonstration of a hardened and passivated coating in relatively high fluence. Closure on this experiment will come with removal and evaluation of the lens coating properties at the shutdown of the Nova laser later in FY99.

## Laser Control

Preparations and presentations for all remaining 100% design reviews were completed. Prototype testing began to pay off by validating performance in some cases and identifying areas for improvement in others. Vendor qualification activities increased at the end of the quarter in preparation for scheduled procurement requisitions. Completion of detailed drawing

packages to support the procurement schedule is currently the largest challenge.

- All first-bundle build-to-specification components for the TSF alignment tower are in fabrication or procurement except for a translation slide requiring manufacturer design modifications and fiber-optic splitters and collimators. Requisitions for these items will be sent to procurement early in the next quarter. Life testing of a commercial positioner for the TSF diagnostic tower showed that longer life limit switches must be incorporated. The build-to-specification procurement package for the diagnostic tower is being held until the positioner vendor makes an appropriate substitution. Detail drawings for build-to-print components on all tower platforms are scheduled for completion in the next quarter.
- The input sensor was assembled, and most of the sensor test stand components were also received. In addition, the hardware and software for running the input sensor motors and shutters were completed. Testing is expected to begin near the end of January. Characteristics of the turning mirror that transmits approximately 1% of the PAM output beam to the input sensor were measured as a function of humidity. Significant transmission variation in the relative humidity range between zero and about 35% suggests that the operating atmosphere for this optic must either be carefully held at near-zero humidity (dry nitrogen, for example) or in the 40±10% range to avoid unacceptable changes in the input sensor energy calibration.
- Instrumentation for measurement of optical coating properties was designed, assembled, and applied to key components. Effects of contamination on sol-gel coatings for diagnostic beam splitters and the stability of antireflection (AR)-coated, beam-sampling gratings in a vacuum environment were among the properties measured. The grating sample efficiency was found to change by 25% over an eight-hour period when the test volume was evacuated. This behavior will be studied further, but measurements so far strongly suggest that an uncoated sampling grating may be required.
- Fibers received in November from Vavilov Institute were tested for dispersion and attenuation at 350 nm. The 10-m sample of large core, 435-$\mu$m-diam fiber was found to have low dispersion as the Russians claimed, but a longer sample is required for an accurate measurement. A change of deliverables for the second half of their current contract was proposed to Vavilov so that a longer sample can be provided. If successful, a single, large-core fiber could replace an entire 19-fiber bundle. A recent sample of 100-$\mu$m core fiber was also tested and found to have high attenuation, 400 dB/km as compared with the predicted 150 dB/km. This discrepancy will be pursued.
- The two vendor-produced deformable mirror prototypes were both retested after repairs by their respective companies. In both cases LLNL personnel participated in some aspects of the repair work. The testing of one of the rebuilt mirrors was completed in December, and it was declared performance qualified, because the test results were essentially indistinguishable from those of the LLNL prototype mirror. However, some concerns about reliability remain. Testing of the other vendor prototype began right before the holidays and is continuing into January. Initial indications are that performance will fall short unless additional changes are made.
- The Nightlight prototype version of wavefront controller software was released after internal testing in the wavefront laboratory as part of closed-loop operation of the prototype deformable mirrors. After release, the

controller was tested by the independent software-testing group, and no defects beyond those already identified in the laboratory were found.
- Full beamline propagation modeling including complete measurement-based models of the prototype deformable mirrors has become a mature tool for system optimization. During the quarter, the latest estimates of pump-induced aberrations and gravity and mounting aberrations for switchyard mirrors were added to the baseline propagation model. The model was also used to perform wavefront correction sensitivity studies with actuator spacing and beam alignment error as variables. These studies showed that a 5% increase in focused energy in the target chamber could be obtained by a small reduction in actuator spacing and that the resulting increase in sensitivity to alignment error was negligible. This improvement, the energy equivalent of adding nine complete beamlines to the NIF, is the direct result of achieving a convincing wavefront system modeling capability.

## Target Experimental Systems

The majority of target chamber subsection welding was completed in the first quarter 1999. The vacuum chamber seams were welded at the LLNL site, see Figure 3. Precision Components Corporation continued to fabricate the weld neck ports.

In Place Machining Corp. has completed and demonstrated a final mockup of the equipment that will be used for boring the holes in the chamber. The machines will use two single-point tool bits that are hydraulically driven.

- The target chamber move date has been changed from March 25, 1999, to June 1, 1999, and the chamber leak check will be performed while the chamber is in the fabrication building. This cuts the Pitt-Des Moines Steel downtime, or Target Building stay-out period, helping Pitt-Des Moines Steel complete the target chamber on schedule, and provides better weather and drier ground conditions for crane site preparation and the target chamber move.
- The analysis of the beam-dump prototype placed on Nova was nearly complete in November. The data reduction and analysis for the titanium samples was completed. As preliminary results indicated, there were no showstoppers. The stainless-steel louvers perform well for both first wall and beam dumps. X-ray fluorescence tests were performed on the Nova contaminated fused silica samples, and the results coordinated well with the damage tests performed on the optics. The results of this work also did not indicate problems with the stainless-steel louvers for first wall and beam dumps.
- The target positioner changes have been completed to eliminate the separate carriage to which the graphite-fiber–reinforced composite boom was to be attached. This will make the boom a single unit with the mounting pads for the linear bearings extending from hoops bonded to

FIGURE 3. Target chamber with temporary ties holding the 18 plates together prior to full welding. (40-60-1298-2447#17pb01)

the boom with an intermediary electrically insulating layer. Changing the double-walled vacuum vessel to a single-wall vessel having the same cross-sectional moment of inertia is nearly complete. This redesign required changes in the linear rail beds and track mounting beams and allowed improvements to the ball screw intermediate supports.

- The interface control document (ICD) for the Diagnostics Data Acquisition System (DAS) cable definition has been completed. The interface definitions in the ICD are done but final cable determination is not available at this time. The design is currently at the 35% level. The standards and guidelines document is presently being revised to include the preliminary Diagnostic Communication Protocol (DCP). The DCP will be the communications interface between the diagnostic controller and the FEP. The DCP messages and their required arguments have been defined, and preliminary DCP application interfaces should follow soon. Software goals for the Penlight version of the Target DAS FEP have been delivered for publication in the Penlight Software Implementation Plan. Work on a Connection Manager daemon is continuing. Ada packages to write a log file for the Connection Manager and time-stamp log file entries are complete. Currently, an Ada package to read and parse a configuration file is under development.
- It has been decided that existing Nova diagnostics will satisfy the Diagnostic Instrument Manipulator (DIM) laser verification experimental requirements. These are the gated x-ray imager and the six-inch manipulator-based streak camera. The resources that were planned for these two diagnostics will be redirected toward the work required to finish the design of the DIM. Design continues on the control and signal cables to support various target configurations on the front end of the target positioner. The mechanical design of the carriage and boom assemblies is changing from two mating components to a single composite assembly that will be more rigid. This new design will have some impact on the attachment of the cable tracking system but will not affect the schedule.
- Design changes are being incorporated into the mirror frames as a result of meetings with several fabricators. These modifications will help reduce the component cost.
- The design layouts for the retractable and removable beam tubes for the lower level that are adjacent to the floor in the upper and lower mirror rooms have been prepared and will be reviewed by the infrastructures and operations groups before proceeding with detailed design.
- Work has been delayed on the tritium environmental protection systems until 2004 to be able to prepare for the introduction of tritium into the facility in 2005. The exception to this delay is the stack monitoring system, which will be in place for the first bundle.
- The 100% review Title II Design Final Optics Assembly (FOA) Review was held in November. The review had been delayed by approximately one month to allow more time for scientific review of the last Beamlet tests using the final optics cell (FOC). The following topics were included in the review: physics overview, subsystem reviews (FOC, integrated optics module, actuation system, debris shield cassette, vacuum isolation valve, 3ω calorimeter chamber, thermal control system, vacuum venting system), and prototype testing results.
- Preparations proceeded well for first-article procurements of the integrated optics module (IOM), the FOC, and 3ω calorimeter chamber. The detail drawings for the IOM are complete and awaiting check. The FOC drawing package was released under Configuration Management.

## Operations Special Equipment

Title II design is proceeding well. This has been a productive quarter with FY99 budget planning process, intensive detailed design continuing, and fast-track prototyping and testing going well in the support laboratory. Several key internal milestones were completed.

- The alpha prototype release of the Operations Special Equipment Controls Supervisor (OSECS) was completed and demonstrated in December in Bldg. 432. The alpha prototype is the first vertical slice of OSECS and implements the Transport and Handling (T&H) cover removal operation for the Top Loading (TL) delivery system. The subsystems included in this release are the supervisory software module and the TL supervisory graphical user interface, both implemented in Java using CORBA, and the TL safety interlock system. The acceptance test procedures for this release have been completed, and the testing will be conducted in January. The detailed design of the Laser Bay Transport System (LBTS) interfaces with OSECS was completed, and the vendor (AGVP) is proceeding on schedule with their software development tasks.
- The detailed design for the Bottom Loading (BL), TL, and Side Loading delivery systems is progressing. The T&H team met with the Optics Assembly Building (OAB) team and discussed the OAB docking port requirements versus the existing design. The decision was made to switch the two docking port (universal and amplifier) locations. The amplifier docking port will now be located closer to the elevator. This will allow the canisters to dock to the OAB without rotating the canisters after a line-replaceable unit (LRU) is inside.
- The design effort for the BL Amplifier Slab Delivery System continues. The primary concentration was on the cover removal mechanism and docking mechanism for the system. A peer review of this system was completed this quarter. All interface partners were in attendance at this review. One of the prototype NIF frame assembly units will be available for testing of the LRU insertion/removal process. This testing is scheduled for December 1999.
- Fabrication of the hardware for the LBTS is continuing. The frame is being fabricated at Alkab, Inc. The majority of the parts that make up the weldments have been machined. Welding of the parts has begun, and AGVP is on schedule and ready to receive the transporter from RedZone.
- Detailed optical assembly and alignment design, prototyping, and procurement are progressing, with most of the prototype equipment now procured, and Phases II and III of OAB installation are complete. Special equipment installation into the OAB was completed in November. Those systems include optic insertion pedestals, Ergotech supports, and granite final supports. Jib cranes for airlocks and BL and TL docking ports were also installed in the OAB. An intensive acceptance test was completed in December for vertical and airlock lifts, and then installation into the OAB followed. Special equipment that will go inside the OAB and mount onto the raised floor is still being specified and procured.

## Start-Up Activities

Overall progress was good. Integrated computer control system (ICCS) Nightlight testing was successfully completed, planning was initiated for OSEC Alpha release testing, and preparation of detailed test flows and test summaries for several priority areas of the Project continued in support of the Master Test Plan development effort.

- Two test plans were generated by the NIF independent test team (ITT): one for the ICCS Nightlight release (NIF-5001097) and one for the OSEC Alpha release (NIF-5001272). Several key test processes were established and demonstrated during ICCS Nightlight release testing. These processes, consistent with industry standards, included use of standard documentation methods and electronic review/approval for test plans and procedures, test readiness reviews, release of software to the ITT under configuration management, adoption of standard software defect severity level classifications, creation of an electronic test log and test incident tracking database, and configuration management of test products such as test procedures and summary reports.
- Tests and demonstrations were completed for all thirteen ICCS Nightlight slices. Overall, software quality was found to be good. A total of 21 software defects were identified, and 20 software enhancements were recommended for development staff consideration as a result of formal testing by the ITT and ad hoc testing by Nova operations personnel. All software issues have been converted to software change requests (SCRs) and are being tracked by the development team. A summary test report (NIF-5001322) was prepared and issued for approval and release. A test procedure is being prepared by the ITT for the OSEC Alpha release.
- To facilitate development of the Master Test Plan (MTP), the NIF system was broken down into approximately 40 "subsystems," and points of contact were assigned from the NIF Operations team to begin investigating test plans being developed by the lead engineers and their support personnel for all high-priority areas. Information collected is being documented using test flow diagrams and test summary spreadsheets, and these products will form the basis for the MTP. To date, preliminary test flows and spreadsheets have been completed for 15% of the subsystems (PAM, injection optics, spatial filter LRUs, transport mirrors, PEPC, and deformable mirror), and another 25% are in progress. In addition to individual subsystem test plans, development of the sequence for subsystem integration was initiated. This effort is approximately 35% complete. A draft outline for the MTP was prepared and issued for review and comment.
- A preliminary plan for a system-wide Component Installation Plan has been prepared. It is initially a series of connected boxes representing cleaning, packaging, transport, or cleanliness validation steps necessary for each NIF subsystem. Each cleaning process is represented by a specific procedure. Creation of these Component Installation Plans will identify similarities as well as conscious differences between subsystems. The identification of similarities will help to ensure that similar subsystems are cleaned by similar processes, using similar equipment and vendors, and are validated to consistent standards. The common processes for cleaning and validating the cleanliness of subsystems identified during the construction of the Component Installation Plans will be documented in engineering procedures referred to as Mechanical Engineering Letters (MELs). Sixteen of the documents have already been written and a few have reached a stage of maturity in which they have been put under configuration control. The contamination control team presented a status report entitled *Organic Cleanliness and Effects on Sol-gel Coatings and Aerosol Generation Status Report* in December. This review completed the major work on organics and their effect on the transmission of sol-gel coatings. The conclusion is that all vacuum com-

ponents need high-pressure or ultrasonic/Brulin washing; elastomers need bakeout at 170°C; and all nitrogen and argon-filled components will be high-pressure or ultrasonic/Brulin washed to protect sol-gel coatings from >0.1% transmission loss in 1000 hours. The status of cleanliness control process maps in support of the systemwide Component Installation Cleanliness Plan was reviewed in December. The discussion included the cleaning process selection chart, components for which specific cleanliness plans are required, and rules for preparing the process flow maps. The status of the flowcharts will be reviewed again in February 1999.

- A baseline approach for a laser operations model has been defined, largely using parts of existing propagation code, BTGain. Interfaces of this model with operational and optics databases, as well as the NIF ICCS, have been explored. A preliminary effort analysis to implement this model has been completed and will be used to decide on an action plan.
- The final revision of the FY98 operability model report was issued. This included incorporation of review comments from the initial release. The model results were presented as part of the NIF RAM and Operations Modeling Assessments Review held in October.

## ES&H and Supporting R&D

**Assurances.** Key Assurance activities during November to support the Project included: construction safety support, QA procedures, audits, and surveillance planning, and preparation for upcoming independent external audits (DOE OAK, Independent Project Assessment). Other activities included: litigation support to the DOE for the settlement of 60(b) (e.g., quarterly reports), the overall litigation against the *Stockpile Stewardship and Management Programmatic Environmental Impact Report*, interface with the Institutional surveillance for buried hazardous/toxic and/or radioactive materials, *Final Safety Analysis Report* preparation, and support for environmental permits and the *Pollution Prevention and Waste Minimization Plan*. All are on schedule.

- The Congressionally mandated Independent Project Assessment is due to begin in January 1999. The proposed presentation material and supporting documents were prepared for the Project Manager's review. The DOE Field Manager has provided the proposed Task A review agenda from the Independent Project Assessment Team. In a related action, the Management Position Descriptions were updated completly and are being edited for the Project Manager's approval.
- The paleontological finds were previously accurately located and reported to the University of California Museum of Paleontology. In December, these bones were carefully covered with sand and then a marker level of gravel. The covering was witnessed by a representative of the Environmental Protection Department.
- Elemental analyses have been completed for the first significant neutron shielding concrete pours in the Target Bay. The results show significant, but manageable, levels of impurities. Activation calculations have shown that the shielding meets the design criteria and specifications. Future Target Bay concrete pours will be sampled as well to ensure continued compliance with specifications.
- The DOE Oakland Annual Management Assessment was completed in draft form and factual comments returned to the assessment team. The report will be issued in January 1999.

**Optics Technology**. Facilitization is all but complete at Hoya and Schott with all contracts placed and pilot activities

already started. Hiring and training for pilot runs is mostly completed. Both laser glass vendors are doing a great job in supporting the NIF schedules.

The Zygo facility was completed in the first quarter 1999, and first-bundle optics (LM3) are now being shaped. Spectra-Physics has completed all major facility work and is in the process of installing equipment, such as the clean line. Currently Spectra-Physics is in the process of installing the new planetary, conditioning stations, and preparing the interferometer area for installation of the new interferometer in the second quarter. The Laboratory for Laser Energetics (LLE) at the University of Rochester has completed the coating and cleaning facilities and is near completion of the metrology facilities that will also be completed in the second quarter.

- The Schott laser glass grinding and polishing has been installed with assistance from Zygo Corporation, and initial results look very good. The flatness specification and process flow time should not be an issue. All fine annealing ovens have been delivered and set up.
- At Hoya, full-scale furnace and lehr are complete. Hoya is still on schedule to start the Laser Glass Pilot run mid-January 1999. Two 120" Lapmaster grit grinder and polishers have been delivered and set up. First-bundle laser glass cladding strips were produced in Japan and delivered on time.
- Six 1000-L crystallizers continued to operate at LLNL. A KDP boule was grown to a size that will yield nearly 20 Pockels cell switch crystals. The two DKDP crystals, one horizontal and one vertical, continued to grow without significant problems. A mathematical model was formulated and tested for the leaching of impurities from the growth tank and their incorporation into the boule.
- Corning has completed the debugging of all facilitization equipment including the boule/blank extraction saw, 84" Blanchard, overarm lapper, 24" Zygo interferometer and fixturing. Pilot production of NIF fused silica blanks has begun. All process and quality assurance procedures have been reviewed and approved by LLNL. The first optics were shipped to Tinsley in December.
- Tinsley's lens and window finishing facility building was completed on schedule, and beneficial occupancy was obtained in November. Most manufacturing equipment was installed into the new building. A few pieces of equipment remain to be installed. They are expected to be installed prior to the optics being ready to be placed on those machines. The facility has been made ready for start of pilot production. Early pilot production of NIF optics has continued at Tinsley. The first three of seven focus lenses are nearing completion. They will be available for ultraviolet laser damage testing in February. The finishing of two cavity mirrors and two debris shields is still in process. Main pilot is scheduled to award at Tinsley in January. Work has begun under the Flexible Finishing Facility contract awarded to Kodak in late September, and LLNL has begun receiving the Kodak Monthly Progress Reports and detailed schedules. All LLNL or government-furnished equipment (GFE) has either been ordered or already received at Kodak. The Pilot Production Option associated with the Kodak Flexible Finishing Facility contract was exercised and awarded during mid-December.
- The automated aqueous cleaning systems from JST Custom Fabrication were completed and ready for delivery to LLNL at the end of December. Chemat Technology Inc. has completed approximately 80% of the mechanical assembly and control software development on the sol dip-coating system.

- Zygo facilitization is complete, and shaping of first-bundle optics has begun.
- The LLE 54" planetary design was completed to allow coating of only NIF optics in the 72" chamber and Omega optics in the 54" chamber. The metrology facilities are under construction. All of the major re-modeling work is complete, but utilities and high-efficiency particulate air (HEPA) filter installation need to be completed. LLE conducted an experiment with an in-situ interferometer to examine the surface flatness of an optic during heating and cooling to improve their model of the appropriate rapid cooldown cycle. This work will also aid in understanding reflected wavefront distortion due to coating versus other contributions.
- Spectra-Physics received beneficial occupancy for the remaining facility in November, contingent on some minor fire sprinkler relocations and landscaping issues. The metrology labs are starting to be populated with equipment. The Large Area Conditioning Station assembly started in December. The isolation pad for the interferometer was sealed to prevent humidity penetration into the dry enclosure, and the vibration isolation table was installed.

# PUBLICATIONS AND PRESENTATIONS OCTOBER–DECEMBER 1998

## A

Albrecht, G. F., Sutton, S. B., George, E. V., Sooy, W. R., and Krupke, W. F., *Solid State Heat Capacity Disk Laser*, Lawrence Livermore National Laboratory, Livermore, CA, UCRL-JC-130963; also in *Laser & Part. Beams* **16**(4), 605–625 (1998).

## B

Back, C. A., Alvarez, S., Spragge, M., Bauer, J., Landen, O. L., Turner, R. E., and Hsing, W., *High Energy Density Experimental Science in Support of SBSS*, Lawrence Livermore National Laboratory, Livermore, CA, UCRL-JC-131975 ABS. Prepared for *Women's Technical and Professional Symp*, San Ramon, CA, Oct 15, 1998.

Back, C. A., Landen, O. L., Turner, R. E., Koch, J. A., Hammel, B. A., MacFarlane, J. J., and Nash, T. J., *Spectroscopic Measurements to Investigate and Diagnose Radiative Heating of Hohlraum Walls*, Lawrence Livermore National Laboratory, Livermore, CA, UCRL-JC-131993 ABS. Prepared for *8th Intl Workshop on Radiative Properties of Hot Dense Matter*, Sarasota, FL, Oct 26, 1998.

Belian, A.P., Latkowski, J. F., and Morse, E. C., "Experimental Studies of Concrete Activation at the National Ignition Facility Using the Rotating Target Neutron Source," *Fusion Tech.* **34**(3), Pt. 2, 1028–1032 (1998).

Berger, R. L., Cohen, B. I., Langdon, A. B., MacGowan, B. J., Rothenberg, J., Still, C. W., Williams, E. A., and Lefebvre, E., *Simulation of the Nonlinear Interaction of Filamentation with Stimulated Backscatter*, Lawrence Livermore National Laboratory, Livermore, CA, UCRL-JC-132598 ABS. Prepared for *1999 Centennial Mtg of the American Physical Society*, Atlanta, GA, Mar 20, 1999.

Berger, R. L., Langdon, A. B., Rothenberg, J. E., Still, C. H., Williams, E. A., and Lefebvre, E., *Stimulated Raman and Brillouin Scattering of Polarization Smoothed and Temporally Smoothed Laser Beams*, Lawrence Livermore National Laboratory, Livermore, CA, UCRL-JC-132259; also in *Phys. of Plasmas* **6**(4), 1043–1047 (1999).

Berger, R. L., Still, C. H., Williams, E. A., and Langdon, A. B., On the *Dominant and Subdominant Behavior of Stimulated Raman and Brillouin Scattering Driven by Nonuniform Laser Beams*, Lawrence Livermore National Laboratory, Livermore, CA, UCRL-JC-132259; also in *Phys. Plasmas* **5**(12), 4337–4356 (1998).

Bibeau, C., Beach, R. J., Mitchell, S. C., Emanuel, M. A., Skidmore, J., Ebbers, C. A., Sutton, S. B., and Jancaitis, K. S., *High Average Power 1 mm Performance and Frequency Conversion of a Diode-End-Pumped Yb:YAG Laser*, Lawrence Livermore National Laboratory, Livermore, CA, UCRL-JC-129612; also in *IEEE J. Quant. Electr.* **34**(10), 2010–2019 (1998).

Bittner, D. N., Collins, G. W., Monsler, E., and Letts, S., *Forming Uniform HD Layers in Shells Using Infrared Radiation*, Lawrence Livermore National Laboratory, Livermore, CA, UCRL-JC-131371. Prepared for *40th Annual Mtg of the Div of Plasma Physics*, New Orleans, LA, Nov 16, 1998.

Boege, S. J., and Bliss, E. S., *Beam Control and Laser Characterization for NIF*, Lawrence Livermore National Laboratory, Livermore, CA, UCRL-JC-129854; also in *Fusion Tech*. **34**(3), Pt. 2, 1117–1121 (1998).

Brereton, S. J., Yatabe, J. M., and Taylor, C. A., *The Safety and Environmental Process for the Design and Construction of the National Ignition Facility*, Lawrence Livermore National Laboratory, Livermore, CA, UCRL-JC-130860; also in *Fusion Tech.* **34**(3), Pt. 2, 760–766 (1998).

Brereton, S. J., Latkowski, J., Singh, M., Tobin, M., and Yatabe, J., *Decommissioning Plan for the National Ignition Facility*, Lawrence Livermore National Laboratory, Livermore, CA, UCRL-JC-130859; also in *Fusion Tech.* **34**(3), Pt. 2, 1041–1046 (1998).

Britten, J. A., and Summers, L. J., *Multiscale, Multifunction Diffractive Structures Wet-Etched into Fused Silica for High-Laser Damage Threshold Applications*, Lawrence Livermore National Laboratory, Livermore, CA, UCRL-JC-130115; also in *Appl. Optics* **37**(30), 7049–7054 (1998).

## C

Chatterjee, I., Hallock, G. A., and Wootton, A. J., *Observation of Multiple Modes of Interior Density Turbulence in the TEXT-U Tokamak*, Lawrence Livermore National Laboratory, Livermore, CA, UCRL-JC-132555.

Colvin, J. D., Amendt, P. A., Dittrich, T. R., Tipton, R. E., and Vantine, H. C., *Analysis of Laser Indirect Drive Double-Shell Capsule Implosion Experiments as a Testbed for Benchmarking Compressible Turbulent Mix Models*, Lawrence Livermore National Laboratory, Livermore, CA, UCRL-JC-132571 ABS. Prepared for *1999 Centennial Mtg of the American Physical Society*, Atlanta, GA, Mar 20, 1999.

Cook, R., Buckley, S. R., Fearon, E., and Letts, S. A., *New Approaches to the Preparation of Pa MS Beads as Mandrels for NIF-Scale Target Capsules*, Lawrence Livermore National Laboratory, Livermore, CA, UCRL-JC-129955; also in *Fusion Tech.* **35**(2), 206–211 (1999).

Cook, R. C., McEachern, R. L., and Stephens, R., *Representative Surface Profile Power Spectra from Capsules Used in Nova and Omega Implosion Experiments*, Lawrence Livermore National Laboratory, Livermore, CA, UCRL-JC-129961; also in *Fusion Tech.* **35**(2), 224–228 (1999).

## D

De Yoreo, J. J., Yan, M., Runkel, M., Staggs, M., Liou, L., Demos, S. G., Carman, L., Zaitseva, N. P., and Rek, Z. U., *Characterization of Optical Performance and Defect Structures in Nonlinear Crystals for Large Aperture Lasers*, Lawrence Livermore National Laboratory, Livermore, CA, UCRL-JC-132557 ABS-S. Prepared for *Conf on Lasers and Electro-Optics '99/Quantum Electronics and Laser Science Conf '99*, Baltimore, MD, May 23, 1999.

Dimonte, G., *Nonlinear Evolution of the Rayleigh–Taylor and Richtmyer–Meshkov Instabilities*, Lawrence Livermore National Laboratory, Livermore, CA, UCRL-JC-132439. Prepared for *40th Annual Mtg of the Div of Plasma Physics*, New Orleans, LA, Nov 16, 1998.

Dimonte, G., and Schneider, M., *Density Ratio Dependence of Rayleigh–Taylor Mixing for Sustained and Impulsive Acceleration Histories*, Lawrence Livermore National Laboratory, Livermore, CA, UCRL-JC-132570. Submitted to *Phys. of Plasmas*.

Dimonte, G., and Schneider, M., *Density Ratio Dependence of Rayleigh–Taylor Mixing for Sustained and Impulsive Acceleration Histories*, Lawrence Livermore National Laboratory, Livermore, CA, UCRL-JC-132570 ABS Rev. Prepared for *7th Intl Workshop on the Physics of Compressible Turbulent Mixing*, St. Petersburg, Russia, Jul 5, 1999.

Dimonte, G., *New Buoyancy-Drag Model for Rayleigh–Taylor Mixing and Comparison with Experiments*, Lawrence Livermore National Laboratory, Livermore, CA, UCRL-JC-132695 ABS. Prepared for *7th Intl Workshop on the Physics of Compressible Turbulent Mixing*, St. Petersburg, Russia, Jul 5, 1999.

Dittrich, T. R., Haan, S. W., Marinak, M. M., Pollaine, S. M., Hinkel, D. E., Munro, D. H., Verdon, C. P., Strobel, G. L., McEachern, R. L., Cook, R. C., Roberts, C. C., Wilson, D. C., Bradley, P. A., Foreman, L. R., and Varnum, W. S., *Review of Indirect-Drive Ignition Design Options for the National Ignition Facility*, Lawrence Livermore National Laboratory, Livermore, CA, UCRL-JC-131383. Submitted to *Phys. of Plasmas*.

Dittrich, T. R., Haan, S. W., Marinak, M. M., Pollaine, S. M., and McEachern, R., *Reduced Scale National Ignition Fusion Capsule Design*, Lawrence Livermore National Laboratory, Livermore, CA, UCRL-JC-131383; also in *Phys. Plasmas* **5**(10), 3708–3713 (1998).

## E

Erlandson, A., Alger, T., Horvath, J., Jancaitis, K., Lawson, J., Manes, K., Marshall, C., Moor, E., Payne, S., Pedrotti, L., Rodriguez, S., Rotter, M., Sutton, S., Zapata, L., Seznec, S., Beullier, J., Carbourdin, O., Grebot, E., Guenet, J., Guenet, M., LeTouze, G., and Maille, X., "Flashlamp-Pumped Nd:Glass Amplifiers for the National Ignition Facility," *Fusion Tech.* **34**(3), Pt. 2, 1105–1112 (1998).

Erlandson, A. C., Jancaitis, K., Marshall, C., Pedrotti, L., Zapata, L., Rotter, M., Sutton, S., Payne, S., Seznec, S., and Beullier, J., *Recent Advances in Flashlamp-Pumped Neodymium-Glass Amplifiers*, Lawrence Livermore National Laboratory, Livermore, CA, UCRL-JC-132461 ABS-S. Prepared for *Conf on Lasers, and Electro Optics/Quantum Electronics and Lasers Science (CLEO/QELS '99)*, Baltimore, MD, May 23, 1999.

Estabrook, K. G., Remington, B. A., Farley, D., Glenzer, S., Back, C. A., Turner, R. E., Glendinning, S. G., Zimmerman, G. B., Harte, J. H., and Wallace, R. J., *Nova Laser Experiments of Radiative Astrophysical Jets*, Lawrence Livermore National Laboratory, Livermore, CA, UCRL-JC-132258 ABS. Prepared for *193rd Mtg of the American Astronomical Society*, Austin, TX, Jan 5, 1999.

## G

Glendinning, S. G., Amendt, P., Cline, B. D., Ehrlich, R. B., Hammel, B. A., Kalantar, D. H., Landen, O. L., Turner, R. E., Wallace, R. J., Weiland, T. J., Dague, N., Jadaud, J.-P., Bradley, D. K., Pien, G., and Morse, S., *Hohlraum Symmetry Measurements with Surrogate Solid Targets*, Lawrence Livermore National Laboratory, Livermore, CA, UCRL-JC-129773; also in *Rev. Sc. Instrum.* **70**(1), 536–542 (1999).

Glendinning, S. G., *Laser-Drive ICF Fundamentals and Recent Experimental Results*, Lawrence Livermore National Laboratory, Livermore, CA, UCRL-JC-132158 ABS. Prepared for *Women's Technical and Professional Symp*, San Ramon, CA, Oct 15, 1998.

Glenzer, S. H., Alley, W. E., Estabrook, K. G., De Groot, J. S., Haines, M., Hammer, J. H., Jadaud, J.-P., MacGowan, B. J., Moody, J. D., and Rozmus, W., *Thomson Scattering from Laser Plasmas*, Lawrence Livermore National Laboratory, Livermore, CA, UCRL-JC-131357-DR. Prepared for *40th Annual Mtg of the Div of Plasma Physics*, New Orleans, LA, Nov 16, 1998.

Gresho, P. M., *Some Aspects of the Hydrodynamics of the Microencapsulation Route to NIF Mandrels*, Lawrence Livermore National Laboratory, Livermore, CA, UCRL-JC- 129963; also in *Fusion Tech.* **35**(2), 157–188 (1999).

## H

Hammel, B. A., Bernat, T. P., Collins, G. W., Haan, S., Landen, O. L., MacGowan, B. J., and Suter, L. J., *Recent Advances in Indirect Drive ICF Target Physics at LLNL*, Lawrence Livermore National Laboratory, Livermore, CA, UCRL-JC-130302. Prepared for *17th Intl Atomic Energy Agency Fusion Energy Conf*, Yokohama, Japan, Oct 19, 1998.

Hammer, J. H., Tabak, M., Wilks, S. C., Lindl, J. D., Bailey, D. S., Rambo, P. W., Toor, A., Zimmerman, G. B., and Porter, J. L., *High Yield ICF Target Design for a Z-Pinch Driven Hohlraum*, Lawrence Livermore National Laboratory, Livermore, CA, UCRL-JC-131389. Prepared for *40th Annual Mtg of the Div of Plasma Physics*, New Orleans, LA, Nov 16, 1998.

Hammer, J. H., Tabak, M., Wilks, S., Lindl, J., Rambo, P. W., Toor, A., Zimmerman, G. B., and Porter, J. L., *High Yield Inertial Fusion Design for a Z-Pinch Accelerator*, Lawrence Livermore National Laboratory, Livermore, CA, UCRL-JC-132152. Prepared for *17th Intl Atomic Energy Agency Fusion Energy Conf*, Yokohama, Japan, Oct 19, 1998.

Hammer, J. H., and Ryutov, D. D., *Linear Stability of an Accelerated Wire Array*, Lawrence Livermore National Laboratory, Livermore, CA, UCRL-JC-132255. Prepared for *40th Annual Mtg of the Div of Plasma Physics*, New Orleans, LA, Nov 16,1998.

Ho, D. D.-M., Chen, Y.-J., Pincosy, P. A., Young, D. A., and Bergstrom, P. M., *Hydrodynamic Modeling of the Plasma Plume Expansion from the Targets for X-Ray Radiography*, Lawrence Livermore National Laboratory, Livermore, CA, UCRL-JC-132181-ABS. Prepared for *1999 Particle Accelerator Conf*, New York City, NY, Mar 29, 1999.

## K

Kalantar, D. H., Remington, B. A., Chandler, E. A., Colvin, J. D., Gold, D. M., Mikaelian, K. O., Weber, S. V., Wiley, L. G., Wark, J. S., and Hauer, A. A., *High Pressure Solid State Experiments on the Nova Laser*, Lawrence Livermore National Laboratory, Livermore, CA, UCRL-JC-129810. Prepared for *1998 Hypervelocity Impact Symp*, Huntsville, AL, Nov 16, 1998.

Kalantar, D. H., Remington, B. A., Colvin, J. D., Gold, D. M., Mikaelian, K. O., Weber, S. V., and Wiley, L. G., *Shock Compressed Solids on the Nova Laser*, Lawrence Livermore National Laboratory, Livermore, CA, UCRL-JC-132687 ABS. Prepared for *11th Topical Conf on Shock Compression of Condensed Matter*, Snowbird, UT, Jun 27, 1999.

Kane, J. O., Arnett, D., Remington, B. A., Glendinning, S. G., Bazan, G., Drake, R. P., and Fryxell, B. A., *Scaling Supernova Hydrodynamics to the Laboratory*, Lawrence Livermore National Laboratory, Livermore, CA, UCRL-JC-132438. Prepared for *40th Annual Mtg of the Div of Plasma Physics*, New Orleans, LA, Nov 16, 1998.

Kastenberg, W. E., *Industrial Ecology Analysis Final Report*, Lawrence Livermore National Laboratory, Livermore, CA, UCRL-CR-132271.

Kauffman, R., *Inertial Confinement Fusion Monthly Highlights*, September 1998, Lawrence Livermore National Laboratory, Livermore, CA, UCRL-TB-128550-98-12.

Kauffman, R., *Inertial Confinement Fusion Monthly Highlights*, October 1998, Lawrence Livermore National Laboratory, Livermore, CA, UCRL-TB-128550-99-1.

Kauffman, R., *Inertial Confinement Fusion Monthly Highlights*, November 1998, Lawrence Livermore National Laboratory, Livermore, CA, UCRL-TB-128550-99-2.

Key, M. H., Cowan, T. E., Hammel, B. A., Hatchett, S. P., Henry, E. A., Kilkenny, J. D., Koch, J. A., Langdon, A. B., Lasinski, B. F., and Lee, R. W., *Progress in Fast Ignitor Research with the Nova Petawatt Laser Facility*, Lawrence Livermore National Laboratory, Livermore, CA, UCRL-JC-132178. Prepared for *17th Intl Atomic Energy Agency Fusion Energy Conf*, Yokohama, Japan, Oct 19, 1998.

Kozioziemski, B., Collins, G. W., Bernat, T. P., and Sater, J. D., *Helium Bubble Dynamics in D-T Layers*, Lawrence Livermore National Laboratory, Livermore, CA, UCRL-JC-130038 ABS Rev. Prepared for *1999 Centennial Mtg, Atlanta*, GA, Mar 20, 1999.

Kruer, W., *Inertial Confinement Fusion Quarterly Report*, January–March 1998, Lawrence Livermore National Laboratory, Livermore, CA, UCRL-LR-105821-98-2.

## L

Landen, O. L., Amendt, P. A., Turner, R. E., Glendinning, S. G., Kalantar, D. H., Decker, C. D., Suter, L. J., Cable, M. D., Wallace, R., and Hammel, B. A., *Time-Dependent, Indirect-Drive Symmetry Control on the Nova and Omega Facilities*, Lawrence Livermore National Laboratory, Livermore, CA, UCRL-JC-130109. Prepared for 17*th Intl Atomic Energy Agency Fusion Energy Conf*, Yokohama, Japan, Oct 19, 1988.

Landen, O. L., Amendt, P. A., Suter, L. J., Turner, R. E., Glendinning, S. G., Haan, S. W., Pollaine, S. M., Hammel, B. A., Rosen, M. D., and Lindl, J. D., *Simple Time-Dependent Model of the P2 Asymmetry in Cylindrical Hohlraums*, Lawrence Livermore National Laboratory, Livermore, CA, UCRL-JC-132445-DR. Prepared for *40th Annual Mtg of the Div of Plasma Physics*, New Orleans, LA, Nov 16, 1998.

Lane, M. A., Van Wonterghem, B. M., and Clower Jr., C. A., *Phased NIF Start-Up*, Lawrence Livermore National Laboratory, Livermore, CA, UCRL-JC-129271; also in *Fusion Tech.* **34**(3), Pt. 2, 1127–1134 (1998).

Lasinski, B. F., Langdon, A. B., Hatchett, S. P., Key, M. H., and Tabak, M., *PIC Simulations of Ultra Intense Pulses Propagating through Overdense Plasma for Fast-Ignitor and Radiography Applications*, Lawrence Livermore National Laboratory, Livermore, CA, UCRL-JC-131245. Submitted to *Phys. of Plasmas*.

Latkowski, J. F., *Neutron Activation of the NIF Final Optics Assemblies and Their Effect upon Occupational Doses*, Lawrence Livermore National Laboratory, Livermore, CA, UCRL-JC-129515; also in *Fusion Tech.* **34**(3), Pt. 2, 767–771 (1998).

Liang, E. P., Wilks, S. C., and Tabak, M., *Pair Production by Ultraintense Lasers*, Lawrence Livermore National Laboratory, Livermore, CA, UCRL-JC-124499 Rev 1; also in *Phys. Rev. Lett.* **81**(22), 4887–4890 (1998).

Lowenthal, M. D., Greenspan, E., Moir, R., Kastenberg, W. E., and Fowler, T. K., "Industrial Ecology for Inertial Fusion Energy: Selection of High-Z Material for HYLIFE-II Targets," *Fusion Tech.* **34**(3), Pt. 2, 619–628 (1998).

## M

MacGowan, B. J., Berger, R. L., Cohen, B. I., Decker, C. D., Dixit, S., Glenzer, S. H., Hinkel, D. E., Kirkwood, R. K., Langdon, A. B., and Lefebvre, E., *Laser Beam Smoothing and Backscatter Saturation Processes in Plasmas Relevant to National Ignition Facility Hohlraums*, Lawrence Livermore National Laboratory, Livermore, CA, UCRL-JC-132191. Prepared for *17th Intl Atomic Energy Agency Fusion Energy Conf*, Yokohama, Japan, Oct 19, 1988.

Marshall, C. D., Erlandson, A., Jancaitis, K., Lawson, J., Sutton, S., and Zapata, L., *Performance of National Ignition Facility Prototype Laser Amplifier Facility*, Lawrence Livermore National Laboratory, Livermore, CA, UCRL-JC-131986 ABS. Prepared for *Lasers and Electro-Optics Society 1998 11th Annual Conf*, Orlando, FL, Dec 1, 1998.

McEachern, R., Matsuo, J., and Yamada, I., *Cluster Ion Beam Polishing for Inertial Confinement Fusion Target Capsules*, Lawrence Livermore National Laboratory, Livermore, CA, UCRL-JC-130683. Prepared for *12th Intl Conf on Ion Implantation Technology*, Kyoto, Japan, Jun 22, 1998.

Meier, W. R., *Systems Modeling and Analysis of Heavy Ion Drivers for Inertial Fusion Energy*, Lawrence Livermore National Laboratory, Livermore, CA, UCRL-JC-130954; also in *Fusion Tech.* **34**(3), Pt. 2, 326–330 (1998).

Moran, M., Brown, C. G., Cowan, T. E., Hatchett, S., Hunt, A., Key, M., Pennington, D., Perry, M. D., Phillips, T., and Sangster, T. C., *Measurements of MeV Photon Flashes in Petawatt Laser Experiments*, Lawrence Livermore National Laboratory, Livermore, CA, UCRL-JC-131359. Prepared for *40th Annual Mtg of the Div of Plasma Physics*, New Orleans, LA, Nov 16, 1998.

## N

Newton, M., and Wilson, M., *Main Amplifier Power Conditioning for the National Ignition Facility*, Lawrence Livermore National Laboratory, Livermore, CA, UCRL-JC-130975; also in *Fusion Tech.* **34**(3), Pt. 2, 1122–1126 (1998).

Norton, M. A., Boley, C. D., Murray, J. E., Sinz, K., and Neeb, K., *Long-Lifetime, Low-Contamination Metal Beam Dumps for NIF Spatial Filters*, Lawrence Livermore National Laboratory, Livermore, CA, UCRL-JC-129768. Prepared for *3rd Annual Intl Conf on Solid State Lasers for Application (SSLA) to Inertial Confinement Fusion (ICF)*, Monterey, CA, Jun 7, 1998.

## P

Payne, S. A., and Bibeau, C., *Picosecond Nonradiative Processes in Neodymium-Doped Crystals and Glasses: Mechanism for the Energy Gap Law*, Lawrence Livermore National Laboratory, Livermore, CA, UCRL-JC-128623; also in *J. Luminescence* **79**(3), 143–159 (1998).

Petzoldt, R. W., *IFE Target Injection and Tracking Experiment*, Lawrence Livermore National Laboratory, Livermore, CA, UCRL-LR-120192; also in *Fusion Tech.* **34**(3), Pt. 2, 831–839 (1998).

Porcelli, F., Rossi, E., Cima, G., and Wootton, A., *Macroscopic Magnetic Islands and Plasma Energy Transport*, Lawrence Livermore National Laboratory, Livermore, CA, UCRL-JC-132568. Prepared for *Workshop on Fusion Related Physics and Engineering in Small Devices*, Trieste, Italy, Oct 6, 1998.

## R

Remington, B. A., *Hydrodynamics Experiments on Intense Lasers*, Lawrence Livermore National Laboratory, Livermore, CA, UCRL-JC-131249 ABS Rev. Prepared for *1999 Centennial Mtg,* Atlanta, GA, Mar 20, 1999.

Rhodes, M. A., Fochs, S., and Biltoft, P., *Plasma Electrode Pockels Cell for the National Ignition Facility*, Lawrence Livermore National Laboratory, Livermore, CA, UCRL-JC-129710; also in *Fusion Tech.* **34**(3), Pt. 2, 1113–1116 (1998).

Roberts, C. C., Letts, S. A., Saculla, M., Hsieh, E. J., and Cook, R., *Polyimide Films from Vapor Deposition: Toward High Strength, NIF Capsules*, Lawrence Livermore National Laboratory, Livermore, CA, UCRL-JC-132194; also in *Fusion Tech.* **35**(2), 138–146 (1999).

Rosen, M., *Physics Issues That Determine Inertial Confinement Fusion Target Gain and Driver Requirements: a Tutorial*, Lawrence Livermore National Laboratory, Livermore, CA, UCRL-JC-131381. Submitted to *Phys. of Plasmas*.

Rossetter, E., *Electronics Cooling in a Diagnostic Instrument Manipulator*, Lawrence Livermore National Laboratory, Livermore, CA, UCRL-ID-132225.

## S

Sanchez, J. J., and Giedt, W. H., *Thermal Control of Cryogenic Cylindrical Hohlraums for Indirect-Drive Inertial Confinement Fusion*, Lawrence Livermore National Laboratory, Livermore, CA, UCRL-JC-132168. Submitted to *J. Appl. Phys.*

Sater, J., Kozioziemski, B., Collins, G. W., Mapoles, E. R., Pipes, J., Burmann, J., and Bernat, T. P., *Cryogenic D-T Fuel Layers Formed in 1 mm Spheres by Beta-Layering*, Lawrence Livermore National Laboratory, Livermore, CA, UCRL-JC-128031. Prepared for *40th Annual Mtg of the Div of Plasma Physics*, New Orleans, LA, Nov 16, 1998.

Sawicki, R., Bowers, J., Hackel, R., Larson, D., Manes, K., and Murray, J., *Engineering the National Ignition Facility*, Lawrence Livermore National Laboratory, Livermore, CA, UCRL-JC-131522; also in *Fusion Tech.* **34**(3), Pt. 2, 1097–1104 (1998).

Small IV, W., Celliers, P. M., Da Silva, L. B., Matthews, D. L., and Soltz, B. A., *Two-Color Mid-Infrared Thermometer Using a Hollow Glass Optical Fiber*, Lawrence Livermore National Laboratory, Livermore, CA, UCRL-JC-128082 Rev 1; also in *Appl. Opt.* **37**(28), 6677–6683 (1998).

Still, C. H., Langer, S. H., Alley, W. E., and Zimmerman, G. B., *Scientific Programming-Shared Memory Programming with Open MP*, Lawrence Livermore National Laboratory, Livermore, CA, UCRL-JC-131544; also in *Comput. Phys.* **12**(6), 577–584 (1998).

## T

Tatartchenko, V., and Beriot, E., *Growth of Large KDP Crystals in the Form of Plates*, Lawrence Livermore National Laboratory, Livermore, CA, UCRL-JC-132196. Prepared for *3rd Annual Intl Conf on Solid State Lasers for Application (SSLA) to Inertial Confinement Fusion (ICF)*, Monterey, CA, Jun 7, 1998.

Turner, R. E., Amendt, P., Landen, O. L., Glendinning, S. G., Bell, P., Decker, C., Hammel, B. A., Kalantar, D., Lee, D., and Wallace, R., *Demonstration of Time Dependent Symmetry Control in Hohlraums by the Use of Drive Beam Staggering*, Lawrence Livermore National Laboratory, Livermore, CA, UCRL-JC-132330. Submitted to *Phys. Rev. Lett.*

## W

Weber, S. V., Kalantar, D. H., Colvin, J. D., Gold, D. M., Mikaelian, K. O., Remington, B. A., and Wiley, L. G., *Nova Experiments Examining Rayleigh–Taylor Instability in Materials with Strength*, Lawrence Livermore National Laboratory, Livermore, CA, UCRL-JC-132739 ABS. Prepared for *7th Intl Workshop on the Physics of Compressible Turbulent Mixing*, St. Petersburg, Russia, Jul 5, 1999.

Wegner, P. J., Henesian, M. A., Salmon, J. T., Seppala, L. G., Weiland, T. L., Williams, W. H., and Van Wonterghem, B. M., *Wavefront and Divergence of the Beamlet Prototype Laser*, Lawrence Livermore National Laboratory, Livermore, CA, UCRL-JC-129724. Prepared for *3rd Intl Conf on Solid State Lasers for Application (SSLA) to Inertial Confinement Fusion (ICF)*, Monterey, CA, Jun 7, 1998.

Wegner, P. J., Auerbach, J. M., Barker, C. E., Burkhart, S. C., Couture, S. A., De Yoreo, J. J., Hibbard, R. L., Liou, L. W., Norton, M. A., and Whitman, P. A., *Frequency Converter Development for the National Ignition Facility*, Lawrence Livermore National Laboratory, Livermore, CA, UCRL-JC-129725. Prepared for *3rd Intl Conf on Solid State Lasers for Application (SSLA) to Inertial Confinement Fusion (ICF)*, Monterey, CA, Jun 7, 1998.

Wharton, K. B., Kirkwood, R. K., Glenzer, S. H., Estabrook, K. G., Afeyan, B. B., Cohen, B. I., Moody, J. D., MacGowan, B. J., and Joshi, C., *Observation of Resonant Energy Transfer between Identical-Frequency Laser Beams*, Lawrence Livermore National Laboratory, Livermore, CA, UCRL-JC-130320-DR. Prepared for *40th Annual Mtg of the Div of Plasma Physics*, New Orleans, LA, Nov 16, 1998.

Wharton, K. B., *Laser–Plasma Interactions Relevant to Inertial Confinement Fusion*, Lawrence Livermore National Laboratory, Livermore, CA, UCRL-LR-132566.

Wilks, S. C., Liang, E. P., and Tabak, M., *Pair Production by Ultraintense Lasers*, Lawrence Livermore National Laboratory, Livermore, CA, UCRL-JC-124499 Rev 1. Submitted to *Phys. Rev. Lett.*

Williams, W., Lawson, J., and Henesian, M., *PHOMGLASS—Interferometry Analysis Software for Laser Glass Slab Blanks*, Lawrence Livermore National Laboratory, Livermore, CA, UCRL-CODE-99001.

## Z

Zaitseva, N., Carman, L., Smolsky, I., Torres, R., and Yan, M., *Effect of Impurities and Supersaturation on the Rapid Growth of KDP Crystals*, Lawrence Livermore National Laboratory, Livermore, CA, UCRL-JC-132677 Rev 1. Submitted to *J. of Crystal Growth*.

**ICF/NIF and HEDES Program**
Lawrence Livermore National Laboratory
P.O. Box 808, L-475
Livermore, California 94551

**Address Correction Requested**